

Ph.D. thesis

**Extended ground state manifolds of
classical Heisenberg magnets and
magnetoelectric selection rules in
åkermanites**

Péter Balla

Supervisor: Karlo Penc
Wigner Research Centre for Physics

Department of Physics
Budapest University of Technology and Economics



BUTE
2022

Contents

1	Introduction	2
1.1	The Heisenberg model	3
1.1.1	Ordering in Heisenberg magnets	4
1.1.2	Geometric frustration	10
1.1.3	Order by disorder selection	13
1.1.4	Classical spin liquids	14
1.2	Magnetooptics of multiferroics	19
1.3	Structure of the thesis	21
2	Phase diagram of the J_1-J_2-J_3 Heisenberg model on the fcc lattice	23
2.1	Introduction	23
2.2	The lattice and the model	24
2.3	The model in \mathbf{q} -space and the Luttinger-Tisza method	25
2.4	Ground state phase diagram and ordering vectors	27
2.5	Commensurate phases	33
2.5.1	The $\Gamma(0, 0, 0)$ ferromagnet	33
2.5.2	The $X(1, 0, 0)$ antiferromagnet, Type I	34
2.5.3	The $L(\frac{1}{2}, \frac{1}{2}, \frac{1}{2})$ antiferromagnet, Type II	36
2.5.4	The $W(1, \frac{1}{2}, 0)$ antiferromagnet, Type III	37
2.6	Incommensurate phases	40
2.7	Ground states of the extended manifolds	41
2.7.1	The $J_1 = 2J_2 > 0, J_3 = 0$ point: The two-dimensional \mathcal{M}^2 ground state manifold	42
2.7.2	The $\Gamma(0, 0, 0) - \Lambda(q, q, q) - L(\frac{1}{2}, \frac{1}{2}, \frac{1}{2})$ triple point: The one-dimensional \mathcal{M}_Λ^1 ground state manifold	44
2.7.3	The $\Gamma(0, 0, 0) - \Delta(q, 0, 0) - X(1, 0, 0)$ triple point: The one-dimensional \mathcal{M}_Δ^1 ground state manifold	50
2.7.4	The $X(1, 0, 0) - W(1, \frac{1}{2}, 0)$ phase boundary (with an endpoint): The one-dimensional \mathcal{M}_Z^1 ground state manifold	55
2.7.5	The $\Gamma(0, 0, 0) - X(1, 0, 0) - W(1, \frac{1}{2}, 0)$ triple point: The one-dimensional $\mathcal{M}_Z^1 \cup \Gamma$ ground state manifold	57
2.8	Summary	59
3	Constructing extended ground state manifolds	62
3.1	Introduction	62
3.2	The Ansatz and symmetries	63
3.3	Examples	67

3.3.1	Examples on the square lattice	67
3.3.2	Examples on the simple cubic and fcc lattices	70
3.4	Free energy and order by disorder	71
3.5	Summary	75
4	Simple theory of directional dichroism in the paramagnetic state of $\text{Sr}_2\text{CoSi}_2\text{O}_7$	76
4.1	Introduction	76
4.2	Basic structural and magnetic properties of the crystal	77
4.3	Spin Hamiltonian and the magnetoelectric coupling	78
4.4	Experiments	80
4.4.1	Experimental methods	80
4.4.2	Experimental results	81
4.5	Magnetoelectric response and absorption	83
4.6	Exact diagonalization	85
4.7	The single-ion problem	85
4.7.1	The Hamiltonian and the symmetries	86
4.7.2	Directional dichroism in the single-ion model	91
4.8	The lattice problem	96
4.8.1	Magneto-chiral dichroism and selection rules in the lattice problem	96
4.8.2	Perturbative effects of the exchange coupling	98
4.9	Summary	101
5	Thesis statements	103
A	Fourier transform conventions and relations	106
B	Phase boundaries of the J_1-J_2-J_3 model	108
C	Some notions of chirality for non-coplanar states	109
C.1	Scalar chirality	109
C.1.1	The $X(1, 0, 0)$ phase, Type I	110
C.1.2	The $L(\frac{1}{2}, \frac{1}{2}, \frac{1}{2})$ phase, Type II	110
C.1.3	The $W(1, \frac{1}{2}, 0)$ phase, Type III	110
C.2	Chiral enantiomers	110
C.3	Time-reversal and chirality	112
D	Tables for the affine construction in two and three dimensions	113
E	Low temperature free energy of spin spirals	115
F	Magneto-optical response	119
G	Reality of matrix elements in a magnetic point group	120

H	Matrix elements for the single Co-ion problem	123
H.1	Large anisotropy and small field: $\Lambda \gg h$	123
H.2	Large field and small anisotropy: $h \gg \Lambda$	124

Acknowledgments

I never thought that after writing the thesis this part will be so hard to complete, especially because of the fear of leaving out someone important.

First and foremost I have to mention late Patrik Fazekas, who inspired me to study magnetism and his dear memory still lingers here whenever I open his book (and realize how much I do not know about the field). I have to express my sincere gratitude to my supervisor Karlo Penc for all the kindness, help and guidance he provided me, not just professionally but also personally. He guided me through the conundra of physics (and the mazes of bureaucracy) and supported me emotionally in the hard times (and there were many of them).

I would like to thank to my colleagues at the Wigner Research Centre for Physics and at the Budapest University of Technology and Economics for their patience, support and inspiration, especially Orsolya Kálmán whose encouragement helped me a lot when starting to write this thesis. I am very grateful to György Mihály and István Kézsmárki for the opportunity to teach solid state physics practice that I really enjoyed. Similarly would I express my gratitude to Marian Wittmann with whom I shared the joy to teach physics to chemist and bioengineer students, and for the long chitchats. I would also like to thank all my students: Teaching them recharged me with energy and enthusiasm so many times.

I really enjoyed the work done together with Yasir Iqbal (he drew our attention to the fcc problem), and it was a pleasure to show him some hidden parts of Budapest.

And last but not least I am very lucky to have a group of very good friends, without them I surely would have been lost. I thank to Sándor Bordács and Kata Bocz for all the time we spent together (and with their gorgeous daughters Emese and Eszti) and Kata's ongoing sincerity that I surely needed sometimes. Thank Sándor and Dávid Szaller for explaining me the details of magneto-optics over and over again, and for answering my simplistic questions patiently. Mari Vida is a valuable friend, and I cannot even remember how many times she helped me (and virtually everybody at the faculty) to cut through the red tape at the university. I cannot address everything and everyone in detail, but I am thankful to my friends Bea Botka¹, Borbála Fehér, Annamária Kiss, Ágnes Orbán, Judit Romhányi², Péter Rácz, Attila Szilva³ for all the joyful conversations we had, oftentimes through hours (about life, the universe and everything, also physics sometimes). I really do appreciate that I can always count on them and that even though we know each other for ages I still enjoy every single second of the time we spend together.

¹Among many-many other things, for providing me shelter in difficult times.

²The month I spent with her, Ági and Julcsika at Okinawa was probably the best time of my life.

³For bringing me back to life.

Chapter 1

Introduction

Based on electronic transport properties –from an oversimplified point of view– materials can either be conductors or insulators. Several types of insulators can be distinguished, *band insulators* where the valence band is filled and the conduction band is empty and they are separated by an energy gap, *Anderson insulators* where disorder localizes the electrons and *Mott insulators* where electron-electron interactions prevent conductance. In the following we will be concerned about Mott insulators and their magnetism.

The simplest model of electron-electron correlations in crystals is the acclaimed *Hubbard model* [1, 2, 3] introduced in the early sixties

$$\mathcal{H}^{\text{Hubbard}} = -t \sum_{\langle i,j \rangle} \left(\hat{c}_{i\sigma}^\dagger \hat{c}_{j\sigma} + \text{h.c.} \right) + U \sum_i \hat{n}_{i\uparrow} \hat{n}_{i\downarrow}. \quad (1.1)$$

This lattice model (with lattice sites i, j representing atomic orbitals) takes into account three basic concepts: (i) The fermionic nature of electrons with spins $\sigma = \{\uparrow, \downarrow\}$, i.e. the Pauli principle (ii) The quantum mechanical tendency of electrons to delocalize, described by the kinetic energy term and quantified by the real hopping amplitude t between adjacent pairs of sites $\langle i, j \rangle$, and (iii) Electron-electron repulsion given by the onsite Coulomb energy $U > 0$ responsible for correlations.

At exact half-filling –when the average number of electrons per site is one– increasing the parameter U/t the electrons *localize* on the lattice sites and the itinerant (metallic) system transforms to an insulator, a phenomenon dubbed as the *Mott transition*. In the limit $U/t \rightarrow \infty$ the model can be mapped to the pure spin-Hamiltonian¹

$$\mathcal{H}^{\text{Heisenberg}} = J \sum_{\langle i,j \rangle} \mathbf{S}_i \cdot \mathbf{S}_j, \quad (1.2)$$

where $J = 4t^2/U > 0$ is the effective exchange interaction between the spins, the remaining degrees of freedom of the localized electrons. This is a result of second order perturbation theory. The model (1.2) is called the *Heisenberg model*² and it will be the starting point of every calculation in this thesis. Going further in perturbation theory, taking into account multiple orbitals per site or spin-orbit coupling, playing with the filling,

¹Sometimes stated poetically as “The charge degrees of freedom are frozen.”

²A positive $J > 0$ prefers an *antiparallel* alignment of neighboring spins, hence this model is called *antiferromagnetic*. Up to my knowledge, there is no such simple way of deriving the *ferromagnetic* model with $J < 0$ from an electronic lattice Hamiltonian similar to (1.1).

introducing further neighbor hoppings or extending the range of the Coulomb repulsion may lead to more and more complicated lattice spins models, but one usually takes a more practical approach. One *assumes* that a magnetic insulator can be described by a lattice spin model, and takes into account all the necessary and symmetry-allowed terms required to describe the physical system at hand.

In what follows we give a brief introduction to Heisenberg models with a special focus on their ground states, e.g. the possible *magnetic orderings*. Afterwards we introduce the notion of *geometric frustration* and its consequences on the ground states of magnets. The last part of the introduction is concerned about magnetoelectric phenomena and how they can be understood based on spin models.

1.1 The Heisenberg model

The most famous model of magnetic insulators is the celebrated *Heisenberg model*

$$\mathcal{H} = \sum_{i,j} J_{ij} \mathbf{S}_i \cdot \mathbf{S}_j, \quad (1.3)$$

that since its introduction almost a century ago [4] is still a subject of active research in its several incarnations. Here we have presented the model in one of its simplest forms: \mathcal{H} is the Hamiltonian, i, j are points of some lattice, and J_{ij} are the exchange constants measuring the interaction strength between the *spins* \mathbf{S}_i sitting on the lattice, and we assume translational and spin rotational invariance (and a finite range of interactions). Note that a negative value of J favors parallel alignment of the spins (ferromagnetism) while a positive one antialigns the spins, favoring antiferromagnetism. In the quantum version of the model \mathbf{S}_i are vectors of spin operators of some spin-length $S = 1/2, 1, 3/2, \dots$. In the extreme quantum case $S = 1/2$ the spin components are just one half of the Pauli matrices, in the other extreme limit $S \rightarrow \infty$ the spins can be thought about as three-dimensional unit vectors $|\mathbf{S}_i| = 1$, resulting the *classical Heisenberg model*. The latter is frequently called the $O(3)$ -model referring to its symmetry under global $O(3)$ rotations, and the spins are called $O(3)$ spins, or simply Heisenberg spins. We can generalize the classical model by changing the dimension of the spin vectors resulting in the $O(n)$ models, where for $n = 2$ we arrive at the so-called *planar* or *XY* model, and for $n = 1$ the spins simply become $\mathbf{S}_i = \{\pm 1\}$ yielding the *Drosophila melanogaster* of statistical physics: The Ising model.

We can generalize the model in several ways, i.e. by defining anisotropic exchanges, where J_{ij} is promoted to a 3×3 real matrix (this matrix can represent symmetric exchanges, and also antisymmetric ones called the *Dzyaloshinskii-Moriya interactions*):

$$\sum_{i,j} J_{ij} \mathbf{S}_i \cdot \mathbf{S}_j \rightsquigarrow \sum_{i,j} \mathbf{S}_i^T \cdot \mathbf{J}_{ij} \cdot \mathbf{S}_j. \quad (1.4)$$

Another type of anisotropy is of the form

$$\mathcal{H}^{\text{an}} = \sum_i \mathbf{S}_i^T \cdot \mathbf{\Lambda}_i \cdot \mathbf{S}_i, \quad (1.5)$$

this is the so-called on-site or single-ion anisotropy (for $S = 1/2$ the on-site anisotropy is missing). We will study models for $S = 3/2$ spins containing both types of the aforementioned anisotropies in Chapter 4 to describe the multiferroic antiferromagnet $\text{Sr}_2\text{CoSi}_2\text{O}_7$, with a simple easy-plane on-site anisotropy of the form $\sum_i \Lambda (S_i^z)^2$, with $\Lambda > 0$, that wants to lay the spins in the xy -plane. Finally one can add an external magnetic field \mathbf{h} to the system described by the *Zeeman-term*:

$$\mathcal{H}^Z = - \sum_i \mathbf{h}^T \cdot \mathbf{g}_i \cdot \mathbf{S}_i, \quad (1.6)$$

where we assume a homogeneous field, but let the gyromagnetic factor become a site dependent matrix (g -tensor anisotropy). In what follows we will mostly consider isotropic antiferromagnets, but we will consider the concrete dependence of J_{ij} on the lattice points in Eq. 1.3 in some detail.

1.1.1 Ordering in Heisenberg magnets

Here we *very briefly* describe the possible orders present in magnets described by the classical isotropic Heisenberg model (1.4) in real and Fourier space, give some illustrative examples on the square lattice and some real world examples (mostly face-centered cubic antiferromagnets). Afterwards we introduce the notion of *geometric frustration* and some of its consequences, and we briefly mention the closely related and very actual topic of *spin liquids*. We rewrite the Heisenberg Hamiltonian in a little more convenient form

$$\mathcal{H} = \frac{1}{2} \sum_{i,\delta} J_\delta \mathbf{S}_i \cdot \mathbf{S}_{i+\delta} = N \sum_{\mathbf{q} \in \text{BZ}} J(\mathbf{q}) \mathbf{S}_{\mathbf{q}} \cdot \mathbf{S}_{-\mathbf{q}}, \quad (1.7)$$

where $i \equiv \mathbf{R}_i$ are points of some lattice with N sites and periodic boundary conditions, and $i + \delta$ is a shorthand for $\mathbf{R}_i + \delta$, and the δ -s are the lattice separation vectors $\mathbf{R}_j - \mathbf{R}_i$. By lattice translation invariance the exchange couplings J_δ are independent of i , and $1/2$ stands against overcounting the bonds. We sort the J_δ -s by the increasing length of δ leading to the common notation of first-, second-, third-, ... neighbor exchanges as J_1, J_2, J_3, \dots , respectively. Conventions for the Fourier transforms and the derivation of Eq. (1.7) are given in Appendix A. The Fourier transform of the exchange coupling is defined as

$$J(\mathbf{q}) = \frac{1}{2} \sum_{\delta} J_\delta e^{-i\mathbf{q} \cdot \delta}, \quad (1.8)$$

and BZ stands for Brillouin zone in Eq. (1.7). We are interested in the *ground state* of the system (magnetic order). When we cool down the system starting from the high temperature, paramagnetic phase we usually observe anomalies in the thermodynamic properties at some finite temperature (dubbed as T_C for Curie temperature in ferromagnets and T_N for Néel temperature in antiferromagnets): We see a sharp cusp in the heat capacity C (and in the magnetic susceptibility χ) signaling a sudden loss of entropy, i.e. ordering.³ In Fig. 1.1(a) we show heat capacity measurements from 1928 [5] on three different kinds of manganese oxides: The most pronounced cusp is observed for MnO around 120 K (the other two compounds presented are MnO_2 and Mn_3O_4). The inverse of the magnetic sus-

³The temperature dependence of the entropy is given as $S(T) = \int_0^T C(T')/T' dT'$.

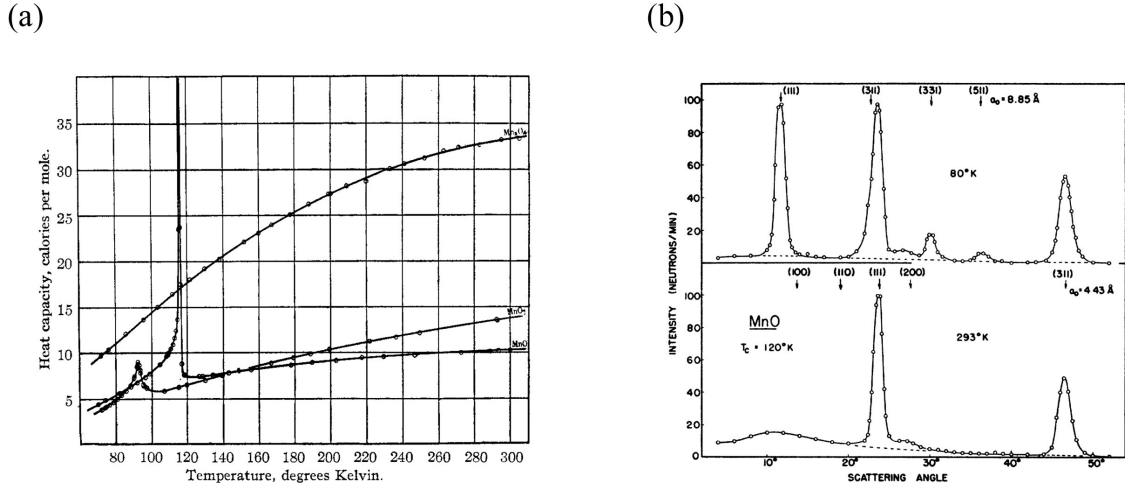


Figure 1.1: (a) Temperature dependence of the heat capacity of MnO, MnO₂ and Mn₃O₄. The most pronounced cusp is observed for MnO at about $T_N \approx 120$ K signaling the phase transition to an antiferromagnetically ordered state [5] (a small cusp at about 90 K can be seen for MnO₂, and there is no apparent sign of a phase transition for Mn₃O₄). (b) Neutron scattering on MnO [6]. Lower panel: Bragg peaks of the underlying lattice in the paramagnetic phase at 293 K. Upper panel: Additional magnetic Bragg peaks appearing in the antiferromagnetically ordered state, measured at 80 K.

ceptibility at high temperature follows the *Curie-Weiss law*: $\chi^{-1} \propto T - \Theta_{CW}$, with Θ_{CW} being the Curie-Weiss temperature. The magnitude and sign of this quantity is characteristic of the magnitude and sign of the exchange interactions (in ferromagnets and simple, nonfrustrated antiferromagnets): $k_B \Theta_{CW} \approx -zJS^2$, where k_B is the Boltzmann constant and z is the coordination number. For simple antiferromagnets $T_N \approx -\Theta_{CW}$, meaning that the exchange energy and the ordering temperature are roughly the same. For a sketch of the inverse susceptibility of an unfrustrated antiferromagnet see Fig. 1.4(a). We will see that the situation is quite different for frustrated systems.

More detailed information about magnetic ordering can be gained by *neutron scattering*: Fig. 1.1(b) shows the appearance of extra reflections (the *magnetic Bragg peaks*) in the neutron diffraction pattern below the ordering temperature signaling the enlargement of the unit cell by the magnetic order in MnO (taken from [6] from 1951, Shull has earned the Nobel prize for this work four decades later in 1994).⁴ This is a quite typical situation:

⁴MnO crystallizes in the rock salt structure, where both the Mn²⁺ and O²⁻ ions form face-centered cubic (fcc) lattices, the magnetic ions Mn²⁺ have spin $S = 5/2$. The magnetic ordering associated with the scattering picture presented in Fig. 1.1(b) consists of $\langle 111 \rangle$ planes ordered ferromagnetically, with the consecutive planes having antiparallel magnetizations. We will dub an order like this as a single- \mathbf{Q} , $L(\frac{1}{2}, \frac{1}{2}, \frac{1}{2})$ -type or Type II ordering and explain it in detail in Section 2.5.3. Many other metal oxides crystallize in the same rock salt structure and are fcc antiferromagnets at a sufficiently low temperature, namely FeO, NiO, CoO and CuO [7], another such an example is the sulfide MnS. This abundance of fcc magnets motivated us to study the $J_1 - J_2 - J_3$ Heisenberg model on the fcc lattice, see Chapter 2 (we found that this model besides being important and interesting was not analyzed before). Another example is GdPtBi [8], a Weyl semimetal, half-Heusler compound, with the magnetic Gd³⁺ ions ($S = 7/2$) forming an fcc lattice: Here all the $J_1 - J_2 - J_3$'s

The appearance of magnetic Bragg peaks in elastic neutron scattering is a signal of magnetic ordering, and the peak positions are related to the type of order (neutron scattering measures the Fourier transform of the spin-spin correlations).⁵ Now we examine and illustrate the correspondence between the real space spin patterns and their Fourier pictures (the magnetic Bragg peak positions) in some simple models on the square lattice.

We consider the *bipartite*⁶ square lattice with primitive lattice translations $\mathbf{a}_1 = (1, 0)$ and $\mathbf{a}_2 = (0, 1)$ and corresponding reciprocal lattice vectors $\mathbf{b}_1 = (2\pi, 0)$ and $\mathbf{b}_2 = (0, 2\pi)$. We define the model (1.7) for $O(3)$ spins on the lattice up to fourth neighbor interactions to show a variety of different ordering patterns together with their Fourier pictures (for the neighbor bonds see Fig. 1.2(a)). We denote the ground space spins by \mathbf{S}_i , and we Fourier expand it as

$$\mathbf{S}_i = \sum_{\mathbf{Q}} \mathbf{S}_{\mathbf{Q}}^0 e^{-i\mathbf{Q}\cdot\mathbf{R}_i}, \quad (1.9)$$

where $\mathbf{S}_{\mathbf{Q}}^0 \in \mathbb{C}^3$ is a complex Fourier amplitude vector, and \mathbf{Q} is the *ordering vector* of the pattern. We will show later (see Subsection 2.3) that the set of possible ordering vectors $\{\mathbf{Q}\}$ correspond to the set of points in Fourier space where *the Fourier transform of the interactions* $J(\mathbf{Q})$ achieves its minimum, and we denote this set as \mathcal{M}_{GS} and call it the *ground state manifold*. Usually this manifold is just a handful of points in the Brillouin zone (BZ), i.e. the actual Bragg peaks. Conditions of having a ground state manifold of higher dimensionality and its consequences on the physics of the system will be a recurrent topic of this thesis.

Before introducing some selected orders, we have an important remark: Every magnetic order breaks the *global* $O(3)$ symmetry (a three-parameter Lie-group) of the Hamiltonian (1.7), a phenomenon called *spontaneous symmetry breaking*. In a ferromagnet the ground state energy is independent of the direction of magnetization, and the system randomly picks one of these equivalent directions. The ground state has a remnant symmetry of a global $U(1)$ about the magnetization direction, and the degeneracy of the possible ground states can be parameterized by the unit sphere S^2 . Similar considerations apply to all the states considered below. This type of degeneracy related to the symmetry breaking is called *trivial* in the context of frustrated systems (not surprisingly we will find other types of degeneracies unrelated to the symmetries of the model). We just mention one dire consequence of the spontaneous breaking of a global continuous symmetry (for interactions of sufficiently short range), the celebrated *Goldstone theorem*: This theorem guarantees the appearance of gapless bosonic quasiparticles in the spectrum, the magnons. Now we turn

are needed to describe the magnon spectrum (the order is $L(\frac{1}{2}, \frac{1}{2}, \frac{1}{2})$ -type or Type II).

⁵The question arises: Why are the intensities of the nuclear and magnetic Bragg-peaks comparable (see the upper panel of Fig. 1.1(b))? Nuclear neutron scattering is mediated by the very short-ranged and strong nuclear forces between the neutron and the nuclei, and magnetic scattering is governed by the long-ranged but very weak dipole-dipole interactions between the magnetic moment of the neutron and the magnetic moments of the electrons. There is no apparent reason why these two different mechanisms would produce scattering intensities of the same magnitude, and up to my knowledge this is sheer accident.

⁶A lattice is bipartite if it can be divided to two sublattices A and B where all the neighbors of the points in A belong to B and vice versa. The cubic lattices in any dimensions are bipartite, just like the body-centered cubic lattice, or the diamond and honeycomb lattices. Non-bipartite lattices are e.g the triangular (hexagonal) lattice or its three dimensional analogue the fcc lattice and the kagome and pyrochlore lattices.

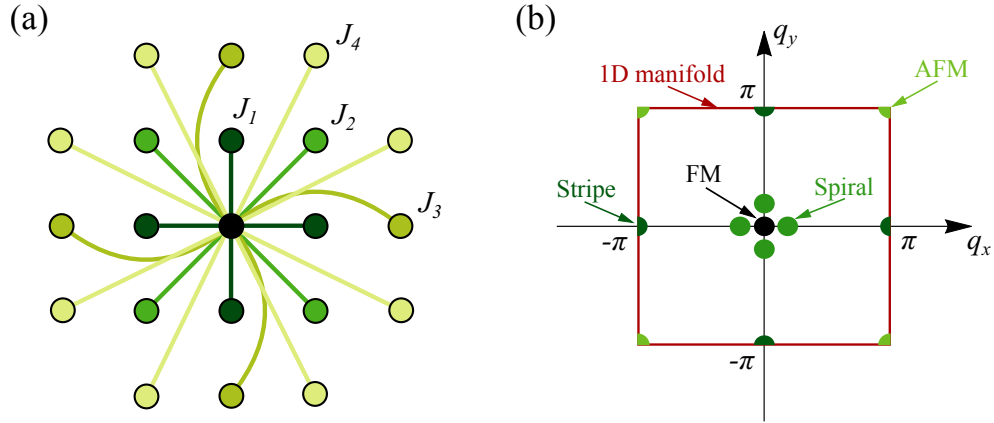


Figure 1.2: (a) The first four nearest neighbor sets of the square lattice, lighter colors indicate further bonds. (b) First Brillouin zone of the square lattice together with the ground state manifolds of different Heisenberg models on the lattice. Magnetic Bragg peaks appear at these points in neutron scattering. The manifolds belong to orders shown in Fig. 1.3. The ground state manifold of the ferromagnet is the zone center, that of the antiferromagnet is the zone corner, spin stripes correspond to manifolds at the midpoints of the zone boundaries, incommensurate spirals have manifolds in general points of the Brillouin zone. The zone boundary corresponds to the one dimensional degenerate ground state manifold of the model with parameters $J_1 = 2J_2 = 1$.

to the examples on the square lattice.

The square lattice with the first four nearest neighbor bond-sets is shown in Fig. 1.2(a). We consider orderings with zero dimensional \mathcal{M}_{GS} 's, the Brillouin zone of the square lattice with the ground state manifolds corresponding to the selected orderings is presented in Fig. 1.2(b). Fig. 1.3 illustrates the selected orderings and here we describe it in detail. The picture consists of two columns, in the first column we give figures of $J(\mathbf{q})$ over the first BZ shown in Fig. 1.2(b), and the contour plot of $J(\mathbf{q})$ in the BZ is also shown. Red dots denote the minima $\{\mathbf{Q}\}$ (ordering vectors) of $J(\mathbf{q})$, i.e. the \mathcal{M}_{GS} in the first BZ. In the second column we give the real space picture of the corresponding spin patterns. Because of the isotropy of the model the global orientation of the spins is arbitrary, and we chose it by aesthetic considerations, color coding of the arrows corresponds to their orientation. The details of the four figures follow, where (i, j) are Cartesian coordinates of the lattice sites:

- (a) **Ferromagnet** Nonvanishing interactions are: $J_1 = -1$, with Fourier transform of the exchanges $J(\mathbf{q}) = -\cos(q_x) - \cos(q_y)$. The ordering vector (the whole \mathcal{M}_{GS}) is $\mathbf{Q} = (0, 0)$, and the real space spin pattern is $\mathbf{S}(i, j) = \mathbf{S}_0 = (1, 1, 0)/\sqrt{2}$. Every ferromagnetic bond can be simultaneously optimized by aligning all the spins, and this is independent of the type of the underlying lattice. The order is *commensurate* since \mathcal{M}_{GS} is a special point in the BZ. Up to the trivial degeneracy due to the $O(3)$ symmetry breaking, the ground state is unique.
- (b) **Antiferromagnet** Nonvanishing interactions are: $J_1 = +1$, with Fourier transform

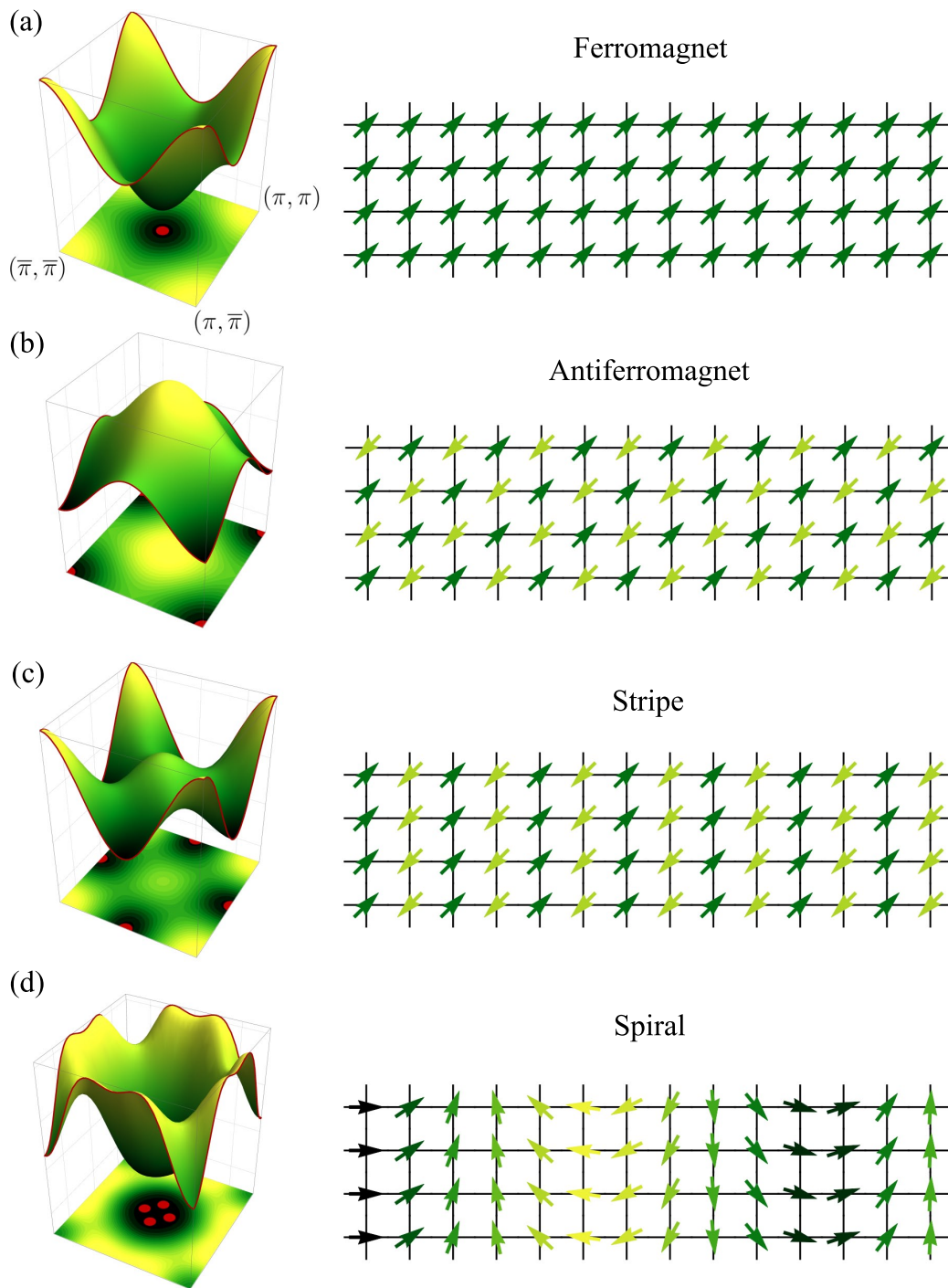


Figure 1.3: Illustration of different spin orderings on the square lattice. The first column shows pictures of $J(\mathbf{q})$ over the BZ (the BZ corners are indicated in (a)), red dots show the minima of $J(\mathbf{q})$ on a contour plot. The second column shows the appropriate spin patterns on the square lattice. For details see the main text.

of the exchanges $J(\mathbf{q}) = +\cos(q_x) + \cos(q_y)$. The ordering vector (the whole \mathcal{M}_{GS}) is $\mathbf{Q} = (\pi, \pi)$, and the real space spin pattern is $\mathbf{S}(i, j) = (-1)^{i+j}\mathbf{S}_0$. Every antiferromagnetic bond can be simultaneously optimized by antialigning the spins in a checkerboard pattern, but this is only allowed because of the *bipartite* nature of the square lattice. The order is *commensurate* since \mathcal{M}_{GS} is a special point in the BZ. Up to the trivial degeneracy due to the $O(3)$ symmetry breaking, the ground state is unique.

- (c) **Stripe** Nonvanishing interactions are: $J_1 = -1$, $J_2 = +2$, with Fourier transform of the exchanges $J(\mathbf{q}) = -\cos(q_x) - \cos(q_y) + 2\cos(q_x + q_y) + 2\cos(q_x - q_y)$. The set of ordering vectors is $\mathcal{M}_{\text{GS}} = \{\mathbf{Q}\} = \{(\pi, 0), (0, \pi)\}$, and we choose $\mathbf{Q} = (\pi, 0)$ in the illustration. The pattern in real space reads $\mathbf{S}(i, j) = (-1)^i\mathbf{S}_0$. The order is *commensurate* since \mathcal{M}_{GS} is a special point of the BZ. Up to the trivial degeneracy due to the $O(3)$ symmetry breaking, the ground state is unique (besides that we could also have chosen $\mathbf{Q} = (0, \pi)$ as the propagation direction of the stripes).
- (d) **Spiral** Nonvanishing interactions are: $J_1 = -1$, $J_2 = -1$, $J_3 = 0$, $J_4 \approx 0.14$, we have tweaked the interactions the way that the possible ordering vectors become $\mathbf{Q} = (\pm 0.6, 0)$ or $\mathbf{Q} = (0, \pm 0.6)$, we choose $\mathbf{Q} = (\pm 0.6, 0)$ for the illustration. This way the wavelength of our spin spiral is a little larger than ten lattice constants, and the real space pattern reads $\mathbf{S}(i, j) = (\cos(0.6i), \sin(0.6i), 0)$. The order is *incommensurate* since the \mathcal{M}_{GS} consists of *general* points of the BZ. The $O(3)$ symmetry breaking manifests itself in the freedom of choice of the plane of rotation of the spins. Here our spins lie in the xy planes (spirals of this kind are sometimes called cycloidal for obvious reasons, when the plane of rotation of the spins is perpendicular to the ordering vector—or pitch vector as it is called sometimes in this context—the spiral is called helicoidal).

Although the orderings described above are all markedly different, they have a thing in common: All their ground state manifolds are zero dimensional, i.e. if we do neutron scattering on these systems, magnetic Bragg peaks will appear at the ordering vectors $\{\mathbf{Q}\}$ as shown in Fig. 1.2(b). Slightly perturbing the interaction parameters will not change this picture, i.e. this is a quite robust feature of these models.

The situation changes dramatically if we choose the parameter set as $J_1 = 2J_2 = 1$: The minimum of $J(\mathbf{q})$ becomes the *whole Brillouin zone boundary*, with $\mathbf{Q} = (\pi, q)$ and (q, π) parameterized by $q \in [-\pi, \pi]$ (see the red square in Fig. 1.2(b)). This is a one-dimensional manifold (or codimension-one manifold, since it has one dimension less than the BZ), and the system is free to choose any $\pm\mathbf{Q}$ pair on this manifold as an ordering vector. What is more: One can even combine such (if one is careful enough of tweaking the Fourier amplitudes in (1.9)) ordering vectors to create a large class—e.g. aperiodic—of ground states. This degeneracy is totally unrelated to any symmetry of the Hamiltonian. We do not discuss this case any further here, since we analyze this model in minutious detail in Subsection 3.3.1. What is important to see here, that this manifold is totally different from the well-known Bragg peaks.

We have seen that the square lattice (or any bipartite lattice) with only nearest neighbor interactions is well suited for antiferromagnetism since the bonds can be simultaneously

satisfied, but introducing *frustrating* further neighbor interactions can lead to more complex patterns, e.g. the aforementioned spin spirals, or the multitude of ground states in the case of the $J_1 = 2J_2 = 1$ model. In the next subsection we discuss lattices where the nearest neighbor interactions alone introduce frustration. This is the so-called *geometric frustration* what we analyze in some detail in the following.

1.1.2 Geometric frustration

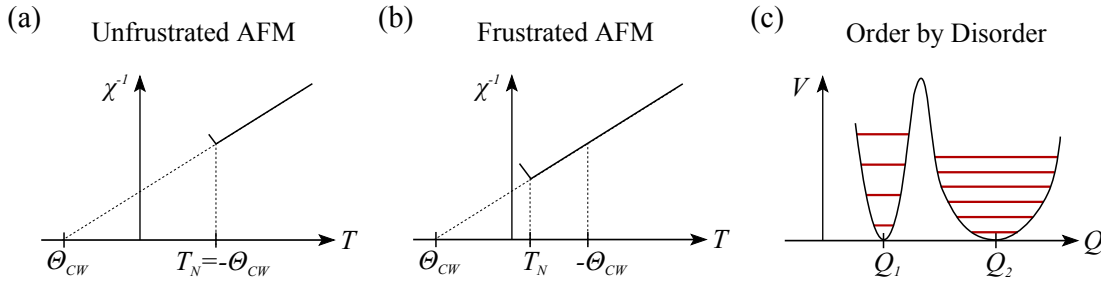


Figure 1.4: (a) Temperature dependence of the inverse susceptibility of an ordinary (unfrustrated) antiferromagnet. The Curie-Weiss temperature Θ_{CW} can be identified by extrapolating the high temperature part of the inverse susceptibility, its value is a good measure of the magnetic interaction strengths. The actual transition temperature (T_N stands for Néel temperature) signaled by an anomaly in the susceptibility (and similarly in the heat capacity) is roughly equal to $|\Theta_{CW}|$. (b) Temperature dependence of the inverse susceptibility of a frustrated antiferromagnet: Nothing dramatic happens to the thermodynamic quantities at $|\Theta_{CW}|$ (extrapolated from the high temperature behavior of the inverse susceptibility and measuring the interaction strengths). The Néel temperature –as signaled by anomalies in the susceptibility and heat capacity– is far below $|\Theta_{CW}|$, indicating fluctuations well below the temperature scale set by the interactions. (c) Illustration for the quantum order by disorder mechanism. Q is some configurational coordinate, $V(Q)$ is a double-well potential, with minima $V(Q_1) = V(Q_2) = 0$. The oscillator at Q_2 is softer than the one at Q_1 . Red lines show the energy levels of the two oscillators at Q_1 and Q_2 : $E_{n_1} \approx \omega_1(n_1 + \frac{1}{2})$ and $E_{n_2} \approx \omega_2(n_2 + \frac{1}{2})$, where the integers $n_i \geq 0$ are the occupation numbers and $\omega_2 < \omega_1$, so the energies are smaller at the second well.

Here we give a brief introduction to geometric frustration in magnets.⁷ We can see in Fig. 1.4(a) that the Curie-Weiss temperature Θ_{CW} , which measures the interaction strength J , is roughly equal to the ordering Néel temperature T_N of the ordering in usual antiferromagnets. In materials with lattices containing triangles the situation is markedly different and the susceptibility is sketched in Fig. 1.4(b): The ordering temperature is well below the energy set by the interactions, i.e. $T_N \ll \Theta_{CW}$ and nothing dramatic happens to the

⁷The book [9] is a good reference on frustrated magnetism covering a wide range of topics, including classical and quantum models, spin liquids, experimental techniques and results, numerical tools, etc. The textbook by Patrik Fazekas [10] is a neat introduction to magnetism, with a particular focus on frustrated systems.

thermodynamic properties at Θ_{CW} . The system wants to order antiferromagnetically but something prevents it: One such reason can be *geometric frustration*. We measure the deviation from the standard antiferromagnetic behavior by the quantity $f = |\Theta_{CW}|/T_N$, and show it for some selected materials in Table 1.1. To understand the reason behind the above

Table 1.1: Properties of some selected two and three dimensional antiferromagnets, taken from [11] and [12], the data in the last line for MnSc_2S_4 are taken from [13] and the data for GdPtBi are taken from [8]. First column: Chemical formula. Second column: The lattice of the magnetic ions. Third column: Curie-Weiss temperature as extracted from the high temperature behavior. Fourth column: Néel-temperature signaled by anomalies in the heat capacity or magnetic susceptibility. Fifth column: The ratio $f = |\Theta_{CW}|/T_N$ measures the strength of frustration, larger f means a more frustrated system.

Compound	Paramagnetic lattice	$-\Theta_{CW}$ [K]	T_N [K]	$f = \Theta_{CW} /T_N$
Two dimensional magnets				
VCl_2	triangular	437	36	12
NaTiO_2	triangular	1000	<2	>500
LiCrO_2	triangular	490	15	33
$\text{SrCr}_8\text{Ga}_4\text{O}_{19}$	kagome	515	3.5	150
Three dimensional magnets				
MnO	fcc	610	116	5.3
MnS	fcc	528	160	3.3
FeO	fcc	570	198	2.9
CoO	fcc	330	291	1.14
NiO	fcc	~ 2000	525	~ 4
K_2IrCl_6	fcc	321	3.1	10
GdPtBi	fcc	38	9	4.2
CsNiFeF_5	pyrochlore	210	4.4	48
$\text{Gd}_3\text{Ga}_5\text{O}_{12}$	garnet	2.3	<0.03	>100
MnSc_2S_4	diamond	22.9	2.1	11

mentioned avoidance of ordering we consider antiferromagnetically coupled ($J > 0$) Ising spins S_i on a triangle. A glimpse at Fig. 1.5(a) shows that only *two* bonds can be simultaneously optimized with energy $-J$ (instead of $-3J$ for all bonds optimized independently) and this ground state is sixfold degenerate (the other two fully polarized states have an energy of $3J$).⁸ The moral is the following: If we have triangles in a lattice with antiferromagnetic interactions the ground state tends to be highly degenerate, and the system cannot pick a single state of the ground state manifold. We can put together the triangles

⁸Every configuration has a spin-flip related partner as a consequence of the $S_i \rightarrow -S_i$ symmetry of the Hamiltonian.

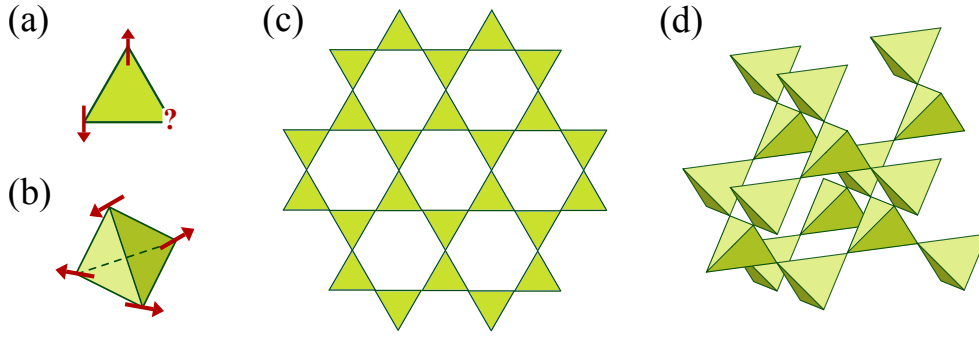


Figure 1.5: (a) Antiferromagnetically coupled Ising spins on a triangle. (b) Antiferromagnetically coupled Heisenberg or $O(3)$ spins on a tetrahedron. (c) The kagome lattice consisting of corner sharing triangles. (d) The pyrochlore lattice consisting of corner sharing tetrahedra.

in an edge-sharing manner to form the triangular lattice and ask about the ground state degeneracy. Wannier [14] has analyzed this model thoroughly and found an *extensively* large ground state degeneracy with a zero-point entropy of $S(T = 0)/N \approx 0.3230k_B$ and that the system does not order at any temperature. Putting together the triangles in a corner-sharing manner we construct the kagome lattice as depicted in Fig. 1.5(c): This lattice is even more frustrated than the triangular one with a zero-point entropy of $S(T = 0)/N \approx 0.50183k_B$ [15].⁹ For some real world triangular and kagome magnets consult Table 1.1.

To further illuminate the connection between frustration and ground state degeneracy let us consider four antiferromagnetically coupled Heisenberg (or $O(3)$) spins on a tetrahedron (see Fig. 1.5(b)) with Hamiltonian

$$\mathcal{H}^{\boxtimes} = J \sum_{\langle i,j \rangle} \mathbf{S}_i \cdot \mathbf{S}_j, \quad (1.10)$$

where $J > 0$ and the summation runs over all six edges of the tetrahedron. To find the ground states we rewrite the Hamiltonian as a *complete square*:

$$\mathcal{H}^{\boxtimes} = \frac{J}{2} (\mathbf{S}_1 + \mathbf{S}_2 + \mathbf{S}_3 + \mathbf{S}_4)^2 - 2J, \quad (1.11)$$

which is minimized if and only if

$$\mathbf{S}_1 + \mathbf{S}_2 + \mathbf{S}_3 + \mathbf{S}_4 = \mathbf{0}, \quad (1.12)$$

which we call the *tetrahedron rule*. The ground state energy becomes $-2J$, much higher than $-6J$ for six independently optimized bonds. We can calculate the number of free parameters describing the degeneracy: The four unit vectors mean eight free parameters, the tetrahedron rule means three constraints (removes three free parameters), and the global rotation of the configuration described by $O(3)$ also removes three free parameters (we do

⁹As a sidenote the ground state manifold of the antiferromagnetic kagome Heisenberg model is the *whole* BZ (the lowest eigenvalue of $\mathbf{J}(\mathbf{q})$ is totally flat), i.e. as degenerate as it can be.

not want to count this trivial degeneracy and $O(3)$ is three-dimensional). So we are left with $2 = 8 - 3 - 3$ free real parameters to describe the degeneracy [16, 17, 18]. We can put together the tetrahedra in an edge-sharing manner to form the fcc lattice (see Fig. 2.1(c)) and ask about the ground state degeneracy. The ground state manifold in \mathbf{q} -space is one dimensional and is depicted in Fig. 2.3(b) and this problem is analyzed in Subsection 2.7.4, for the calculation of the entropy see Ref. [19]. Putting together the tetrahedra in a corner-sharing manner we construct the pyrochlore lattice as depicted in Fig. 1.5(d). This lattice is even more frustrated than the fcc one. The ground state manifold of the pyrochlore Heisenberg model is the *whole* BZ, i.e. as degenerate as it can be. For some real world fcc and pyrochlore magnets consult Table 1.1.

Here we have only considered frustration as an effect of lattice geometry, but we can find similar behavior even on bipartite lattices if we introduce frustrating further neighbor exchanges (see examples on the square lattice in Subsection 3.3.1). As an example it was theoretically proposed in Ref. [20] that introducing a frustrating second neighbor interaction on the bipartite diamond lattice results in a two dimensional ground state manifold, and this manifold was found via neutron scattering for the spinel MnSc_2S_4 [21] where the Mn^{2+} ions with $S = 5/2$ on the A -sites form a diamond lattice (it turned out later that this compound besides being a *spin liquid* even forms a “fractional antiferromagnetic skyrmion lattice” [22], for some data on the material see the last line in Table 1.1).

As a summary, if not all bonds can be simultaneously satisfied the system is frustrated, frustration can lead to large ground state degeneracy (a large number of ground state configurations and extended manifolds in Fourier space visible by neutron scattering), and frustration prevents the system from antiferromagnetic ordering down to very low temperatures. We have only considered classical models so far. In the next section we describe a mechanism of choosing a particular ground state from the degenerate ones if we introduce quantum (or thermal) fluctuations.

1.1.3 Order by disorder selection

Regarding energies all states are equal on a ground state manifold, but some states are more equal than others. Here we show a mechanism where thermal or quantum fluctuations select a state from the classically degenerate ground state manifold as the true ground state: The *order by disorder* mechanism (the original references are [16, 23, 24, 18] and the first chapter of [9] is a pedagogical introduction to the subject). We assume that we have a quantum particle in the double-well potential $V(Q)$ depicted in Fig. 1.4(c), where Q is some configurational coordinate. We choose the two minima to be equal $V(Q_1) = V(Q_2) = 0$, and we approximate the potential harmonically about the minima as

$$V(Q - Q_1) \approx \frac{1}{2}\omega_1^2(Q - Q_1)^2 \quad \text{and} \quad V(Q - Q_2) \approx \frac{1}{2}\omega_2^2(Q - Q_2)^2, \quad (1.13)$$

with $\omega_1 > \omega_2$. The approximate eigenenergies for a particle around the minima are $E_{n_1} \approx \omega_1(n_1 + \frac{1}{2})$ and $E_{n_2} \approx \omega_2(n_2 + \frac{1}{2})$, where the integers $n_i \geq 0$ are the occupation numbers (these energy levels are denoted by horizontal red lines in Fig. 1.4(c)). The two minima are classically degenerate, at zero temperature the system cannot choose between the two minima, but zero point *quantum fluctuations* will choose the one with lower

energy and select Q_2 (at $T = 0$, $n_1 = n_2 = 0$ and the energies are $\omega_2/2 < \omega_1/2$). This selection of a definite state by fluctuations is the order by disorder mechanism.

Thermal fluctuations work similarly. Let us suppose that we have a statistical physical system, with a degenerate set of ground states parameterized by some configurational coordinate Q with the ground state energy \mathcal{E}_0 being independent of Q . The free energy to minimize at finite T is

$$\mathcal{F}(Q) = \mathcal{E}_0 - T\mathcal{S}(Q), \quad (1.14)$$

where the entropy $\mathcal{S}(Q)$ *does depend* on the configuration Q : The state with larger entropy (larger density of states) will be selected thermally, i.e. thermal fluctuations (disorder) select an order.¹⁰

How can we apply the above considerations to our spin systems? Let us take the antiferromagnetic tetrahedron as an example (see Fig. 1.5(b)). The ground states all satisfy the tetrahedron rule in Eq. (1.12), and they can be parameterized by two real parameters for Heisenberg spins and by one real parameter for planar spins. These parameters play the role of the configurational coordinate Q . The analogue of the oscillator potential wells depicted in Fig. 1.4(c) is the following. Let us pick a spin \mathbf{S}_1 , the other spins act on it with the effective molecular field (see Eq. (1.10))

$$\mathbf{h}_1^{\text{eff}} = -\frac{\partial \mathcal{H}^{\boxtimes}}{\partial \mathbf{S}_1} = -J(\mathbf{S}_2 + \mathbf{S}_3 + \mathbf{S}_4), \quad (1.15)$$

and make \mathbf{S}_1 precess about $\mathbf{h}_1^{\text{eff}}$ with some frequency ω governed by the equation

$$\dot{\mathbf{S}}_1 = \mathbf{S}_1 \times \mathbf{h}_1^{\text{eff}}. \quad (1.16)$$

Since the effective field is configuration dependent so is the frequency. In lattice systems the modes are the propagating spin precessions, the magnons. The selected ground states –if the order by disorder mechanism works at all– can be found in principle by calculating the spectrum of excitations above all the possible ground states, counting their energies and choosing the lowest one. Details matter, but a tendency (see Refs. [18, 9]) towards selecting *collinear* (or at least coplanar) orders is general (both for the thermal and quantum mechanisms). It can be shown (see Ref. [9]) that for a tetrahedron of Heisenberg spins thermal order by disorder is absent, but it selects a collinear configuration for planar spins. Heisenberg spins on the pyrochlore lattice do not show order by disorder but planar spins do. Heisenberg spins on the kagome lattice order coplanarly [25, 26] and planar spins show no order by disorder on the kagome lattice. In what follows we say a few words about interesting phases of matter strongly related to frustration, the *spin liquids*.

1.1.4 Classical spin liquids

Spin liquids are notoriously hard to define, because of almost philosophical reasons: Their most intuitive definition is based on the *lack* of properties.¹¹ Spin liquids are not ordinary

¹⁰For concrete examples of thermal order by disorder calculations of some Heisenberg models on the simple cubic and fcc lattices see Section 3.4 and for the details of these calculations see Appendix E.

¹¹The intrigued reader is directed to the literature: We have already mentioned the book [9] which reviews several basic properties, experimental techniques, theoretical and numerical tools related to the study of frus-

paramagnets (spin “gas” without magnetic Bragg peaks) and they do not show magnetic order with well defined magnetic Bragg peaks, but something in between. Let us assume that we have a material with frustration parameter f large enough to have a temperature range $T_N < T \ll \Theta_{CW}$, in this range the system is not ordered (there are strong fluctuations because of the large number of energetically equivalent states), but there are short range correlations (corresponding to broad features in Fourier space), this state is sometimes dubbed a “cooperative paramagnet”. In what follows we illustrate the above mentioned properties of *classical spin liquids*¹² by some concrete examples.

Detailed information about the nature of spin ordering (or the lack of it) is encoded in the *spin-spin correlation functions*

$$G^{\alpha\beta}(\mathbf{R}_j - \mathbf{R}_i) \equiv G^{\alpha\beta}(\boldsymbol{\delta}) = \langle S_i^\alpha S_{i+\boldsymbol{\delta}}^\beta \rangle, \quad (1.17)$$

where the average $\langle \dots \rangle$ is either a thermal one or an average over the ground state manifold (and we denote the lattice separation by $\boldsymbol{\delta} = \mathbf{R}_j - \mathbf{R}_i$).¹³ The Fourier transform of the above function is the *static spin structure factor*

$$\mathbf{S}^{\alpha\beta}(\mathbf{q}) = \frac{1}{N} \sum_{ij} G^{\alpha\beta}(\mathbf{R}_j - \mathbf{R}_i) e^{i\mathbf{q} \cdot (\mathbf{R}_j - \mathbf{R}_i)} = \langle S_{\mathbf{q}}^\alpha S_{-\mathbf{q}}^\beta \rangle, \quad (1.18)$$

and elastic neutron scattering measures the projected part

$$\mathbf{S}(\mathbf{q}) = \sum_{\alpha\beta} \left(\delta_{\alpha\beta} - \frac{q_\alpha q_\beta}{q^2} \right) \mathbf{S}^{\alpha\beta}(\mathbf{q}). \quad (1.19)$$

This function is also called the magnetic structure factor.

In the paramagnetic phase –e.g. for the Ising ferromagnet– correlations decay exponentially at long distances and are completely structureless: $G(\delta) \sim f(\delta)e^{-\delta/\xi}$, with a temperature dependent *correlation length* $\xi(T)$. The function $f(\delta) \propto \delta^{-(d-1)/2}$ decays algebraically in d -dimensional space. This function in Fourier space has the Ornstein-Zernike form being proportional to $1/(q^2 + \xi^{-2})$. Approaching the transition temperature ξ diverges, and the decay of correlations *at the transition temperature* becomes algebraic, called critical behavior. With all these at hand we can formulate a bit more precisely what we expect from a spin liquid, i.e. More structure than the featureless and exponentially decaying form of the paramagnetic correlations, but much less than the sharp Bragg peaks produced by the ordered moments illustrated by dots in Fig. 1.2(b). Now let us give some concrete examples of classical spin liquids.

trated systems including (proposed) spin liquids (for the problems of the definition of quantum spin liquids see the beginning of Chapter 16 of [9]). Examples of *classical* spin liquids are covered in [25, 26], the review [27] is a compact introduction, collecting concrete materials, theoretical definitions and experimental probes of the spin liquid phase. The excellent review [28] is concerned about *quantum spin liquids*, where theoretical models, numerical methods and materials are proposed.

¹²Quantum spin liquids are well beyond the scope of this work.

¹³Occasionally one is only interested in the trace of this matrix $\sum_\alpha G^{\alpha\alpha}(\boldsymbol{\delta}) = \langle \mathbf{S}_i \cdot \mathbf{S}_{i+\boldsymbol{\delta}} \rangle$, or even just its large-distance (small- q) asymptotic. Sometimes one defines the correlation function for just the fluctuations of the spins, i.e. one removes the part $\langle S_i^\alpha \rangle \langle S_{i+\boldsymbol{\delta}}^\beta \rangle$ from $G^{\alpha\beta}(\boldsymbol{\delta})$.

- **Antiferromagnetic Ising model on the triangular lattice** This model shows no order at any temperature and has an extensive ground state degeneracy (finite zero point entropy). Stephenson studied the correlations of this model in Refs. [29, 30] analytically: At finite $T > 0$ he found an exponential decay of correlations with some oscillations in δ . Much more interesting is the ground state manifold $T = 0$, where the correlations decay slowly with a *power law* (with oscillations) $G(\delta) \propto \delta^{-1/2} \cos(2\pi\delta/3)$, i.e. like in some critical point.
- **Ising models on the pyrochlore lattice: Spin ice** Here we mainly follow the argumentation about the correlations by Henley presented in Refs. [31, 32], and Chapter 12 of [9] is a pedagogical review about spin ice physics. We take the titanates $\text{Dy}_2\text{Ti}_2\text{O}_7$ and $\text{Ho}_2\text{Ti}_2\text{O}_7$ as examples, where the rare-earth ions occupy a pyrochlore sublattice with $S = 15/2$ for Dy^{3+} and $S = 8$ for Ho^{3+} . The pyrochlore lattice consisting of corner-sharing tetrahedra is depicted in Fig. 1.5(d). We pick one tetrahedron with its four spins on the vertices (corners). Very strong crystal fields force the spins on a vertex of the tetrahedron to lie on the line joining the center of the tetrahedron with the vertex, making the spin effectively Ising-like, i.e. the spin can either point inward or outward. Although the interactions between the spins are mainly the long-ranged dipole-dipole ones they can be understood by a short ranged and *ferromagnetic* model. Ferromagnetic interactions are corroborated by the measured Curie-Weiss temperature (for $\text{Ho}_2\text{Ti}_2\text{O}_7$) $\Theta_{CW} \approx 2\text{K}$, a *positive* quantity. But the system does not order down to $\sim 20\text{mK}$, meaning it is a *strongly frustrated ferromagnet*.

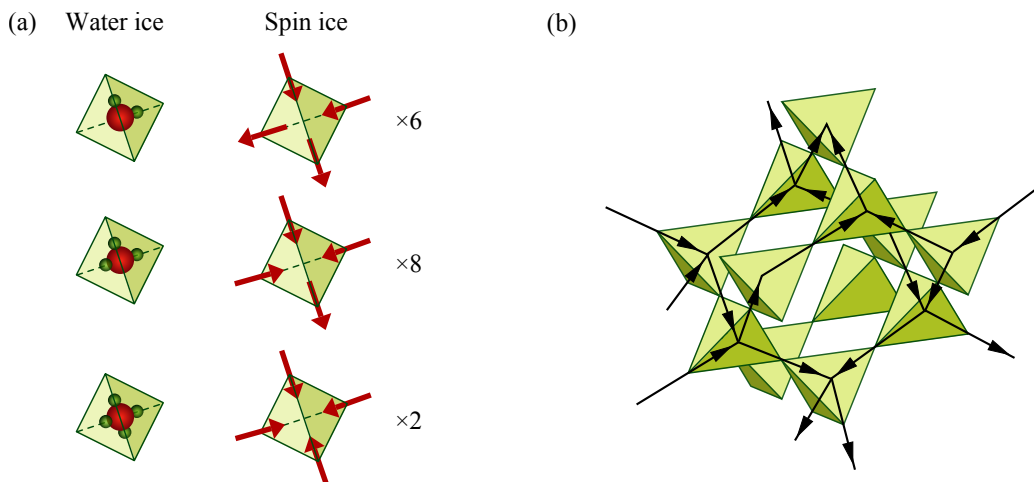


Figure 1.6: (a) Configurations in water ice and spin ice. Red balls are the O^{2-} ions, green balls are the protons H^+ (only the protons close to the oxygen ions are shown). Numbers show the degeneracy of the configurations. (b) Mapping the ground state configuration of the spins on the pyrochlore lattice to its dual diamond lattice (black arrows).

We can understand this frustration: A single tetrahedron has sixteen possible states, two of them are the all-in or all-out ones with zero net magnetization (this configu-

ration is shown at the bottom of Fig. 1.6(a)). Eight of the states are the three-in one-out configurations (or their flipped partners the one-in three-out ones), with nonzero net magnetization (middle of Fig. 1.6(a)). The six energetically favorable states are the two-in two-out ones, yielding the largest net magnetization (top of Fig. 1.6(a)). Consequently the degenerate ground state manifold is spanned by the configurations where all the tetrahedra are in the two-in two-out states having the Pauling zero point entropy per mole tetrahedra of approximately $S(T = 0) \approx R \ln(3/2)$ in complete analogy with water ice (R is the gas constant).¹⁴ Measurements confirmed the value of the zero point entropy, for recent state-of-the-art data on $\text{Dy}_2\text{Ti}_2\text{O}_7$ see Ref. [34]. Now we turn to the description of fluctuations.

The spin ice states can be mapped to a model living on the bonds of the dual lattice of the pyrochlore lattice: The lattice connecting the midpoints of the tetrahedra forming a diamond lattice. We can draw arrows on the diamond network, simply inherited from the spin directions, and the two-in two-out states will map to configurations where in each vertex of the diamond lattice two arrows will “flow” in and two out, see Fig. 1.6(b). Finally one can sum up the vectors around each vertex (a tetrahedron of the original pyrochlore lattice) to define a vector field on the points of the diamond lattice. This field is called *polarization* in Refs. [31, 32] but in the literature it is usually called an emergent *magnetic field*, and after coarse-graining the resulting field becomes $\mathbf{B}(\mathbf{r})$. The magnetic field notation is fortunate since this field inherits from the two-in two-out configurations (on the ground state manifold) the constraint of being solenoidal: $\nabla \cdot \mathbf{B}(\mathbf{r}) = 0$, i.e. being on the ground state manifold of the original model translates to having no magnetic monopoles in the emergent field theory. In Fourier space the divergence-free condition reads

$$\mathbf{q} \cdot \mathbf{B}(\mathbf{q}) = 0. \quad (1.20)$$

The total free energy can be taken as

$$\mathcal{F}_{\text{tot}}(\mathbf{B}(\mathbf{r}))/T = \int \frac{1}{2} \kappa |\mathbf{B}(\mathbf{r})|^2 d\mathbf{r} = \frac{1}{2} \kappa \sum_{\mathbf{q}} |\mathbf{B}(\mathbf{q})|^2, \quad (1.21)$$

completing the analogy with magnetostatics (or charge-free electrostatics, hence the name the “Coulomb phase”). The condition Eq. (1.20) projects out the *longitudinal* part of the correlations of $\mathbf{B}(\mathbf{q})$, and together with the form of the free energy

¹⁴In ordinary (hexagonal I_h) water ice the O^{2-} ions form a sublattice with almost perfect tetrahedral bonding angles (in cubic ice I_c the oxygen ions form a diamond lattice with perfect tetrahedral coordination) and the protons H^+ sit on the O-O bonds. Each proton is either close to one or the other oxygen (see Fig. 1.6(a)). An oxygen is surrounded by four protons and to minimize proton-proton repulsion two protons are close to the selected O-ion, and the other two are far. These are the *ice rules* and they can be satisfied in an extensively large number of ways and are responsible for the residual entropy of water ice. For Pauling’s original estimate of the entropy see [33], note the unit used there is entropy unit (E. U.=cal/K mol) and the gas constant is $R \approx 1.9872\text{E. U.}$

Eq. (1.21) this yields to the correlations in Fourier and real space

$$\begin{aligned}\langle B_{\mathbf{q}}^{\alpha} B_{-\mathbf{q}}^{\beta} \rangle &= \frac{1}{\kappa} \left(\delta_{\alpha\beta} - \frac{q_{\alpha} q_{\beta}}{q^2} \right), \\ \langle B^{\alpha}(\mathbf{0}) B^{\beta}(\mathbf{r}) \rangle &\cong \frac{4\pi}{\kappa} \left[\delta(\mathbf{r}) + \frac{1}{r^3} (\delta_{\alpha\beta} - 3\hat{r}_{\alpha}\hat{r}_{\beta}) \right],\end{aligned}\quad (1.22)$$

at large separations \mathbf{r} with $\hat{\mathbf{r}} = \mathbf{r}/r$. So the correlations have the form of classical *dipole-dipole interactions*, this long-range, power law form is the consequence of the *local* constraint $\nabla \cdot \mathbf{B}(\mathbf{r}) = 0$ (and in the original model, the ice rules). The angular dependence and the power law decay $1/r^3$ clearly distinguishes this type of spin liquid from paramagnets with no structure and exponential decay of correlations.

It is not trivial to connect the real spin data to the ones expressed with the effective field $\mathbf{B}(\mathbf{r})$ above, but it can be shown [31] that the characteristic decay $1/r^3$ remains intact, and the dipolar character manifests itself as *pinch point (or bow-tie)* type singularities in the reciprocal space of the pyrochlore lattice. These pinch points show up without a doubt in neutron scattering, see e.g. Ref. [34] for $\text{Dy}_2\text{Ti}_2\text{O}_7$ and Fig. 3 of the review [32] for $\text{Ho}_2\text{Ti}_2\text{O}_7$.

As a last side-note, one can leave the ground state configurations by e.g. flipping one spin, thereby creating two adjacent tetrahedra of one-in three-out and three-in one-out type, these excitations translate to a pair of *magnetic monopoles* in the language of the field $\mathbf{B}(\mathbf{r})$ (breaking the divergence-free constraint).

- **Subextensive manifolds, MnSc_2S_4** Our last example of classical spin liquids is MnSc_2S_4 [21] where the Mn^{2+} ions with $S = 5/2$ form a bipartite diamond lattice. It was showed in Ref. [20] that for a finite range of the ratio J_2/J_1 of the first and second neighbor AFM interactions on the diamond lattice the ground state manifold is *two dimensional*.¹⁵ The exchange parameters for MnSc_2S_4 fall in that range, thereby realizing a spin liquid with a two dimensional ground state manifold. In Fig. 1.7(a)-(d) we reproduce the results of Fig. 1 of Ref. [21]. The diamond lattice of the Mn^{2+} ions together with the interactions is shown in Fig. 1.7(a), Fig. 1.7(b) shows the manifold in light gray. Fig. 1.7(c) shows the neutron scattering data revealing the manifold and Fig. 1.7(c) shows the Monte-Carlo results for the spin correlations of the $J_1 - J_2$ model on the diamond lattice in excellent agreement with the measured data. For more details see the caption of the figure. What we can see here is the structured correlations, i.e. the “cooperative paramagnetic” behavior of the spin liquid. The measurement was taken at $T = 2.9\text{K}$, slightly above the Néel-temperature $T_N = 2.1\text{K}$ and well below Curie-Weiss temperature $|\Theta_{CW}| = 22.9\text{K}$.

The fcc lattice consisting of edge-sharing tetrahedra is another typical frustrated lattice and abundant in nature. Quite surprisingly no systematic study could be found on this system in the literature. Therefore in Chapter 2 we considered the fcc model up to third neighbor interactions (first in the hope of finding incommensurate spin spirals), and we have found a

¹⁵We have already showed such a codimension-one manifold for the square lattice in Fig. 1.2(b).

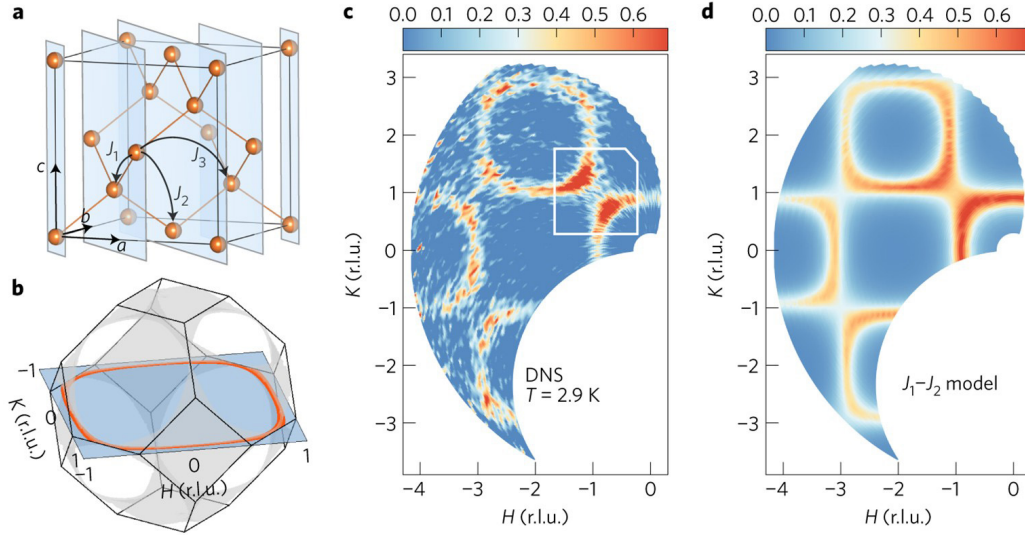


Figure 1.7: Reproduction of Fig. 1 of [21]. (a) The diamond sublattice of the magnetic Mn^{2+} ions with $S = 5/2$ in MnSc_2S_4 together with the nearest neighbor interactions up to third neighbors. (b) The Brillouin zone of the parent face-centered cubic lattice, the light gray surface is the calculated ground state manifold with exchange ratio $J_2/J_1 = 0.85$. The $(HK0)$ plane is shown in blue, together with its section with the ground state manifold highlighted by the orange curve. (c) Neutron diffuse scattering intensities in the $(HK0)$ plane measured at $T = 2.9\text{K}$. (d) Monte-Carlo simulation of the spin-spin correlations on the $(HK0)$ plane for the $J_1 - J_2$ model with $J_2/J_1 = 0.85$ at $T/J_1 = 0.55$.

rich phase diagram with commensurate and incommensurate phases and extended ground state manifolds of dimension one and two providing potential hosts to spin liquid phases. Inspired by the discovery of the two dimensional manifold we have constructed a recipe for *generating* models with such large ground state degeneracies on Bravais lattices in Chapter 3. Here we finish our introduction about spin systems in general.

1.2 Magneto-optics of multiferroics

And now for something completely different. In our last Chapter 4 we study the magneto-optical response (and especially the *nonreciprocal directional dichroism (NDD)*) of the antiferromagnet $\text{Sr}_2\text{CoSi}_2\text{O}_7$ in its high temperature, paramagnetic phase in strong external magnetic fields in collaboration with experimentalists.

$\text{Sr}_2\text{CoSi}_2\text{O}_7$ is a planar antiferromagnet with a small canting of the moments, that simultaneously shows electric polarization making the substance a magnetoelectric (ME) *multiferroic* material. In these ME materials the magnetic and electric degrees of freedom are usually coupled, meaning that we can control static (DC) electric polarization via magnetic fields, and the other way around: Controlling magnetic moments via electric fields. At the level of linear response theory the magnetoelectric cross-effects can be captured by the *magnetoelectric susceptibilities*. For the definitions of these magnetoelectric response

functions consult Appendix F.

Several models for the microscopic origin of the magnetoelectric coupling were proposed and here we briefly mention some of them. Our starting point will always be some magnetic insulator described by a Heisenberg model, and we ask the question how electric polarization can be induced by ordered magnetic moments (for a thorough discussion see [35, 36, 37]). In all these mechanisms the spins affect the charge or lattice degrees of freedom, the main differences being the symmetry restrictions and the number of spins (one or two) involved in the process.

- **Inverse Dzyaloshinskii-Moriya or spin current mechanism** This is the most frequent mechanism of magnetically induced polarization in magnets where the spin-orbit coupling induced Dzyaloshinskii-Moriya (DM) interactions or magnetic frustration leads to non-collinear spin spirals [38]. Two spins \mathbf{S}_i and \mathbf{S}_j at sites i and j connected by the vector \mathbf{e}_{ij} induce a polarization on the bond of the form

$$\mathbf{P}_{ij} \propto \mathbf{e}_{ij} \times (\mathbf{S}_i \times \mathbf{S}_j). \quad (1.23)$$

This mechanism is inactive for collinear spins. Even for non-collinear spins the finite individual bond-polarizations may sum to zero and give no net polarization.

- **Magnetostriction or exchange striction** is another two-site mechanism that does not require spin-orbit coupling, and also works for collinear spins. When the symmetric exchange $J(\mathbf{e}_{ij}) \mathbf{S}_i \cdot \mathbf{S}_j$ energy depends on the bond vector the magnetic ordering may deform the lattice a way that leads to a net polarization.
- **Metal-ligand or $p - d$ hybridization** This is an on-site (or single-site) mechanism, involving one spin only and its ligands. This mechanism is only viable for spins with $S \geq 1$. When the site of the magnetic ion is not an inversion center the following form of polarization is allowed:

$$\mathbf{P} \propto \sum_{\alpha} (\mathbf{S} \cdot \mathbf{e}_{\alpha})^2 \mathbf{e}_{\alpha}, \quad (1.24)$$

where the vectors \mathbf{e}_{α} point to the p -ligands surrounding the magnetic d -ion with spin \mathbf{S} . The microscopic reason behind this form of polarization is the following: Because of the spin-orbit interaction the hybridization between the p - and d -orbitals depends on the orientation of the magnetic moment, affecting the charge distribution of the ligands [39].

For $\text{Sr}_2\text{CoSi}_2\text{O}_7$ metal-ligand hybridization is the relevant mechanism: The Co^{2+} ions have $S = 3/2$, and their sites are not inversion centers (the Co-ions are surrounded by four O^{2-} ligands forming a tetrahedron, see Fig. 4.4). The consequences of Eq. (1.24) are detailed in Section 4.3. None of the two-site mechanisms are effective in this material. Although the DM interactions are active, the polarization contributions of the bonds cancel. All the nearest neighbor Co-Co bonds have the same exchange energy so they cannot result a net ferroelectric polarization either. In the following we say a few words about the *dynamical* (specially, optical) consequences of the multiferroic couplings.

The magnetoelectric cross-correlations can also manifest themselves in the finite frequency excitations leading e.g. to the so-called *electromagnons* [40, 41, 42, 43] and to optical anisotropies such as ME polarization rotation or NDD. A substance shows NDD if it absorbs counter-propagating lightbeams differently (even if they are unpolarized) [44]: One-way transparency is an extreme case of this property when the crystal is transparent from one side and completely opaque from the other side.¹⁶ Some multiferroics, such the melilites¹⁷ $\text{Ba}_2\text{CoGe}_2\text{O}_7$, $\text{Ca}_2\text{CoSi}_2\text{O}_7$ and $\text{Sr}_2\text{CoSi}_2\text{O}_7$ have almost ideal one-way transparency [46]. Two simple cases of NDD are usually distinguished: *Magneto-chiral dichroism* [47] (MChD) and *toroidal dichroism* [48]. In the first case the light propagates along the magnetization of a *chiral*¹⁸ magnet $\mathbf{k} \parallel \mathbf{M}$ and in the second case $\mathbf{k} \parallel \mathbf{P} \times \mathbf{M}$, where \mathbf{M} and \mathbf{P} mean magnetization and ferroelectric polarization of the material, respectively. The presence of magnetic order requires the breaking of time-reversal symmetry, and the presence of net polarization needs space inversion to be broken, together with the lack of symmetries connecting counter-propagating beams NDD is expected to be present only in crystals of sufficiently low symmetry.

Therefore multiferroics (having necessarily low symmetry) are a good place to search for such magnetoelectric phenomena. Indeed large NDD was found in the collective excitations of some multiferroics, typically in the GHz-THz frequency range, see [49, 50, 41, 42, 46, 51, 52] in their *magnetically ordered states*. Our goal was to find and understand NDD in the *paramagnetic phase* of $\text{Sr}_2\text{CoSi}_2\text{O}_7$, where an applied external magnetic field was used to break time-reversal symmetry.

1.3 Structure of the thesis

The main text of the thesis is divided into two essentially unrelated parts: (i) Chapters 2 and 3 consider the ground state properties of classical Heisenberg models, and (ii) Chapter 4 discusses the magnetooptics of $\text{Sr}_2\text{CoSi}_2\text{O}_7$. Every chapter closes with its *own summary*.

- In Chapter 2 we define the Heisenberg model on the fcc lattice. Following the introduction of the Luttinger-Tisza method we construct the ground state ($T = 0$) phase diagram of the classical isotropic Heisenberg model up to third neighbor interactions. We find three distinct types of phases, (i) *Commensurate* ones: We construct and describe the ground states and their degeneracies, (ii) *Incommensurate spin spirals*, and (iii) *Codimension-one and -two manifolds* at phase boundaries and triple points, where we explicitly construct large classes of orderings (e.g. aperiodic ones). We explain the appearance of manifolds in Fourier space by rewriting the Hamiltonian as a positive definite sum of complete squares defined on finite motifs tessellating the lattice.

¹⁶Although this phenomenon seems a bit counter-intuitive it should not come as a big a surprise: If there is no element in the point group of a crystal that connects the wave-vectors of the counter-propagating light beams $\pm\mathbf{k} \rightarrow \mp\mathbf{k}$ (leaving its polarization intact) then NDD is allowed, see [45] for details and a bunch of example materials.

¹⁷Åkermanites are subspecies of melilites.

¹⁸In this context chirality simply means a crystal with a point group consisting only of pure rotations, without inversion, mirror planes or roto-reflections.

- In Chapter 3 we give a recipe for the construction of Heisenberg models on Bravais lattices having codimension-one ground state manifolds (i.e. the manifolds are curves in two, and surfaces in three dimensions). We illustrate the construction on the square, simple cubic and fcc lattices in detail (all the necessary ingredients to apply the construction to other lattices are given in Appendix D). We close this chapter by showing how the thermal or quantum order by disorder mechanisms select commensurate orders on the degenerate manifolds (details of the calculations are given in Appendix E).
- In Chapter 4 we provide a theory for the absorption measurements on the magnetoelectric multiferroic $\text{Sr}_2\text{CoSi}_2\text{O}_7$ showing non-reciprocal directional dichroism in the paramagnetic phase in strong external magnetic fields. We describe the optical measurements based on a small-cluster exact diagonalization calculation. To further elucidate the physics we employ a simple model based on *one* magnetic ion with strong on-site anisotropy and analyze it via group theory to describe the selection rules in detail, and the excitation energies semi-quantitatively. We also derive a quite simple but powerful result: The time-reversed (antiunitary) symmetry elements force the matrix elements of perturbing operators to be either real or pure imaginary (up to our knowledge this observation is new, its proof and generalization to arbitrary spin length and magnetic point group are given in Appendix G). In this magneto-optical situation applying this result is just as useful as the standard selection rules. We extend the symmetry analysis to the lattice model, and by considering the interactions between the magnetic ions perturbatively we refine our analysis and justify the success of the one-ion model.
- *Thesis statements* 5 contains my new results and the corresponding publications.
- The thesis concludes with a number of technical Appendices.

Chapter 2

Phase diagram of the J_1 - J_2 - J_3 Heisenberg model on the fcc lattice

2.1 Introduction

Neutron scattering on MnO –a face-centered cubic (fcc) magnet– provided the first proof of existence of an antiferromagnetic order (for details see the Introduction 1.1.1). In the most common metal oxides –besides a number of other magnetic materials– the magnetic ions form the fcc lattice (c.f. Table 1.1). The wide range of frustration parameters f hints to a large variety of possible interactions and consequently ground states in these substances. A recent paper about the half-Heusler compound GdPtBi [8] showed that the inclusion of a third neighbor interaction to the Heisenberg Hamiltonian is inevitable (the order is of Type-II) in order to understand the neutron scattering picture . Surprisingly we could not find results on Heisenberg magnets beyond second neighbor exchanges in the literature. Therefore in this chapter we provide a systematic study of the ground state structure of the Heisenberg model on the frustrated fcc lattice up to third neighbor interactions of arbitrary sign.

The structure of this chapter is as follows. We introduce the fcc lattice and our Heisenberg model in Sec. 2.2 and we give an overview of the literature on magnetic models on the fcc lattice. In Sec. 2.3 we give the model in q -space and we describe the Luttinger-Tisza method in some detail. (More technical details on Fourier transform conventions and some technical derivations of used formulas are given in Appendix A. A summary of the relationship between spin structures in real and reciprocal space together with some illustration of spin patterns on the square lattice were given in the Introduction 1.1.1.) The phase diagram is described in Sec. 2.4, the details of the commensurate orderings are given in Sec. 2.5, while the properties of the incommensurate orders are briefly summarized in Sec. 2.6. We dedicate Sec. 2.7 to the description of the phases with degenerate manifolds and this is the place where we construct a large number of aperiodic ground states. Chiral properties of the orders are discussed in detail in Appendix C. The chapter closes with a summary and outlook for further studies in Sec. 2.8.

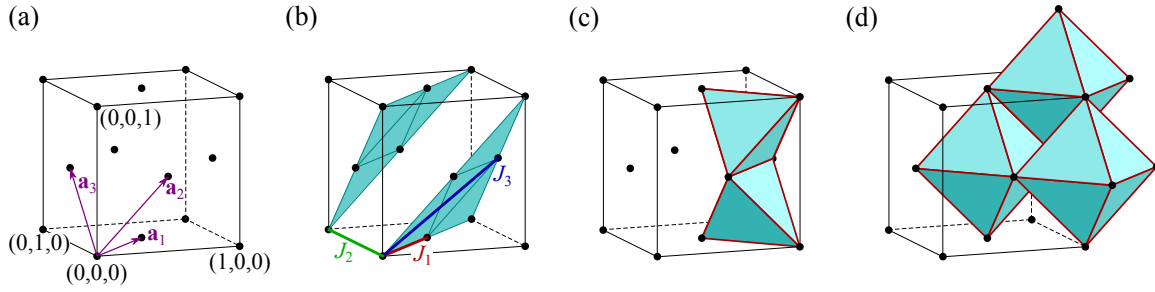


Figure 2.1: Geometry and exchange interactions of the fcc lattice: the encompassing unit cube is the conventional cell. (a) Primitive lattice vectors $\mathbf{a}_1 = \frac{1}{2}(1, 1, 0)$, $\mathbf{a}_2 = \frac{1}{2}(1, 0, 1)$, $\mathbf{a}_3 = \frac{1}{2}(0, 1, 1)$ join the first neighbors. (b) The first neighbor J_1 , second neighbor J_2 , and third neighbor J_3 interactions on the lattice are shown (c.f. the Hamiltonian Eq. (2.2)). There are 12 first, 6 second and 24 third neighbors. The $(1\bar{1}\bar{1})$ planes are triangular lattices and are indicated by a light cyan color: Interactions J_1 and J_3 are first and second neighbor interactions of these triangular lattices, respectively, and J_2 connects the planes. We can cover the lattice by edge sharing elementary tetrahedra (c) or by edge sharing octahedra (d).

2.2 The lattice and the model

The fcc lattice is generated by the

$$\mathbf{a}_1 = \left(\frac{1}{2}, \frac{1}{2}, 0\right), \quad \mathbf{a}_2 = \left(\frac{1}{2}, 0, \frac{1}{2}\right), \quad \mathbf{a}_3 = \left(0, \frac{1}{2}, \frac{1}{2}\right), \quad (2.1)$$

primitive lattice translations depicted in Fig. 2.1(a). We will refer to the lattice points by their Cartesian components, i.e. we set the lattice constant to one: $\mathbf{R}_i = (x, y, z)$. Note that either all the Cartesian coordinates are either integers, or two of them are half-integers, so that $x + y + z$ is always an integer. This lattice is an archetype of *frustration*: it can be built from (111) triangular planes, in an $ABCABC$ type stacking style, see Fig. 2.1(b). This frustration can be made even more manifest if we cover the lattice by edge sharing tetrahedra¹, the two differently oriented tetrahedral building blocks are depicted in Fig. 2.1(c). Another way of constructing the lattice is an edge sharing octahedral covering, see Fig. 2.1(d). We will see that these coverings –among others– play an essential role in understanding the ground state structure of the Heisenberg model presented in the following.

The Hamiltonian of the classical isotropic Heisenberg model reads

$$\mathcal{H} = J_1 \sum_{\langle i,j \rangle_1} \mathbf{S}_i \cdot \mathbf{S}_j + J_2 \sum_{\langle i,j \rangle_2} \mathbf{S}_i \cdot \mathbf{S}_j + J_3 \sum_{\langle i,j \rangle_3} \mathbf{S}_i \cdot \mathbf{S}_j, \quad (2.2)$$

where the \mathbf{S}_i are three dimensional unit vectors $|\mathbf{S}_i| = 1$ at the sites \mathbf{R}_i of the fcc lattice, interacting with first (J_1), second (J_2), and third neighbor (J_3) exchange interactions. The

¹This covering also shows that this lattice can be viewed as the three-dimensional analogue of the triangular lattice.

summation indices $\langle i, j \rangle_\delta$ with $\delta = 1, 2, 3$ refer to the δ 'th neighbor pairs. There are twelve first, six second and twenty-four third neighbor vectors in the fcc structure. One vector of each neighbor set is drawn in Fig. 2.1(b), and their coordinates are

$$\boldsymbol{\delta}_1 = \left(\frac{1}{2}, \frac{1}{2}, 0 \right), \boldsymbol{\delta}_2 = (0, 1, 0), \boldsymbol{\delta}_3 = \left(1, \frac{1}{2}, \frac{1}{2} \right). \quad (2.3)$$

The reciprocal lattice vectors corresponding to the primitive vectors Eq. (2.1) are:

$$\mathbf{b}_1 = 2\pi (1, 1, -1), \mathbf{b}_2 = 2\pi (1, -1, 1), \mathbf{b}_3 = 2\pi (-1, 1, 1). \quad (2.4)$$

We will refer to any point in reciprocal space by its q -triplet, e.g. $\mathbf{q} = (q_x, q_y, q_z) = (2\pi, 2\pi, -2\pi) = \mathbf{b}_1$. Special points and lines in the Brillouin zone (BZ) have more or less commonly used labels, we will refer to them either by their labels, or the labels with their Cartesian coordinates in parenthesis in units of 2π . For example one of the BZ corners of the fcc lattice can be referred to as W , $W(1, \frac{1}{2}, 0)$, or $(2\pi, \pi, 0)$. The BZ takes the form of a truncated octahedron, it is depicted in Fig. 2.3(a) together with some symmetry points and their names and positions (note that the coordinates in this figure are measured in units of 2π). Next we overview the literature of the fcc magnets.

Here we go over the vast literature of the $O(n)$ fcc magnets, their thermodynamics and critical theory [53].² After decades of debates over the $n = 1$ (Ising) model [55, 56, 57, 58, 59] the dust probably has settled, and this model is believed to have a first order transition to the Type-I (see Subsection 2.5 for the types of commensurate phases) AFM phase [60, 61, 62, 63, 64, 65, 66]. However our knowledge about the planar $n = 2$ model seems to be limited [67, 53]. The $n = 3$ (Heisenberg) model has also been debated for a long time [68, 67, 69, 17], but the verdict seems to be a first order transition to a collinear Type-I AFM state [70]. Quantum fluctuations were considered by a few studies in the large- S [71] or small- S limits [72], but after more than 70 years since Anderson's paper [73], the ground state of the quantum AFM Heisenberg model on the fcc lattice is still unknown.

Our goal is to find the *ground states* of the model (2.2) using the method developed by Luttinger and Tisza [74], i.e. by finding the minimum of the exchange interaction in Fourier space $J(\mathbf{q})$ [75]. We devote the next section to the introduction of the Luttinger-Tisza method. We will see that in frustrated models like ours the ground states are far from being unique, and we wish to classify and describe them in detail.

2.3 The model in q-space and the Luttinger-Tisza method

Here we briefly describe the Luttinger-Tisza method that we will use extensively to find the ground states of classical isotropic Heisenberg models. We do not present the method in full generality, since we will only be concerned about isotropic Heisenberg models on Bravais lattices. Generalizing the method to anisotropic exchanges and/or non-Bravais lattices is

²This article also contains a lot of examples of real world fcc magnets, together with their ordering types, and the order of their phase transitions. For other examples of commensurately ordering fcc magnets and their corresponding J_1, J_2 values see [54].

possible but it complicates the formalism considerably (the exchanges –both in real and Fourier space– become matrices, and we have to minimize their \mathbf{q} -dependent *eigenvalues*).

A general Heisenberg Hamiltonian in Fourier space reads

$$\mathcal{H} = \sum_{\langle i,j \rangle} J_{ij} \mathbf{S}_i \cdot \mathbf{S}_j = N \sum_{\mathbf{q} \in \text{BZ}} J(\mathbf{q}) \mathbf{S}_{\mathbf{q}} \cdot \mathbf{S}_{-\mathbf{q}} = N \sum_{\mathbf{q} \in \text{BZ}} J(\mathbf{q}) |\mathbf{S}_{\mathbf{q}}|^2, \quad (2.5)$$

where the summation runs over the BZ, and N is the total number of sites of the lattice with periodic boundary conditions.³ The Fourier form of the actual Hamiltonian (2.2) on the fcc lattice becomes

$$J(\mathbf{q}) = 2J_1 \left(\cos \frac{q_x}{2} \cos \frac{q_y}{2} + \cos \frac{q_x}{2} \cos \frac{q_z}{2} + \cos \frac{q_y}{2} \cos \frac{q_z}{2} \right) + J_2 (\cos q_x + \cos q_y + \cos q_z) \\ + 4J_3 \left(\cos q_x \cos \frac{q_y}{2} \cos \frac{q_z}{2} + \cos \frac{q_x}{2} \cos q_y \cos \frac{q_z}{2} + \cos \frac{q_x}{2} \cos \frac{q_y}{2} \cos q_z \right). \quad (2.6)$$

We want to minimize the Hamiltonian (2.5) subject to the so-called *local* or *strong* constraints $|\mathbf{S}_i|^2 = 1$, for each site i , which is clearly a formidable task because of the large number of constraints (N constraints for a lattice consisting of N sites). Instead of attacking this problem we solve a simpler one. We only require the fulfillment of the much weaker *global* constraint

$$\sum_i |\mathbf{S}_i|^2 = N \Leftrightarrow \sum_{\mathbf{q} \in \text{BZ}} |\mathbf{S}_{\mathbf{q}}|^2 = 1, \quad (2.7)$$

i.e. we only fix the spin length ”on average” (for a proof of equivalence of the real and Fourier space norms consult Appendix A). Note that under the global constraint the energy per site

$$\varepsilon = \frac{\mathcal{H}}{N} = \sum_{\mathbf{q} \in \text{BZ}} J(\mathbf{q}) |\mathbf{S}_{\mathbf{q}}|^2, \quad (2.8)$$

is a *convex combination*⁴ of the real numbers $J(\mathbf{q})$ with non-negative coefficients $|\mathbf{S}_{\mathbf{q}}|^2 \geq 0$, which is clearly minimized if we pick the points in the BZ where $J(\mathbf{q})$ achieves its minimum. We denote this set of points $\{\mathbf{Q}\}$ –the *ordering vectors*– by \mathcal{M}_{GS} , and dub it as the *ground state manifold* (note that $J(\mathbf{Q})$ is –by definition– constant on \mathcal{M}_{GS}). In order to satisfy the global constraint $\sum_{\mathbf{Q} \in \mathcal{M}_{\text{GS}}} |\mathbf{S}_{\mathbf{Q}}|^2 = 1$ is still required, *but there is nothing to guarantee the fulfillment of the local constraints*. Nevertheless, we have found a lower bound to the true ground state energy per site ε_0

$$\varepsilon_0 = \frac{\langle \mathcal{H} \rangle_0}{N} \geq \varepsilon(\mathbf{Q}) = \sum_{\mathbf{Q} \in \mathcal{M}_{\text{GS}}} J(\mathbf{Q}) |\mathbf{S}_{\mathbf{Q}}|^2 = J(\mathbf{Q}), \quad (2.9)$$

where the “0” indices refer to the true ground state properties. If we are able to choose the complex amplitudes $\mathbf{S}_{\mathbf{Q}}$ the way that $\mathbf{S}_i = \sum_{\mathbf{Q} \in \mathcal{M}_{\text{GS}}} \mathbf{S}_{\mathbf{Q}} e^{-i\mathbf{Q} \cdot \mathbf{R}_i}$ is of unit length for every

³Details of the Fourier transform conventions and calculations are presented in Appendix A.

⁴By the convex combination of some quantities J_q we mean the weighted sum $\sum_q p_q J_q$, with non-negative weights p_q that sum to one: $\sum_q p_q = 1$. Here the quantities are $J_q \leftrightarrow J(\mathbf{q})$ and the weights are $p_q \leftrightarrow |\mathbf{S}_{\mathbf{q}}|^2$.

i , than we have achieved our goal, since we have found *a true ground state* (hence the “0” index on the amplitudes). In this case Eq. (2.9) becomes an equality and the energy per site is simply the Fourier transform of the exchange parameters evaluated on the \mathcal{M}_{GS}

$$\varepsilon_0 = \varepsilon(\mathbf{Q}) = J(\mathbf{Q}), \quad (2.10)$$

note that $\varepsilon(\mathbf{Q})$ only depends on the ordering vector parametrically.

What we do in practice is the following. We minimize $J(\mathbf{q})$ with respect to \mathbf{q} , i.e. we equate its gradient to zero, and if this equation is satisfied at $\mathbf{q} = \mathbf{Q}$ we check the positive semidefiniteness of the Hessian

$$\left. \frac{\partial J(\mathbf{q})}{\partial q_\alpha} \right|_{\mathbf{q}=\mathbf{Q}} = 0, \quad \text{and} \quad \left. \frac{\partial^2 J(\mathbf{q})}{\partial q_\alpha \partial q_\beta} \right|_{\mathbf{q}=\mathbf{Q}} \geq 0. \quad (2.11)$$

for $\alpha, \beta = x, y, z$. The conditions above are necessary, but not sufficient to have a global minimum: to find a true ground state we have to compare the different local minima and choose the lowest one. In order not to miss a phase and scan the phase boundaries in the three-dimensional parameter space of the exchanges –beside the analytical solutions– we numerically minimized $J(\mathbf{q})$ for randomly chosen exchanges and compared the numerical minima to the values at symmetric points and lines in the BZ. This way a rough picture of the phase diagram was drawn and later it was refined by analytical means.

We have seen in the Introduction 1 that the physics of the system strongly depends on the dimension (and of course shape) of the \mathcal{M}_{GS} : For zero dimensional manifolds of commensurate orders (magnetic Bragg peaks) on the square lattice and the corresponding orderings see Fig. 1.2(b) and Fig. 1.3. Spin spirals (helices, cycloids) [76, 77, 78] have zero dimensional manifolds too, see also Fig. 1.3(d) and Section 2.6. The J_1 - J_2 model on the square lattice [79, 80] may possess a one-dimensional manifold (see also Subsection 3.3.1), just like the honeycomb lattice [81, 82, 83]. The first neighbor antiferromagnetic model on the fcc lattice [71, 19] also has a one-dimensional \mathcal{M}_{GS} , see Fig. 2.3(b) and Subsection 2.7.4. Two dimensional manifolds (*spin spiral surfaces*) were found in the $J_1 - J_2$ model on the diamond [20], fcc [69, 84],⁵ body-centered cubic [85], and hexagonal close packed [86] lattices. Moreover the kagome [87, 88] and pyrochlore [89, 90, 91] lattices have the whole BZ as the ground state manifold (see Figs. 1.5(c) and (d)). Fluctuations on the extended manifolds make these systems good candidates for realizing classical spin liquids in some temperature range, see Subsection 1.1.4 and Refs. [25, 26, 20, 21, 92]. In the following we construct the ground state phase diagram of the model in exchange parameter space by minimizing the energy $\varepsilon(\mathbf{q})$ with respect to the wave-vector.

2.4 Ground state phase diagram and ordering vectors

In this section we calculate the classical, zero temperature, ground state phase diagram of the model Eq. (2.2) in the $J_1 - J_2 - J_3$ parameter space. $T = 0$ means that the local

⁵For an expanded version of our paper [84] on the affine lattice construction of spin spiral surfaces consult Chapter 3.

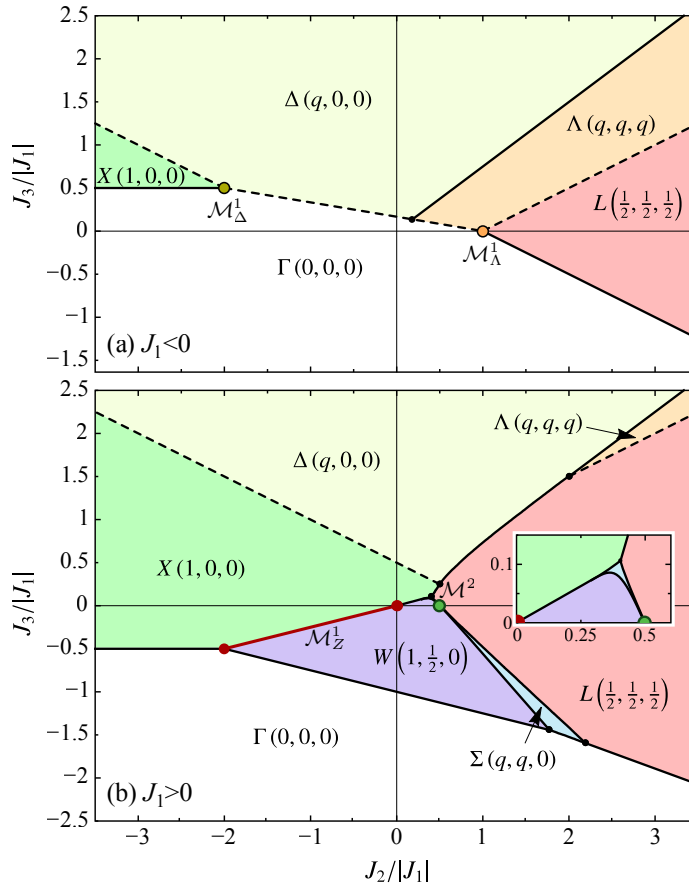


Figure 2.2: Phase diagram of the classical J_1 - J_2 - J_3 Heisenberg model (2.2) on the fcc lattice for (a) ferromagnetic $J_1 < 0$ and (b) antiferromagnetic $J_1 > 0$ first neighbor interactions. Essential information about the phases is given in Table 2.1. First order phase transitions are denoted by solid black lines, dashed black lines stand for continuous (second order) transitions. Equations of the phase boundaries are given in Table B.1. Phases are labeled by their ordering vectors in units of 2π (c.f. Fig. 2.3). The four *commensurate* phases are the ferromagnet $\Gamma(0, 0, 0)$, and three types of antiferromagnets: $X(1, 0, 0)$, $L(\frac{1}{2}, \frac{1}{2}, \frac{1}{2})$, and $W(1, \frac{1}{2}, 0)$. The commensurate ordering vectors are shown in Fig. 2.3(a) (these phases are already present in the $J_3=0$ models [17, 93]). A finite J_3 causes the *incommensurate* phases $\Delta(q, 0, 0)$, $\Lambda(q, q, q)$ and $\Sigma(q, q, 0)$ to appear, where q has to be optimized according to Eqs. (2.44)-(2.46) (for the ordering vectors see Fig. 2.3(d)-(f)). The phase $\Sigma(q, q, 0)$ in (b) has a bow-tie shape (enlarged in the inset) with a neck being the single point $J_2 = J_1/2$ and $J_3 = 0$ (green dot), and at this point the L and W phases meet. The dark red $X - W$ phase boundary emanating from the first-neighbor antiferromagnetic point $J_2 = J_3 = 0$ is degenerate. Along this line *any* of the ground states have ordering vectors on the one-dimensional manifold \mathcal{M}_Z^1 defined by $\mathbf{Q} = (2\pi, q, 0)$ with $q \in [-\pi, \pi]$. The manifold is shown in Fig. 2.3(b). In (a) the two triple points also have one-dimensional ground state manifolds: \mathcal{M}_Δ^1 (Fig. 2.3(d)) and \mathcal{M}_Λ^1 (Fig. 2.3(e)). At the green dot $J_3 = 0$, $J_2 = J_1/2 > 0$, this point has a *two-dimensional* ground state manifold shown in Fig. 2.3(c). Basic properties of the manifolds are given in Table 2.2.

spin length constraint is satisfied. In the spirit of the Luttinger-Tisza method we compare the energies $\varepsilon(\mathbf{Q})$ of the possible orderings and choose the lowest one for a given set of parameters. We do not bother about the real space picture of the orderings yet, since we will analyze the fulfillment of the local length constraints in the following sections in great detail. The energies and ordering vectors⁶ are collected in Table 2.1, and the detailed phase diagram is shown in Fig. 2.2.

Table 2.1: Symmetry points and lines –the possible ordering vectors \mathbf{Q} – with their labels in the Brillouin zone of the fcc lattice are given in the first column. The number of arms of the star ($|\star|$) of the point or line (degeneracy) is given in the second column. Third column: The energy per site $\varepsilon(\mathbf{Q})$ for the given ordering. Fourth column: The exchange parameter regions where the Hessian [Eq. (2.11)] is positive definite (stability criterion). In the fifth column conventional names of the commensurate antiferromagnetic phases are given. For the phase diagram see Fig. 2.2. The ordering vectors in the Brillouin zone are given in Fig. 2.3. The optimized incommensurate ordering vectors are given in Eqs. (2.44)–(2.46). About notation: we refer to points in the Brillouin zone either by their names and coordinates in units of 2π or by their respective wave-vector, i.e. $W(1, \frac{1}{2}, 0) \equiv (2\pi, \pi, 0) = \mathbf{Q}_W$.

Label(\mathbf{Q})	$ \star $	$\varepsilon(\mathbf{Q})$	Local stability	Type
$\Gamma(0, 0, 0)$	1	$6J_1 + 3J_2 + 12J_3$	$J_1 < -J_2 - 6J_3$	–
$X(1, 0, 0)$	3	$-2J_1 + 3J_2 - 4J_3$	$J_2 < 4J_3 < 2J_1 - 2J_2$	I
$L(\frac{1}{2}, \frac{1}{2}, \frac{1}{2})$	4	$-3J_2$	$J_1 - 2J_2 < 2J_3 < J_1 + J_2$	II
$W(1, \frac{1}{2}, 0)$	6	$-2J_1 + J_2 + 4J_3$	$8J_3 < 2J_2 < J_1 - 2J_3$	III
$\Delta(q_\Delta, 0, 0)$	6	$\frac{2-2J_1^2+2J_1J_2+J_2^2-24J_3^2}{2J_2+8J_3}$		
$\Lambda(q_\Lambda, q_\Lambda, q_\Lambda)$	8	$-\frac{3(J_1^2+2J_1(J_2-2J_3)+(J_2+2J_3)^2)}{8J_3}$		
$\Sigma(q_\Sigma, q_\Sigma, 0)$	12	$\varepsilon(\mathbf{Q}_\Sigma)^7$		

Next we compare the ground state energies $\varepsilon(\mathbf{Q})$ of the adjacent phases to find the phase boundaries. The boundaries are of first order if the ordering vector jumps discontinuously

⁶We recall that the *star* of a wave-vector \mathbf{q} is its orbit under the action of the point group \mathcal{G} of the crystal, i.e. $\star\mathbf{q} = \{g\mathbf{q} \mid g \in \mathcal{G}\}$, elements of the star are called *arms* (we only count inequivalent arms in Table 2.1, i.e. those arms that only differ in a reciprocal lattice vector are identified). The notation $|\star|$ for the number of arms of the star is nonstandard. Since our exchanges are point group symmetric $J(\mathbf{q}) = J(g\mathbf{q})$; specifically the ground state energies $\varepsilon(\mathbf{Q})$ are degenerate for all the arms of the star of the ordering vector \mathbf{Q} .

⁷The $\varepsilon(\mathbf{Q}_\Sigma = (q_\Sigma, q_\Sigma, 0))$ Fourier transform is:

$$\varepsilon(\mathbf{Q}_\Sigma) = \frac{J_1^3 + 6J_1^2J_2 - 66J_1^2J_3 + 12J_1J_2^2 - 120J_1J_2J_3 + 12J_1J_3^2 + 8J_2^3 + 24J_2^2J_3 - 120J_2J_3^2 + 296J_3^3}{432J_3^2} + \frac{(-J_1^2 - 4J_1J_2 + 44J_1J_3 - 4J_2^2 - 8J_2J_3 - 100J_3^2) \sqrt{(J_1 + 2(J_2 + J_3))^2 - 48J_3(J_1 - 2J_3)}}{432J_3^2}.$$

Table 2.2: Multiple points of the phase diagram, corresponding to the degenerate manifolds in wave-vector-space. First column: The label of the manifold is given (the superscripts 1, 2 refer to the dimension of the manifold), see Fig. 2.2. The manifolds are shown in Figs. 2.3(b)-(e). In the second column we give the phases that meet at the special parameter values given in the third column. In the fifth column we give the defining equation of the manifolds in \mathbf{q} -space, we show only one of the crystallographically equivalent directions. Fifth column: The energy per site on the manifold.

Label	Phases	Constraints on J -s	Def. of \mathcal{M}_{GS}	$\varepsilon(\mathbf{Q})$
$\mathcal{M}_{\frac{1}{2}}^1 \cup \Gamma$	$\Gamma - X - W$	$J_2 = -2J_1, J_3 = -\frac{J_1}{2}, J_1 > 0$	$\mathbf{Q} = (2\pi, q, 0)$	$-6J_1$
$\mathcal{M}_{\frac{1}{2}}^1$	$X - W$	$J_3 = \frac{J_2}{4}, -2J_1 < J_2 < 0, J_1 > 0$	$\mathbf{Q} = (2\pi, q, 0)$	$2(J_2 - J_1)$
\mathcal{M}_{Δ}^1	$\Gamma - \Delta - X$	$J_2 = 2J_1, J_3 = -\frac{J_1}{2}, J_1 < 0$	$\mathbf{Q} = (q, 0, 0)$	$+6J_1$
\mathcal{M}_{Λ}^1	$\Gamma - \Lambda - L$	$J_2 = -J_1, J_3 = 0, J_1 < 0$	$\mathbf{Q} = (q, q, q)$	$+3J_1$
\mathcal{M}^2	$L - W - \Sigma$	$J_2 = \frac{J_1}{2}, J_3 = 0, J_1 > 0$	$f(\mathbf{Q}) = 0$ ⁸	$-\frac{3}{2}J_1$

while crossing the boundary, and they are of second order if the ordering vector deforms continuously through the phase boundary; solid lines (dashed lines) show the first order (second order) transitions in Fig. 2.2. The matching phases and the equations of the phase boundaries together with the order of the transitions are given in Table B.1 of Appendix B. There are points (and a line) of the phase diagram that need special attention, the triple points (where three phases meet) and the boundary $X(1, 0, 0) - W(1, \frac{1}{2}, 0)$. At these points the \mathcal{M}_{GS} 's extend to lines and a surface showing large (but subextensive) degeneracy of the ground states. Elementary information about these points and the corresponding ground state manifolds are given in Table 2.2. The ordering vectors for the commensurate and incommensurate phases together with the extended manifolds are presented in Fig. 2.3. We will analyze the different orderings in real space in detail in Sections 2.5–2.7, here we only summarize the basic properties of these phases.

Essentially, we have found three basic types of phases:

- (i) We have found four *commensurate* orderings with ordering vectors at high symmetry points of the BZ [19, 17, 93, 95]:
 - (a) The ordinary *ferromagnet* with ordering vector $\mathbf{Q} = \Gamma(0, 0, 0)$.
 - (b) An *antiferromagnet* with ordering vectors $\mathbf{Q} = X(1, 0, 0)$ and its symmetry related partners, commonly dubbed the Type I phase.
 - (c) Another *antiferromagnet* with ordering vectors $\mathbf{Q} = L(\frac{1}{2}, \frac{1}{2}, \frac{1}{2})$ and its symmetry related partners (Type II).
 - (d) And yet another *antiferromagnet* with ordering vectors $\mathbf{Q} = W(1, \frac{1}{2}, 0)$ and its symmetry related partners (Type III).

⁸The equation of the two-dimensional manifold \mathcal{M}^2 is: $f(\mathbf{Q}) = \cos \frac{Q_x}{2} + \cos \frac{Q_y}{2} + \cos \frac{Q_z}{2} = 0$.

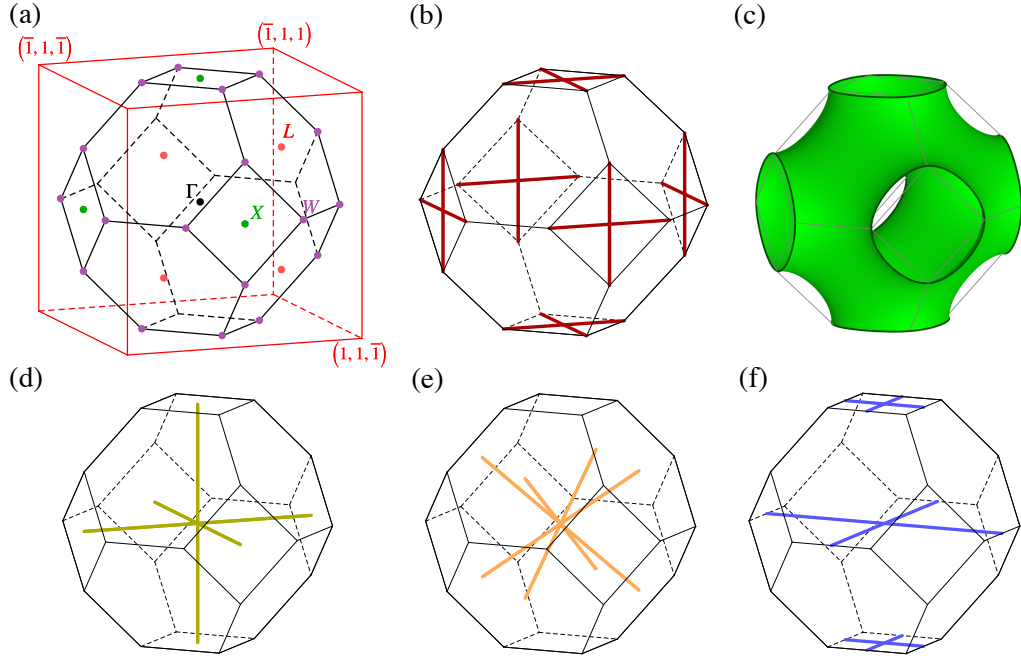


Figure 2.3: Brillouin zone (truncated octahedron) of the fcc lattice together with ordering vectors and ground state manifolds of the phases in Fig. 2.2. (a) Commensurate ordering vectors, the encompassing red cube contains two BZ's. $\Gamma(0, 0, 0)$: The ferromagnet with a one armed star. $X(1, 0, 0)$: The Type-I antiferromagnet (three arms). $L(\frac{1}{2}, \frac{1}{2}, \frac{1}{2})$: The Type-II antiferromagnet (four arms). $W(1, \frac{1}{2}, 0)$ is the Type-III antiferromagnet (four arms). (b) Degenerate wave-vectors (Z -lines) on the $X(1, 0, 0) - W(1, \frac{1}{2}, 0)$ phase boundary ($J_1 > 0$ and $J_3 = J_2/4$) forming a one-dimensional manifold $\mathcal{M}_{\frac{1}{2}}^1$, c.f. the dark red line in Fig. 2.2(b). *Every* point on the crisscrosses is energetically degenerate. (c) Two-dimensional energetically degenerate manifold \mathcal{M}^2 (a Schwarz P surface [94], see also our paper [84] and Subsection 3.3.2) belonging to the point $J_3 = 0$, $J_2 = J_1/2 > 0$ (green dot in Fig. 2.2(b)). The second row (d)–(f) shows the wave-vectors of incommensurate orders (spin spirals): Depending on the exchange parameter values [c.f. Eq. (2.44)–(2.46)] a single $\pm\mathbf{Q}$ pair of wave-vectors is chosen as the ordering vector. This row also corresponds to the one-dimensional degenerate manifolds of the special points of the phase diagram. (d) Incommensurate ordering vectors $\Delta(q, 0, 0)$ of the spin spirals propagating along the cubic axes with 6 arms. This is also the manifold \mathcal{M}_{Δ}^1 of the $\Gamma - \Delta - X$ triple point, see the yellow dot in Fig. 2.2(a). (e) Incommensurate ordering vectors $\Lambda(q, q, q)$ of the spin spirals propagating along the body diagonals of the enclosing cube with 8 arms. This is also the manifold \mathcal{M}_{Λ}^1 of the $\Gamma - \Lambda - L$ triple point, see the orange dot in Fig. 2.2(a). (f) Incommensurate ordering vectors $\Sigma(q, q, 0)$ of the spin spirals propagating along the face diagonals of the cubic cell (pictured only in the horizontal planes for better visibility; 12 arms). About notation: Brillouin zone points are denoted either by their names and coordinates in units of 2π (fractional coordinates) or their wave-vector, e.g. $W(1, \frac{1}{2}, 0) \equiv \mathbf{Q}_W = (2\pi, \pi, 0)$.

For the ordering vectors in the BZ see Fig. 2.3(a). All these phases have already been found in the $J_1 - J_2$ model (see the $J_3 = 0$ lines in Fig. 2.2) and they are analyzed in detail in Sec. 2.5.

- (ii) We have also found three types of *incommensurate* spin spirals (helices or cycloids [96, 76, 77, 78, 97])⁹ as the result of the frustrating effect of the J_3 interaction. The length of the pitch (or ordering) vector \mathbf{Q} of these spirals is fixed by the exchange parameters values, and the pitch vectors point in high-symmetry directions of the crystal. The incommensurate ordering vectors reside on the lines $\Delta(q, 0, 0)$, $\Lambda(q, q, q)$ and $\Sigma(q, q, 0)$ (see Fig. 2.3(d)–(f)). These spirals are absent in the pure $J_1 - J_2$ models, for a few details see Sec. 2.6. Although these phases can be experimentally significant (the fcc lattice is quite common, and –up to our knowledge– this is the simplest model producing incommensurate orders on it), there is nothing much to tell about them theoretically.
- (iii) We have also found four phases with *large ground state degeneracy* and possessing several different types of orderings. One of these ground state manifolds is two-dimensional $\mathcal{M}_{\text{GS}} = \mathcal{M}^2$ (for a detailed description of this spiral surface see Subsection 3.3.2), and three of them is one-dimensional : \mathcal{M}_{Σ}^1 , \mathcal{M}_{Δ}^1 , and \mathcal{M}_{Λ}^1 . Upper indices on the manifold labels denote the dimensionality of the manifold.
 - (a) The two-dimensional manifold $\mathcal{M}_{\text{GS}} = \mathcal{M}^2$ [84, 69, 98] resides at the triple point $L\left(\frac{1}{2}, \frac{1}{2}, \frac{1}{2}\right) - \Sigma(q, q, 0) - W\left(1, \frac{1}{2}, 0\right)$: The surface is depicted in Fig. 2.3(c). The presence of this codimension-one manifold at special values of exchanges $J_2 = J_1/2$ and $J_3 = 0$ is not an accident but a manifestation of our general construction [84] presented in detail in Chapter 3.
 - (b) One of the one-dimensional manifolds resides at the $X(1, 0, 0) - W\left(1, \frac{1}{2}, 0\right)$ phase boundary (see the red line with endpoints in Fig. 2.2(b)), that extends from the first neighbor antiferromagnetic model [19, 17] $J_1 > 0$, $J_2 = J_3 = 0$. This manifold is called \mathcal{M}_{Σ}^1 and it is depicted in Fig. 2.3(b): The lines are connecting the $X(1, 0, 0)$ and $W\left(1, \frac{1}{2}, 0\right)$ points of the BZ, these lines are sometimes called "Z", hence the name of the manifold.
 - (c) Another one-dimensional manifold resides at the triple point $\Gamma(0, 0, 0) - \Delta(q, 0, 0) - X(1, 0, 0)$ and its $\mathcal{M}_{\text{GS}} = \mathcal{M}_{\Delta}^1$ coincides with the collection of $\Delta(q, 0, 0)$ -s depicted in Fig. 2.3(d).
 - (d) The last one-dimensional manifold resides at the triple point $\Gamma(0, 0, 0) - \Lambda(q, q, q) - L\left(\frac{1}{2}, \frac{1}{2}, \frac{1}{2}\right)$ and its $\mathcal{M}_{\text{GS}} = \mathcal{M}_{\Lambda}^1$ coincides with the collection of $\Lambda(q, q, q)$ -s depicted in Fig. 2.3(e).

These degenerate phases can be found at carefully chosen parameter values where other more conventional phases meet, for details consult Sec. 2.7. In the following sections we analyze the possible configurations¹⁰ in detail, starting with the commensurate ones.

⁹The model being isotropic there is nothing to fix the plane of rotation of the spirals to the pitch vector \mathbf{Q} or to the crystallographic axes, for an illustration of a spin spiral on the square lattice see Fig 1.3(d).

¹⁰We make one last sidenote about the illustrations of ground state patterns on the fcc lattice (or the lack

2.5 Commensurate phases

In this section we describe and investigate the four commensurate orders in detail, for the ordering vectors see Fig. 2.3(a). We calculate the Fourier amplitudes participating in the orders and show how the local spin length constraints manifest themselves in Fourier space, and also describe the orders in real space. We also count the degeneracies: The number and type of free parameters characterizing the order that remain after removing the trivial, global $O(3)$ rotations of the symmetry breaking. To get the correct number of free parameters in Fourier space one must consider the periodicity of reciprocal space: equivalent wave-vectors must not be distinguished. Here by equivalence we mean differing only in some reciprocal lattice vector \mathbf{G} , i.e. $\mathbf{q} \sim \mathbf{q}'$ if $\mathbf{q} = \mathbf{q}' + \mathbf{G}$ for an arbitrary wave-vector \mathbf{q} .

We calculate the Fourier amplitude constraints (and correspondingly the number/type of free parameters) as follows. We expand the spins $\mathbf{S}_i = \sum_{\mathbf{Q} \in \mathcal{M}_{\text{GS}}} \mathbf{S}_{\mathbf{Q}}^0 e^{-i\mathbf{Q} \cdot \mathbf{R}_i}$ in Fourier space, and we keep only the amplitudes $\mathbf{S}_{\mathbf{Q}}^0$ of the arms of the star of the respective ordering vector (i.e. the \mathcal{M}_{GS} for commensurate orderings) finite. Next we impose the constraints that for every lattice point the spins have to be real unit vectors (the *local* length constraints), and solve the equations [99, 93, 100] for the Fourier amplitudes. This procedure results the following rules:

$$\mathbf{S}_{\mathbf{Q}}^0 = \mathbf{S}_{-\mathbf{Q}}^{0*}, \quad (2.12)$$

this is a consequence of the reality of the real space spins \mathbf{S}_i . The *global* length constraints (by unitarity of the Fourier transform, see Appendix A) gives us

$$\sum_{\mathbf{Q}} |\mathbf{S}_{\mathbf{Q}}^0|^2 = 1. \quad (2.13)$$

And by exploiting the *local* length constraints we have the following equation in Fourier space:

$$\sum_{\mathbf{Q}} \mathbf{S}_{\mathbf{Q}}^0 \cdot \mathbf{S}_{\mathbf{Q}-\mathbf{q}'}^{0*} = 0, \quad \forall \mathbf{q}' \neq 0. \quad (2.14)$$

In order to make this last equation useful one has to choose \mathbf{q}' such a way that $\mathbf{Q} - \mathbf{q}'$ lies on the \mathcal{M}_{GS} . We prove these equations in Appendix A.

2.5.1 The $\Gamma(0, 0, 0)$ ferromagnet

This phase is the usual ferromagnet: All the spins point in the same direction and we only have the trivial $O(3)$ degeneracy of the symmetry breaking. The single $\Gamma(0, 0, 0)$ point sits in the center of the BZ, see the black dot in Fig. 2.3(a).

of them). We illustrated some typical spin patterns on the square lattice in the Introduction 1 (see. Fig. 1.3). Drawing the same illustrations for the fcc lattice is much harder, not just because of its three-dimensional nature and connectivity, but also because of the complexity of the resulting patterns. As an example, the ground state of the Type III or *W*-phase consists of 32 (!) magnetic sublattices, c.f. Subsection 2.5.4. Even though I tried real hard I could not find a proper way of illustrating such complicated patterns.

2.5.2 The $X(1, 0, 0)$ antiferromagnet, Type I

In this *antiferromagnetic* phase we have three nonequivalent ordering vectors:

$$\mathbf{X}_1 = (2\pi, 0, 0), \quad \mathbf{X}_2 = (0, 2\pi, 0), \quad \mathbf{X}_3 = (0, 0, 2\pi), \quad (2.15)$$

forming the star of \mathbf{X} . These arms point to the midpoints of the square-shaped faces of the BZ (see the green dots in Fig. 2.3(a)) we can combine them with the appropriate Fourier amplitudes to construct a triple-Q order [99]. We expand the real space spins by choosing the complex Fourier amplitudes $\mathbf{S}_{\mathbf{X}_\alpha}^0$ in

$$\mathbf{S}_i = \sum_{\alpha=1}^3 \mathbf{S}_{\mathbf{X}_\alpha}^0 e^{-i\mathbf{X}_\alpha \cdot \mathbf{R}_i}, \quad (2.16)$$

and we enforce some constraints on the amplitudes to make the real space spins real unit vectors. The opposite square faces of the BZ are identified, so $\mathbf{X}_\alpha \sim -\mathbf{X}_\alpha$ and the phase factors $e^{-i\mathbf{X}_\alpha \cdot \mathbf{R}_i}$ are just ± 1 -s, so the amplitudes have to be real to ensure the reality of \mathbf{S}_i :

$$\mathbf{S}_{\mathbf{X}_\alpha}^0 \in \mathbb{R}^3, \quad \forall \alpha. \quad (2.17)$$

Using Eqs. (2.13–2.14) we get the following four constraints to fix the spin lengths:

$$\sum_{\alpha=1}^3 |\mathbf{S}_{\mathbf{X}_\alpha}^0|^2 = 1 \quad (1 \text{ constraint}), \quad (2.18)$$

$$\mathbf{S}_{\mathbf{X}_\alpha}^0 \cdot \mathbf{S}_{\mathbf{X}_\beta}^0 = 0, \quad \forall \alpha \neq \beta \quad (3 \text{ constraints}), \quad (2.19)$$

and the second set of equations follows if we choose $\mathbf{q}' = \mathbf{X}_\alpha - \mathbf{X}_\beta$ in Eq. (2.14). The three real amplitudes $\mathbf{S}_{\mathbf{X}_\alpha}^0$ provide 9 free real parameters. The global $O(3)$ freedom removes 3 of them ($O(3)$ is a three-parameter Lie group), and Eqs. (2.18) and (2.19) give four additional constraints, leaving two free parameters to characterize the degeneracy of the ground state in this phase [17]. The global $O(3)$ rotational freedom and the mutual orthogonality and normalization of the *real* $\mathbf{S}_{\mathbf{X}_\alpha}^0$ allows us to parametrize the Fourier amplitudes as

$$(\mathbf{S}_{\mathbf{X}_1}^0 | \mathbf{S}_{\mathbf{X}_2}^0 | \mathbf{S}_{\mathbf{X}_3}^0) = \left(\begin{array}{c|c|c} \xi & 0 & 0 \\ 0 & \eta & 0 \\ 0 & 0 & \zeta \end{array} \right), \quad (2.20)$$

where all the parameters ξ , η , and ζ are real, and they satisfy the additional constraint:¹¹ $\xi^2 + \eta^2 + \zeta^2 = 1$. The ground state manifold can thus be parametrized by a unit vector (ξ, η, ζ) . In what follows we construct and describe the order in real space.

With the parametrization given in Eq. (2.20) the spin on lattice point $\mathbf{R}_i = (x, y, z)$ becomes (the coordinates can be either integers or half-integers):

$$\mathbf{S}_i = \begin{pmatrix} (-1)^{2x} \xi \\ (-1)^{2y} \eta \\ (-1)^{2z} \zeta \end{pmatrix}. \quad (2.21)$$

¹¹Because of the $O(3)$ symmetry we can choose \mathbf{X}_1 to point in the x -direction, then by mutual orthogonality we choose the other two amplitudes in the y and z directions, and then we use the constraint (2.18).

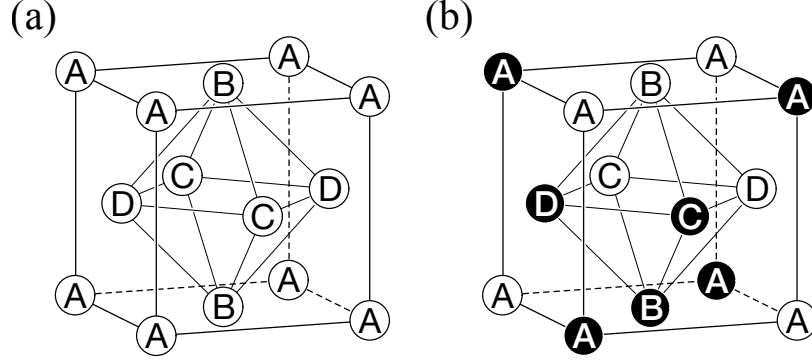


Figure 2.4: (a) Type-I $X (1, 0, 0)$ 4-sublattice antiferromagnetic order. The sublattice spins are \mathbf{S}_A , \mathbf{S}_B , \mathbf{S}_C and \mathbf{S}_D , respectively. The sublattices are simple cubic with lattice vectors $(1, 0, 0)$, $(0, 1, 0)$, and $(0, 0, 1)$. The different spins $A - B - C - D$ sit on the vertices of elementary tetrahedra of the fcc lattice, and they satisfy the *tetrahedron rule*: $\mathbf{S}_A + \mathbf{S}_B + \mathbf{S}_C + \mathbf{S}_D = \mathbf{0}$. (b) Type-II $L (\frac{1}{2}, \frac{1}{2}, \frac{1}{2})$ antiferromagnetic order, with four pairs of antiferromagnetically ordered sublattices: inverted colors correspond to opposite spins, i.e. $\mathbf{S}_{\bar{A}} = -\mathbf{S}_A$ is a white letter on a black disk. Each sublattice forms an fcc lattice with a doubled lattice constant with respect to the original fcc lattice. On each elementary octahedron of the original fcc lattice the spins form antiparallel pairs on opposite vertices of the octahedra.

The superlattice vectors (the primitive vectors of the magnetically ordered crystal) form a simple cubic lattice with a unit cell being the conventional cell of the fcc lattice (the black cube in Fig. 2.1(a) containing four lattice points) with primitive lattice translations

$$\mathbf{a}_1^X = (1, 0, 0), \quad \mathbf{a}_2^X = (0, 1, 0), \quad \mathbf{a}_3^X = (0, 0, 1). \quad (2.22)$$

The four magnetic sublattices form tetrahedra with spins

$$(\mathbf{S}_A | \mathbf{S}_B | \mathbf{S}_C | \mathbf{S}_D) = \begin{pmatrix} \xi & -\xi & -\xi & \xi \\ \eta & -\eta & \eta & -\eta \\ \zeta & \zeta & -\zeta & -\zeta \end{pmatrix}, \quad (2.23)$$

see Fig. 2.4(a). These are the elementary tetrahedra of the original fcc lattice. The spins on every elementary tetrahedron sum to zero:

$$\mathbf{S}_A + \mathbf{S}_B + \mathbf{S}_C + \mathbf{S}_D = \mathbf{0}, \quad (2.24)$$

and we refer to this situation as the *tetrahedron rule* (the easiest way to see this is by summing up every row in Eq. 2.23). We check the Fourier space degeneracy counting in real space. The four sublattice spins mean four unit vectors providing eight free parameters, the global $O(3)$ symmetry and also the tetrahedron rule remove three of them, and we are left with two free parameters as expected.

If we use all three arms of the star (all the \mathbf{X}_α -s) and create a triple-Q order (with all ξ, η, ζ finite in Eq. 2.20), then the spins are non-coplanar. If one of the parameters is zero, e.g. $\zeta = 0$, the configuration is coplanar, and if only ξ remains, it is collinear. Thermal

or quantum order by disorder effects select a *single* arm of the star resulting in a collinear structure [17].

One may ask the question: Can this phase be *chiral*? Even if we restrict ourselves to the study of spin systems there are multiple definitions of chirality scattered in the literature, so we dedicate Appendix C to this question. We review some notions of chirality there, and analyze our commensurate orders according to the different notions.

2.5.3 The $L\left(\frac{1}{2}, \frac{1}{2}, \frac{1}{2}\right)$ antiferromagnet, Type II

In this *antiferromagnetic* phase the nonequivalent \mathbf{Q} -vectors are

$$\mathbf{L}_1 = (\pi, \pi, \pi), \mathbf{L}_2 = (\pi, -\pi, -\pi), \mathbf{L}_3 = (-\pi, \pi, -\pi), \mathbf{L}_4 = (-\pi, -\pi, \pi), \quad (2.25)$$

forming a four-armed star (see the red dots in Fig. 2.3(a)). Since these arms reside on the midpoints of the hexagonal faces of the BZ we can construct a quadruple- \mathbf{Q} order out of them [99]. We expand the real space spins in Fourier amplitudes as

$$\mathbf{S}_i = \sum_{\alpha=1}^4 \mathbf{S}_{\mathbf{L}_\alpha}^0 e^{-i\mathbf{L}_\alpha \cdot \mathbf{R}_i} \in \mathbb{R}^3. \quad (2.26)$$

Just like in the former case $\mathbf{L}_\alpha \sim -\mathbf{L}_\alpha$ and the phase factors are $e^{-i\mathbf{L}_\alpha \cdot \mathbf{R}_i} = \pm 1$, the amplitudes have to be real to ensure the reality of \mathbf{S}_i , i.e.

$$\mathbf{S}_{\mathbf{L}_\alpha}^0 \in \mathbb{R}^3, \forall \alpha. \quad (2.27)$$

We can express the spins in real space as

$$\mathbf{S}_i = (-1)^{x+y+z} \mathbf{S}_{\mathbf{L}_1}^0 + (-1)^{y+z-x} \mathbf{S}_{\mathbf{L}_2}^0 + (-1)^{x+z-y} \mathbf{S}_{\mathbf{L}_3}^0 + (-1)^{x+y-z} \mathbf{S}_{\mathbf{L}_4}^0, \quad (2.28)$$

with $\mathbf{R}_i = (x, y, z)$. Substituting the lattice points in the above equation yield four *independent* spins on an elementary tetrahedron

$$\mathbf{S}_A = \mathbf{S}(\mathbf{0}) = \mathbf{S}_{\mathbf{L}_1}^0 + \mathbf{S}_{\mathbf{L}_2}^0 + \mathbf{S}_{\mathbf{L}_3}^0 + \mathbf{S}_{\mathbf{L}_4}^0, \quad (2.29a)$$

$$\mathbf{S}_B = \mathbf{S}(\mathbf{a}_1) = -\mathbf{S}_{\mathbf{L}_1}^0 + \mathbf{S}_{\mathbf{L}_2}^0 + \mathbf{S}_{\mathbf{L}_3}^0 - \mathbf{S}_{\mathbf{L}_4}^0, \quad (2.29b)$$

$$\mathbf{S}_C = \mathbf{S}(\mathbf{a}_2) = -\mathbf{S}_{\mathbf{L}_1}^0 + \mathbf{S}_{\mathbf{L}_2}^0 - \mathbf{S}_{\mathbf{L}_3}^0 + \mathbf{S}_{\mathbf{L}_4}^0, \quad (2.29c)$$

$$\mathbf{S}_D = \mathbf{S}(\mathbf{a}_3) = -\mathbf{S}_{\mathbf{L}_1}^0 - \mathbf{S}_{\mathbf{L}_2}^0 + \mathbf{S}_{\mathbf{L}_3}^0 + \mathbf{S}_{\mathbf{L}_4}^0, \quad (2.29d)$$

where the vectors \mathbf{a}_i are the primitive vectors of the fcc lattice, see Eq. (2.1). The tetrahedron rule does *not* hold anymore, since the J_1 interactions cancel. Inverting the above equations Eqs. (2.29) for the Fourier amplitudes of a given configuration on a tetrahedron yields

$$\mathbf{S}_{\mathbf{L}_1}^0 = \frac{1}{4} (\mathbf{S}_A - \mathbf{S}_B - \mathbf{S}_C - \mathbf{S}_D), \quad (2.30a)$$

$$\mathbf{S}_{\mathbf{L}_2}^0 = \frac{1}{4} (\mathbf{S}_A + \mathbf{S}_B + \mathbf{S}_C - \mathbf{S}_D), \quad (2.30b)$$

$$\mathbf{S}_{\mathbf{L}_3}^0 = \frac{1}{4} (\mathbf{S}_A + \mathbf{S}_B - \mathbf{S}_C + \mathbf{S}_D), \quad (2.30c)$$

$$\mathbf{S}_{\mathbf{L}_4}^0 = \frac{1}{4} (\mathbf{S}_A - \mathbf{S}_B + \mathbf{S}_C + \mathbf{S}_D). \quad (2.30d)$$

Shifting the elementary tetrahedron by $\delta = (1, 0, 0)$ flips the spins, resulting in an 8-sublattice antiferromagnet of spin pairs of $\mathbf{S}_A, \mathbf{S}_B, \mathbf{S}_C$ and \mathbf{S}_D , and $\mathbf{S}_A = -\mathbf{S}_{\bar{A}}$ (where $\mathbf{S}_{\bar{A}}$ is the site of the spin shifted by $(1, 0, 0)$ with respect to \mathbf{S}_A , and so on). The order is shown in Fig. 2.4(b).

The magnetic superlattice is an fcc lattice doubled in linear size with respect to the original one, with primitive lattice vectors

$$\mathbf{a}_1^L = (1, 1, 0), \mathbf{a}_2^L = (1, 0, 1), \mathbf{a}_3^L = (0, 1, 1). \quad (2.31)$$

We calculate the degeneracies in real space. The four independent sublattice spins mean 8 free real parameters (four independent unit spheres), the global $O(3)$ freedom removes 3 parameters resulting 5 independent real degrees of freedom [17]. On every (111) triangular plane only four out of eight spin directions are present, forming a regular 4-sublattice order [101]. About the chiral properties of this phase consult Appendix C.

2.5.4 The $W(1, \frac{1}{2}, 0)$ antiferromagnet, Type III

We have 24 symmetry related \mathbf{W} -vectors (the corners of the BZ, see the purple dots in Fig. 2.3(a)) in this order. The 24 vectors fall into 6 equivalency classes forming 6-armed star. This can be understood since each corner of the BZ is shared by four truncated octahedra. The six arms form three \pm pairs: $\mathbf{Q}_\alpha = \pm \mathbf{W}_1, \pm \mathbf{W}_2, \pm \mathbf{W}_3$ with classes

$$\begin{aligned} \mathbf{W}_1 &\sim \{(\pi, 0, 2\pi), (-\pi, -2\pi, 0), (-\pi, 2\pi, 0), (\pi, 0, -2\pi)\}, \\ \mathbf{W}_2 &\sim \{(2\pi, \pi, 0), (-2\pi, \pi, 0), (0, -\pi, -2\pi), (0, -\pi, 2\pi)\}, \\ \mathbf{W}_3 &\sim \{(0, 2\pi, \pi), (-2\pi, 0, -\pi), (0, -2\pi, \pi), (2\pi, 0, -\pi)\}. \end{aligned} \quad (2.32)$$

Since $\mathbf{W}_\alpha \approx -\mathbf{W}_\alpha$ to make the spins real in real space we have to combine the $\pm \mathbf{W}_\alpha$ pairs:

$$\mathbf{S}_i = \sum_{\alpha=1}^3 \mathbf{S}_{\mathbf{W}_\alpha}^0 e^{-i\mathbf{W}_\alpha \cdot \mathbf{R}_i} + \mathbf{S}_{-\mathbf{W}_\alpha}^0 e^{+i\mathbf{W}_\alpha \cdot \mathbf{R}_i}, \quad (2.33)$$

where the amplitudes form complex conjugate pairs

$$\mathbf{S}_{-\mathbf{W}_\alpha}^0 = \mathbf{S}_{\mathbf{W}_\alpha}^{0*}. \quad (2.34)$$

This type of ordering is also called a triple-Q one (we have three pairs of ordering vectors). The local spin length constraint results the following restrictions for the Fourier amplitudes:

$$\sum_{\alpha=1}^3 \mathbf{S}_{\mathbf{W}_\alpha}^{0*} \cdot \mathbf{S}_{\mathbf{W}_\alpha}^0 = \frac{1}{2}, \quad (2.35a)$$

$$\mathbf{S}_{\mathbf{W}_\alpha}^0 \cdot \mathbf{S}_{\mathbf{W}_\alpha}^0 \in i\mathbb{R}, \quad \forall \alpha, \quad (2.35b)$$

$$\mathbf{S}_{\mathbf{W}_\alpha}^0 \cdot \mathbf{S}_{\mathbf{W}_\beta}^0 = \mathbf{S}_{\mathbf{W}_\alpha}^{0*} \cdot \mathbf{S}_{\mathbf{W}_\beta}^0 = 0, \quad \forall \alpha \neq \beta. \quad (2.35c)$$

Since $\mathbf{S}_{\mathbf{W}_\alpha}^{0*} = \mathbf{S}_{-\mathbf{W}_\alpha}^0$ the first equation is the consequence of Eq. (2.13):

$$\sum_{\alpha=1}^3 (\mathbf{S}_{\mathbf{W}_\alpha}^{0*} \cdot \mathbf{S}_{\mathbf{W}_\alpha}^0 + \mathbf{S}_{-\mathbf{W}_\alpha}^{0*} \cdot \mathbf{S}_{-\mathbf{W}_\alpha}^0) = 1. \quad (2.36)$$

The last two equations follow from Eq. (2.14) with the choice $\mathbf{q}' = 2\mathbf{W}_\alpha$ and $\mathbf{q}' = \mathbf{W}_\alpha \pm \mathbf{W}_\beta$.

To calculate the number and properties of the free parameters we decompose the complex amplitudes into real vectors yielding

$$\mathbf{S}_{\pm\mathbf{W}_\alpha}^0 = \mathbf{u}_\alpha \mp i\mathbf{v}_\alpha, \quad \mathbf{u}_\alpha, \mathbf{v}_\alpha \in \mathbb{R}^3, \quad \alpha = 1, 2, 3 \quad (2.37)$$

and we express the complex constraints Eqs. (2.35) for the real and imaginary parts of the amplitudes as

$$\frac{1}{2} = \sum_{\alpha=1}^3 (|\mathbf{u}_\alpha|^2 + |\mathbf{v}_\alpha|^2) \quad (1 \text{ constraint}), \quad (2.38a)$$

$$|\mathbf{u}_\alpha| = |\mathbf{v}_\alpha|, \quad \forall \alpha \quad (3 \text{ constraints}), \quad (2.38b)$$

$$0 = \mathbf{u}_\alpha \cdot \mathbf{u}_\beta, \quad \forall \alpha \neq \beta \quad (3 \text{ constraints}), \quad (2.38c)$$

$$0 = \mathbf{v}_\alpha \cdot \mathbf{v}_\beta, \quad \forall \alpha \neq \beta \quad (3 \text{ constraints}), \quad (2.38d)$$

$$0 = \mathbf{u}_\alpha \cdot \mathbf{v}_\beta, \quad \forall \alpha \neq \beta \quad (3 \text{ constraints}). \quad (2.38e)$$

The three pairs of the real vectors \mathbf{u}_α and \mathbf{v}_α mean 18 free parameters, the equations above give 13 constraints and together with the global $O(3)$ degrees of freedom (3 free parameters) we are left with 2 free real parameters for the nontrivial degeneracy analogously to the Type-I phase.

As we have done to the Type-I phase, with the use of the global $O(3)$ freedom and the orthogonality and normalization of the \mathbf{u}_α real amplitudes we parametrize them as (see Footnote 2.18):

$$(\mathbf{u}_1 | \mathbf{u}_2 | \mathbf{u}_3) = \frac{1}{2} \left(\begin{array}{c|c|c} \xi & 0 & 0 \\ 0 & \eta & 0 \\ 0 & 0 & \zeta \end{array} \right), \quad (2.39)$$

where all the parameters are real and they satisfy the constraint: $\xi^2 + \eta^2 + \zeta^2 = 1$. We use the orthogonality relations between the real and imaginary parts \mathbf{u}_α and \mathbf{v}_α (see Eqs. (2.38c)–(2.38e)) resulting for the \mathbf{v}_α -s

$$(\mathbf{v}_1 | \mathbf{v}_2 | \mathbf{v}_3) = \frac{1}{2} \left(\begin{array}{c|c|c} \pm\xi & 0 & 0 \\ 0 & \pm\eta & 0 \\ 0 & 0 & \pm\zeta \end{array} \right), \quad (2.40)$$

and at this point any of the eight possible combination of the above signs can be chosen. We can ask the question: are all these eight choices *physically* different? The answer is no, in the following sense: There are only two independent phases forming chiral/enantiomorphic

partners, i.e. the two phases are related by space inversion, but there is no proper space group element that maps the two phases to each other. One class consists of the sign distribution in Eq. 2.40 with an odd number of minus signs, while in the other class the number of minus signs is even. Deriving the above statement is tedious, and we refer to Section IV.D and Appendix C of our original paper [102]. The above notion of chirality is explained in detail in Section C.2.

Substituting the real parametrization (2.39) and (2.40) in Eq. (2.37) and using Eq. (2.33) yields for the spin components in real space

$$\mathbf{S}_i(\xi, \eta, \zeta) = \sqrt{2} \begin{pmatrix} \xi \cos(\mathbf{W}_1 \cdot \mathbf{R}_i \pm \frac{\pi}{4}) \\ \eta \cos(\mathbf{W}_2 \cdot \mathbf{R}_i \pm \frac{\pi}{4}) \\ \zeta \cos(\mathbf{W}_3 \cdot \mathbf{R}_i \pm \frac{\pi}{4}) \end{pmatrix} = \sqrt{2} \begin{pmatrix} \xi \cos(\pi(x + 2z) \pm \frac{\pi}{4}) \\ \eta \cos(\pi(y + 2x) \pm \frac{\pi}{4}) \\ \zeta \cos(\pi(z + 2y) \pm \frac{\pi}{4}) \end{pmatrix}, \quad (2.41)$$

where we have used the Cartesian coordinates $\mathbf{R}_i = (x, y, z)$, and in the fcc lattice the coordinates x , y , and z can either be integers or some half integer combinations.

The last form of the spins in Eq. (2.41) is very handy in understanding the spin pattern. We just have to follow the phase shifts of the components when applying transformations, e.g. space group elements or time reversal. These transformation properties are described in detail in Section IV.D and Appendix C of our original paper [102]. It is seen that translating system by 2 in any of the Cartesian directions leaves the pattern unchanged. We have to change all the x , y , and z coordinates by an *even* number to achieve a 2π phase shift in all the spin components (see Eq. (2.41)) to leave them intact, and the smallest possible choices for such translations are the vectors

$$\mathbf{a}_1^W = (2, 0, 0), \quad \mathbf{a}_2^W = (0, 2, 0), \quad \mathbf{a}_3^W = (0, 0, 2). \quad (2.42)$$

Therefore we conclude that the resulting magnetic unit cell is just the conventional Bravais cell doubled in linear size and the resulting magnetic superlattice is a simple cubic one with the above vectors as primitive lattice translations. The usual cubic cell depicted in Fig. 2.1 contains four lattice points, so the magnetic unit cell contains 32 of them.

This 32-sublattice order is very complicated and we have found no elucidating way to visualize it, but nevertheless we enumerate some of its properties. The moments point to eight directions forming four \pm pairs (just like in the Type-II phase), but the four spin directions are connected by a tetrahedron rule (just like in Eq. (2.24)): Spins on every elementary tetrahedron sum up to zero. We can calculate the degeneracy in real space: Four unit vectors mean 8 parameters and the tetrahedron rule together with the global $O(3)$ removes six of them leading to the correct value of two for the number of free parameters.

One can ask the question: Is there a way to build up the 32-site order from an elementary tetrahedron satisfying the tetrahedron rule? The answer is positive: For example translating a tetrahedron by the vector $(1, 1, 1)$ and flipping all the spins is a symmetry of the configuration. Tetrahedra separated by vectors such as $(1, 0, 0)$ are also related by spin flips and carefully chosen two-fold rotations.

Our one last note is about the coplanar and collinear states. If we form a coplanar or double-Q order by setting e.g. $\zeta = 0$ in Eq. (2.41) the magnetic cell is halved to 16 sites, since $(0, 0, 1)$ is now a lattice translation (see Eq. (2.41)). The collinear, single-Q order has a 4-site unit cell: With $\eta = \zeta = 0$ the lattice translations become $(1, \frac{1}{2}, \frac{1}{2})$, $(0, 1, 0)$, and $(0, 0, 1)$.

2.6 Incommensurate phases

In this section we study the incommensurate phases (spin spirals), i.e. the phases that have ordering vectors \mathbf{Q} at general positions in the BZ (for an illustration of a spiral on the square lattice see Fig. 1.3(d)). We started to study the $J_1 - J_2 - J_3$ isotropic problem in order to find the simplest Heisenberg model on the fcc lattice having incommensurate phases, which we have actually found. But we discovered much more interesting ground states, for the details see the next section.

All the previously discussed commensurate phases are present in the $J_1 - J_2$ models [95, 17, 93], see the $J_3 = 0$ lines in Fig. 2.2(a) and (b). A new feature of the $J_3 \neq 0$ model is the presence of incommensurate orderings with propagation vectors (also called pitch vectors) along special directions [103, 104, 105] of high symmetry. The possible pitch vectors of the three incommensurate orderings are depicted in Fig. 2.3(d)–(e), and here we give the dependence of the wave-vectors on the exchange parameters and give their accessible ranges.

Since the ordering vectors are incommensurate we have to combine both $\pm\mathbf{Q}$, and a general spin spiral looks like

$$\mathbf{S}_i = \mathbf{s}_1 \cos(\mathbf{Q} \cdot \mathbf{R}_i + \varphi) \pm \mathbf{s}_2 \sin(\mathbf{Q} \cdot \mathbf{R}_i + \varphi), \quad (2.43)$$

where \mathbf{s}_1 and \mathbf{s}_2 are two arbitrary orthogonal unit vectors that span the plane of spin rotations, φ is an arbitrary phase, and \pm accounts for the two possible senses of rotations of the spiral, i.e. the two chiral enantiomers in the sense explained in Sec. C.2. Since the model is isotropic, nothing fixes the plane of rotation of the spins relative to the wave-vector or to the crystallographic axes (another manifestation of the spontaneous breaking of the global $O(3)$ symmetry).¹² Since the wave-vectors are incommensurate we are unable to build any multiple- \mathbf{Q} ground states out of their stars [99]. In the following we give the data about the three possible incommensurate orderings: The ordering vectors, the number of the arms of the stars, and the ranges of the ordering vectors and their optimized values as a function of the exchange parameters.

The three feasible directions of the pitch vectors are $\Delta(q, 0, 0)$ having a 6-armed star (see Fig. 2.3(d)), $\Lambda(q, q, q)$ having an 8-armed star (see Fig. 2.3(e)) and $\Sigma(q, q, 0)$ having a 12-armed star (see Fig. 2.3(f)).

- We can see in Fig. 2.2(a) that $\Delta(q, 0, 0)$ smoothly connects the two phases $\Gamma(0, 0, 0)$ and $X(1, 0, 0)$ so the possible q -values extend to the whole $\Delta(q, 0, 0)$ -star, i.e. $q \in (-2\pi, 2\pi]$. The optimized q -value of the spiral is

$$\cos \frac{q_\Delta}{2} = \frac{-J_1 - 2J_3}{J_2 + 4J_3}. \quad (2.44)$$

¹²One sometimes calls special cases of spirals when the orientation of the spin rotation plane contains (is perpendicular to) the propagation vector as cycloids (helices). We also note that a tiny homogeneous external field breaks the rotational symmetry of the system, and without changing the pitch vector aligns the spin rotation plane perpendicular to the field, and cants the spins a little bit in the direction of the field.

- The phase $\Lambda(q, q, q)$ smoothly interpolates between the phases $\Gamma(0, 0, 0)$ and $\Lambda(\frac{1}{2}, \frac{1}{2}, \frac{1}{2})$ and the possible q -values extend to the whole $\Lambda(q, q, q)$ -star $q \in (-\pi, \pi]$. The optimized q -value of the spiral is

$$\cos q_\Lambda = -\frac{J_1 + J_2 + 2J_3}{4J_3}. \quad (2.45)$$

- The case of the $\Sigma(q, q, 0)$ star is quite different, the possible q -values are restricted to the interval $1.28\pi \lesssim q \leq 2\pi$, making the transition between $\Gamma(0, 0, 0)$ and $\Sigma(q, q, 0)$ first order. The optimized q -value of the spiral is

$$\cos \frac{q_\Sigma}{2} = \frac{\sqrt{(J_1 + 2(J_2 + J_3))^2 - 48J_3(J_1 - 2J_3)}}{24J_3} - \frac{J_1 + 2(J_2 + J_3)}{24J_3}. \quad (2.46)$$

The vector $\mathbf{Q} = (\pi, \pi, 0)$ on the $\Sigma(q, q, 0)$ -line –although it is *not* a special point in the BZ– corresponds to a Néel-type commensurate antiferromagnetic order, and is called the Type-IV order. This type of ordering is realized in CoN [106, 71]. Since the quantum order by disorder mechanism favors collinear orders we tried to stabilize this type of order by including quantum fluctuations (in the spirit of [107]), but the available q -values for the $\Sigma(q, q, 0)$ phase are far from π , and our attempts failed.

2.7 Ground states of the extended manifolds

The degenerate ground state manifold \mathcal{M}_Z^1 for the first-neighbor antiferromagnetic Heisenberg model ($J_1 > 0$, $J_2 = J_3 = 0$) on the fcc lattice was found in [58, 19]. The degeneracy here means that the ordering pattern corresponding to *any* \mathbf{Q} -point on this manifold has the same energy, no matter how differently the real space patterns may look like. If we are lucky enough we may even mix different points on the manifold to create e.g. aperiodic ground state patterns. We will see plenty of examples in the following. A family of ground states were composed in [19] of (100)-directed, *noninteracting* (independent) AFM planes. In this section we characterize the phases with extended \mathcal{M}_{GS} -s of energetically degenerate ordering vectors (for the manifolds see Fig. 2.3(b)–(e)) that correspond to large ground state degeneracies at special points of the phase diagram shown in Fig. 2.2. These degeneracies found in Fourier space can be understood by a construction in real space: We cover the lattice with finite motifs (shown in Fig. 2.5), and write the Hamiltonian as a positive definite sum of complete squares of spins over these motifs. The minimization of the Hamiltonian imposes local constraints on the spins on these motifs, and *any* state that satisfies these local constraints is a good ground state. These constraints can be satisfied in several ways thereby explaining the degeneracy. We generalize the construction given in [19] for the other degenerate manifolds (besides \mathcal{M}_Z^1) and build up ground states from noninteracting planes (ferro- or antiferromagnetic, or even mixed). We have also found ground states consisting of ferromagnetically ordered chains (although these chains are interacting).

We solved the models of the extended manifolds for Ising spins $\mathbf{S}_i \in \{1, -1\}$, for finite, symmetric clusters. Details of the Ising calculations are given in Appendix D of the original

paper [102]. We also simulated the model numerically for planar (also called $O(2)$ or XY) spins $\mathbf{S}_i = (S_x, S_y)_i$, $S_x^2 + S_y^2 = 1$ as a guide to our intuition of the possible ground states of the $O(3)$ model.

The structure of this section is the following: We will consider all the five degenerate manifolds in different subsections, starting with the two-dimensional \mathcal{M}^2 followed by the one-dimensional ones. In every subsection we describe the finite motif covering and rewrite the Hamiltonian according to it. In the one-dimensional cases we construct several classes of unusual –e.g. aperiodic– ground states based on these coverings, but a *caveat* comes here. These constructions are sometimes quite complicated geometrically, and they are very hard to understand just by looking at two-dimensional pictures (although we tried to do our best when drawing the illustrations). The best way to understand such constructions is by building a real world ball-and-stick model, e.g. by using Geomag© (as we actually did). Therefore for the ones only interested in the resulting ground state patterns (or living without a properly colored fcc-model) every subsection closes with a short summary enumerating the ground state patterns found.

Table 2.3: Finite motifs we used to cover the face-centered cubic lattice (for pictures of them see Fig. 2.5). Second column: Symbols of the motifs used in formulas. Overcounting of the sites and the J_1 first, J_2 second, and J_3 third neighbor bonds. E.g. in a tetrahedral covering (see Fig. 2.5(a)) we put two tetrahedra of different orientation on each site, and as a consequence each first neighbor bond is shared by two tetrahedra, and no longer bonds are covered. In the seventh column we give the reference of the subfigures in Fig. 2.5 for the given motif.

Motif	Symbol	Site	J_1	J_2	J_3	Subfigure
Tetrahedron	tetra	2	2	–	–	(a)
Signed rectangle	rect ₁	6	2	4	1	(b)
Signed rectangle	rect ₂	6	2	4	1	(c)
Square	square	3	2	2	–	(d)
Octahedron	octa	1	2	1	–	(e)

2.7.1 The $J_1 = 2J_2 > 0$, $J_3 = 0$ point: The two-dimensional \mathcal{M}^2 ground state manifold

In this subsection we consider the two-dimensional ground state manifold \mathcal{M}^2 , give its finite-motif covering (and explain the technique in some detail), and rewrite the Hamiltonian based on this covering as a positive definite sum of complete squares of spins.

At the point $J_1 = 2J_2 > 0$, $J_3 = 0$ (see the green dot in Fig. 2.2(b)) the ordering vectors of the possible ground states form the two-dimensional \mathcal{M}^2 manifold, defined by

$$\cos \frac{Q_x}{2} + \cos \frac{Q_y}{2} + \cos \frac{Q_z}{2} = 0, \tag{2.47}$$

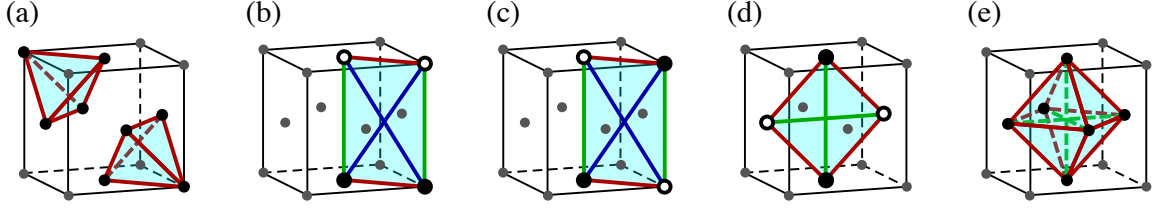


Figure 2.5: Finite motifs we have used to cover the face-centered cubic lattice to create the Heisenberg exchanges for models with high ground state degeneracies. Red, green and blue lines correspond to first, second, and third neighbor bonds of a motif, respectively. By covering the crystal with these motifs we count bonds and sites multiple times: This overcounting is given for every motif in Table 2.3. (a) the elementary tetrahedra (index “tetra” in formulas). On each lattice point we put two tetrahedra of different orientation: This way we cover every first neighbor bond twice (and no further neighbor bond is covered). (b) A signed rectangle (index “rect₁” in formulas): We can put 6 differently oriented rectangles on every site and we cover every first, second and third neighbor bond (for the overcounting the sites and bonds see Table 2.3). “Signed” here means that when we write the complete squares of the spin sums in Eq. (2.68) to construct the Hamiltonian we have to assign a minus sign to the spins sitting in the vertices denoted by white dots, black dots mean a plus sign for the appropriate spins. Together with the tetrahedra we use this motif to construct the ground states of the phase corresponding to the manifold $\mathcal{M}_{\frac{1}{2}}^1$, see Fig. 2.3(b). (c) A differently signed rectangle (index “rect₂” in formulas), very similar to the former one but with different sign distribution, see Eq. (2.69). We cover the lattice with this motif for the phase with ground state manifold \mathcal{M}_{Δ}^1 . (d) A signed square: (index “square” in formulas), by 3 differently oriented squares per site we cover the lattice for the phase with ground state manifold \mathcal{M}_{Λ}^1 , see Eq. (2.52). (e) Elementary octahedron (“octa” in formulas): We cover the lattice with one edge-sharing octahedron per site for the phase with the two-dimensional ground state manifold \mathcal{M}^2 , see Eq. (2.49).

and shown in Fig. 2.3(c). Ordering patterns corresponding to general points of this manifold correspond to spin spirals, so surfaces like this are called *spin spiral surfaces*. This is the only point of the phase diagram with such a large degeneracy [69, 98], however extending the model with a fourth neighbor coupling J_4 another two-dimensional manifold appears, see our paper [84], Section 3.4 and especially Fig. 3.6. We mention that the $W(1, \frac{1}{2}, 0)$ and $L(\frac{1}{2}, \frac{1}{2}, \frac{1}{2})$ points are parts of this manifold: Not surprisingly, since this is the point of the phase diagram where the $W(1, \frac{1}{2}, 0)$ and $L(\frac{1}{2}, \frac{1}{2}, \frac{1}{2})$ phases meet at the neck of the $\Sigma(q, q, 0)$ phase [93], see also Fig. 2.2(b). The Hamiltonian at this point becomes

$$\mathcal{H} = \frac{J_1}{4} \left(\sum_{\langle i,j \rangle_1} 4 \mathbf{S}_i \cdot \mathbf{S}_j + \sum_{\langle i,j \rangle_2} 2 \mathbf{S}_i \cdot \mathbf{S}_j \right). \quad (2.48)$$

We can express this Hamiltonian as a sum of complete squares of spins on the vertices of the edge-sharing elementary octahedra covering the lattice (for a picture of the covering

motif see Fig. 2.5(e))

$$\mathcal{H} = \frac{J_1}{4} \sum_{\text{octa}} (\mathbf{S}_1 + \mathbf{S}_2 + \mathbf{S}_3 + \mathbf{S}_4 + \mathbf{S}_5 + \mathbf{S}_6)^2 - \frac{3}{2} J_1 N, \quad (2.49)$$

where $\mathbf{S}_1, \dots, \mathbf{S}_6$ denote the six spins on the vertices of an octahedron. Every first neighbor bond is covered twice, and every second neighbor bond once (see Table 2.3), and consequently Eq. (2.49) exactly reproduces Eq. (2.48). This is why we chose the octahedra to cover the lattice for these particular values of the exchange parameters. Since $J_1 > 0$ Eq. (2.49) is minimized if the spins sum to zero on *every* octahedron:

$$\mathbf{S}_1 + \mathbf{S}_2 + \mathbf{S}_3 + \mathbf{S}_4 + \mathbf{S}_5 + \mathbf{S}_6 = \mathbf{0}, \quad (2.50)$$

and we dub this equation the *octahedron rule*. Every such configuration is a ground state, and every ground state satisfies the octahedron rule. The additional constant $-\frac{3}{2}J_1N$ gives the correct ground state energy with N being the number of sites (compare this to Table 2.2).¹³ The following commensurate orderings automatically satisfy the octahedron rule: The $L(\frac{1}{2}, \frac{1}{2}, \frac{1}{2})$ and $W(1, \frac{1}{2}, 0)$ -type ground states, see Fig. 2.4(b) and Eq. (2.41). A general spin spiral with ordering vectors on the manifold $\mathbf{Q} \in \mathcal{M}^2$ also follows the octahedron rule: We can check this by putting an arbitrary \mathbf{Q} in Eq. (2.43), and summing the spins on octahedra. The sum vanishes if and only if \mathbf{Q} satisfies the equation (2.47) of the surface \mathcal{M}^2 . Order by disorder effects (either thermal or quantum) at the harmonic level select the $L(\frac{1}{2}, \frac{1}{2}, \frac{1}{2})$ points on the \mathcal{M}^2 surface, see our paper [84] and Section 3.4, the technical details of the free energy calculations are presented in Appendix E. The appearance of such a large \mathcal{M}_{GS} is not an accident at all: Codimension-one manifolds (surfaces in three dimensions and curves in two dimensions) are guaranteed to form for models with special parameters, and we devote the whole Chapter 3 to a recipe for constructing such models on Bravais lattices.

In the next subsection we describe the finite motif covering corresponding to the one-dimensional \mathcal{M}_Λ^1 ground state manifold, and construct some unusual ground state configurations.

2.7.2 The $\Gamma(0, 0, 0)$ - $\Lambda(q, q, q)$ - $L(\frac{1}{2}, \frac{1}{2}, \frac{1}{2})$ triple point: The one-dimensional \mathcal{M}_Λ^1 ground state manifold

In this subsection we consider the one-dimensional ground state manifold \mathcal{M}_Λ^1 , we give its finite-motif covering and rewrite the Hamiltonian based on this covering as a positive definite sum of complete squares of spins. We construct several classes of unusual –e.g.

¹³It is worth emphasizing that comparing the additional constant to the true ground state energies calculated by the Luttinger-Tisza method and enlisted in Table 2.2 is crucial: (i) We have shown in Eq. (2.9) that the Luttinger-Tisza energy is a lower bound to the true ground state energy, (ii) Nothing guarantees the uniqueness of a finite covering of the lattice for a given set of exchange parameters, and the different coverings can have different ground state energies (like the additional constant in Eq. (2.49)). But if the additional constant of the Hamiltonian in its motif-covering form (like Eq. (2.49)) agrees with the Luttinger-Tisza value given in Table 2.2 we can be sure that configurations satisfying the motif rule (e.g. Eq. (2.50)) give correct ground state configurations since they achieve the smallest possible ground state energy.

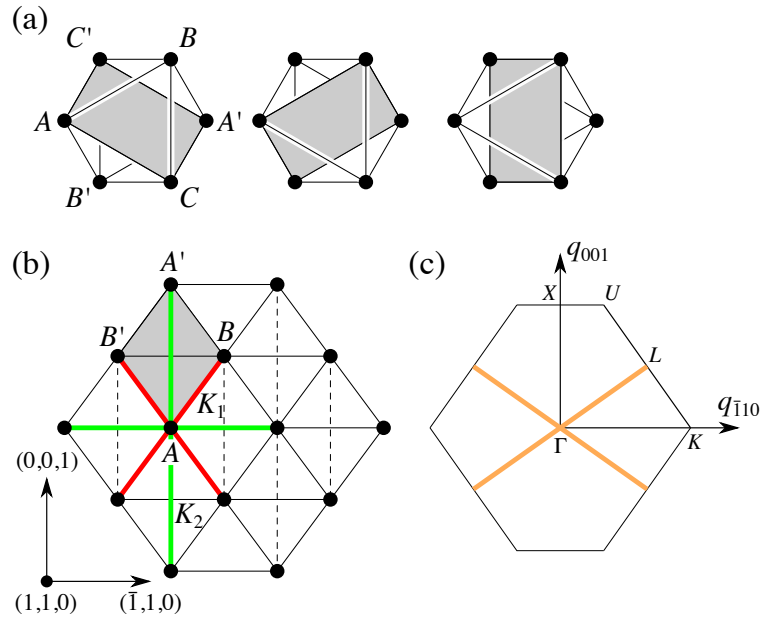


Figure 2.6: (a) Octahedra covering the face-centered cubic lattice (see also Fig. 2.1(d) and Fig. 2.5(e)). We show the three realizable orientations of the signed squares (depicted in Fig. 2.5(d)) inscribed in the octahedron. (b) The face-centered cubic lattice viewed from the (110) direction. This is the two-dimensional lattice of the (110) ferromagnetic chains that form a class of possible ground state solutions of the model in the $\Gamma - \Lambda - L$ point of the phase diagram (with exchange parameters $J_1 = 2J_2 > 0$, $J_3 = 0$, see also the green dot in Fig. 2.2(b)). The bond strengths of the effective two-dimensional Hamiltonian (2.60) for the chains are K_1 for the first neighbor red bonds, and K_2 for the second neighbor green bonds. Note that this lattice of interacting chains is topologically equivalent to a first and second neighbor model on the square lattice. The gray rhombus is the projection of one of the covering signed squares also shown in Fig. 2.5(d), minus signs of the spins are associated to one pair of opposite vertices, say to A and A' . (c) Brillouin zone of the lattice shown in Fig. 2.6(b), together with the ground state manifold (orange cross) of the Hamiltonian Eq. (2.60), this manifold is nothing but the section of \mathcal{M}_Λ^1 (see Fig. 2.3(e)) with the (110) q -plane passing through the origin. We note that this BZ is *not* a perfect hexagon. Symmetry points of the original three dimensional BZ (see Fig. 2.3(a)) are depicted, together with some points less frequently considered: $K \left(\frac{3}{4}, \frac{3}{4}, 0 \right)$ and $U \left(\frac{1}{4}, \frac{1}{4}, 1 \right)$.

aperiodic— ground states based on these coverings. These constructions are sometimes very technical and quite complicated geometrically, and they are very hard to understand just by looking at two-dimensional pictures, therefore for the ones only interested in the resulting ground state patterns every subsection closes with a short summary enumerating the ground state patterns found.

At the triple point $J_2 = -J_1 > 0$, $J_3 = 0$ (see the orange dot in the phase diagram Fig. 2.2(a)) the \mathcal{M}_{GS} is \mathcal{M}_Λ^1 depicted in Fig. 2.3(e). The possible ordering vectors $\Lambda(q, q, q)$ smoothly connect $\Gamma(0, 0, 0)$ and $L \left(\frac{1}{2}, \frac{1}{2}, \frac{1}{2} \right)$, explaining the shape of the manifold. The

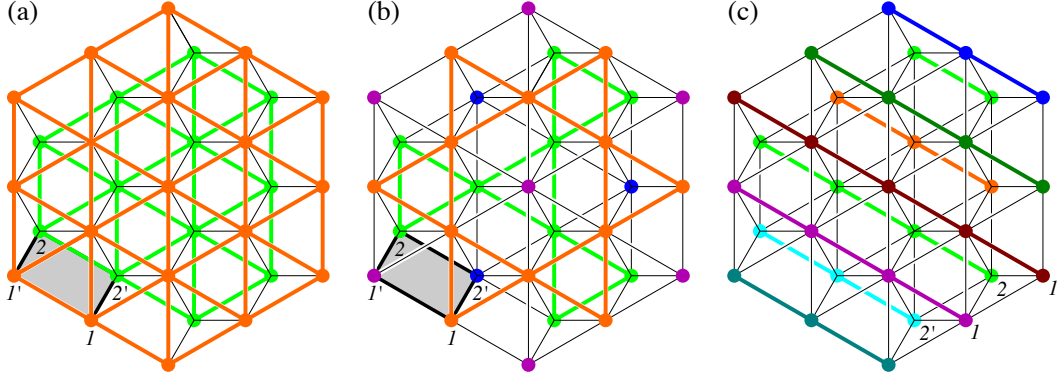


Figure 2.7: The face-centered cubic lattice viewed from the (111) direction. (a) Neighboring (111) planes are shown in orange and green, the octahedra connecting the planes are denoted by thin, black hexagons. The planes form triangular lattices. We can see the 6 first neighbor (J_1) in-plane bonds (in orange) emerging from the central site, and the 3 black J_1 lines connecting the central site to the green plane (the enumeration of all the intra- and interplane bonds is given in Table 2.4). The gray parallelogram denotes the projection of a covering square also shown in Fig. 2.5(d). (b) A solution of the model $\Gamma - \Lambda - L$ point of the phase diagram, see the orange dot in Fig. 2.2(a). Kagome sublattices of majority spins that are ordered ferromagnetically (S_1 orange, and green S_2) are shown on the triangular (111) planes. Minority spins are shown by purple $S_{1'}$ and blue $S_{2'}$ dots. (c) Highlighted $(\bar{1}10)$ lines on the (111) planes. These chains order ferromagnetically in a class of solutions of the model in the $\Gamma - \Lambda - L$ point of the phase diagram. The chains interact by the interactions given in Eq. (2.60), see also Fig. 2.6(b).

Hamiltonian at this point becomes

$$\mathcal{H} = J_1 \sum_{\langle i,j \rangle_1} \mathbf{S}_i \cdot \mathbf{S}_j - J_1 \sum_{\langle i,j \rangle_2} \mathbf{S}_i \cdot \mathbf{S}_j, \quad (2.51)$$

note that this is a mixed ferro-antiferromagnetic model. We cover the lattice by signed squares (for the sign distribution see Fig. 2.5(d))

$$\mathcal{H} = -\frac{J_1}{4} \sum_{\text{square}} (\mathbf{S}_1 - \mathbf{S}_2 + \mathbf{S}_3 - \mathbf{S}_4)^2 + 3J_1 N, \quad (2.52)$$

to every site we can draw 3 squares, directed in each of the $\{100\}$ planes. Consequently every first and second neighbor bond is covered twice, see Table 2.3. Just like in the previous subsection the Hamiltonian is minimized if and only if the

$$\mathbf{S}_1 - \mathbf{S}_2 + \mathbf{S}_3 - \mathbf{S}_4 = \mathbf{0} \quad (2.53)$$

sums vanish on *every* square (a *square rule*), the ground state energy per site can be inferred from the additional constant $\varepsilon = +3J_1$ (compare this to Table 2.2).

The three equations on the three signed squares are dependent, and instead of them we can use the octahedra containing these squares to cover the lattice (see Fig. 2.1(d) and

Fig. 2.6(a)). Out of the 3 square equations on orthogonal squares only two equations are independent per octahedron. With the notations of Fig. 2.6(a) for the sites of an octahedron, the ground state spin configuration satisfies the equations

$$\mathbf{S}_A + \mathbf{S}_{A'} = \mathbf{S}_B + \mathbf{S}_{B'} = \mathbf{S}_C + \mathbf{S}_{C'} = 2\mathbf{m}, \quad (2.54)$$

where the auxiliary vector \mathbf{m} is proportional to the magnetization of an octahedron. We can solve them introducing the \mathbf{a} , \mathbf{b} , and \mathbf{c} vectors

$$\mathbf{S}_A = \mathbf{m} + \mathbf{a}, \quad \mathbf{S}_{A'} = \mathbf{m} - \mathbf{a}, \quad (2.55a)$$

$$\mathbf{S}_B = \mathbf{m} + \mathbf{b}, \quad \mathbf{S}_{B'} = \mathbf{m} - \mathbf{b}, \quad (2.55b)$$

$$\mathbf{S}_C = \mathbf{m} + \mathbf{c}, \quad \mathbf{S}_{C'} = \mathbf{m} - \mathbf{c}. \quad (2.55c)$$

The spin length constraint $|\mathbf{S}_A|^2 = |\mathbf{S}_{A'}|^2 = 1$ implies $(\mathbf{m} \pm \mathbf{a}) \cdot (\mathbf{m} \pm \mathbf{a}) = 1$ (and we have analogous equations for \mathbf{b} and \mathbf{c}). Adding and subtracting these equations result the set

$$|\mathbf{m}|^2 + |\mathbf{a}|^2 = 1, \quad \mathbf{m} \cdot \mathbf{a} = 0, \quad (2.56a)$$

$$|\mathbf{m}|^2 + |\mathbf{b}|^2 = 1, \quad \mathbf{m} \cdot \mathbf{b} = 0, \quad (2.56b)$$

$$|\mathbf{m}|^2 + |\mathbf{c}|^2 = 1, \quad \mathbf{m} \cdot \mathbf{c} = 0. \quad (2.56c)$$

The vectors above can differ from octahedron to octahedron, as long as they satisfy some compatibility conditions: Sharing an edge creates a dependence among them (in what follows we omit the octahedron index for simplicity). Having spins with N_s components the \mathbf{a} , \mathbf{b} , \mathbf{c} , and \mathbf{m} mean $4N_s$ degrees of freedom, and there are 6 constraints in Eq. (2.56): We expect $4N_s - 6$ free continuous parameters describing the ground state of an octahedron. A *ferromagnetic* order obeys the rule given by Eq. (2.54) or Eq. (2.53) trivially, since the

Table 2.4: Number of bonds connecting a single lattice point to its neighbors on the nearby (111) planes, see Fig. 2.1(b) and especially Fig. 2.7(a). The first column contains the separation of consecutive planes: “0” means the (111) plane containing the chosen point, “1” means the two first neighbor (111) planes to the point, and “2” means the two second neighbor (111) planes. The second column contains the number of first neighbor bonds connecting the chosen point to the planes of the given separation, the last two columns give the number of further neighbor bonds between planes of the indicated separation.

Separation	J_1	J_2	J_3
0	6	0	6
1	6	6	12
2	0	0	6

$\Gamma(0, 0, 0)$ point is part of this manifold.

For a ferromagnet $\mathbf{a} = \mathbf{b} = \mathbf{c} = \mathbf{0}$. For $\mathbf{m} = \mathbf{0}$ we have an *antiferromagnetic* $L(\frac{1}{2}, \frac{1}{2}, \frac{1}{2})$ order: All the Type II states given in Sec. 2.5.3 and depicted in Fig. 2.4(b) can

be constructed this way. As an example we can choose the single ordering vector (π, π, π) and get a set of alternating (111) ferromagnetic planes, see Eq. (2.28) with only the amplitude $S_{L_1}^0$ being nonzero, and Fig. 2.4(b) with $S_B = -S_C = S_D = S_A$. This suggests other feasible candidate ground states: We may construct a family of ground states by stacking ferromagnetic (111) planes (these planes form triangular lattices as shown in Fig. 2.7(a)).

Stacking of independent $\{111\}$ ferromagnetic planes

Assuming a ground state consisting of ferromagnetically ordered (111) planes, we can represent a plane by a single effective superspin given by the unit vector s_i . Here “ i ” indexes the consecutive planes and we can derive an effective one-dimensional model for these effective spins

$$\mathcal{H}_\Lambda^{(111)} = \frac{1}{4} (6J_1 + 6J_2 + 12J_3) \sum_{i=1}^{L^{(111)}} s_i \cdot s_{i+1} + \frac{1}{2} (6J_1 + 6J_3) L^{(111)}, \quad (2.57)$$

where we can deduce the effective exchanges either from Table 2.4 or from Fig. 2.7(a). Here $L^{(111)}$ is the number of (111) planes in the lattice, and the additional constant is inferred from the in-plane couplings. If we substitute the actual values $J_2 = -J_1$ and $J_3 = 0$ in Eq. (2.57), we realize that the first term disappears, so the planes disentangle (become noninteracting), and the last term gives $+3J_1$ for the correct ground state energy per site of the original model, see Table 2.2. The ordering pattern we get is of the form $F_1 F_2 F_3 F_4 \dots$, with F_i labeling the independent ferromagnetic planes. As seen in Fig. 2.7(a) only the first neighbor planes are connected by the covering squares. With the notation of Fig. 2.7(a) we can see that $S_{1'} = S_1$ and $S_{2'} = S_2$, since these pairs lie on FM planes. Therefore Eq. (2.54) is automatically satisfied since $S_1 + S_2 = S_{1'} + S_{2'}$.

A state like this can be constructed by choosing ordering vectors solely from the (q, q, q) line of the \mathcal{M}_Λ^1 manifold,

$$\mathbf{S}_{(x,y,z)} = \sum_{q \in [-\pi, \pi]} \mathbf{S}_{(q,q,q)}^0 e^{-iq(x+y+z)}. \quad (2.58)$$

Any point on the $\Lambda(q, q, q)$ line can be present in the above sum, as long as we include both (q, q, q) and $-(q, q, q)$, and carefully choose the Fourier amplitudes to satisfy the local spin length constrains. We can choose any of the symmetry related $\langle 111 \rangle$ directions in the above expansion.

By solving the Ising problem on finite clusters (see Appendix D of our original paper [102] for details) we have found the $\{111\}$ stacking of *independent* ferromagnetic planes: The Fourier transform of these ordering patterns consists only of one line of ordering vectors in \mathcal{M}_Λ^1 . Another ordering pattern was also found, consisting of up and down spins forming two interpenetrating pyrochlore lattices: The unit cell contains 8 lattice points, see Fig. 2.4(b) with $S_A = S_B = S_C = S_D = 1$ and $S_{\bar{A}} = S_{\bar{B}} = S_{\bar{C}} = S_{\bar{D}} = -1$.

Stacking of almost independent $\{111\}$ “kagome” planes

Numerical simulations on $O(2)$ spins revealed yet another class of ground state solutions, where the $3/4$ majority fraction of the spins on the triangular (111) planes formed a ferro-

magnetic order on a *kagome* sublattice of these planes (see the orange and green sublattices in Fig. 2.7(b)). The minority of the spins (purple and blue dots in Fig. 2.7(b)) seemed to be independent of the majority ones, and a similar pattern was found on every consecutive (111) plane. In the following we will use the notations of Fig. 2.7(b). We can apply the *octahedral constraint* of Eq. (2.56): We assume the kagome-style pattern on consecutive planes indexed by $1, 2, 3, \dots$, and follow the consequences of the constraints propagate as we move along the octahedra between the planes. We set the majority spins to \mathbf{S}_1 and the minority spins to $\mathbf{S}_{1'}$ on the first layer. For Ising spins fixing the spins on plane “1” determines the spins on all of the consecutive layers, and the resulting ordering is the quadruple- \mathbf{Q} order consisting of interpenetrating pyrochlore lattices described above. For $O(2)$ spins, if $\mathbf{S}_{1'} \neq -\mathbf{S}_1$ we get four feasible solutions for $\{\mathbf{S}_{2'}, \mathbf{S}_2\}$: This results in a \mathbb{Z}_4 degree of freedom. If $\mathbf{S}_{1'} = -\mathbf{S}_1$ we can pick any $\mathbf{S}_{2'} = -\mathbf{S}_2$ pairs meaning an $O(2)$ degree of freedom. For $O(3)$ spins, if $\mathbf{S}_{1'} \neq -\mathbf{S}_1$ we have an $O(2) \times \mathbb{Z}_2$ freedom for choosing $\{\mathbf{S}_{2'}, \mathbf{S}_2\}$. If $\mathbf{S}_{1'} = -\mathbf{S}_1$ we can pick any $\mathbf{S}_{2'} = -\mathbf{S}_2$: This is a degree of freedom parametrized by the unit sphere S^2 . We may safely call this very small dependence of the consecutive kagome planes “almost independence”.

Interacting $\langle 110 \rangle$ ferromagnetic linear chains

In the numerical simulation of the $O(2)$ spins we have found ordering patterns consisting of apparently independent chains ordered ferromagnetically [108, 109] lying in the $\{111\}$ planes and pointing in one of the $\langle \bar{1}10 \rangle$ directions, a set of such lines is shown in Fig. 2.7(c). Based on these numerically found patterns we may reason the following way: We *assume* a ferromagnetic order along the (110) chains (the bond strengths along the chains are $J_1 < 0$ ferromagnetic), and we can deduce an effective two-dimensional model with the chains substituted by a single effective unit length superspin \mathbf{s}_i , here the index “ i ” refers to points of the lattice formed by the chains, this two-dimensional lattice is shown in Fig. 2.6(b). The effective interactions K_δ (here δ points to the neighboring chains) are in general very complicated (each point has 16 neighbors, and usually they are connected by multiple bonds of the original fcc lattice). But the actual exchange parameters ($J_2 = -J_1$ and $J_3 = 0$) simplify the situation considerably resulting in a remarkably simple set of nonzero effective exchanges:

$$K_1 = 2J_1 + 2J_3 = 2J_1 < 0, \quad (2.59a)$$

$$K_2 = J_1 + 2J_2 = -J_1 > 0, \quad (2.59b)$$

where the bonds can be found in Fig. 2.6(b). We can deduce these interactions from the gray rhombus in Fig. 2.6(b) that shows the projection of the covering squares (one out of three) shown in Fig. 2.5(d). To get the correct effective exchanges we need to consider all the three differently oriented squares. This lattice built of the chains is topologically equivalent to a first and second neighbor FM-AFM model with bond strengths $K_2 = -K_1/2 > 0$ on the square lattice, that is known to be highly frustrated and we construct it from a different point of view in Subsection 3.3.1. The effective two-dimensional model becomes

$$\mathcal{H}_\Lambda^{(\bar{1}10)} = \frac{1}{2} \sum_{i,\delta} K_\delta \mathbf{s}_i \cdot \mathbf{s}_{i+\delta} + J_1 N^{(\bar{1}10)}, \quad (2.60)$$

and the additional constant can be deduced from the couplings within a chain, $N^{(\bar{1}10)}$ is the number of chains. This model is strongly frustrated with a codimension-one ground state manifold as seen in Fig. 2.6(c): This manifold is just the section of \mathcal{M}_Δ^1 with the $(\bar{1}10)$ \mathbf{q} -plane passing through the origin (the $q_{110} = 0$ plane, when using the notation of Fig. 2.6(b) and (c)). The degeneracy can also be explained by noting that the Hamiltonian can be written as a sum of complete squares on signed rhombi (the gray rhombus in Fig. 2.6(b)): the resulting rhombus rule $\mathbf{S}_A + \mathbf{S}_{A'} - \mathbf{S}_B - \mathbf{S}_{B'} = \mathbf{0}$ is just the signed square rule inherited from the original three dimensional problem (see also Subsection 3.3.1). Any state satisfying the rhombus rule is a ground state for the $(\bar{1}10)$ chains, this is also consistent with the numerical finding in $O(2)$ models: We saw apparently random chains obeying the rhombus rule.

Summary

As a summary we suggest the following candidate ground states for the model at the $\Gamma(0, 0, 0) - \Lambda(q, q, q) - L(\frac{1}{2}, \frac{1}{2}, \frac{1}{2})$ triple point:

- Stacking of *independent* ferromagnetic $\{111\}$ planes in the stacking style $F_1 F_2 F_3 F_4 \dots$. Such an ordering is realized in all the Ising, $O(2)$ and $O(3)$ models.
- *Almost independent* ferromagnetic kagome sublattices in the $\{111\}$ triangular planes. Such an ordering is realized in the $O(2)$ and $O(3)$ models. For Ising spins this order simplifies to the commensurate, quadruple-L order of intercalating pyrochlore lattices.
- *Interacting* ferromagnetic chains in the $\langle 110 \rangle$ directions, these are not present in the Ising models.

In the next subsection we describe the finite motif covering corresponding to the one dimensional \mathcal{M}_Δ^1 ground state manifold, and construct some unusual ground state configurations.

2.7.3 The $\Gamma(0, 0, 0) - \Delta(q, 0, 0) - X(1, 0, 0)$ triple point: The one-dimensional \mathcal{M}_Δ^1 ground state manifold

In this subsection we consider the one-dimensional ground state manifold \mathcal{M}_Δ^1 , we give its finite-motif covering and rewrite the Hamiltonian based on this covering as a positive definite sum of complete squares of spins. We construct several classes of unusual –e.g. aperiodic– ground states based on these coverings. These constructions are sometimes very technical and quite complicated geometrically, and they are very hard to understand just by looking at two-dimensional pictures, therefore for the ones only interested in the resulting ground state patterns every subsection closes with a short summary enumerating the ground state patterns found.

The triple point $J_2 = 2J_1$, $J_3 = -J_1/2$, with $J_1 < 0$ is shown by a yellow dot in the phase diagram Fig. 2.2(a). The feasible ordering vectors $\Delta(q, 0, 0)$ smoothly connect the

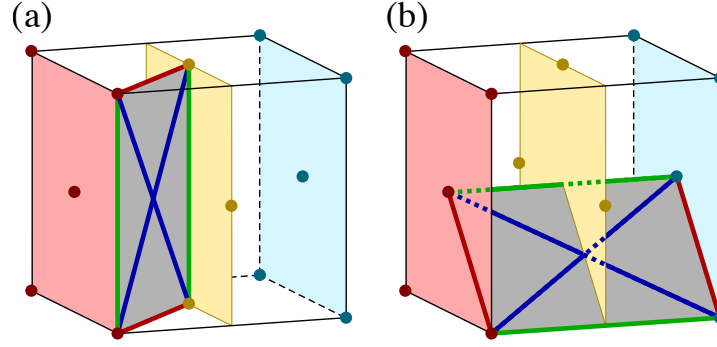


Figure 2.8: Consecutive (100) planes of the face-centered cubic lattice. (a) First neighbor planes are shown together with the signed rectangle motifs rect_1 or rect_2 connecting them (see Fig. 2.5(b) and (c), sign distribution is not indicated here). The coloring of the bonds is as follows: First (red, J_1), second (green, J_2) and third (blue, J_3) bonds connecting the consecutive planes. We only show one of the four possible orientations of the connecting rectangles. We show only one intraplane J_2 bond in the planes. (b) Second neighbor planes are connected with signed rectangle motifs rect_1 and rect_2 (see Fig. 2.5(b) and (c)), first (red, J_1), second (green, J_2) and third (blue, J_3) bonds connect the second neighbor planes. We only show one of the possible four orientations of the connecting rectangles. We show only one intraplane J_1 bond. For a total number of bonds connecting the appropriate planes see Table 2.5.

$\Gamma(0, 0, 0)$ and $X(1, 0, 0)$ points, explaining the shape of the manifold \mathcal{M}_Δ^1 ; for a picture of the manifold see Fig. 2.3(d). The Hamiltonian becomes

$$\mathcal{H} = J_1 \sum_{\langle i,j \rangle_1} \mathbf{S}_i \cdot \mathbf{S}_j + 2J_1 \sum_{\langle i,j \rangle_2} \mathbf{S}_i \cdot \mathbf{S}_j - \frac{J_1}{2} \sum_{\langle i,j \rangle_3} \mathbf{S}_i \cdot \mathbf{S}_j. \quad (2.61)$$

We can tessellate the lattice by signed rectangles (denoted by “ rect_2 ”) with signs distributed according to Fig. 2.5(c):

$$\mathcal{H} = -\frac{J_1}{4} \sum_{\text{rect}_2} (\mathbf{S}_1 - \mathbf{S}_2 + \mathbf{S}_3 - \mathbf{S}_4)^2 + 6J_1 N. \quad (2.62)$$

Since $-J_1/4 > 0$ the Hamiltonian is minimized if and only if $\mathbf{S}_1 - \mathbf{S}_2 + \mathbf{S}_3 - \mathbf{S}_4 = \mathbf{0}$ on every rectangle, so the ground state energy per site becomes $+6J_1$. A ferromagnetic order automatically obeys the above *rectangle rule* (and $\Gamma(0, 0, 0)$ and $X(1, 0, 0)$ are part of the manifold), as does any $X(1, 0, 0)$ (Type I) ordering. Choosing a single arm of the X -star, i.e. only $\xi \neq 0$ in Eq. (2.21) we have an ordering pattern of alternating ferromagnetic (100) planes, see Eq. (2.23) with $\eta = \zeta = 0$ and Fig. 2.4(a) with $-\mathbf{S}_B = -\mathbf{S}_C = \mathbf{S}_D = \mathbf{S}_A$. This suggests the following strategy: Probably we can build a state of (100) ferromagnetic planes (these planes themselves are square lattices). Although one cannot *a priori* exclude antiferromagnetism on these planes, If we choose $\xi = 0$ but $\eta \neq 0$ and $\zeta \neq 0$ in Eq. (2.23) we get an antiferromagnetic pattern on the (100) planes, with $\mathbf{S}_B = -\mathbf{S}_C$ and $\mathbf{S}_D = -\mathbf{S}_A$ in Fig. 2.4(a).

Table 2.5: Total number of bonds connecting a selected site to its neighbors on the nearby (100) planes, see Fig. 2.1(b) and especially Fig. 2.8. First column: The separation of consecutive planes: “0” means the (100) plane containing the chosen point, “1” means the two first neighbor (100) planes (see Fig. 2.8(a)), “2” means the two second neighbor (100) planes (see Fig. 2.8(b)). The last three columns give the number of first, second and third neighbor bonds (J_1 , J_2 , J_3) connecting the selected site to the points on the neighboring planes of indicated separations.

Separation	J_1	J_2	J_3
0	4	4	0
1	8	0	16
2	0	2	8

Stacking of independent $\{100\}$ ferro- or antiferromagnetic planes

Like in the discussion of Subsection 2.7.2. we can build a family of ground state patterns of ferromagnetically ordered (100) planes, see Fig. 2.8. Just like before we represent a plane by a single effective unit length superspin \mathbf{s}_i , where “ i ” indexes the consecutive planes and we deduce an effective one-dimensional model:

$$\begin{aligned} \mathcal{H}_\Delta^{(100)} = & \frac{1}{4} (8J_1 + 16J_3) \sum_{i=1}^{L^{(100)}} \mathbf{s}_i \cdot \mathbf{s}_{i+1} + \frac{1}{4} (2J_2 + 8J_3) \sum_{i=1}^{L^{(100)}} \mathbf{s}_i \cdot \mathbf{s}_{i+2} \\ & + \frac{1}{2} (4J_1 + 4J_2) L^{(100)}, \end{aligned} \quad (2.63)$$

where the effective exchange can be deduced either from Table 2.5 or Fig. 2.8, and $L^{(100)}$ is the number of (100) planes of the crystal. If we substitute the appropriate values $J_2 = 2J_1$ and $J_3 = -J_1/2$, we can see that the first two terms vanish, and consequently the planes disentangle. The last term gives $+6J_1$ for the correct ground state energy per site of the original model, see Table 2.2. This type of pattern is of the form $F_1 F_2 F_3 F_4 \dots$, where F_i indicates the independent ferromagnetic planes. This independence of the planes can be corroborated by noting that both the first and second neighbor planes are connected by the covering rectangles, and the rectangle rule is satisfied *bondwise* on every ferromagnetic plane: See the rectangles in Fig. 2.8, and the sign distribution in Fig. 2.5(c) and use that the planes are ferromagnetic.

We can Fourier decompose this pattern of ferromagnetically aligned, independent (100) planes as

$$\mathbf{S}_{(x,y,z)} = \sum_{q \in [-2\pi, 2\pi)} \mathbf{S}_{(q,0,0)} e^{-iqx}. \quad (2.64)$$

Any symmetric set of points on the $\Delta(q, 0, 0)$ line can be present in the above sum, as long as we care about the careful choice of the Fourier amplitudes to satisfy the local spin length constrain. We could have chosen any of the symmetry related directions in the above expansion.

We do not have such a large freedom if we want to build a ground state by stacking antiferromagnetic planes: A rect_2 can connect neighboring planes by J_1 bonds, in this case the J_2 bonds lie in-plane (connecting parallel spins, so they trivially satisfy the J_2 in-plane bonds), see Fig. 2.8(a). A rect_2 can also connect second neighbor planes by J_2 bonds, and the J_1 bonds lie in-plane (connecting antiparallel spins), see Fig. 2.8(b). Second neighbor antiferromagnetic planes are therefore *locked*: They need to possess the *same* antiferromagnetic order to satisfy the rectangle rule. Consequently we have two ways to stack the planes: Either we build the ground state from two types of independent antiferromagnetic planes $A_1A_2A_1A_2\dots$, or we can put independent ferromagnetic planes between the antiferromagnetic ones: $A_1F_1A_1F_2A_1F_3\dots$.

By solving the Ising problem on finite clusters (see Appendix D of our original paper in Ref. [102] for details) we have found the $\{100\}$ $F_1F_2F_3F_4\dots$ style stacking of *independent* ferromagnetic planes. We also have found the FM stacking with intercalating AFM planes in the $AF_1AF_2A\dots$ style. We do not have the alternating AFM stacking here: For Ising spins it is just an alternating FM stacking $F_1F_2F_1F_2\dots$ viewed from a perpendicular direction.

Interacting $\langle 100 \rangle$ ferromagnetic linear chains

In the numerical simulation of the $O(2)$ spins we have found ordering patterns consisting of apparently independent chains ordered ferromagnetically along the $\langle 100 \rangle$ directions. The Fourier transforms of these patterns correspond to points on *two* perpendicular lines of \mathcal{M}_Δ^1 in \mathbf{q} -space. Based on these numerically found orderings we may try the following: We *assume* a ferromagnetic order along the (100) chains. These chains form a square lattice with primitive lattice translations $(0, 1/2, 0)$ and $(0, 0, 1/2)$, as depicted Fig. 2.9(a). We represent such a chain by a single effective unit length superspin \mathbf{s}_i , where i indexes points of the square lattice and δ -s point to the neighbors of the lattice, and we arrive at the effective two-dimensional model

$$\mathcal{H}_\Delta^{(100)} = \frac{1}{2} \sum_{i,\delta} K_\delta \mathbf{s}_i \cdot \mathbf{s}_{i+\delta} + J_2 N^{(100)}, \quad (2.65)$$

$$K_1 = 2J_1, \quad K_2 = J_1 + 2J_3, \quad K_3 = J_2, \quad K_4 = 2J_3. \quad (2.66)$$

At the \mathcal{M}_Δ^1 ground state manifold the effective interactions become: $K_1 = 2J_1$, $K_2 = 0$, $K_3 = 2J_1$, and $K_4 = -J_1$, the effective exchanges are depicted in Fig. 2.9(a). The exchanges along the chains are strong and ferromagnetic with bond strengths $J_2 = 2J_1 < 0$, $N^{(100)}$ is the number of (100) chains in the system. This effective two-dimensional model has a ground state manifold of codimension one. In the BZ of the square lattice (for the lattice see Fig. 2.9(a)) the \mathcal{M}_{GS} forms the cross connecting the zone center to the midpoints of the zone boundary and the zone corner is also part of this manifold, as depicted in Fig. 2.9(c). This manifold is the intersection of \mathcal{M}_Δ^1 with the (100) \mathbf{q} -plane passing through the origin. The energy per site is $6J_1 = -6|J_1|$ ($4J_1$ comes from the interactions and $J_2 = 2J_1$ from the additional constant). This effective Hamiltonian can also be rewritten as a sum of squares on signed rectangles, these rectangles are inherited from the rect_2 -s projected to the (100) plane, see Fig. 2.9(a). Numerical investigations on

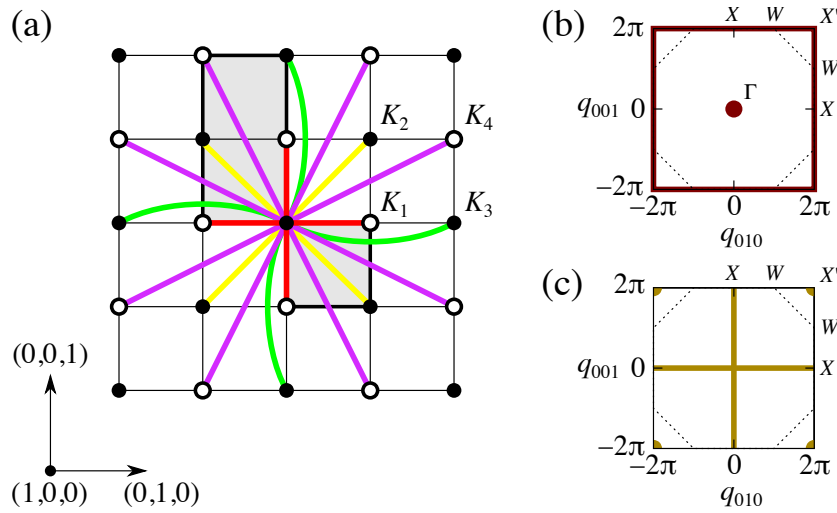


Figure 2.9: Two dimensional effective model of ferromagnetic chains pointing in the (100) direction, the chains form a square lattice and each chain is represented by an effective s_i superspin, resulting the model in Eq. (2.65). (a) Face-centered cubic lattice viewed from the (100) direction. The black and white dots indicate the (100) chains, lattice points on the differently colored chains are shifted by a vector $(1/2, 0, 0)$ (perpendicularly to the paper), but these points are equivalent in the two-dimensional model of chains. Primitive lattice translations of the square lattice of the chains are $(1/2, 0)$ and $(0, 1/2)$. Effective interactions of the chains K_δ in Eq. (2.65) are represented by colored bonds, exchanges up to fourth neighbors on the square lattice are generated. The gray rectangle: Projection of one covering rectangle of the original model, these rectangular motifs are depicted in Figs. 2.5(b) and (c). Black and white dots here have a totally different meaning than the sign distribution on rectangles in Figs. 2.5(b) and (c). Gray square: Projection of the elementary tetrahedron of the original three-dimensional model shown in Fig. 2.5(a). (b) Brillouin zone of the square lattice depicted in Fig. 2.9(a), together with the ground state manifold (red square) of the effective Hamiltonian Eq. (2.65), on the $X - W$ phase boundary of the original model. At the $\Gamma - X - W$ triple point this red $\Gamma(0, 0)$ point has to be included in the manifold. This manifold is the section of $\mathcal{M}_{\frac{1}{2}}^1$ (shown in Fig. 2.3(b)) with the (100) \mathbf{q} -plane passing through the origin. Symmetry points of the original three dimensional BZ (see Fig. 2.3(a)) are also indicated. (c) Brillouin zone of the square lattice shown in Fig. 2.9(a), the ground state manifold (dark yellow cross plus the zone corner) of the Hamiltonian at the $\Gamma - \Delta - X$ triple point (see Eq. (2.65)) is also shown. This manifold is the section of \mathcal{M}_{Δ}^1 (see Fig. 2.3(d)) with the (100) \mathbf{q} -plane passing through the origin. Symmetry points of the original three dimensional Brillouin zone (see Fig. 2.3(a)) are also indicated.

$O(2)$ spins is consistent with the above conclusions: We have found seemingly disordered FM chains respecting the projected rectangle rule.

Summary

As a summary, we have found the following classes of ground states for the $\Gamma(0, 0, 0) - \Delta(q, 0, 0) - X(1, 0, 0)$ triple point:

- $F_1F_2F_3F_4 \dots$ -style stacked *independent ferromagnetic* $\{100\}$ planes. We have found this type of ordering in all the Ising, $O(2)$ and $O(3)$ models.
- $AF_1AF_2AF_3 \dots$ -style stacked *independent ferromagnetic planes* separated by the same *antiferromagnetic* $\{100\}$ layers. We have found this type of ordering in all the Ising, $O(2)$ and $O(3)$ models.
- Stacking of two independent $\{100\}$ *antiferromagnetic layers* alternating in the style of $A_1A_2A_1A_2 \dots$. We have found this type of ordering in all the Ising, $O(2)$ and $O(3)$ models.
- Interacting *ferromagnetic chains* in the $\langle 100 \rangle$ directions, these are absent in the Ising models.

In the next subsection we describe the finite motif covering corresponding to the one dimensional $\mathcal{M}_{\frac{1}{2}}$ ground state manifold, and construct some unusual ground state configurations.

2.7.4 The $X(1, 0, 0) - W(1, \frac{1}{2}, 0)$ phase boundary (with an endpoint): The one-dimensional $\mathcal{M}_{\frac{1}{2}}$ ground state manifold

In this subsection we consider the one-dimensional ground state manifold $\mathcal{M}_{\frac{1}{2}}$, we give its finite-motif covering and rewrite the Hamiltonian based on this covering as a positive definite sum of complete squares of spins. We construct several classes of unusual –e.g. aperiodic– ground states based on these coverings. These constructions are sometimes very technical and quite complicated geometrically, and they are very hard to understand just by looking at two-dimensional pictures, therefore for the ones only interested in the resulting ground state patterns every subsection closes with a short summary enumerating the ground state patterns found.

On the phase boundary line separating the $W(1, \frac{1}{2}, 0)$ and $X(1, 0, 0)$ phases (the dark red line in Fig. 2.2(b)) we have the one-dimensional $\mathcal{M}_{\frac{1}{2}}$ ground state manifold in Fourier space, for this manifold see Fig. 2.3(b). This \mathcal{M}_{GS} is the crisscross connecting the points $X(1, 0, 0)$ and $W(1, \frac{1}{2}, 0)$ on the square faces of the BZ boundary. The phase boundary is given by $J_1 > 0$, $J_3 = J_2/4$, $-2 \leq J_2 \leq 0$ and the Hamiltonian at the boundary reads

$$\mathcal{H} = J_1 \sum_{\langle i,j \rangle_1} \mathbf{S}_i \cdot \mathbf{S}_j + J_2 \sum_{\langle i,j \rangle_2} \mathbf{S}_i \cdot \mathbf{S}_j + \frac{J_2}{4} \sum_{\langle i,j \rangle_3} \mathbf{S}_i \cdot \mathbf{S}_j. \quad (2.67)$$

We have two free parameters (J_1 and J_2) so writing this Hamiltonian as the sum of complete squares on finite motifs is a little bit more complicated than it was before. Here we use the elementary tetrahedra of the fcc lattice and the signed rectangles “rect₁”, the motifs are presented in Figs. 2.5(a) and (b). The overcountings of the bonds as seen in Table 2.3 are the following: Two tetrahedra and two rectangles cover a nearest neighbor bond, and four rectangles cover a second neighbor bond, and each third neighbor bond is covered once by a rectangle. For the sign distribution of the spins on the signed rectangle see Fig. 2.5(b), (minus signs belong to the white dots and plus signs to the black dots). The Hamiltonian reads

$$\mathcal{H} = \left(\frac{J_1}{4} + \frac{J_2}{8} \right) \sum_{\text{tetra}} (\mathbf{S}_1 + \mathbf{S}_2 + \mathbf{S}_3 + \mathbf{S}_4)^2 - \frac{J_2}{8} \sum_{\text{rect}_1} (\mathbf{S}'_1 + \mathbf{S}'_2 - \mathbf{S}'_3 - \mathbf{S}'_4)^2 + 2(J_2 - J_1)N. \quad (2.68)$$

Just like before, since $J_2 < 0$ all the prefactors are positive, and consequently the Hamiltonian is minimized if and only if the spins sum up to zero on every tetrahedron and on every rectangle (with the appropriate sign distribution): We have a *tetrahedron and rectangle rule*. The additional constant $2(J_2 - J_1)N$ (with N being the number of sites in the crystal) gives the correct ground state energy, see Table 2.2. The signed sum on the rect₁-s can be achieved by subtracting the spin sums of two edge-sharing tetrahedra, and consequently every configuration satisfying the tetrahedron rule automatically obeys the signed rectangle rule.

Stacking of independent $\{100\}$ antiferromagnetic planes

At the first neighbor $J_2 = J_3 = 0$, $J_1 > 0$ point the signed rectangles are unnecessary, and we only have the tetrahedron rule [17] (this is the point where the Σ -phase meets the $X - W$ phase boundary line). It was shown in Ref. [19] that one can construct ground states of (100) *independent antiferromagnetically* ordered planes in this point. The spins form a checkerboard pattern on the (100) layers and the independent stacking is of $A_1 A_2 A_3 \dots$ style. Here A_i denotes the i th antiferromagnetic plane. This construction extends without modification to the whole $X(1, 0, 0) - W(1, \frac{1}{2}, 0)$ boundary (see the dark red line emanating from the origin in Fig. 2.2(b)). An AFM stacking like this is truly a ground state: Both the tetrahedron and the rectangle rules are satisfied *bondwise* (the motifs and the sign distribution on the rectangles are presented in Fig. 2.5(a) and (b). The planes connected by the rectangles are shown in Fig. 2.8(a) and (b)): Spins on first neighbor bonds in a (100) layer are antiparallel and on second neighbor bonds they are parallel. As seen in Section 2.7.3 the planes disentangle, and the intraplane contribution of exchange couplings gives the correct ground state energy per spin as $2(J_2 - J_1)$, compare this to the Luttinger-Tisza value in Table 2.2.

The above spin pattern can be Fourier expanded by combining ordering vectors from the (100) directed lines of the $\mathcal{M}_{\frac{1}{2}}$ manifold (see Fig. 2.3(b)): This neatly explains the shape of $\mathcal{M}_{\frac{1}{2}}$, both the direction of the stacking, and that the planes are antiferromagnetically ordered. We also could have chosen the stacking direction of planes as (010) or (001) . We have found these ground states in the Ising solution, but there are only two choices for AFM directions in every plane.

Interacting $\langle 100 \rangle$ ferromagnetic linear chains

Simulating $O(2)$ spins we have found (100)-directed *ferromagnetic chains*, in an apparently random distribution. We can deduce an effective two-dimensional model for the FM chains sitting on a (100) square lattice resulting Eq. (2.65) with effective exchanges $K_1 = 2J_1$, $K_2 = J_1 + J_2/2$, $K_3 = J_2$, and $K_4 = J_2/2$, where $J_1 > 0$ and $-2 < J_2 \leq 0$ (we exclude the $J_2 = -2$, $\Gamma - X - W$ triple point here, and it will be considered in Subsection 2.7.5). We depict the interactions between the chains in Fig. 2.9(a). This model has a codimension-one ground state manifold: In the BZ of the square lattice the minima sit on the boundary of the BZ, see Fig. 2.9(c). But be careful: We have to *exclude* $\Gamma(0, 0)$ the BZ-center for the time being. The Fourier transform of the effective interactions has a local but not global minimum at the zone center, which gets lower and lower as we slide along the $X - W$ line towards the $\Gamma - X - W$ point, and this local minimum becomes degenerate with the \mathcal{M}_{GS} on the BZ boundary as we arrive at the point $J_2 = -2J_1$. This \mathcal{M}_{GS} is just the intersection of \mathcal{M}_Z^1 with the (100) \mathbf{q} -plane passing through the origin. The ground state energy per site becomes $2(J_2 - J_1)$ (where $J_2 - 2J_1$ comes from the interactions and J_2 from the additional constant in Eq. (2.65)), compare this to the Luttinger-Tisza value shown in Table 2.2. We can rewrite this Hamiltonian as a sum of complete squares on signed rectangles inherited from the tetrahedra and rect_1 -s projected to the (100) plane, see Fig. 2.9(a) (the projected tetrahedron rule is what prevents the ferromagnetic point $\Gamma(0, 0)$ being a global minimum). All the patterns found in the numerical solutions of $O(2)$ spins satisfied the projected rectangle and tetrahedron rules, but seemed otherwise randomly distributed.

Summary

The candidate ground states for the $X(1, 0, 0) - W(1, \frac{1}{2}, 0)$ phase boundary line are:

- Independently stacked *antiferromagnetic* $\{100\}$ planes of $A_1A_2A_3A_4\dots$ -style stacking. These ground states were found in all the Ising, $O(2)$ and $O(3)$ models.
- We have also found *interacting ferromagnetic chains* in the $\langle 100 \rangle$ directions, but they are not present the Ising models.

At the $J_2 = -2J_1$ and $J_3 = -J_1/2$ endpoint, where the phase boundary touches the $\Gamma(0, 0, 0)$ phase (the $\Gamma(0, 0, 0) - X(1, 0, 0) - W(1, \frac{1}{2}, 0)$ triple point), the tetrahedron rule vanishes in Eq. (2.68), and only the rectangle constraint remains $\mathbf{S}'_1 + \mathbf{S}'_2 - \mathbf{S}'_3 - \mathbf{S}'_4 = \mathbf{0}$, this rule is less restrictive and allows for other types of ground states, we describe this triple point $\mathcal{M}_Z^1 \cup \Gamma$ in the next subsection.

2.7.5 The $\Gamma(0, 0, 0) - X(1, 0, 0) - W(1, \frac{1}{2}, 0)$ triple point: The one-dimensional $\mathcal{M}_Z^1 \cup \Gamma$ ground state manifold

In this subsection we consider the one-dimensional ground state manifold $\mathcal{M}_Z^1 \cup \Gamma$, we give its finite-motif covering and rewrite the Hamiltonian based on this covering as a positive definite sum of complete squares of spins. We construct several classes of unusual –e.g.

aperiodic– ground states based on these coverings. These constructions are sometimes very technical and quite complicated geometrically, and they are very hard to understand just by looking at two-dimensional pictures, therefore for the ones only interested in the resulting ground state patterns every subsection closes with a short summary enumerating the ground state patterns found.

The $\Gamma(0, 0, 0) - X(1, 0, 0) - W(1, \frac{1}{2}, 0)$ triple point is very similar to the triple point $\Gamma(0, 0, 0) - \Delta(q, 0, 0) - X(1, 0, 0)$ described in Subsection 2.7.3, and has a much richer ground state structure than the remaining part of the $X(1, 0, 0) - W(1, \frac{1}{2}, 0)$ phase boundary line. This point sits at the $J_2 = -2J_1, J_3 = -J_1/2, J_1 > 0$ point of the phase diagram (see Fig. 2.2(b), this is the red dot where the $X - W$ line touches the Γ phase), and the ground state manifold is $\mathcal{M}_{\frac{1}{2}} \cup \Gamma$, see Table 2.2 for the properties of the manifold, and for a picture of it see Fig. 2.3(b). We can tessellate the lattice by signed rectangles (here the tetrahedron rule does not apply), with sign distribution presented in Fig. 2.5(b), and the Hamiltonian becomes

$$\mathcal{H} = \frac{J_1}{4} \sum_{\text{rect}_1} (\mathbf{S}_1 + \mathbf{S}_2 - \mathbf{S}_3 - \mathbf{S}_4)^2 - 6J_1 N, \quad (2.69)$$

since $J_1/4 > 0$ the Hamiltonian takes its minimum when $\mathbf{S}_1 + \mathbf{S}_2 - \mathbf{S}_3 - \mathbf{S}_4 = \mathbf{0}$ on every rectangle, with the ground state energy per site being $-6J_1$ (compare this to Table 2.2 for the Luttinger-Tisza value of the ground state energy). This constraint allows for ferromagnetism.

The models $\Gamma(0, 0, 0) - X(1, 0, 0) - W(1, \frac{1}{2}, 0)$ can be mapped $\Gamma(0, 0, 0) - \Delta(q, 0, 0) - X(1, 0, 0)$ to each other with a change of sign of J_1 but keeping the other two exchanges unchanged. We have investigated the triple point $\Gamma(0, 0, 0) - \Delta(q, 0, 0) - X(1, 0, 0)$ in detail, in what follows we will use the similarity of the two points, and for the details we refer to Subsection 2.7.3.

Stacking of independent $\{100\}$ ferro- or antiferromagnetic planes

We can stack (100) ferro- and antiferromagnetic layers perfectly analogously as was done in Subsection 2.7.3, we only need to interchange the words “antiferromagnetic” and “ferromagnetic”, and we have to change rect_2 to rect_1 everywhere. These ground states were found in all the Ising and $O(2)$ calculations. The possible alternation of layers is the following: We can either use two independent FM layers: $F_1 F_2 F_1 F_2 \dots$, or we can use a set of independent AFM planes in an $A_1 A_2 A_3 A_4 \dots$ -style, and mix the two, resulting independent AFM planes separated by FM layers of fixed spin direction: $F A_1 F A_2 F A_3 \dots$.

Interacting $\langle 100 \rangle$ ferromagnetic linear chains

In the simulation of $O(2)$ spins ground state patterns formed by *ferromagnetic* (100) chains appear again, and we can reuse the effective two-dimensional model for the chains presented in Eq. (2.65) on the square lattice, with the new effective exchanges $K_1 = 2J_1, K_2 = 0, K_3 = -2J_1$, and $K_4 = -J_1$. Strong ferromagnetic $J_2 = -2J_1 < 0$ bonds are present along the chains again. We have a codimension-one ground state manifold again:

The minimum is achieved on the boundary of the BZ of the square lattice, and we have to co-opt the $\Gamma(0, 0)$ point, as depicted in Fig. 2.9(b). Note that this manifold is nothing but the intersection of $\mathcal{M}_Z^{\frac{1}{2}}$ with the (100) \mathbf{q} -plane passing through the origin extended with the $\Gamma(0, 0, 0)$ point. The energy per site is $-6J_1$, compare this with Table 2.2. We can rewrite the Hamiltonian as a sum of squares on signed rectangles inherited from the rect_1 -s, projected to the (100) plane, see Fig. 2.9(a). All the $O(2)$ spin configurations of ferromagnetic chains seemed to be randomly distributed to the naked eye, but they actually satisfied this projected rectangle rule.

We can map all the spin patterns described above to the ground states of the $\Gamma(0, 0, 0) - \Delta(q, 0, 0) - X(1, 0, 0)$ model: We pick chains along one of the $\langle 100 \rangle$ directions and flip all the spins on every second chain in a checkerboard pattern, i.e. we change the sign of the spins on all the white (100) chains in Fig. 2.9(a).

Summary

We found the following ordering patterns for the $\Gamma(0, 0, 0) - X(1, 0, 0) - W(1, \frac{1}{2}, 0)$ triple point:

- We can stack *independent AFM* $\{100\}$ layers in an $A_1A_2A_3A_4\dots$ style. We have found this pattern in all the Ising, $O(2)$ and $O(3)$ models.
- We can stack *independent AFM* $\{100\}$ layers, separated by ferromagnetic planes (having the same spin direction) on the $\{100\}$ in a style of $A_1FA_2FA_3F\dots$. We have found this pattern in all the Ising, $O(2)$ and $O(3)$ models.
- We can stack two alternating *independent FM* $\{100\}$ layers $F_1F_2F_1F_2\dots$, this pattern is realized in all the Ising, $O(2)$ and $O(3)$ models.
- Finally, we have also found *interacting ferromagnetic* chains in the $\langle 100 \rangle$ directions, these are not present in the Ising models.

We close our chapter on the fcc-models with a summary of our results and with an outlook for further studies.

2.8 Summary

We studied in detail the ground state phase diagram of the classical isotropic J_1 - J_2 - J_3 Heisenberg model on the frustrated face-centered cubic lattice within the Luttinger-Tisza framework, which is exact in this case. The *commensurate* Type I, II and III ground state structures already present in the J_1 - J_2 models occupy a sizeable part of the phase diagram. We explicitly constructed the corresponding ground states and described their degeneracies. In these phases the possibility of multiple- \mathbf{Q} –non-collinear or even non-coplanar– orders were considered. We thoroughly analyzed the *chiral* Type III phase, yet undiscussed in the literature. Besides the commensurate phases we have shown that the frustrating effect of the third neighbor coupling introduces the *qualitatively new* feature of the model by

the emergence of *incommensurate* spin spirals, with pitch vectors pointing along high-symmetry directions of the crystal.

Subextensively degenerate *ground state manifolds* of dimension one and two in reciprocal space were also identified at particular phase boundaries and triple points of the phase diagram. We explained these degeneracies found in Fourier space by tessellating the lattice of finite motifs in real space, and by rewriting the Hamiltonian as a positive definite sum of complete squares of spins on these motifs. With the aid of this construction we were able to find large classes of ground states consisting of independent, aperiodically stacked ferromagnetic or antiferromagnetic layers of special crystal planes. We have also found solutions of frustratingly interacting, ferromagnetically ordered linear chains along special crystallographic directions. We related the real and Fourier pictures to each other.

We solved the model for Ising spins on finite, symmetric clusters, and we numerically simulated $O(2)$ spins, these solutions guided our intuition in finding the ground states and corroborated the analytical calculations. Numerical calculations on $O(3)$ spins resulted in even more complicated ground states, calling for further studies.

This work can be thought of as the starting point for further research: Investigating the classical phase diagram at *finite temperature* (including critical phenomena), former studies mainly focused on the first neighbor model (and to a less extent on the second neighbor model). Large degeneracy of the ground state manifolds may lead to the realization of *classical or quantum spin liquids* on the fcc lattice [110, 98, 111], provided that order by disorder mechanisms do *not* lift the degeneracy (as in the case for pyrochlore [25, 26, 91] and hyper-hyperkagome lattices [112]).

Finding non-coplanar and even chiral orders leads to other promising directions to look into: Topological structures such as skyrmions, hedgehogs or merons may emerge in non-coplanar magnets with potential future applications [113, 114]. Another interesting aspect of chirality is present in the $S = 1/2$ isotropic triangular quantum antiferromagnet with nearest and next nearest neighbors [115]: Chiralities defined on triangular plaquettes behave like Ising variables and they order at finite temperature.¹⁴ A promising experimental realization of these ideas on the kagome lattice is proposed in Ref. [116]. One possible consequence of such an order with finite scalar chirality of the localized spins in a triangular Kondo lattice model is the itinerant electrons' acquiring a Berry phase leading to an anomalous Hall effect [117].

Of particular experimental importance is the incorporation of finite *external magnetic fields* to the model and the study of its effect on the phase diagram (i.e. the introduction of new phases) and ground state properties.

The triple points in the J_1 - J_2 - J_3 Heisenberg model on the simple cubic and body-centered cubic lattices are known to allow for a quantum paramagnetic phase for $S = 1/2$ [118, 119, 120, 105]. Since three of the degenerate manifolds found for the fcc model support a ferromagnetic order there is a possibility that in the absence of long-range dipolar magnetic ordering, multipolar (or nematic) orders such as quadrupolar [121, 122, 123, 124, 125, 126, 127, 128, 129, 130, 131], and octupolar [88] could be stabilized in both classical and quantum models. Disorder effects are known to stabilize [18, 132] non-collinear/non-

¹⁴Although the global continuous symmetry of the Heisenberg model would prevent ordering at finite T by the Mermin-Wagner theorem, the emergent discrete symmetry of the chiralities allows their ordering.

coplanar phases, calling for further studies in this direction.

Chapter 3

Constructing extended ground state manifolds

3.1 Introduction

Among classical Heisenberg models the nearest neighbor kagome and pyrochlore lattices (Figs. 1.5(c) and (d)) have the largest ground state degeneracy possible: Their ground state manifolds (\mathcal{M}_{GS} 's) extend over their whole BZ's. Thereby these lattices provide the largest playground for a system to explore and realize a classical spin liquid, for details we refer to Subsection 1.1.4. What is the second best chance? An obvious guess would be to search for models with \mathcal{M}_{GS} 's of one less dimension (or codimension-one manifolds). On the diamond lattice with first and second neighbor interactions with $J_2/J_1 > 1/8$ the system develops a two dimensional ground state manifold (a *spin spiral surface*) as realized by MnSc_2S_4 [20, 21], see Subsection 1.1.4 for details.

We have also seen examples of codimension-one ground state manifolds (curves in two and surfaces in three dimensions) in some occasions on Bravais lattices at very special points in the phase diagram: On the square lattice with exchange ratio $J_2/J_1 = 1/2$ and on the fcc lattice again with $J_2/J_1 = 1/2$ (for the manifolds see the red square in Fig. 1.2(b) and Fig. 2.3(c)). At this point one starts to become suspicious¹ that there must be some deeper reason behind this pattern. The feeling is right: There is a *general construction scheme* for creating models with codimension-one ground state manifolds, with special interaction parameters.

Having an extended \mathcal{M}_{GS} is not sufficient to realize a classical spin liquid. One may fear that thermal order by disorder (see Subsection 1.1.3) selects a unique ground state, thereby preventing the development of the spin liquid phase. Even if the order by disorder mechanism is effective, there is still a possible temperature window $T_N < T \ll \Theta_{CW}$ (see Subsection 1.1.4) where the existence of the spin liquid phase is allowed [20, 21, 92].

The structure of the chapter is the following: First we define our setting. Section 3.2 is the heart of our results, there we give the recipe of constructing Heisenberg models on Bravais lattices having codimension-one \mathcal{M}_{GS} 's. In Section 3.3 we illustrate the method on the square (Subsection 3.3.1) and simple cubic and face-centered cubic (Subsection 3.3.2) lattices. Finally we calculate the low temperature free energy of the simple cubic and face-centered cubic models in order to determine their ground states selected by the thermal

¹'Once is happenstance. Twice is coincidence. The third time it's enemy action.' Ian Fleming, Goldfinger (1959)

order by disorder mechanism.

As usual, the classical isotropic Heisenberg Hamiltonian reads

$$\mathcal{H} = \frac{1}{2} \sum_{i,\delta} J_\delta \mathbf{S}_i \cdot \mathbf{S}_{i+\delta} = N \sum_{\mathbf{q} \in \text{BZ}} J(\mathbf{q}) \mathbf{S}_{\mathbf{q}} \cdot \mathbf{S}_{-\mathbf{q}}, \quad (3.1)$$

where \mathbf{S}_i are three-dimensional unit vectors at the sites \mathbf{R}_i of a *Bravais lattice*² Λ , with N sites and periodic boundary conditions, and $i + \delta$ is just a shorthand for $\mathbf{R}_i + \delta$. The J_δ are the exchange couplings between spins at sites with separation vectors δ belonging to the same orbits of the point group of the lattice (hence the J_δ 's are equal on these bonds). With this type of summation we count each bond twice, the prefactor $1/2$ counteracts against this overcounting. We sort the J_δ 's by the increasing length of δ , so we adopt the usual notation for first-, second-, third-, ... exchanges as J_1, J_2, J_3, \dots , respectively.³ Conventions for the Fourier transforms and the derivation of Eq. (3.1) are given in Appendix A. As usual the Fourier transform of the exchange couplings is defined as

$$J(\mathbf{q}) = \frac{1}{2} \sum_{\delta} J_\delta e^{-i\mathbf{q} \cdot \delta}. \quad (3.2)$$

Just a reminder: We search for the ground state manifold denoted by $\mathcal{M}_{\text{GS}} = \{\mathbf{Q}\}$, and it is the set of points where $J(\mathbf{q})$ takes its minimal value. In what follows we give the recipe of constructing models with codimension-one ground state manifolds.

3.2 The Ansatz and symmetries

Our wish is to construct Heisenberg models with codimension-one ground state manifolds. The best is to think about a three dimensional crystal (with three dimensional reciprocal space) having a two-dimensional *surface* as the \mathcal{M}_{GS} in the Brillouin zone, for an illustration see Fig. 2.3(c). Using the Luttinger-Tisza method [74] one can find the ground state of Eq. (3.1) by minimizing $J(\mathbf{q})$ (details of the method are described in Section 2.3). So our task is reduced to find a function $J(\mathbf{q})$ that takes its minimum on a whole surface (in three dimensions), and is the *Fourier transform of a genuine Heisenberg exchange interaction*.

The idea is quite simple: First we consider a real function $f(\mathbf{q})$ that satisfies the defining equation of the \mathcal{M}_{GS} $f(\mathbf{Q}) = 0$ with $\mathbf{Q} \in \mathcal{M}_{\text{GS}}$. Second, to ensure that $f(\mathbf{Q}) = 0$ is the minimum surface of $J(\mathbf{q})$ we make the following Ansatz:

$$J(\mathbf{q}) = f^2(\mathbf{q}) - C, \quad (3.3)$$

with C a tunable constant defined for convenience. Since $f(\mathbf{q})$ is real $f(\mathbf{q})^2 \geq 0$ and $f(\mathbf{q})^2 = 0$ if and only if $f(\mathbf{q}) = 0$. We would like to construct a Hamiltonian –see

²This condition of having a Bravais lattice can surely be lifted, but than the J_δ 's become matrices and the formalism gets complicated, but results much more realistic models without fine tuned parameters, see the $J_1 - J_2$ isotropic models on the honeycomb[83] and diamond[20] lattices (both lattices have a two site basis).

³More precisely: The bonds emanating from a point fall into orbits under the action of the point group of the lattice, and we consider models where in each orbit every bond has the same strength thereby discarding spatially anisotropic models.

Eq. (3.2)– on the Bravais lattice Λ that has the full translational symmetry of the lattice, so we try to find $f(\mathbf{q})$ in the form

$$f(\mathbf{q}) = \sum_{\xi \in \Xi} c_{\xi} e^{i\mathbf{q} \cdot \xi}, \quad (3.4)$$

where Ξ is a finite set of points in real space, and $f(\mathbf{q})$ is a *real* function of the wave-vector.⁴ Using Eq. (3.3) $J(\mathbf{q})$ takes the form

$$J(\mathbf{q}) = \sum_{\xi, \xi' \in \Xi} c_{\xi} c_{\xi'} e^{i\mathbf{q} \cdot (\xi + \xi')} - C. \quad (3.5)$$

The question arises: What are the constraints on Ξ and c_{ξ} to produce a lattice symmetric Heisenberg model on the Bravais lattice Λ ? $J(\mathbf{q})$ has to satisfy Eq. 3.2 with $\delta = \mathbf{R}_j - \mathbf{R}_i$, where $\mathbf{R}_i, \mathbf{R}_j \in \Lambda$ (basically we have to compare Eq. 3.2 and Eq. 3.5). We enumerate the consequences of the constraints:

- Since $f(\mathbf{q})$ –defined in Eq. (3.4)– is real, for every $\xi \in \Xi$ also $-\xi$ is contained in Ξ , so the point set Ξ is *inversion symmetric*. Another consequence of the reality of $f(\mathbf{q})$ is the following for the coefficients: $c_{-\xi} = c_{\xi}^*$.
- Now we can substitute $\xi' \rightarrow -\xi'$ in Eq. (3.5) yielding $\xi - \xi' \in \Lambda$. So Ξ is, by definition, an inversion symmetric finite subset of an *affine lattice* Λ^* , i.e. Λ shifted by some arbitrary vector δ^* :

$$\Lambda^* = \Lambda + \delta^*, \text{ and } \Xi \subset \Lambda^*. \quad (3.6)$$

This concept of an affine lattice is just the discrete version of the definition of an affine space in ordinary linear algebra. This δ^* must not be confused with the lattice separation vector δ of the original lattice.

- Substituting $\xi' \rightarrow \xi$ in Eq. (3.5) yields:

$$2\delta^* \in \Lambda. \quad (3.7)$$

There are at most four choices for Λ^* in two dimensions and eight in three dimensions, but not all of these choices result in a Hamiltonian having the full point symmetry of Λ . If we denote the primitive lattice vectors of Λ as $\mathbf{a}_1, \mathbf{a}_2, \mathbf{a}_3$, (in three dimensions) then the four possible choices for the shift vector δ^* in two dimensions are $\delta^* \in \frac{1}{2} \{0, \mathbf{a}_1, \mathbf{a}_2, \mathbf{a}_1 + \mathbf{a}_2\}$, and the eight choices in three dimensions are $\delta^* \in \frac{1}{2} \{0, \mathbf{a}_1, \mathbf{a}_2, \mathbf{a}_3, \mathbf{a}_1 + \mathbf{a}_2, \mathbf{a}_1 + \mathbf{a}_3, \mathbf{a}_2 + \mathbf{a}_3, \mathbf{a}_1 + \mathbf{a}_2 + \mathbf{a}_3\}$. Of course we only enumerated the simplest shift vectors, but any equivalent vector to those mentioned above, further away from the "origin" would do as well.

⁴A complex $f(\mathbf{q}) = f'(\mathbf{q}) + i f''(\mathbf{q})$ with $J(\mathbf{q}) = |f(\mathbf{q})|^2 - C$ would result in a codimension-two \mathcal{M}_{GS} defined by $f'(\mathbf{q}) = 0$ and $f''(\mathbf{q}) = 0$ (of course this can still be interesting in three dimensional space, see Fig. 2.3(b), (d), and (e)). Another possibility is to combine several appropriate $f(\mathbf{q})$'s, e.g. as a positive definite sum. This surely works, but results more and more complicated interactions, so we concentrate on the individual building blocks and consider only a single function (for the moment).

Let us summarize what we have achieved so far: To construct a Heisenberg model with a codimension-one \mathcal{M}_{GS} we use Eq. (3.5), where the finite point set Ξ is an inversion symmetric (inversion centered at some point of the lattice Λ of the original Hamiltonian Eq. (3.1)) subset of the affine lattice $\Lambda^* = \Lambda + \delta^*$, with $2\delta^* \in \Lambda$. But this is not enough: Let us assume having a square lattice with primitive vectors $\mathbf{a}_1 = (1, 0)$ and $\mathbf{a}_2 = (0, 1)$, and choose $\delta^* = (1/2, 0)$. Using Eq. (3.4) with $\Xi = \{(1/2, 0), (-1/2, 0)\}$ and $c_\xi = 1$ one gets $f(\mathbf{q}) = 2 \cos(q_x/2)$, and with the aid of Eq. (3.3) choosing $C = 2$ the exchange in Fourier space becomes $J(\mathbf{q}) = 2 \cos(q_x)$. This model clearly has the full translational symmetry of the square lattice Λ , but the result is quite unsatisfactory: The model is totally anisotropic (in real space). It is a collection of first neighbor coupled chains in the x -direction (with $J_1^x = 2$), but the chains are totally disentangled in the y -direction, i.e. all the exchanges on the y -directed bonds are zero ($J_1^y = 0$). Though the construction works: The \mathcal{M}_{GS} consists of the two y -sides of the BZ boundary $\mathcal{M}_{\text{GS}} = (\pm\pi, q_y)$ with $-\pi \leq q_y \leq \pi$, so it is one-dimensional, but this is not what we wished for. The problem is that the model does not have the *point group symmetry* of Λ , this is what we rectify in the next paragraph.⁵

So far we have only utilized the translational properties of the lattice Λ , now we turn to exploit its point group properties to reduce the possible choices for δ^* . First we give a few definitions: The point group of Λ (centered at some lattice point) is denoted by \mathcal{G} , a general element of it is $g \in \mathcal{G}$, the matrix of g acting on real or reciprocal space points is denoted by \mathbf{g} , i.e. it is either an $O(2)$ or $O(3)$ matrix. The *action* of the group elements on a vector \mathbf{r} is denoted by $\mathbf{g} \cdot \mathbf{r} = g\mathbf{r}$, and similarly for a reciprocal vector \mathbf{q} : $\mathbf{g} \cdot \mathbf{q} = g\mathbf{q}$. The totally symmetric irreducible representation (irrep) of \mathcal{G} is denoted by Γ^{1+} , that is the one whose matrix representatives are all just the number “1”. In what follows we will only use one-dimensional real representations (generally denoted by Γ), whose matrix representatives are $\Gamma(g) = \chi^\Gamma(g) = \pm 1$ -s, and of course these “matrices” coincide with their characters $\chi^\Gamma(g)$.

Let us formulate our desire for the construction scheme of the Hamiltonian. We want to have a totally symmetric (i.e. \mathcal{G} -invariant) J_δ , or equivalently a totally symmetric $J(\mathbf{q})$, a situation that we will refer to as $J(\mathbf{q}) \sim \Gamma^{1+}$, i.e. $J(g\mathbf{q}) = J(\mathbf{q})$ for all $g \in \mathcal{G}$. To achieve this goal first we make our Ξ set \mathcal{G} -symmetric, i.e. we use the full orbit of a chosen vector $\delta_\alpha^* \in \Lambda^*$ under \mathcal{G} :

$$\Xi_\alpha := \{g\delta_\alpha^* \mid g \in \mathcal{G}\}. \quad (3.8)$$

And here comes one big *caveat*: The above defined \mathcal{G} -orbit must be compatible with the translational properties of Λ , so it has to be contained in Λ^* , i.e. *the site symmetry group of δ_α^* (just like any other point in Λ^*) must be isomorphic to the point group \mathcal{G} of Λ , and consequently the shift vector δ^* also has to have this property*. Of course $\delta^* = \mathbf{0}$ always satisfies this constraint, and other such $\delta^* \neq \mathbf{0}$ vectors can be looked up in crystallographic tables [133]: One has to search for the “Wyckoff position” (this is our δ^*) and its site symmetry group. Checking the tables results the following: Such $\delta^* \neq \mathbf{0}$ exists for all Bravais lattices except for the triangular (often called hexagonal) lattice in 2D and the

⁵One is tempted to cure this problem by coopting the vectors $(0, \pm 1/2)$ orthogonal to δ^* to construct a new, square symmetric Ξ , but this will not work: These newly coopted vectors are *not* elements of Λ^* and consequently the resulting J_δ 's will not respect the translational symmetries of the original lattice Λ .

body-centered cubic lattice in 3D; these points are tabulated in Appendix D for all the 2D and 3D Bravais lattices.

Now we are ready to present our full recipe for the construction of the Hamiltonian:

- Choose an *appropriate* shift vector δ^* as discussed above to construct the affine lattice $\Lambda^* = \Lambda + \delta^*$ (we have seen that there are only a few choices for δ^* , for details see Appendix D).
- Choose some points $\delta_\alpha^* \in \Lambda^*$ and create the orbits (shells) under the action \mathcal{G} of this point $\Xi_\alpha = \{g\delta_\alpha^* \mid g \in \mathcal{G}\}$. The larger the δ_α^* -s are the longer the range of the induced interactions in the Hamiltonian become, and also the number of free parameters in the Hamiltonian grows.
- Based on each shell we use *Wigner's machine* and define the symmetry adapted functions [134]:

$$f_\alpha^\Gamma(\mathbf{q}) = \sum_{g \in \mathcal{G}} \chi^\Gamma(g) e^{i\mathbf{q} \cdot (g\delta_\alpha^*)}, \quad (3.9)$$

where $\chi^\Gamma(g) = \Gamma(g) = \pm 1$ are the characters of a 1D real irrep Γ . Since for this type of irreps $\Gamma \otimes \Gamma = \Gamma^{1+}$, the resulting $J(\mathbf{q})$ will be \mathcal{G} -symmetric, see Eq. (3.3).⁶ For illustrative purposes we will mostly use the totally symmetric irrep $\Gamma := \Gamma^{1+}$, which clearly only generates pure AFM models, incorporating irreps with $\Gamma(g) = -1$ will result in models having both AFM and FM bonds. As seen from Eq. (3.9) this is nothing more but a Γ -symmetric coloring of the points of $g\delta_\alpha^* \in \Xi_\alpha$ by ± 1 -s according to $g\delta_\alpha^* \mapsto \chi^\Gamma(g)$.⁷

- Now we can combine the orbits Ξ_α resulting the set $\Xi = \bigcup_\alpha \Xi_\alpha$, and we fix the corresponding constants $c_\alpha \in \mathbb{R}$ or $i\mathbb{R}$ to get the real⁸

$$f^\Gamma(\mathbf{q}) = \sum_{\alpha \in \text{orbits}} c_\alpha f_\alpha^\Gamma(\mathbf{q}). \quad (3.10)$$

And finally using Eq. (3.3) we construct a Heisenberg model with a codimension-one \mathcal{M}_{GS} defined by $f^\Gamma(\mathbf{Q}) = 0$.

In what follows we will –with one exception– use the totally symmetric representation ($\chi^\Gamma(g) = 1$) of \mathcal{G} , and therefore drop the index Γ . Now we give a few examples illustrating the above stated results.

⁶There are representation theoretical theorems guaranteeing this property in a much more general setting, but the statement here is nothing deeper than recognizing that $(\pm 1)^2 = 1$.

⁷ There is a caveat here, and one should not have too bold expectations: Not all such "alternating" irreps will generate useful results, simply because not all Ξ -s are compatible with such colorings. For example out of the three such irreps of the symmetry group of a square (4mm) only one is allowed, the one where the diagonally opposite vertices have the same color, and the adjacent ones are differently colored (a glimpse at the character table shows that the twofold rotation is always represented by +1, meaning that the diagonally opposite vertices have to have the same color, and this requires that the diagonal reflections have to be represented by +1, and the reflections parallel to the edges have to be represented by -1, and there is only one such irrep). For the cubic group (O_h) similar reasoning shows that there is no such coloring at all for an octahedron (here we have three twofold rotations giving very strict constraints), but there is one for the cube.

⁸Of course we will have cosines (needing a real constant) and sines (needing a pure imaginary constant) in the resulting Fourier transformed Hamiltonian.

3.3 Examples

Here we give some two and three dimensional examples of the construction described above. In our two dimensional examples we will consider the square lattice as Λ , because –besides being simple– it illustrates all the important aspects of the construction (illustrative figures of some spin patterns are given in Fig. 1.3). The three dimensional examples will be the simple cubic (sc) and face-centered cubic (fcc) lattices.

3.3.1 Examples on the square lattice

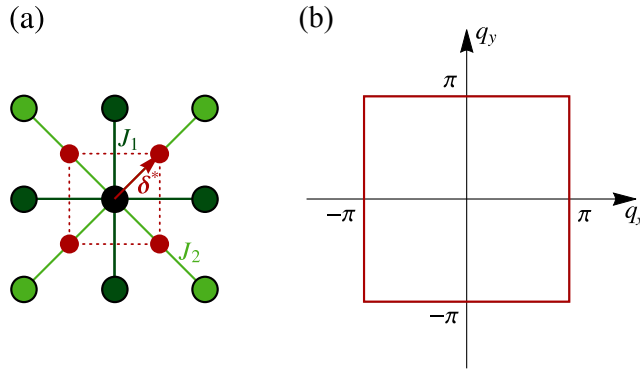


Figure 3.1: Construction of a codimension-one ground state manifold \mathcal{M}_{GS} of a purely AFM model on the square lattice Λ , given by the minima of $J(\mathbf{q})$ defined by $f(\mathbf{Q}) = 0$ via Eq. (3.3). (a) Affine lattice construction with $\Lambda^* = \Lambda + \delta^*$, and $\delta_1^* = \delta^*$. The red arrow connects the origin (black dot) with the points of the set $\Xi_1 \subset \Lambda^*$ (red dots), dark green dots are the nearest-neighbor points to the origin of Λ with exchange coupling $J_1 > 0$, light green dots show the second nearest-neighbor points with $J_2 = J_1/2$. (b) The degenerate \mathcal{M}_{GS} (red square) for $\Lambda^* = \Lambda + \delta_1^*$, which corresponds to the zeros of the function $f(\mathbf{q})$ in Eq. (3.11), is pinned to the Brillouin zone boundary.

We start with the square lattice with primitive lattice translations $\mathbf{a}_1 = (1, 0)$ and $\mathbf{a}_2 = (0, 1)$, they are shown in Fig. 3.1(a) and Fig. 3.2(a) (see the dark green disks forming a cross around the origin). As can be seen in Table D.1, for the shift vector we can only choose $\delta^* = \mathbf{0}$ and $\delta^* = (\frac{1}{2}, \frac{1}{2})$: They are the ones that have $\mathcal{G} = D_4 \equiv 4\text{mm}$ as the site symmetry group.⁹

First, let us consider the $\delta^* = (\frac{1}{2}, \frac{1}{2})$ case, here the first shell of the generated affine lattice Λ^* is shown as the four red dots in Fig. 3.1(a). We choose this first shell $\Xi = \Xi_1$ with cardinality $z_1 = |\Xi_1| = 4$ and consisting of the orbit of $\delta_1^* = \delta^*$. Using Eq. (3.9) with all the $\chi^\Gamma(g) = 1$, $\alpha = 1$ (we use only *one* orbit here), and $\mathcal{G} = 4\text{mm}$ is the 8-element

⁹Here one can also choose e.g. the isomorphic $\mathcal{G} = C_{4h} \cong D_4$ as a site group (the point group notation was developed for three dimensional groups), we just have to remember, that we have the eight symmetry elements of the square: The cyclic group generated by a fourfold rotation and two perpendicular pairs of reflection axes, sometimes this purely two-dimensional group is denoted as 4mm or as D_4 referring to *dihedral group*.

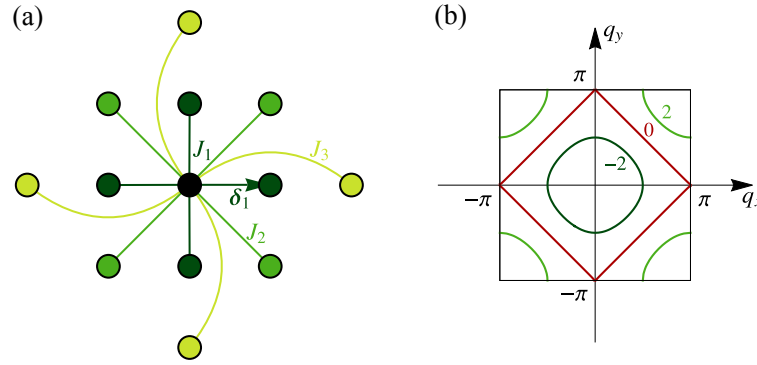


Figure 3.2: Construction of a codimension-one ground state manifold \mathcal{M}_{GS} of a purely AFM model on the square lattice Λ , given by the minima of $J(\mathbf{q})$ defined by $f(\mathbf{Q}) = 0$ via Eq. (3.3). (a) Construction when $\Xi_0, \Xi_1 \subset \Lambda$, Ξ_0 has one point, the origin ($\delta_0 = 0$) and Ξ_1 is the orbit of $\delta_1 = \mathbf{a}_1$ (dark green dots, i.e. the first neighbors of Λ). We get a Heisenberg model with nearest-neighbor exchanges J_1 (dark green) and further neighbor exchanges $J_3 = J_2/2$ (denoted by lighter colors). (b) \mathcal{M}_{GS} for $\Lambda^* = \Lambda$, given by $f(\mathbf{q}) = 0$ in Eq. (3.17), are shown as thick colored curves for $J_1/J_2 = 2, 0$, and -2 . One can see that the shape and topology of \mathcal{M}_{GS} is controlled by the parameter J_1/J_2 .

symmetry group of the square results

$$f(\mathbf{q}) = c_1 f_1(\mathbf{q}) = c_1 8 \cos \frac{q_x}{2} \cos \frac{q_y}{2}, \quad (3.11)$$

and we have a single orbit, so we do not really need Eq. (3.10), but we use its only existing $c_1 = 1/\sqrt{8}$ to make the numbers in the derived formulas a little bit more aesthetically pleasing. Following Eq. (3.3) with $C = 2$ gives

$$J(\mathbf{q}) = 2(\cos q_x + \cos q_y) + [\cos(q_x + q_y) + \cos(q_x - q_y)], \quad (3.12)$$

and defines a J_1 - J_2 AFM-AFM Heisenberg model—see Eq. (3.2)—with exchange couplings $J_1 = 2$ and $J_2 = 1$ [79]. The \mathcal{M}_{GS} coincides with the BZ boundary $\mathbf{Q} = (\pi, q)$ and (q, π) parametrized by $q \in [-\pi, \pi]$, (see the red square in Fig. 3.1(b)). It is worth mentioning, that the simple AFM (checkerboard pattern) ground state with $\mathbf{Q} = (\pi, \pi)$ is part of this manifold, i.e. it is a special spin spiral. What is important to see here is, that we have generated a totally *constrained* model: There are no tunable parameters here, the ratio $J_1/J_2 = 2$ is fixed. The Hamiltonian is the sum of edge sharing four-site complete graphs (squares with diagonals) over the square lattice Λ

$$\mathcal{H} = \sum_{\boxtimes} [(\mathbf{S}_1 + \mathbf{S}_2 + \mathbf{S}_3 + \mathbf{S}_4)^2 - 4], \quad (3.13)$$

which is minimized when the spins sum up to zero in every graph, and every such configuration is a proper ground state, explaining the degeneracy. We have seen plenty of similar coverings for the fcc lattice in Sec. 2.7. We note that an alternative approach to construct this \mathcal{M}_{GS} was presented in Ref. [85].

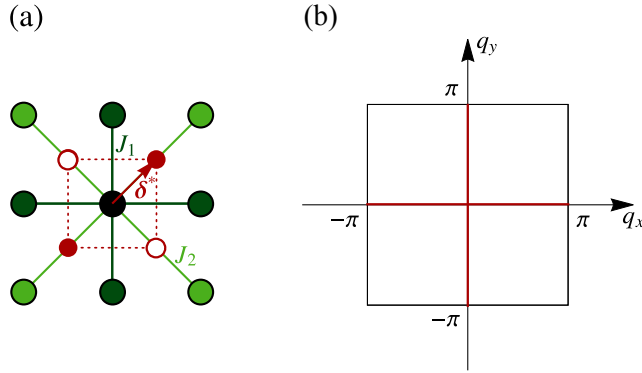


Figure 3.3: Construction of the codimension-one ground state manifold \mathcal{M}_{GS} of the FM-AFM model on the square lattice Λ , given by the minima of $J(\mathbf{q})$ defined by $f(\mathbf{Q}) = 0$ via Eq. (3.3). (a) Affine lattice construction with $\Lambda^* = \Lambda + \delta^*$, and $\delta_1^* = \delta^*$. The red arrow connects the origin (black dot) with the points of the set $\Xi_1 \subset \Lambda^*$ (red dots: Empty dots are the ones that pick up a minus sign in the construction Eq. (3.9)). Dark green dots are the nearest-neighbor points to the origin of Λ with exchange coupling $J_1 < 0$, light green dots show the second nearest-neighbor points with $J_2 = -J_1/2$. (b) The degenerate \mathcal{M}_{GS} (red crisscross), which corresponds to the zeros of the function $f(\mathbf{q})$ in Eq. (3.11).

As was briefly explained in Footnote 7, we can construct FM-AFM models on the square lattice, with only a slight modification of the above construction (this also shows that mixed FM-AFM models can be just as frustrated as the pure AFM ones). The only thing that needs to be changed is the used irrep of the group 4mm. Instead of the totally symmetric irrep we need to use the one where the reflections through the coordinate axes and the C_4 rotations are represented by -1 (i.e. we color the diagonally opposite points $(-\frac{1}{2}, \frac{1}{2})$ and $(\frac{1}{2}, -\frac{1}{2})$ by -1 , see Fig. 3.3(a)). This results

$$f(\mathbf{q}) = -\sqrt{8} \sin \frac{q_x}{2} \sin \frac{q_y}{2}, \quad (3.14)$$

and defines a model with

$$J(\mathbf{q}) = -2(\cos q_x + \cos q_y) + [\cos(q_x + q_y) + \cos(q_x - q_y)], \quad (3.15)$$

describing a J_1 - J_2 FM-AFM Heisenberg model with exchange couplings $J_1 = -2$ and $J_2 = 1$. The \mathcal{M}_{GS} coincides with the crisscross on the \mathbf{q} -axes $\mathbf{Q} = (0, q)$ and $(q, 0)$ parametrized by $q \in [-\pi, \pi]$, [see the red cross in Fig. 3.3(b)]. It is worth mentioning, that the simple FM ground state with $\mathbf{Q} = (0, 0)$ is part of this manifold. The Hamiltonian again can be written as the sum of edge sharing elementary squares with diagonals over the square lattice Λ , but now the diagonally opposite spins get a prefactor of -1 :

$$\mathcal{H} = \sum_{\boxtimes} [(\mathbf{S}_1 - \mathbf{S}_2 + \mathbf{S}_3 - \mathbf{S}_4)^2 - 4]. \quad (3.16)$$

A similar covering was used for the fcc lattice in Sec. 2.7, see Fig. 2.5(d).

In our last square lattice example we use two orbits to get a tunable model. The simplest such case is where $\delta^* = \mathbf{0}$, so $\Lambda^* = \Lambda$, and we choose the first two shells $\Xi = \Xi_0 \cup \Xi_1$, where $\Xi_0 = \{\mathbf{0}\}$ and $\Xi_1 = \{\mathbf{a}_1, \mathbf{a}_2, -\mathbf{a}_1, -\mathbf{a}_2\}$, i.e the origin and the first neighbors in the original lattice, with cardinalities $z_0 = 1$ and $z_1 = 4$. This results (again with a prefactor $c_1 = 1/\sqrt{8}$):

$$f(\mathbf{q}) = f_1(\mathbf{q}) + c_0 = \sqrt{2}(\cos q_x + \cos q_y) + c_0 \quad (3.17)$$

following Eq. (3.10). Eq. (3.3) with $C = 2 + c_0^2$ then generates a model with $J_1 = \sqrt{8}c_0$, $J_2 = 2$, and a constrained $J_3 = J_2/2 = 1$ (see Fig. 3.2(a)), also discussed in [86]. By tuning the parameter $\sqrt{2}c_0 = J_1/J_2$ one can control the shape and topology of \mathcal{M}_{GS} , as shown in Fig. 3.2(b). $J_1 = 0$, equivalent to $c_0 = 0$ is a topological transition (Lifshitz) point [135].¹⁰ Next we turn to our three dimensional examples: The simple cubic (sc) and fcc lattices.

3.3.2 Examples on the simple cubic and fcc lattices

In what follows, we construct models for the sc and fcc lattices based on the affine lattice construction Λ^* with $\delta^* \neq \mathbf{0}$, both having $\mathcal{G} = O_h$ (cubic or octahedral group) as a point group. Not a big surprise: The \mathcal{M}_{GS} surface of the fcc lattice will be the one we found and analyzed in Subsection 2.7.1. In what follows we will only use one orbit, so we drop the orbit indices for clarity, and choose the factor c in Eq. (3.10) to get the simplest formulas, and give the exchanges normalized to the nicest form.

Primitive lattice translations of the sc lattice are $(1, 0, 0)$, $(0, 1, 0)$ and $(0, 0, 1)$. In our affine construction we start with the orbit of the vector $\delta^* = (\frac{1}{2}, \frac{1}{2}, \frac{1}{2})$ (vertices of the little red cube in Fig. 3.4(a), with cardinality $z = 8$), and from Eqs. (3.9) and (3.10) we get

$$f(\mathbf{q}) = 8 \cos \frac{q_x}{2} \cos \frac{q_y}{2} \cos \frac{q_z}{2}. \quad (3.18)$$

This generates a third-neighbor J_1 - J_2 - J_3 model [see Fig. 3.4(a)], with $J_3 = J_2/2 = J_1/4 = 1$. The resulting \mathcal{M}_{GS} is the cubic BZ boundary shown in Fig. 3.5(a) (the coloring is to be understood later). As in Eq. (3.13), the Hamiltonian is the sum of face sharing eight-site complete graphs (elementary cubes with face and body diagonals), which is minimized when the spins sum to zero in every graph: The analogy with the AFM-AFM square lattice model Eq. (3.11) is perfect. In comparison, the construction with $\delta^* = \mathbf{0}$ and two shells gives $J_4 = J_2/2 = 1$ and an adjustable $J_1 = 2c_0$ (analogy again).

Primitive lattice translations of the fcc lattice are $(\frac{1}{2}, \frac{1}{2}, 0)$, $(\frac{1}{2}, 0, \frac{1}{2})$ and $(0, \frac{1}{2}, \frac{1}{2})$. In our affine construction we start with the orbit of the vector $\delta^* = (0, 0, \frac{1}{2})$ and $\Xi = \{(\pm\frac{1}{2}, 0, 0), (0, \pm\frac{1}{2}, 0), (0, 0, \pm\frac{1}{2})\}$ (vertices of the little red octahedron in Fig. 3.4(b), with cardinality $z = 6$), this results

$$f(\mathbf{q}) = 2 \left(\cos \frac{q_x}{2} + \cos \frac{q_y}{2} + \cos \frac{q_z}{2} \right). \quad (3.19)$$

¹⁰One may wonder where all those $\sqrt{8}$ -s come from, especially when one takes a look at the original paper [84], where the numbers are much more beautiful. The reason is the following: Here I have defined the Fourier transform of the exchange as Eq. 3.2, with a 1/2 in it, to be consistent with the rest of the thesis, while in the article this 1/2 is missing. Of course this is physically irrelevant, what matters is the *ratio* of the exchanges.

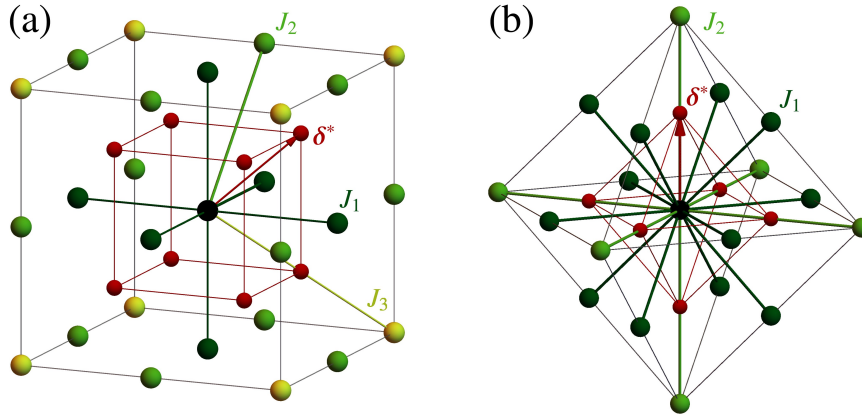


Figure 3.4: Affine lattice constructions for the simple cubic (a) and face-centered cubic (b) lattices. The shift vector δ^* (red arrow) defines the affine lattice $\Lambda^* = \Lambda + \delta^*$. Red balls with a cage show the set $\Xi \subset \Lambda^*$ (a cube and an octahedron). The "origin" of Λ is a black ball in the middle, lighter and lighter balls correspond to further and further neighbors: Dark green balls are points coupled to the origin by the exchange J_1 , light green balls show the second neighbor points with exchange strengths $J_2 = J_1/2$ for both lattices. For the simple cubic lattice a third neighbor exchange (yellowish-green balls) $J_3 = J_2/2$ is also generated.

The model just constructed is a J_1 - J_2 one, with $J_2 = J_1/2 = 1$ (see Fig. 3.4(b)): This is the model we discussed in Subsection 2.7.1 and was also studied in Ref. [69]. The \mathcal{M}_{GS} is shown in Fig. 3.5(b) (to see it without the coloring take a look at Fig 2.3(c)). And again the Hamiltonian is the sum of edge sharing six-site complete graphs (octahedra with diagonals: c.f. Fig. 2.5(e)). But the $\delta^* = \mathbf{0}$ construction provides a model with $J_4 = J_3/2 = J_2/4 = 1$ and adjustable $J_1 = 4 + 2c_0$, and the \mathcal{M}_{GS} is the same as for the diamond lattice [20] (whose Bravais lattice is actually fcc). In the next section we will calculate the free energies of the aforementioned models on the \mathcal{M}_{GS} -s in order to find the states stabilized by thermal (or quantum) fluctuations, in the spirit of [20] (see its supplement for details).

3.4 Free energy and order by disorder

In what follows we calculate the free energies of the sc and fcc models to find the states selected by thermal fluctuations in a low temperature approximation, where the spin deviations from the ground state are small. At zero temperature any $\mathbf{Q} \in \mathcal{M}_{\text{GS}}$ defines a good ground state spin spiral (of course if \mathbf{Q} is not a highly symmetric point in the BZ then $-\mathbf{Q}$ must also be included in the construction of the spiral, for details see Section 2.6), and for symmetric points even multiple- \mathbf{Q} structures are allowed, for several detailed examples on the fcc lattice, see Section 2.5 and Ref. [99]. At zero temperature the ground state energy $\mathcal{E}_0 = J(\mathbf{Q})$ is constant on the whole \mathcal{M}_{GS} but at finite temperature the spins start to fluctuate giving an explicitly \mathbf{Q} dependent contribution to the free energy $\mathcal{F}(\mathbf{Q})$ lifting the ground state degeneracy. Thermal fluctuations then choose the state(s) with the lowest free energy. In the harmonic approximation, the fluctuations can be integrated out in the

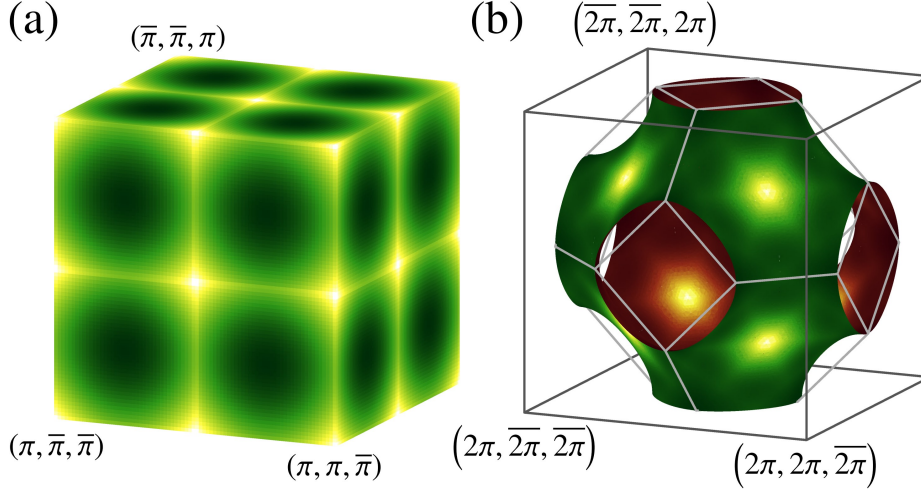


Figure 3.5: Two examples of the ground state manifolds of 3D lattices, the surfaces are defined as $f(\mathbf{Q}) = 0$, where $f(\mathbf{q})$ is given in Eqs. (3.18) and (3.19). They are colored according to their free energies. Lighter colors correspond to states with smaller values of $\mathcal{A}(\mathbf{Q})$ [Eq. (3.21)], and the minima are selected by thermal fluctuations. (a) Simple cubic lattice: the ground state manifold is the Brillouin zone boundary, the degenerate minima are the inequivalent points $(\pi, 0, 0)$, $(\pi, \pi, 0)$ and (π, π, π) and their symmetry related partners. (b) Face-centered cubic lattice: The degenerate minima are the points $\langle \pi, \pi, \pi \rangle$, i.e. the L -points. The Brillouin zone boundary is shown as a light wireframe, the enclosing cube is a guide to the eye.

partition sum, and give rise to a linear T dependence in $\mathcal{F}(\mathbf{Q})$. Following Ref. [20] (and especially its supplement) the free energy above the spiral surface can be calculated. In the calculations we heavily use that we have a single spiral, and that the model is isotropic. The calculation is very tedious, so it is relegated to Appendix E, and here we only cite the results. The low temperature free energy has the form

$$\mathcal{F}(\mathbf{Q}) = \mathcal{E}_0 - NT \ln T + NT \mathcal{A}(\mathbf{Q}) + \mathcal{O}(T^2), \quad (3.20)$$

where $-\mathcal{A}(\mathbf{Q})$ is the \mathbf{Q} -dependent part of the low temperature entropy density, and it reads

$$\mathcal{A}(\mathbf{Q}) = \frac{1}{N} \sum_{\mathbf{q} \in \text{BZ}} \ln \omega_{\mathbf{q}}^2(\mathbf{Q}), \quad (3.21)$$

where the summation is over the whole Brillouin zone, and

$$\omega_{\mathbf{q}}(\mathbf{Q}) = \left(\frac{1}{2} [J(\mathbf{q}+\mathbf{Q}) + J(\mathbf{q}-\mathbf{Q}) - 2J(\mathbf{Q})] [J(\mathbf{q}) - J(\mathbf{Q})] \right)^{1/2}. \quad (3.22)$$

States with minimal $\mathcal{A}(\mathbf{Q})$ correspond to the minimal free energy value: This is the entropic (or thermal) order-by-disorder selection mechanism discussed in Refs. [16, 23, 24, 18] and in the Introduction 1.1.3. This is what we could have achieved analytically, the BZ-sum has to be performed numerically. $\mathcal{A}(\mathbf{Q})$ is plotted for the sc and fcc lattices

in Fig. 3.5: The lightest points on the surfaces are the \mathbf{Q} -vectors of the selected minima. Furthermore, the energy of the spin waves¹¹ is $\hbar S \omega_{\mathbf{q}}(\mathbf{Q})$ in the semi-classical (long spin $S \gg 1$) approximation. Therefore *quantum* fluctuations behave qualitatively similarly to the thermal ones, and they choose the state with the lowest zero-point energy

$$\mathcal{E}_{\text{ZP}}(\mathbf{Q}) = \sum_{\mathbf{q} \in \text{BZ}} \frac{\hbar S}{2} \omega_{\mathbf{q}}(\mathbf{Q}). \quad (3.23)$$

For the sc lattice with $J_1 = 2J_2 = 4J_3$ the selected minima are the inequivalent point sets $\langle \pi, 0, 0 \rangle$, $\langle \pi, \pi, 0 \rangle$ and $\langle \pi, \pi, \pi \rangle$ [119] (there are seven such points, remember: $\langle \mathbf{Q} \rangle$ is the set of \mathbf{Q} together with its cubic symmetry related partners). In these highly symmetric points multi- \mathbf{Q} states are allowed, they correspond to an ordering in real space where in a cube formed by eight neighboring lattice sites the spins sum up to zero (a cube rule), and this cube is repeated through the whole lattice (the magnetic superlattice is sc again doubled in linear size). Performing low-T expansions for such ordering patterns it is found that the free energy minima correspond to any 8-sublattice collinear state (satisfying the cube rule), including the single- \mathbf{Q} states with $\langle \pi, 0, 0 \rangle$, $\langle \pi, \pi, 0 \rangle$ and $\langle \pi, \pi, \pi \rangle$. In fact, more is true: *Any* collinear ground state has exactly the same entropy in the harmonic approximation. We believe that higher order corrections will split this degeneracy.

For the fcc lattice with $J_1 = 2J_2$ the four L -points $\langle \pi, \pi, \pi \rangle$ are selected, the multiple- L states are described in detail in Section 2.5.3. Here again entropy selects the collinear, single- \mathbf{Q} states forming the type-II AFM structure.¹²

The question arises: Can different \mathcal{M}_{GS} 's obtained by different Λ^* be continuously deformed into each other by, e.g., including more shells. The $f(\mathbf{q})$ for $\Lambda^* = \Lambda$ has full reciprocal lattice periodicity (let us say that it is even), while the $f(\mathbf{q})$ in Eqs. (3.18) and (3.19) changes sign when translated by a unit reciprocal lattice vector ($f(\mathbf{q})$ is odd). This even-odd property cannot be changed continuously, therefore the two types of constructions provide two different topological classes of \mathcal{M}_{GS} 's. The odd parity of $f(\mathbf{q})$ also pins the $f(\mathbf{Q}) = 0$ surface to the boundary of the BZ for the SC lattice (i.e. the $\langle \pi, q_1, q_2 \rangle$ planes) and to the $\langle \pi/2, q, \pi - q \rangle$ lines in the case of the FCC lattice (diagonals on the hexagonal faces of the BZ), while there is no such restriction for the even $f(\mathbf{q})$ function when $\delta^* = \mathbf{0}$.¹³

The topological distinction is corroborated by the Euler characteristics χ ¹⁴ (or equiv-

¹¹A spin wave spectrum like this is most easily calculated in a local co-rotating coordinate system, see e.g. Ref. [136]

¹²We note that Monte-Carlo simulations in Ref. [69] found a type III, $\mathbf{Q} = (2\pi, \pi, 0)$ order at low temperatures (a W -state). These results call for further investigation.

¹³Very similarly in one dimension: An odd function has to cross the origin, but an even has not.

¹⁴The Euler characteristic $\chi(M)$ for a compact two dimensional surface M without boundary (all our \mathcal{M}_{GS} 's belong to this class when we look at them as surfaces in the first Brillouin zone with the appropriate faces of the zone identified) can be calculated via the celebrated Gauss-Bonnet theorem:

$$\chi(M) = \frac{1}{2\pi} \int_M K dA, \quad (3.24)$$

where dA is the surface element of M and K is the Gaussian curvature of M .

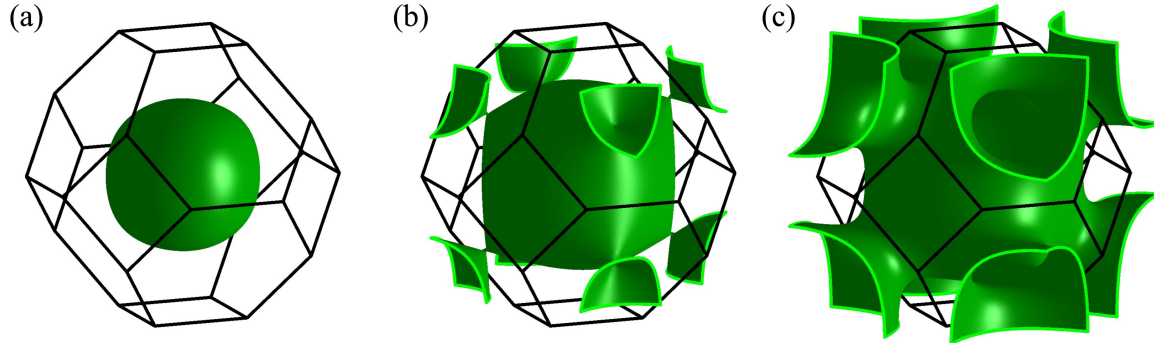


Figure 3.6: Topological (Lifshitz) transition of \mathcal{M}_{GS} of a model on the face-centered-cubic lattice Λ , given by the minima of $J(\mathbf{q})$ defined by $f(\mathbf{Q}) = 0$ via Eq. (3.3). Here Ξ consists of $\Xi_0, \Xi_1 \subset \Lambda$, Ξ_0 is the origin and Ξ_1 consists of the first neighbors. The resulting Heisenberg model is a fourth-neighbor one with $J_1 = 4 + 2c_0$, $J_2 = 4$, $J_3 = 2$, and $J_4 = 1$, and the tunable parameter c_0 drives the transition. (a) $c_0 = -3$, the surface is homeomorphic to the sphere S^2 , with Euler characteristic $\chi = 2$ and no genus $g = 0$. (b) $c_0 = 0$, the transition point, where the surface intersects itself at the midpoints of the hexagonal faces of the BZ. (c) $c_0 = 3/2$, the surface is homeomorphic to the Schoen IWP surface, with $\chi = -6$ (see the tubes on the antipodal hexagons of the BZ surface that are glued together), and we have four handles and genus $g = 4$.

alently the number of genera g^{15}) of these triply periodic surfaces [94]. We focus on the FCC lattice. The $f(\mathbf{Q}) = 0$ surface from Eq. (3.19) is homeomorphic to the so called Schwarz-P surface with $\chi = -4$, see Fig. 3.5(b) (the easiest way to see this is the following: There are six “tubes” emanating from this surface, but the antipodal tubes are glued together because of the periodicity of reciprocal space, so what we have here is basically a sphere with three handles attached). On the other hand, we can extend Eq. (3.17) to the fcc lattice, i.e. for Ξ we choose the origin together with the first neighbors (so $\Lambda^* = \Lambda$). This will create a fourth-neighbor model with $J_1 = 4 + 2c_0$, $J_2 = 4$, $J_3 = 2$, and $J_4 = 1$.¹⁶ For $-12 < c_0 < 0$, we have a surface homeomorphic to the sphere (but having only cubic symmetry) with $\chi = 2$ (see Fig. 3.6(a)). At $c_0 = 0$, a Lifshitz transition occurs [135] (the surface is not even a manifold, see the eight “necks” in Fig. 3.6(b)), and for $0 < c_0 < 4$ the surface changes to a different manifold, homeomorphic to a Schoen IWP surface, with $\chi = -6$ (remember: Tubes on the antipodal hexagons of the BZ are glued together so we have four handles $g = 4$, see Fig. 3.6(c)). The surfaces in the case of the diamond lattice [20] belong to this latter class (having the same \mathcal{M}_{GS} ’s when some parameters are varied). We close this chapter with a summary.

¹⁵The genus (plural genera) of a surface is the number of “holes” on it, or the number of “handles”. For a closed surface (we always have closed surfaces without boundary here) $\chi = 2 - 2g$. A sphere has $g = 0$, a torus has $g = 1$.

¹⁶The fourth neighbors (there are 12 of them) are the orbits of $\delta_4 = (1, 1, 0)$ under O_h .

3.5 Summary

As a summary, we gave a recipe of the construction of classical Heisenberg models on Bravais lattices having degenerate ground state manifolds of codimension one, with spin spirals as ground states. These models are fine tuned, with no or a few free parameters, this has to be contrasted with models on non-Bravais lattices (e.g. diamond or honeycomb) where there *are* free parameters. In certain cases we have provided real space coverings of the lattice by finite motifs (complete graphs), where the ground states correspond to states with the only rule that the spins must sum up to zero on each graph: This explains the large degeneracy. We also have found topological (Lifshitz) transitions in models with free parameters: Here varying the parameters changes the topology of the ground state manifold (this can be monitored by e.g. the Euler characteristic of the manifold). We gave a few worked out examples in two and three dimensions, and gave the necessary ingredients to use the method for every Bravais lattice. We analyzed the effect of thermal or quantum fluctuations, and found that they select commensurate (and likely collinear) states on the ground state manifold. An outlook and proposed further investigations follow.

Although we have constructed model families, we barely started their analysis. No real quantum or hardcore numerical investigations have been performed yet, and we know that these frustrated models can host very interesting effects e.g. in the extreme quantum regimes (small spin length). One of these is that they can provide a playground for realizing quantum spin liquids, see [86], a topic very popular nowadays, so we believe that attacking these models with state-of-the-art numerical methods is a promising direction for future studies.

Chapter 4

Simple theory of directional dichroism in the paramagnetic state of $\text{Sr}_2\text{CoSi}_2\text{O}_7$

4.1 Introduction

In this chapter we describe the non-reciprocal directional dichroism (NDD) of the magneto-electric (ME) multiferroic $\text{Sr}_2\text{CoSi}_2\text{O}_7$ belonging to the family of åkermanites (a subspecies of melilites) in the *paramagnetic* phase and in strong external magnetic fields. The melilite crystals lack inversion symmetry (see Fig. 4.1) and applying a magnetic field in the paramagnetic phase breaks time reversal as well: Thereby the necessary conditions for NDD are fulfilled.

It was shown in Refs. [137, 138] that in $\text{Sr}_2\text{CoSi}_2\text{O}_7$ the static (DC) ME effect¹ persists even in the paramagnetic phase in a high external magnetic field. Since the DC ME susceptibility is related to NDD by the ME sum rule [139] we expect the NDD to appear under the same circumstances. This expectation motivated the experimental investigation of NDD in this compound via optical absorption. Indeed, markedly different absorption by magnetic excitations were found in positive and negative magnetic fields, the hallmark of NDD. To interpret the experimental results we developed a single-site analytical model showing that the finite NDD arises if all the three are present: Magnetic field, spin anisotropy and ME coupling.

The structure of this chapter is the following: Basic structural and magnetic properties of $\text{Sr}_2\text{CoSi}_2\text{O}_7$ are given in Section 4.2. The spin Hamiltonian and the form of the spin-induced polarization of the material are introduced in Section 4.3 together with the coupling to the oscillating electromagnetic field. Experimental methods and results are presented in Section 4.4. The Kubo formula as applied to the magnetoelectric response connects the experiments and calculations and is described in Section 4.5. Exact diagonalization of the Hamiltonian on a small cluster and the calculation of ME susceptibilities is explained in Section 4.6. The single-ion model is introduced and analyzed in Section 4.7. The single ion model and its symmetry analysis is promoted to a lattice model in Section 4.8, and by treating the exchange interactions perturbatively the remarkable success of the single-ion model was justified in retrospect. We close the chapter with a summary in Section 4.9.

¹The nonvanishing magnetoelectric susceptibility at $\omega = 0$. For the definition of this response function see Appendix F.

4.2 Basic structural and magnetic properties of the crystal

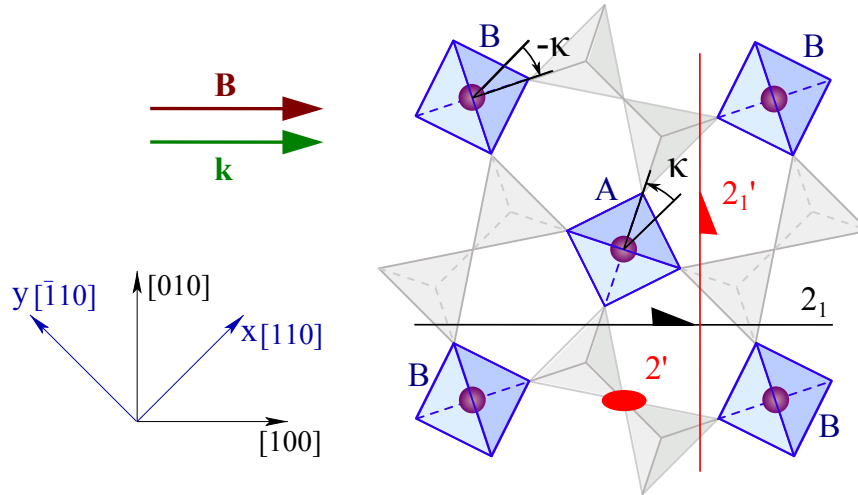


Figure 4.1: Illustration of a layer of $\text{Sr}_2\text{CoSi}_2\text{O}_7$. The whole crystal has space group symmetry $\text{P}\bar{4}2_1\text{m}$. Coordinate axes are also shown: The black arrows are the crystallographic ones, the blue axes $x \parallel [110]$ and $y \parallel [\bar{1}10]$ point in the directions of the Co-Co bonds used in the calculations. Purple disks denote the Co^{2+} ions carrying the $S = 3/2$ moments and sitting in the centers of the O^{2-} tetrahedral cages (blue), the Si_2O_7 units are in grey, and the Sr ions separating the layers are not shown. A and B denote the two types of tetrahedra tilted by $+\kappa$ and $-\kappa$ ($\kappa \approx 22.4^\circ$) about the $[001]$ axis away from $[110]$. In the experiment the THz light propagates along the direction of the magnetic field, $\mathbf{k} \parallel \mathbf{B} \parallel [100]$. The magnetic field breaks time reversal symmetry and for this field direction the remaining unitary symmetry operation is the 2_1 screw axis, (black half-arrow), the two antiunitary operations are the twofold rotation about the $[001]$ axis followed by time reversal and denoted by $2'$ (red ellipse) and a screw axis followed by time reversal and denoted by $2'_1$ (red half-arrow): The magnetic point group reduced to $2'2'_1$ by the introduction of the field.

Here we describe the most important features of the $\text{Sr}_2\text{CoSi}_2\text{O}_7$ crystal, and its magnetic properties relevant for understanding this chapter. This crystal is the sister compound of $\text{Ba}_2\text{CoGe}_2\text{O}_7$, with analogous structural, electric and magnetic properties. Since $\text{Ba}_2\text{CoGe}_2\text{O}_7$ was synthesized much earlier and its literature is vast, we mostly refer to its literature when describing $\text{Sr}_2\text{CoSi}_2\text{O}_7$ in this section (e.g. we could use the same model with the same parameters used in [37] describing $\text{Ba}_2\text{CoGe}_2\text{O}_7$). The basic static (or DC) measurements on the magnetic field dependence of the magnetization, polarization, and structural information on $\text{Sr}_2\text{CoSi}_2\text{O}_7$ can be found in [137, 138].

The space group of the high temperature paramagnetic phase of the crystal is the tetragonal $\text{P}\bar{4}2_1\text{m}$ with point group $\bar{4}2\text{m}$ (or D_{2d} in Schoenflies notation). A schematic of the crystal and its symmetry elements are presented in Fig. 4.1. This group is non-centrosymmetric (there is no space inversion present), but it is neither polar nor chiral,² and –naturally– has

²We call a point group *chiral* if it contains no roto reflections, i.e. it consists of pure rotations (elements

time reversal symmetry, preventing magneto-chiral dichroism (MChD) in the paramagnetic state.

The crystal is layered, the layers are stacked along the tetragonal axis [001], one such layer is shown in Fig. 4.1. The basic building blocks are Co^{2+} ions sitting in the centers of O^{2-} tetrahedra forming a square lattice. The tetrahedra are slightly distorted along the [001] direction, and are connected by Si_2O_7 units, and the layers are separated by Sr^{2+} ions. Since the layers are weakly coupled we will concentrate on the Co^{2+} ions forming a single layer, and all the magnetic properties can be understood by looking at this structure. These ions form a square lattice with two nonequivalent Co ions in the unit cell due to the two different orientations of the O-cages (see the different tiltings $\pm\kappa$ in Fig. 4.1, the actual value of κ is very close to $\pi/8$). Let us now turn to the magnetic properties.

Co^{2+} ions in such a tetrahedral environment carry a spin $S = 3/2$.³ The material is an easy-plane antiferromagnet (with a strong uniaxial on-site anisotropy): Below the Néel temperature $T_N = 7$ K the moments order and lie in the tetragonal planes. The lack of an inversion center on the midpoints of the Co-Co bonds allows for a Dzyaloshinskii-Moriya interaction (see Eq. 4.1), and this results in a small in-plane canting of the spins. The reduced symmetry of the Néel-state makes the crystal chiral: The paramagnetic point group $\bar{4}2m1'$ is consequently reduced to $22'2'$, the prime here refers to time reversal. We can also break time reversal symmetry in the paramagnetic phase, and make the group chiral by applying a magnetic field along the [100] direction, thereby canting the moments in the direction of the field causing a net magnetization, and reducing the symmetry to $22'2'$ [50] (see these remaining symmetry elements in Fig. 4.1).

Under this symmetry we expect MChD for light propagation along the magnetic field, i.e. in the so-called Faraday geometry. Showing that this is the case, and taking the first steps to understand the details of the phenomenon is the subject of the rest of this chapter. In the next section we define the spin Hamiltonian describing the material together with the way electric polarization is induced by the magnetic moments.

4.3 Spin Hamiltonian and the magnetoelectric coupling

Here we introduce the anisotropic Heisenberg Hamiltonian describing the spin system, and give the form of the spin-induced on-site electric polarization. With the aid of the Kubo formula [140, 139] we define magnetic and magnetoelectric response functions that can be calculated once the aforementioned Hamiltonian is diagonalized. With these response functions (susceptibilities) we can calculate the absorption coefficients thereby connecting

of $SO(3)$). A point group is said to be *polar* if it allows for the presence of a polar vector component: i.e. there is at least one component of a polar vector –say the net polarization \mathbf{P} itself– that transforms according to totally symmetric irrep of the said group $P^\alpha \sim \Gamma^{1+}$.

³The crystal field of the O^{2-} ions on the tetrahedron lifts the five-fold degenerate d -levels of the Co^{2+} ion to a low lying two-fold degenerate e level, and to a higher lying, three-fold degenerate t_2 level (here we neglect the slight distortion of the tetrahedron and use the tetrahedral group T_d of a perfect tetrahedron). Four out of the seven electrons of the Co^{2+} ion first fill the e level, and the remaining three electrons occupy the t_2 level with all their spins aligned, resulting an $S = 3/2$ state (here we have assumed that the crystal field is much weaker than Hund's coupling).

the theoretical spin model to the measurements.

For the Hamiltonian of a single layer of Co^{2+} spins with $S = 3/2$ forming a square lattice –see Fig. 4.1– we consider the following anisotropic Heisenberg model

$$\begin{aligned} \mathcal{H} = & J \sum_{\langle i,j \rangle} (S_i^x S_j^x + S_i^y S_j^y) + J_z \sum_{\langle i,j \rangle} S_i^z S_j^z + \Lambda \sum_i (S_i^z)^2 \\ & + D_z \sum_{\langle i,j \rangle} (S_i^x S_j^y - S_i^y S_j^x) - g\mu_B \mathbf{B} \cdot \sum_i \mathbf{S}_i, \end{aligned} \quad (4.1)$$

where S_i^α is the α 's component of the spin on site i , J and J_z are the anisotropic antiferromagnetic exchange constants, $\Lambda > 0$ is the on-site anisotropy parameter (favoring an easy-plane configuration), D_z is the z component of the Dzyaloshinskii-Moriya vector (allowed since the midpoints of Co-Co bonds are not inversion centers), and the last term is the Zeeman interaction with gyromagnetic ratio g , and μ_B is the Bohr magneton. Here \mathbf{B} is the external static field, and $\langle i, j \rangle$ denotes summation over nearest neighbor Co-Co bonds always connecting sites on different sublattices A and B .

The absence of inversion symmetry on the Co sites allows for a ME coupling. A microscopic model was devised for the form of this coupling: The so-called p - d hybridization or metal-ligand hybridization [39] where the spin of the metal ion (Co^{2+} in our case) deforms the charge distribution of the ligands (the tetrahedral cage of O^{2-} ions in our case) via spin-orbit coupling, thereby creating a net polarization on a site. We note that it is an on-site mechanism, since only one Co spin is included in the process. Other mechanisms of spin induced polarization involving two magnetic sites were considered in Ref. [141] (see also the Introduction 1.2). The electric polarization is quadratic in spin components and it is given by [36, 37] as

$$\mathbf{P} \propto \sum_{\alpha=1}^4 (\mathbf{S} \cdot \mathbf{e}_\alpha)^2 \mathbf{e}_\alpha, \quad (4.2)$$

where \mathbf{e}_α is the unit vector pointing from the center of the (distorted) tetrahedron (the Co^{2+} ion) toward the four $\alpha = 1, \dots, 4$ ligands (the O^{2-}) at the vertices of the tetrahedron, and \mathbf{S} is the spin of the Co^{2+} ion. This form of the polarization is quadratic in spin components, hence time-reversal invariant.

Since $\text{Sr}_2\text{CoSi}_2\text{O}_7$ is composed of tetrahedra alternating on the sublattices A and B , the polarization components are

$$\begin{aligned} P_j^x & \propto -\cos 2\kappa_j (S_j^x S_j^z + S_j^z S_j^x) - \sin 2\kappa_j (S_j^y S_j^z + S_j^z S_j^y), \\ P_j^y & \propto \cos 2\kappa_j (S_j^y S_j^z + S_j^z S_j^y) - \sin 2\kappa_j (S_j^x S_j^z + S_j^z S_j^x), \\ P_j^z & \propto \cos 2\kappa_j ((S_j^y)^2 - (S_j^x)^2) - \sin 2\kappa_j (S_j^x S_j^y + S_j^y S_j^x), \end{aligned} \quad (4.3)$$

where j is either A (B), with tilt angle $\kappa_j = \kappa$ ($\kappa_j = -\kappa$) [37], see Fig. 4.1.

The interaction with the oscillating electric and magnetic fields of the light ($\mathbf{E}_\omega(t)$ and $\mathbf{B}_\omega(t)$, respectively) with the material is described by the –supposed to be perturbatively weak to be treated by linear response theory– Hamiltonian

$$\mathcal{H}^{EM}(t) = -\mathbf{E}_\omega(t) \cdot \mathbf{P} - \mathbf{B}_\omega(t) \cdot \mathbf{M}. \quad (4.4)$$

The total polarization is the sum of the sublattice polarizations and the total magnetization is the sum of the sublattice magnetizations

$$\mathbf{P} = \mathbf{P}_A + \mathbf{P}_B, \quad \text{and} \quad \mathbf{M} = \mathbf{M}_A + \mathbf{M}_B, \quad (4.5)$$

where the sublattice polarizations and magnetizations are defined as

$$\mathbf{P}_A = \sum_{i \in A} \mathbf{P}_i, \quad \text{and} \quad \mathbf{M}_A = g\mu_B \sum_{i \in A} \mathbf{S}_i, \quad (4.6)$$

and similarly for sublattice B . The full Hamiltonian with the spin model Eq. (4.1) and electromagnetic interaction Eq. (4.4) becomes finally

$$\mathcal{H}^{\text{int}} = \mathcal{H} + \mathcal{H}^{EM}(t). \quad (4.7)$$

In what follows we briefly describe the experimental methods and results.

4.4 Experiments

In this section we give a *very* brief summary of the experimental methods and results. This work was done in close collaboration with experimentalists, and though I was not directly involved in the measurements, I feel an urge to describe them in some detail.

4.4.1 Experimental methods

Samples of $\text{Sr}_2\text{CoSi}_2\text{O}_7$ designed for THz spectroscopy⁴ were thin, disk-shaped single crystals with axis parallel to $[100]$. The frequency dependence of the absorption of linearly polarized THz light was measured with varying external magnetic field and temperature. The static external magnetic field \mathbf{B} and the propagation direction of light \mathbf{k} were both in the $[100]$ direction, $\mathbf{k} \parallel \mathbf{B} \parallel [100]$. This setup of the static magnetic field being parallel to the wave vector of the light is called the Faraday configuration, and when $\mathbf{k} \perp \mathbf{B}$ the configuration is called the Voigt configuration (no measurements in Voigt configuration will be covered here but we describe the possibility of having NDD in the Voigt configuration).

The absorption coefficient α^\pm for magnetic fields $\pm B$ is calculated as

$$\alpha^\pm = -\frac{1}{d} \ln \frac{I(\pm B, T)}{I(B = 0 \text{ T}, T_{\text{ref}})}, \quad (4.8)$$

where $I(B, T)$ is the transmitted intensity in a magnetic field B at temperature T and $I(0 \text{ T}, T_{\text{ref}})$ is some reference intensity and d is the sample width. If we are interested

⁴This is a side note about unit conversions often used in spectroscopy. A photon with energy of $E = 1 \text{ meV}$, has frequency $f = 0.242 \text{ THz}$, has a wavenumber $k = 8.06 \text{ cm}^{-1}$, and has a wavelength $\lambda = 1.24 \text{ mm}$. The energy $E = 1 \text{ meV}$ corresponds to a temperature $T = 11.6 \text{ K}$. The energy $E = 1 \text{ meV}$ when compared with the Zeeman energy $E = g\mu_B B$ shows that the equivalent magnetic field is $B = 8.63 \text{ T}$, where $g = 2$ was chosen for the gyromagnetic ratio and μ_B is the Bohr magneton. These conversion factors are useful when comparing energy scales: It is seen e.g. that in our case the external magnetic field, the anisotropy energy, and the temperature are all comparable.

in the field dependence at some fixed $T = T_{\text{ref}}$, the absorption coefficient is denoted by α_B^\pm , and if B is fixed and T is varied, the absorption coefficient is denoted by α_T^\pm . α^\pm was determined for two polarizations $\mathbf{E}_\omega \parallel [010]$ and $\mathbf{E}_\omega \parallel [001]$, where \mathbf{E}_ω denotes the oscillating electric field of the incident light (for the chosen coordinates see Fig. 4.1).

The quantity $\alpha^+ - \alpha^-$ measures the NDD (note that this is a *signed* quantity) and is proportional to the imaginary part of an appropriate magnetoelectric susceptibility. The presence of NDD was monitored by changing the direction of the magnetic field from $+B$ to $-B$ instead of changing the light direction (or flipping the sample together with the external field), i.e. from $\mathbf{B} \uparrow\uparrow \mathbf{k}$ to $\mathbf{B} \downarrow\uparrow \mathbf{k}$. Due to the two-fold rotation symmetry along the $[001]$ axis the reversal of \mathbf{B} is equivalent to the reversal of \mathbf{k} . We turn to the description of the experimental results.

4.4.2 Experimental results

Figs. 4.2 (a) and (b) show the temperature dependence of the absorption coefficients α_T^\pm for the light propagation directions $\pm\mathbf{k} \parallel [100]$ between 3 K and 100 K in two polarizations of the THz radiation in magnetic field ± 14 T, where $\mathbf{B} \parallel [100]$. We recall that the measure of the NDD is $\alpha_T^+ - \alpha_T^-$, so one has to subtract the blue curve from the red one to have a feeling about the magnitude of dichroism.

Below 7 K, in the magnetically ordered phase, the spectrum is dominated by three resonances at 18 cm^{-1} , 28 cm^{-1} and 32 cm^{-1} just like in $\text{Ba}_2\text{CoGe}_2\text{O}_7$ already studied in Ref. [46]. Also the DC properties, namely the magnetic field dependence of the static polarization and magnetization are quite similar in $\text{Sr}_2\text{CoSi}_2\text{O}_7$ and $\text{Ba}_2\text{CoGe}_2\text{O}_7$ [36, 137]. This almost identical behavior of the two compounds allows us to identify and characterize the modes in the ordered phase based on the study of $\text{Ba}_2\text{CoGe}_2\text{O}_7$ [43].

The 18 cm^{-1} mode is the Goldstone mode of the easy-plane antiferromagnet gapped by the in-plane magnetic field whereas the other two resonances correspond to the spin stretching modes.⁵ The spectra are clearly different for $\mathbf{k} \uparrow\uparrow \mathbf{B}$ and $\mathbf{k} \uparrow\downarrow \mathbf{B}$. With increasing temperature the spin-stretching modes merge and fade away above 30 K, so they are not interesting for us now, since we want to study the high temperature behavior of the system. However, the lowest energy mode survives up to 100 K: This *paramagnetic* mode is whose behavior we want to capture. Furthermore MChD is very sensitive to the polarization of light in the paramagnetic phase. When $\mathbf{E}_\omega \parallel [010]$, α_T^+ is nearly zero (see the flat red line in Fig. 4.2 (a)) while α_T^- has a strong peak at the resonance (see the pronounced bump on the blue line in Fig. 4.2 (a)). When $\mathbf{E}_\omega \parallel [001]$, the lowest energy resonance has weak MChD (the blue and red curves almost overlap in Fig. 4.2 (b)) and it even changes sign between 10 K and 15 K.

Fig. 4.3 (a) and (b) show the magnetic field dependence of α_B^\pm at 30 K⁶ for the two polarizations. The average intensity of the resonance line, $(\alpha_B^+ + \alpha_B^-)/2$, observed at this

⁵Without an in-plane component of the external field the system has a $U(1)$ symmetry about $[001]$ (almost: There is a small in-plane anisotropy usually neglected in calculations), and the Goldstone mode corresponds to the free in-plane rotations of the spins. The spin stretching modes are dubbed this way because the spin can also *shrink* in these modes allowing for multipolar excitations, this is the consequence of the on-site anisotropy (possible for $S > 1/2$ only) discussed later.

⁶This temperature is high enough to say that we are really in the paramagnetic phase, but low enough to

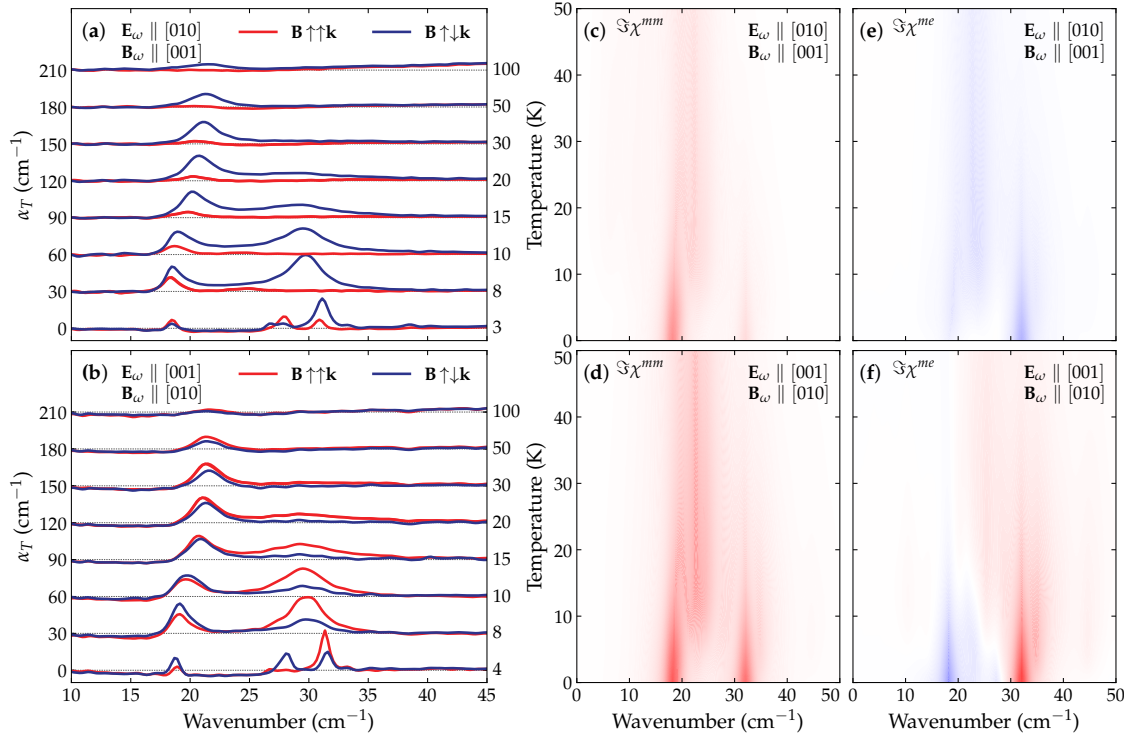


Figure 4.2: Temperature dependence of the measured THz absorption spectra (a-b) and calculated susceptibilities (c-f) of Sr₂CoSi₂O₇ in 14 T. The THz absorption spectra for a magnetic field $\mathbf{B} \uparrow \uparrow \mathbf{k} \parallel [100]$ (α_T^+ : red line) and $\mathbf{B} \uparrow \downarrow \mathbf{k}$ (α_T^- : blue line) are measured using linearly polarized radiation where in (a) $\mathbf{E}_\omega \parallel [010]$ and $\mathbf{B}_\omega \parallel [001]$, and in (b) the polarization is rotated by 90°, so that $\mathbf{E}_\omega \parallel [001]$ and $\mathbf{B}_\omega \parallel [010]$. The measure of the non-reciprocal directional dichroism for a given polarization is $\alpha_T^+ - \alpha_T^-$, i.e. the blue line subtracted from the red one. The spectra measured at each temperature are shifted by a constant baseline. (c) and (e) are the imaginary parts of the magnetic susceptibility $\chi^{mm}(\omega)$ and the magnetoelectric susceptibility $\chi^{me}(\omega)$ for the polarization $\mathbf{E}_\omega \parallel [010]$ and $\mathbf{B}_\omega \parallel [001]$. (d) and (f) are the imaginary parts of $\chi^{mm}(\omega)$ and $\chi^{me}(\omega)$ for the polarization $\mathbf{E}_\omega \parallel [001]$ and $\mathbf{B}_\omega \parallel [010]$. Red (positive) and blue (negative) colors indicate the sign of the imaginary part of the susceptibility. The saturation of the color corresponds to the magnitude of the corresponding susceptibility matrix elements $\Im \chi^{mm}(\omega)$ and $\Im \chi^{me}(\omega)$. The susceptibilities were calculated by exact diagonalization of a four site cluster. To compare the measured values with the calculated ones remember: $\alpha_T^+(\omega) - \alpha_T^-(\omega) = \frac{4\omega}{c} \Im \chi^{me}(\omega)$ as given in Eq. (4.11).

temperature is nearly the same for both polarizations and the dependence of the resonance frequency on the field also seems to be polarization independent. Although the strength of the MChD shows the same polarization dependence discussed before: When $\mathbf{E}_\omega \parallel [010]$ the MChD is strong, and it is weak when $\mathbf{E}_\omega \parallel [001]$. In the next section we define the magnetoelectric susceptibilities, the way they can be calculated via Kubo's formula and

have dichroism of a decent magnitude.

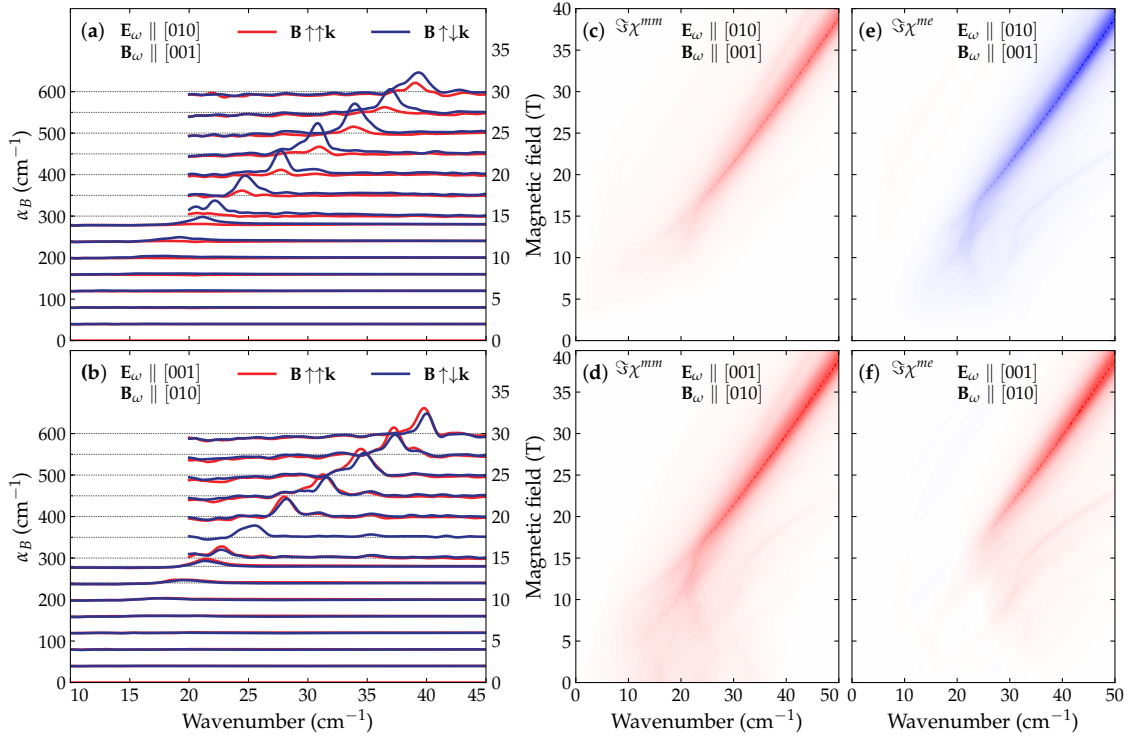


Figure 4.3: Magnetic field dependence of the measured THz absorption spectra (a-b) and calculated susceptibilities (c-f) of $\text{Sr}_2\text{CoSi}_2\text{O}_7$ at 30 K. The THz absorption spectra for a magnetic field $\mathbf{B} \uparrow \uparrow \mathbf{k} \parallel [100]$ (α_B^+ : red line) and $\mathbf{B} \uparrow \downarrow \mathbf{k}$ (α_B^- : blue line) are shown for two light polarizations. The measure of the non-reciprocal directional dichroism for a given polarization is $\alpha_B^+ - \alpha_B^-$, i.e. the blue line subtracted from the red one. The spectra are shifted in proportion to the absolute value of the magnetic field. (c) and (e) are the imaginary parts of the magnetic susceptibility $\chi^{mm}(\omega)$ and the magnetoelectric susceptibility $\chi^{me}(\omega)$ for the polarization $\mathbf{E}_\omega \parallel [010]$ and $\mathbf{B}_\omega \parallel [001]$. (d) and (f) are $\Im\chi^{mm}(\omega)$ and $\Im\chi^{me}(\omega)$ for the polarization $\mathbf{E}_\omega \parallel [001]$ and $\mathbf{B}_\omega \parallel [010]$. Red (positive) and blue (negative) colors indicate the sign of susceptibility. The saturation of the color corresponds to the magnitude of $\Im\chi^{mm}(\omega)$ and $\Im\chi^{me}(\omega)$. The susceptibilities were calculated by the exact diagonalization of a four site cluster. To compare the measured values with the calculated ones remember: $\alpha_B^+(\omega) - \alpha_B^-(\omega) = \frac{4\omega}{c} \Im\chi^{me}(\omega)$ as given in Eq. (4.11).

their relationship to the optical properties.

4.5 Magnetolectric response and absorption

The linear response (susceptibilities) to the external fields at finite temperature can be described by the Kubo formula (for Kubo's original paper see [140], and for its application to the magnetolectric problem described here see [139]). The magnetic susceptibility tensor

is defined as

$$\chi_{\mu\mu}^{mm}(\omega) = \sum_{i,f} \frac{|\langle f|M^\mu|i\rangle|^2}{\hbar\omega - E_i + E_f + i\delta} \frac{e^{-\beta E_f} - e^{-\beta E_i}}{Z}, \quad (4.9)$$

and the magnetoelectric susceptibility tensor is defined as

$$\chi_{\mu\nu}^{me}(\omega) = \sum_{i,f} \frac{\langle i|M^\mu|f\rangle\langle f|P^\nu|i\rangle}{\hbar\omega - E_i + E_f + i\delta} \frac{e^{-\beta E_f} - e^{-\beta E_i}}{Z}, \quad (4.10)$$

where $Z = \sum_i e^{-\beta E_i}$ is the partition sum, with inverse temperature $\beta = 1/k_B T$, $|i\rangle$ and $|f\rangle$ are initial and final states of the spin system (4.1) with energies E_i and E_f (i.e. $\mathcal{H}|i\rangle = E_i|i\rangle$), ω is the angular frequency, and δ is a phenomenological inverse lifetime giving a finite width to the absorption peaks. Note the indices of the susceptibilities: Upper indices refer to the type of response (the type of operators in the Kubo formula), and lower indices are the tensor component indices x, y, z .

The experimentally measured NDD is related to the imaginary⁷ and time-reversal odd part of the ME susceptibility[139]⁸ as

$$\alpha^+(\omega) - \alpha^-(\omega) = \frac{4\omega}{c} \Im \chi_{\mu\nu}^{me}(\omega), \quad (4.11)$$

where c is the speed of light in vacuum, μ points in the direction of \mathbf{B}_ω and ν points in the direction of \mathbf{E}_ω of the light.

The contribution of a given transition $|i\rangle \rightarrow |f\rangle$ to the dissipative (imaginary) part of the magnetic and ME susceptibility reads

$$\Im \{ \chi_{\mu\mu}^{mm}(\omega) \}_{i \rightarrow f} \propto |\langle i|M^\mu|f\rangle|^2 \delta(\omega - \omega_{if}) \quad (4.12)$$

and

$$\Im \{ \chi_{\mu\nu}^{me}(\omega) \}_{i \rightarrow f} \propto \Re \{ \langle i|M^\mu|f\rangle \langle f|P^\nu|i\rangle \} \delta(\omega - \omega_{if}), \quad (4.13)$$

⁷ $\Im\{z\}$ denotes the imaginary part of the complex number z , and similarly $\Re\{z\}$ denotes its real part.

⁸The absorption is given by

$$\alpha^\pm(\omega) = \frac{2\omega}{c} \Im \mathcal{N}_\pm(\omega),$$

where the complex index of refraction \mathcal{N}_\pm for the $\pm k$ direction of light propagation is

$$\mathcal{N}_\pm(\omega) = \sqrt{[\epsilon_{\nu\nu} + \chi_{\nu\nu}^{ee}(\omega)] [\mu_{\mu\mu} + \chi_{\mu\mu}^{mm}(\omega)] \pm \chi_{\mu\nu}^{me}(\omega)}.$$

$\epsilon_{\nu\nu}$ and $\mu_{\mu\mu}$ are real background dielectric permittivity and magnetic permeability unrelated to the spin system, respectively. $\chi_{\mu\nu}^{me}(\omega)$ is the time-reversal odd part of the ME susceptibility. For the derivation and limitations of this formula see Ref. [139] and references therein. In the limit of small spin contribution to the susceptibilities $\chi_{\nu\nu}^{ee}(\omega) \ll \epsilon_{\nu\nu}$, $\chi_{\mu\mu}^{mm}(\omega) \ll \mu_{\mu\mu}$, the index of refraction becomes

$$\mathcal{N}_\pm(\omega) \approx \sqrt{\epsilon_{\nu\nu}\mu_{\mu\mu}} + \frac{\sqrt{\mu_{\mu\mu}}}{2\sqrt{\epsilon_{\nu\nu}}} \chi_{\nu\nu}^{ee}(\omega) + \frac{\sqrt{\epsilon_{\nu\nu}}}{2\sqrt{\mu_{\mu\mu}}} \chi_{\mu\mu}^{mm}(\omega) \pm \chi_{\mu\nu}^{me}(\omega).$$

where $\hbar\omega_{if} = E_f - E_i$ is the transition energy (of course the Dirac-deltas broaden to Lorentzians with finite width δ). It is important to remember that only the *real part* of the matrix element product is time reversal odd in Eq. (4.13), and this real part governs the NDD, see Eq. (4.11). Exact diagonalization calculations (ED) can be performed on finite (actually, small) clusters of spins to describe the absorption spectra, and we describe them in the next section.

4.6 Exact diagonalization

Exact diagonalization studies were performed⁹ on a cluster of four Co^{2+} ions (two unit cells) of spin $S = 3/2$ at finite temperature (an ED calculation on $\text{Ba}_2\text{CoGe}_2\text{O}_7$ has been already performed at zero temperature in Ref. [37]). The local Hilbert space is $2S + 1 = 4$ dimensional, so the cluster has a Hilbert space of dimension $(2S + 1)^4 = 256$, and the sums in Eqs. (4.9) and (4.10) run over $256^2 = 65536$ terms. Although the cluster seems to be small, the results are in surprisingly good agreement with the high temperature measurements.

As was already mentioned the low temperature excitations and ground state properties as well as the DC measurements (e.g. the field dependence of the magnetization) of $\text{Sr}_2\text{CoSi}_2\text{O}_7$ [36] bear striking resemblance to the ones of $\text{Ba}_2\text{CoGe}_2\text{O}_7$ [137], so we did not try to fit the parameters of the Hamiltonian (4.1) but used the values that were already successful in describing the excitations of $\text{Ba}_2\text{CoGe}_2\text{O}_7$ in an ED calculation at zero temperature before [43]: $\Lambda = 13.4$ K, $J = 2.3$ K, $J_{zz} = 1.8$ K, $D_z = -0.1$ K, $\kappa = 22.4^\circ$, and $g = 2.3$.¹⁰ It is worth mentioning that this is an unusual set of parameters: The anisotropy is about seven times as large as the exchanges (this has also a profound effect on the low temperature excitations, for details see [43]). The susceptibilities $\chi^{mm}(\omega)$ and $\chi^{me}(\omega)$ as given in Eqs. (4.9) and (4.10) were calculated and are presented in Fig. 4.2(c)-(f) and Fig. 4.3(c)-(f).

Just like in the experiments at sufficiently high temperature and field a single mode is present in the ED calculations and below 20 K a second mode appears. To our pleasant surprise, not just the presence of the NDD, but also its sign, and for $\mathbf{E}_\omega \parallel [001]$ even the sign change between 10 K and 15 K is reproduced by the numerics, see Fig. 4.2(b) and (f). In the following we try to understand the above mentioned results in a simplified model of a single Co-ion, and analyze the symmetry properties of this model.

4.7 The single-ion problem

We have seen that the ED calculations describing the NDD of $\text{Sr}_2\text{CoSi}_2\text{O}_7$ and the experiments are in a remarkably good agreement. To understand the essential physics of the high temperature MChD we construct the simplest model possible. We consider only one

⁹The ED calculations presented were performed by Karlo Penc.

¹⁰To compare these scales with the experiments the parameters in wavenumber units are given as $\Lambda = 9.31$ cm^{-1} , $J = 1.6$ cm^{-1} , $J_{zz} = 1.25$ cm^{-1} , $D_z = -0.07$ cm^{-1} . A field of $B = 1$ T with $g = 2.3$ is equivalent to an energy of 1.54 K or 1.07 cm^{-1} .

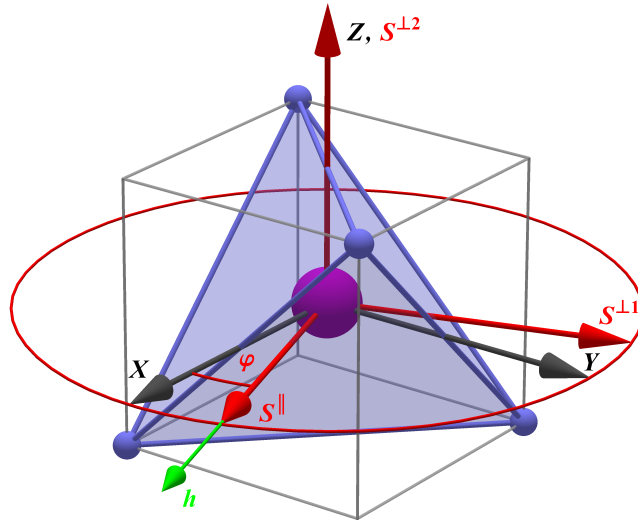


Figure 4.4: Coordinate systems for the single-ion problem. The tetrahedron-fixed coordinate system $\{X, Y, Z\}$ (black arrows) and the rotated, field-fixed coordinate system $\{\parallel, \perp 1, \perp 2\}$ (red arrows). The purple ball in the center is the Co^{2+} ion with spin $S = 3/2$, and the blue tetrahedron is the cage of O^{2-} ions. The quantization axis (with spin component S^{\parallel}) points along the direction of the static external magnetic field h (green arrow), while the perpendicular axis with spin component $S^{\perp 2}$ is parallel to Z .

Co^{2+} spin sitting in the center of a tetrahedron, and feeling a magnetic field and the strong easy-plane anisotropy, i.e. we neglect the interactions in Eq. (4.1) and only keep the on-site terms. This choice is motivated by the following: The anisotropy and a typical field of 10 T is about seven times larger than the exchanges, and 30 K (the actual temperature of the measurements) is about fifteen times larger than the exchanges. Furthermore in the paramagnetic phase with increasing temperature the correlation between the neighboring spins decreases. This tetrahedral building block has the same magnetic group as the magnetic point group of the real material when placed in a magnetic field¹¹. We calculate the eigensystem of this model and we analyze the symmetries of the system to find the selection rules. As a very interesting side effect we will find a way to use the non-unitary symmetries to tell us something about the *reality/imaginariness* of the matrix elements of the perturbing operators. A glimpse at the Kubo formula in Eq. (4.13) shows that in this magneto-optical situation this information can be just as useful as an old fashioned selection rule.

4.7.1 The Hamiltonian and the symmetries

Spin Hamiltonian and electric polarization

We consider a single $S = 3/2$ spin in the center of a tetrahedron, and switch on an external magnetic field of magnitude $h = g\mu_B B$ pointing in some direction in the XY plane. A comfortable choice of coordinates is shown in Fig. 4.4: The \parallel axis points along the field

¹¹A [100] directed field in the material corresponds to the *chiral* case of the single-ion model (see Subsection 4.7.2 for the description of this case), both have $22'2'$ as the magnetic point group.

direction, the $\perp 2$ axis is parallel to the Z axis, and the $\perp 1$ is chosen such a way that $\perp 1$, $\perp 2$ and \parallel form a right-hand system. We will call this coordinate system *field-fixed*, and the relationship between the XYZ and the field-fixed system is given by

$$\begin{aligned} S^X &= \cos \varphi S^{\parallel} - \sin \varphi S^{\perp 1}, \\ S^Y &= \sin \varphi S^{\parallel} + \cos \varphi S^{\perp 1}, \\ S^Z &= S^{\perp 2}. \end{aligned} \quad (4.14)$$

The spin components in the field-fixed frame follow the usual commutation relations $[S^{\perp 1}, S^{\perp 2}] = iS^{\parallel}$ (and cyclic permutations). Keeping only the on-site terms in Eq. (4.1), and concentrating on a single spin results in the following Hamiltonian

$$\mathcal{H} = \Lambda (S^{\perp 2})^2 - hS^{\parallel}. \quad (4.15)$$

We choose the quantization axis along the magnetic field, the eigenvalues and eigenvectors of S^{\parallel} are $\{+3/2, +1/2, -1/2, -3/2\}$ and $\{\uparrow, \uparrow, \downarrow, \downarrow\}$, respectively.

The tetrahedron lacks inversion symmetry, and it is responsible for the polarization (see Eq. (4.2))¹²:

$$\begin{aligned} P^X &= \eta_{XY}(S^Z S^Y + S^Y S^Z), \\ P^Y &= \eta_{XY}(S^Z S^X + S^X S^Z), \\ P^Z &= \eta_Z(S^X S^Y + S^Y S^X), \end{aligned} \quad (4.16)$$

and for a regular tetrahedron $\eta_{XY} = \eta_Z$. The components in the field-fixed system read as

$$\begin{aligned} P^X &= \cos \varphi P^{\parallel} - \sin \varphi P^{\perp 1}, \\ P^Y &= \sin \varphi P^{\parallel} + \cos \varphi P^{\perp 1}, \\ P^Z &= P^{\perp 2}. \end{aligned} \quad (4.17)$$

Solution of the Hamiltonian

The matrix representation of the Hamiltonian (4.15) in the basis $\{\uparrow, \uparrow, \downarrow, \downarrow\}$ reads

$$\hat{\mathcal{H}} = \begin{pmatrix} \frac{3}{4}\Lambda - \frac{3}{2}h & 0 & -\frac{\sqrt{3}}{2}\Lambda & 0 \\ 0 & \frac{7}{4}\Lambda - \frac{1}{2}h & 0 & -\frac{\sqrt{3}}{2}\Lambda \\ -\frac{\sqrt{3}}{2}\Lambda & 0 & \frac{7}{4}\Lambda + \frac{1}{2}h & 0 \\ 0 & -\frac{\sqrt{3}}{2}\Lambda & 0 & \frac{3}{4}\Lambda + \frac{3}{2}h \end{pmatrix}, \quad (4.18)$$

and we denote the 4×4 matrix representatives of the operators with a hat.

¹²A perfect tetrahedron has a symmetry group $T_d \equiv \bar{4}3m$ called the *achiral or full tetrahedral group* having 24 elements including 6 mirror planes and 6 fourfold roto reflections (S_4). This group is apolar. Distorting this tetrahedron in the Z -direction as in the real material reduces this group to the achiral and apolar $D_{2d} \equiv \bar{4}2m$. This group is isomorphic to the point group of the material in the paramagnetic phase in the absence of external field.

A twofold rotation C_2^\parallel about the magnetic field is the symmetry of the Hamiltonian (4.15),¹³ so its operator \hat{C}_2^\parallel commutes with $\hat{\mathcal{H}}$, $[\hat{\mathcal{H}}, \hat{C}_2^\parallel] = 0$. Therefore the eigenvalues $\pm i$ of

$$\hat{C}_2^\parallel = e^{i\pi\hat{S}^\parallel} = \begin{pmatrix} -i & 0 & 0 & 0 \\ 0 & i & 0 & 0 \\ 0 & 0 & -i & 0 \\ 0 & 0 & 0 & i \end{pmatrix} \quad (4.19)$$

are good quantum numbers and we will use these eigenvalues to label the states. Since our spin is half-integer $(\hat{C}_2^\parallel)^2 = -\hat{\mathbf{1}}$, where $\hat{\mathbf{1}}$ is the 4×4 unit matrix. Another consequence of this symmetry is that only the states with the same label $\pm i$ are mixed. We denote the eigenenergies as $\varepsilon_j^{(\pm i)}$, and the corresponding eigenstates as $|\psi_j^{(\pm i)}\rangle$.

The eigenvalues of $\hat{\mathcal{H}}$ in increasing order of the energies are ($h, \Lambda > 0$)

$$\varepsilon_1^{(-i)} = -\frac{h}{2} + \frac{5\Lambda}{4} - \sqrt{h^2 + h\Lambda + \Lambda^2}, \quad (4.20a)$$

$$\varepsilon_2^{(+i)} = \frac{h}{2} + \frac{5\Lambda}{4} - \sqrt{h^2 - h\Lambda + \Lambda^2}, \quad (4.20b)$$

$$\varepsilon_3^{(-i)} = -\frac{h}{2} + \frac{5\Lambda}{4} + \sqrt{h^2 + h\Lambda + \Lambda^2}, \quad (4.20c)$$

$$\varepsilon_4^{(+i)} = \frac{h}{2} + \frac{5\Lambda}{4} + \sqrt{h^2 - h\Lambda + \Lambda^2}, \quad (4.20d)$$

and the corresponding unnormalized eigenstates are

$$|\psi_1^{(-i)}\rangle \propto \left(2h + \Lambda + 2\sqrt{h^2 + h\Lambda + \Lambda^2}\right) |\uparrow\uparrow\rangle + \sqrt{3}\Lambda |\downarrow\rangle, \quad (4.21a)$$

$$|\psi_2^{(+i)}\rangle \propto \left(2h - \Lambda + 2\sqrt{h^2 - h\Lambda + \Lambda^2}\right) |\uparrow\rangle + \sqrt{3}\Lambda |\downarrow\rangle, \quad (4.21b)$$

$$|\psi_3^{(-i)}\rangle \propto \left(2h + \Lambda + 2\sqrt{h^2 + h\Lambda + \Lambda^2}\right) |\downarrow\rangle - \sqrt{3}\Lambda |\uparrow\rangle, \quad (4.21c)$$

$$|\psi_4^{(+i)}\rangle \propto \left(2h - \Lambda + 2\sqrt{h^2 - h\Lambda + \Lambda^2}\right) |\downarrow\rangle - \sqrt{3}\Lambda |\uparrow\rangle. \quad (4.21d)$$

The phases for the eigenvectors above are chosen in such a way that we recover the basis $\{|\uparrow\uparrow\rangle, |\uparrow\rangle, |\downarrow\rangle, |\downarrow\rangle\}$ for $h \gg \Lambda$, e.g. $|\psi_1^{(-i)}\rangle \rightarrow |\uparrow\uparrow\rangle$, and so on. The field dependence of the eigenenergies is shown in Fig. 4.5(b), colors of the different curves correspond to the quantum numbers $\pm i$.

¹³One may ask the question: What about the other symmetries of the Hamiltonian (4.15)? The full symmetry group of the Hamiltonian is $D_{2h}(C_{2h}) \equiv m'm'm$ with elements $\{E, C_2^\parallel, \sigma^\parallel, I, \Theta C_2^{\perp 2}, \Theta C_2^{\perp 1}, \Theta\sigma^{\perp 1}, \Theta\sigma^{\perp 2}\}$, where I is space inversion, Θ is time reversal and σ is a mirror plane perpendicular to the indicated axis, i.e. $\sigma^\parallel = IC_2^\parallel$. So why do not we use the other generators of this group to refine the labeling of the eigenstates? The answer is twofold. First, we *will* use the time reversed elements later in a different context. Second, we can choose the inversion I as the other generator of the unitary subgroup $C_{2h} \equiv 2/m = \{E, C_2^\parallel, \sigma^\parallel, I\}$, but it is not very useful for us: Space inversion on spin states can be represented by the unit matrix of dimension $2S + 1$ [142]. This argumentation also shows that if we have σ^\parallel instead of C_2^\parallel as a symmetry of the Hamiltonian we can use it the same way to classify spin states and operators as we use C_2^\parallel here.

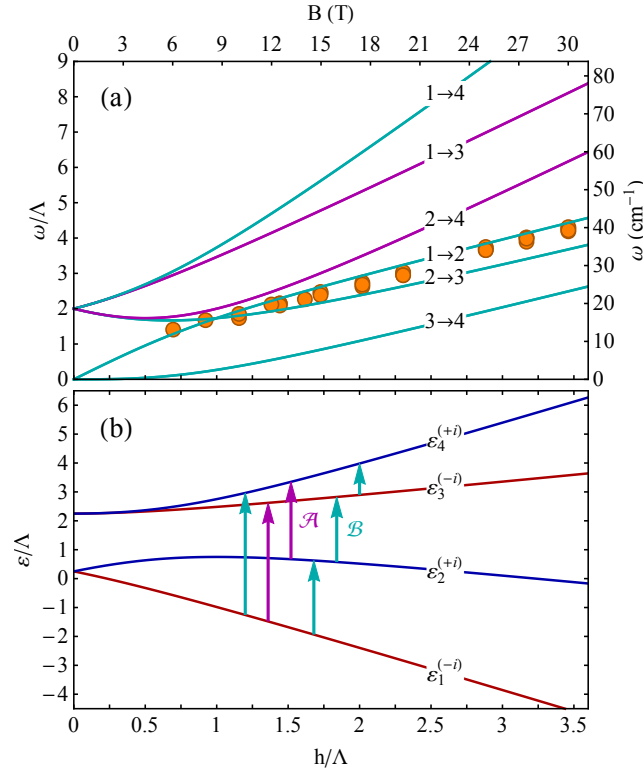


Figure 4.5: Transition energies ω (a) and energy levels ε (b) of the single-ion model (4.15) with easy plane anisotropy Λ in a magnetic field $h = g\mu_B B$ within the easy plane as a function of h/Λ . States 1 and 3 (red curves) are multiplied by $-i$ after a π -rotation about the field (C_2^{\parallel}), while states 2 and 4 (blue) get a factor of i . Magenta arrows represent transitions between states with the same symmetry, induced by operators \mathcal{A} even under C_2^{\parallel} , such as S^{\parallel} , P^{\parallel} (see Table 4.1). Cyan arrows connect states with different symmetries induced by operators \mathcal{B} odd under C_2^{\parallel} , which include the perpendicular components of the magnetization and polarization operators. The color of the curves in panel (a) corresponds to the color of the arrows in panel (b). The orange circles show the experimental results, to compare the model with the experiments we used the values $g = 2.3$ and $\Lambda = 13.4$ K, or equivalently $\Lambda = 9.31$ cm $^{-1}$.

Transition matrix elements

In this subsection we uncover rules that govern the existence of transitions between two states, from a symmetry point of view. These are the *selection rules*. Let us assume that we have a Hamiltonian which we perturb somehow (see e.g. Eq. (4.7) perturbed with the electromagnetic field). When a matrix element of the perturbing operator between the states of the unperturbed Hamiltonian vanishes, then the transition mediated by the perturbing operator is forbidden (in first order). Based on the symmetry properties of the perturbing operator and the states one can derive such rules [134]. A matrix element $\langle \psi_{\beta} | \mathcal{O} | \psi_{\alpha} \rangle$ of a perturbing operator \mathcal{O} between states of the unperturbed Hamiltonian $|\psi_{\alpha}\rangle$ and $|\psi_{\beta}\rangle$ can only be nonvanishing (though nothing guarantees the *existence* of such a matrix element)

if it transforms according to the totally symmetric A irrep¹⁴ of the group of the unperturbed Hamiltonian $A \subseteq \Gamma^{\beta*} \otimes \Gamma(\mathcal{O}) \otimes \Gamma^\alpha$. Here \mathcal{O} transforms according to the irrep $\Gamma(\mathcal{O})$, and $|\psi_\alpha\rangle$ transforms according to the irrep Γ^α , and the star denotes the complex conjugate representation. In our case the unperturbed Hamiltonian is (4.15), and the perturbing operators are the magnetization and polarization components (4.16) and (4.17), since they couple to the oscillating electromagnetic fields. In the following two paragraphs we give a digression as a reminder to a more familiar example of selection rules

We recall a familiar example of selection rules, and use this example as a reference on how things will change in our magneto-optical context. We put a spin of length S (the dimension of the Hilbert space is $2S + 1$) in a \hat{z} -directed magnetic field with Hamiltonian $\mathcal{H} = -B^z S^z$, and we perturb the system by an \hat{x} -directed oscillating magnetic field $\mathcal{H}' \propto S^x B_\omega \cos(\omega t)$. The Hamiltonian is invariant under all the elements of rotations about \hat{z} : $[\mathcal{H}, S^z] = 0$, these rotations form the group $U(1)$. The eigenvalues $m = S, S-1, \dots, -S+1, -S$ of S^z are therefore good quantum numbers $S^z |m\rangle = m |m\rangle$, and the eigenenergies are $\mathcal{H} |m\rangle = \varepsilon_m |m\rangle$ with $\varepsilon_m = -B^z m$. We wish to emphasize that the *mere existence* of the quantum number m is the consequence of the $U(1)$ invariance of the Hamiltonian. In the perturbing operator we can replace $S^x = (S^+ + S^-)/2$ (where $S^\pm = S^x \pm iS^y$), and we see that the transition matrix elements $\langle m' | (S^+ + S^-)/2 | m \rangle$ are only nonvanishing if $m' = m \pm 1$, this is a form of a selection rule for *magnetic dipole transitions*.

The above argument can be understood by means of group theory: $U(1)$ being Abelian its complex unitary projective representations are one-dimensional and they can be indexed by the number $m = 0, \pm 1/2, \pm 1, \pm 3/2, \dots$. A rotation R_φ of angle φ about \hat{z} is represented on the $2S + 1$ dimensional Hilbert space of the spin by the diagonal matrix $e^{i\varphi S^z} = \text{diag}\{e^{i\varphi S}, e^{i\varphi(S-1)}, \dots, e^{i\varphi(-S+1)}, e^{i\varphi(-S)}\}$. Therefore the states transform according to $R_\varphi: |m\rangle \rightarrow e^{i\varphi m} |m\rangle$ and $R_\varphi: \langle m'| \rightarrow e^{-i\varphi m'} \langle m'|$. The spin raising and lowering operators transform according to $R_\varphi: S^\pm \rightarrow e^{\pm i\varphi} S^\pm$, independently of the dimension of the representation. Consequently the matrix elements transform as $R_\varphi: \langle m' | S^\pm | m \rangle \rightarrow e^{i\varphi(m-m'\pm 1)} \langle m' | S^\pm | m \rangle$, since they transform according to the product representation $e^{-i\varphi m'} \otimes e^{\pm i\varphi} \otimes e^{i\varphi m}$. Finally the matrix elements are invariant under any rotation if $m' = m \pm 1$, since the phase factor $e^{i\varphi(m-m'\pm 1)}$ has to be unity for *every* angle φ . Now let us connect these results to our one-ion model with Hamiltonian (4.15). The symmetries are much lower now, see Footnote 13. The perturbing operators are the magnetization and polarization components M^α and P^α (the analogues of S^x here), the states $|\psi_j^{(\pm i)}\rangle$ are given in Eqs. (4.21) and their irrep indices (the analogues of the magnetic quantum number m here) are merely the $(\pm i)$'s reflecting their transformational properties under C_2^\parallel as given in Eq. (4.19) (and C_2^\parallel is the analogue of the $U(1)$ rotations $R_\varphi = e^{i\varphi S^z}$ here). After this digression let us continue with the analysis of the one-ion model and its selection rules.

The transformation properties of the operators and states under the rotation C_2^\parallel are summarized in Table 4.1. Note the transformation properties of the states: Those are the same what we have calculated by hand using the matrix \hat{C}_2^\parallel before. Since our spin is half-integer we need to use the double group corresponding to the group C_2 [134]. If an

¹⁴Usually we denote the totally symmetric irrep of an abstract group as Γ^{1+} , here we use A, that is standard in the point group tables.

Table 4.1: Character table of the double group corresponding to the group C_2 . In the last column the operators and states are classified according to their transformation properties. The group element $\bar{1}$ is the 2π -rotation with the property $\bar{1}^2 = 1$.

Irrep	1	C_2^{\parallel}	$\bar{1}$	\bar{C}_2^{\parallel}	Operators
A	1	1	1	1	$S^{\parallel}, P^{\parallel}$
B	1	-1	1	-1	$S^{\perp 1}, S^{\perp 2}, P^{\perp 1}, P^{\perp 2}$
\bar{E}_1	1	i	-1	$-i$	$ \downarrow\rangle, \uparrow\rangle, \langle\uparrow , \langle\downarrow $
\bar{E}_2	1	$-i$	-1	i	$ \uparrow\rangle, \downarrow\rangle, \langle\downarrow , \langle\uparrow $

operator \mathcal{A} transforms according to A and an operator \mathcal{B} according to B, and the spin states according to \bar{E}_1 and \bar{E}_2 of the double group of C_2 , (see Table 4.1) then the nonvanishing matrix elements are

$$\langle\psi_{\beta}^{(\pm i)}|\mathcal{A}|\psi_{\alpha}^{(\pm i)}\rangle \text{ and } \langle\psi_{\beta}^{(\mp i)}|\mathcal{B}|\psi_{\alpha}^{(\pm i)}\rangle. \quad (4.22)$$

Allowed transitions between states of the same symmetry are of type \mathcal{A} and allowed transitions between states of different symmetry are of type \mathcal{B} . The transitions are depicted in Fig. 4.5(b), the magenta \mathcal{A} -transitions connect states with the same symmetry and the cyan \mathcal{B} -transitions connect states with different symmetry. In Fig. 4.5(a) we show the calculated and measured transition energies, e.g. $\omega^{1\rightarrow 2} = \varepsilon_2 - \varepsilon_1$.

Now we consider the effect of antiunitary symmetries containing the time-reversal operation Θ on the matrix elements. We show in Appendix G that any linear operator \hat{O} , if the symmetry operation $\Theta C_2^{\perp 2}$ is present (as in the case of a magnetic field applied in the XY plane), must satisfy $\hat{O} = \pm \hat{O}^*$. Therefore the matrix elements of any linear operator even (odd) under the symmetry operation $\Theta C_2^{\perp 2}$ are either real (pure imaginary).

To summarize: The unitary symmetries determine the selection rules, and the antiunitary symmetry elements force the matrix elements to be either real or pure imaginary. The reality of the matrix elements is crucial for the presence of NDD: We will consider this problem in the next subsection.

4.7.2 Directional dichroism in the single-ion model

The imaginary part of the ME susceptibility $\Im \{\chi_{\mu\nu}^{me}(\omega)\}$ gives rise to the NDD [143, 49, 50], see Eq. (4.11). For a given transition $|i\rangle \rightarrow |f\rangle$ the dissipative and time-reversal odd part of the ME susceptibility is proportional to the real part of the matrix element product of the components of the magnetization and electric polarization operators [139], as was given in Eq. (4.13) which we reproduce here

$$\Im \{\chi_{\mu\nu}^{me}(\omega)\}_{i\rightarrow f} \propto \Re \{ \langle i | M^{\mu} | f \rangle \langle f | P^{\nu} | i \rangle \} \delta(\omega - \omega_{if}). \quad (4.23)$$

Consequently NDD is non-zero if *both* of the matrix elements, $\langle i | M^{\mu} | f \rangle$ and $\langle f | P^{\nu} | i \rangle$, are finite for the same pair of states $|i\rangle$ and $|f\rangle$. This is allowed by symmetry if M^{μ} and P^{ν}

Table 4.2: Matrix elements of the spin and polarization operators for the transitions indicated in the first column, first in small field h , then for small anisotropy Λ in the single-ion model (4.15). The first non-vanishing order in either the external field h or the anisotropy Λ is shown, and c stands for a real constant.

transition	S^{\parallel}	$S^{\perp 1}$	$S^{\perp 2}$	$P_{\text{chiral}}^{\parallel}, P_{\text{polar}}^{\perp 1}$	$P_{\text{chiral}}^{\perp 1}, P_{\text{polar}}^{\parallel}$	$P_{\text{chiral}}^{\perp 2}$	$P_{\text{polar}}^{\perp 2}$
1 \rightarrow 2	–	c, c	ic, ic	–	ih, ic	h, c	–
2 \rightarrow 3	–	c, c	ih, ic	–	$ic, i\Lambda$	c, Λ	–
3 \rightarrow 4	–	h^2, c	ic, ic	–	ih, ic	h, c	–
1 \rightarrow 3	c, Λ	–	–	ic, ic	–	–	c, c
2 \rightarrow 4	c, Λ	–	–	ic, ic	–	–	c, c
1 \rightarrow 4	–	c, Λ^2	$ih, i\Lambda^2$	–	$ic, i\Lambda$	c, Λ	–

transform according to the same irrep of the group of unitary symmetries of the single-ion Hamiltonian (4.15).

Moreover the product of the M^μ and P^ν matrix elements must have a finite real part in order to have a finite NDD in accordance with Eq. (4.23). We have seen in the previous subsection that the matrix elements are either real or pure imaginary because of the presence of the antiunitary symmetry $\Theta C_2^{\perp 2}$, so to have a real product either both matrix elements have to be real or both imaginary. So both the operators M^μ and P^ν have to be either even or odd under $\Theta C_2^{\perp 2}$ at the same time. The properties of all spin and polarization operator matrix elements for $S = 3/2$ in the single-ion model are presented for all the transitions in Table 4.2: They are either real, imaginary, or symmetry-forbidden.

In the following we analyze the symmetry properties of the operators for different directions of the external field with respect to the tetrahedron to find out the details about the existence of NDD.¹⁵

Magneto-chiral dichroism (chiral case): $\varphi = 0$

When the external field is parallel to one of the twofold rotation axis, i.e. $\varphi = 0$ (see Fig. 4.4), the system has the chiral and apolar symmetry $D_2(C_2) \equiv 22'2'$ (see Fig. 4.6(a) of the tetrahedron from the point of view of the external field direction, and for the stereographic projection of the group). Note that this group is isomorphic to the point group of the real material in a [100] directed external field, i.e. the experimental situation (see Fig. 4.1). The character table and the transformation properties of physical quantities under this group are given in Table 4.3. The polarization operators in the field-fixed coordinate

¹⁵Note that the group used here is the group of the Hamiltonian (4.15), and the tetrahedron dictates the form of the polarization operator.

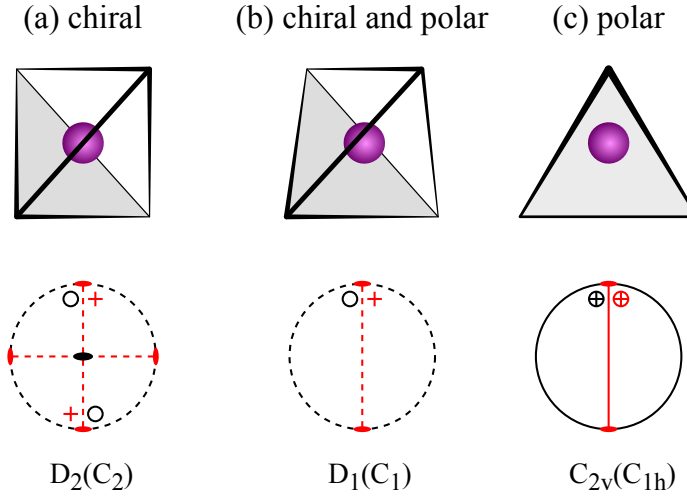


Figure 4.6: The tetrahedron in the (a) chiral ($\varphi = 0$), (b) low symmetry, and (c) polar ($\varphi = \pi/4$) cases as seen from the point of view of the static external magnetic field \mathbf{B} . The magenta ball represents the Co^{2+} ion at the center of the tetrahedron. The stereographic projections of the magnetic point groups are shown below the tetrahedra for each case, black color refers to the unitary symmetry elements and red color refers to the time reversed elements (this depiction of symmetries is explained in [134]).

system read via (4.17)

$$P_{\text{chiral}}^{\parallel} = \frac{\eta_{XY}}{2i} [(S^+)^2 - (S^-)^2], \quad (4.24a)$$

$$P_{\text{chiral}}^{\perp 1} = \frac{\eta_{XY}}{2i} [S^{\parallel}(S^+ - S^-) + (S^+ - S^-)S^{\parallel}], \quad (4.24b)$$

$$P_{\text{chiral}}^{\perp 2} = \frac{\eta_Z}{2} [S^{\parallel}(S^+ + S^-) + (S^+ + S^-)S^{\parallel}], \quad (4.24c)$$

where $S^{\pm} = S^{\perp 1} \pm iS^{\perp 2}$. For $\varphi = n\pi/2$ with n being an integer the situation is the same (up to a sign), due to the S_4 symmetry of the distorted oxygen tetrahedron. Note that the perpendicular components $P^{\perp 1}$ and $P^{\perp 2}$ change the S^{\parallel} quantum number by ± 1 (magnetic dipolar excitation), but $P_{\text{chiral}}^{\parallel}$ changes it by ± 2 (magnetic quadrupolar excitation) [144].

Since the group is apolar none of the components of \mathbf{P} transforms according to the fully symmetric irrep A_+ , see Table 4.3, and therefore the expectation value of the static polarization is zero in the ground state. But the operators $S^{\perp 2}$ and $P^{\perp 1}$ belong to the same irrep B_- of $D_2(C_2)$, so the dynamic ME susceptibility is allowed. As the oscillating magnetization $S^{\perp 2}$ and polarization $P^{\perp 1}$ are perpendicular to each other and to the external magnetic field, we expect NDD in the Faraday geometry, when the light is propagating parallel to the field: This is the magnetochiral dichroism (MChD). The same is true for the operators $S^{\perp 1}$ and $P^{\perp 2}$ belonging to the irrep B_+ , therefore NDD is allowed irrespective of polarizations of the incident light in Faraday geometry. Direct evaluation of the matrix elements (see Appendix H and Table 4.2) using the eigenstates given in Eqs. (4.21a)-(4.21d) corroborates the above symmetry analysis.

From Table 4.3 we can also interpret the selection rules with respect to the quantum

Table 4.3: Character tables for the magnetic point groups and symmetry-allowed operators for three orientations of the applied magnetic field in the easy plane, see Fig. 4.4, describing chiral ($\varphi = 0$), polar ($\varphi = \pi/4$), and low symmetry cases.

$\varphi = 0$: Chiral case, the point group is $D_2(C_2)$						
Irrep.	1	C_2^{\parallel}	$\Theta C_2^{\perp 2}$	$\Theta C_2^{\perp 1}$	Operator(s)	NDD
A_+	1	1	1	1	S^{\parallel}	–
A_-	1	1	–1	–1	P^{\parallel}	–
B_+	1	–1	1	–1	$S^{\perp 1}, P^{\perp 2}$	Faraday
B_-	1	–1	–1	1	$S^{\perp 2}, P^{\perp 1}$	Faraday

$\varphi = \pi/4$: Polar case, the point group is $C_{2v}(C_{1h})$						
	1	σ^{\parallel}	$\Theta C_2^{\perp 2}$	$\Theta \sigma^{\perp 1}$		
A_+	1	1	1	1	$S^{\parallel}, P^{\perp 2}$	Voigt
A_-	1	1	–1	–1	$P^{\perp 1}$	–
B_+	1	–1	1	–1	$S^{\perp 1}$	–
B_-	1	–1	–1	1	$S^{\perp 2}, P^{\parallel}$	Voigt

$\varphi \neq 0$ nor $\pi/4$: The point group is $D_1(C_1)$						
	1	$\Theta C_2^{\perp 2}$				
Γ_+	1	1			$S^{\parallel}, S^{\perp 1}, P^{\perp 2}$	Both
Γ_-	1	–1			$S^{\perp 2}, P^{\parallel}, P^{\perp 1}$	Both

numbers $\pm i$, i.e. the eigenvalues of the \hat{C}_2^{\parallel} rotation operator (4.19). The S^{\parallel} and P^{\parallel} are even under C_2^{\parallel} , so they excite only type \mathcal{A} transitions between states with the same quantum number (see Fig. 4.5 (b)), i.e. between states 1 and 3 and between states 2 and 4. However, there is no NDD for the \mathcal{A} type transitions as P^{\parallel} and S^{\parallel} belong to different irreps.

The perpendicular components of \mathbf{P} and \mathbf{S} have finite matrix elements between states with different C_2^{\parallel} quantum numbers, which corresponds to type \mathcal{B} transitions, i.e. the transitions $1 \rightarrow 2$, $1 \rightarrow 4$, $2 \rightarrow 3$, and $3 \rightarrow 4$ (see Fig. 4.5 (b)). The $S^{\perp 2}$ and $P^{\perp 1}$ are both odd under $\Theta C_2^{\perp 2}$ (Table 4.3), thus both of them have imaginary matrix elements, so their product is real in Eq. (4.23), and they provide finite imaginary $\chi_{\perp 2, \perp 1}^{me}(\omega)$ causing a finite MChD. Similarly, the $S^{\perp 1}$ and $P^{\perp 2}$ are both even under $\Theta C_2^{\perp 2}$, with real matrix elements, providing a finite imaginary $\chi_{\perp 1, \perp 2}^{me}(\omega)$. In any other configuration the $\Im \{ \chi_{\mu\nu}^{me}(\omega) \} = 0$. In consequence, the MChD is present only in the Faraday geometry when $\mathbf{k} \parallel \mathbf{B}$.

Toroidal dichroism (polar case): $\varphi = \frac{\pi}{4}$

If the external magnetic field is directed parallel to the upper edge of the tetrahedron, $\varphi = \frac{\pi}{4}$ in Fig. 4.4, the polarization operators in the field-fixed coordinate system become via (4.17)

$$P_{\text{polar}}^{\parallel} = \frac{\eta_{XY}}{2i} [S^{\parallel}(S^{+} - S^{-}) + (S^{+} - S^{-})S^{\parallel}], \quad (4.25a)$$

$$P_{\text{polar}}^{\perp 1} = \frac{\eta_{XY}}{2i} [(S^{-})^2 - (S^{+})^2], \quad (4.25b)$$

$$P_{\text{polar}}^{\perp 2} = \frac{\eta_Z}{4} [4(S^{\parallel})^2 - (S^{-})^2 - (S^{+})^2 - S^{-}S^{+} - S^{+}S^{-}]. \quad (4.25c)$$

The roles of the parallel and perpendicular operators have exchanged with respect to the chiral case: The perpendicular operators change the S^{\parallel} quantum number by 0 and ± 2 (spin quadrupolar transition), and the parallel operator by ± 1 (spin dipolar transition). We note that $P_{\text{polar}}^{\parallel} = P_{\text{chiral}}^{\perp 1}$ and $P_{\text{polar}}^{\perp 1} = -P_{\text{chiral}}^{\parallel}$. The symmetry group of the spin Hamiltonian is $C_{2v}(C_{1h}) = 2'm'm$ (see Fig. 4.6(c)), this group is achiral but polar: A static $P^{\perp 2}$ polarization is allowed (hence the name *polar* for this case). The character table and the transformations of physical quantities under this group are given in Table 4.3.

Since σ^{\parallel} is present, the $S^{\perp 1}$ and $P^{\perp 2}$ belong to different irreps, and similarly do $S^{\perp 2}$ and $P^{\perp 1}$: NDD is forbidden in the Faraday geometry. Indeed, in Faraday geometry $\mathbf{k} \parallel \mathbf{B}$, the oscillating electromagnetic field transforms under σ^{\parallel} as $\mathbf{B}_{\omega} \rightarrow -\mathbf{B}_{\omega}$, $\mathbf{E}_{\omega} \rightarrow \mathbf{E}_{\omega}$, and $\mathbf{k} \rightarrow -\mathbf{k}$. The two directions of the radiation propagation are connected by the symmetry element σ^{\parallel} , and as a consequence the NDD in the Faraday geometry vanishes [139].

Instead, $S^{\perp 2}$ and P^{\parallel} transform according to the same irrep B_{-} . Consequently a finite ME susceptibility $\chi_{\perp 2, \parallel}^{me}$ will appear in the Voigt geometry when \mathbf{k} is parallel to $\perp 1$ and $\mathbf{E}^{\omega} \parallel \mathbf{B}$ (remember in the Voigt configuration the static external field is perpendicular to the light propagation direction). Similarly, S^{\parallel} and $P^{\perp 2}$ both belong to A_{+} , resulting a finite $\chi_{\parallel, \perp 2}^{me}$. Since the operators belonging to the same irrep in Table 4.3 have the same parity under the $\Theta C_2^{\perp 2}$ transformation, their matrix elements are either both real (for $S^{\perp 2}$ and P^{\parallel}), or they are both pure imaginary (for S^{\parallel} and $P^{\perp 2}$), allowing NDD in the Voigt configuration in both light polarizations.

As was briefly explained in Footnote 13 the matrices in spin space $\hat{\sigma}^{\parallel}$ and \hat{C}_2^{\parallel} are the same (4.19), we can repeat all the arguments we have used in the chiral case to determine the selection rules. The S^{\parallel} and $P^{\perp 2}$ operators have finite matrix elements between states with the same $\hat{C}_2^{\parallel} \equiv \hat{\sigma}^{\parallel}$ quantum number, i.e. the \mathcal{A} -type transitions $1 \rightarrow 3$ and $2 \rightarrow 4$ are allowed. The $S^{\perp 2}$ and P^{\parallel} change the quantum number $\pm i \rightarrow \mp i$, and \mathcal{B} -type transitions $1 \rightarrow 2$, $1 \rightarrow 4$, $2 \rightarrow 3$, and $3 \rightarrow 4$ are allowed.

Low symmetry case: $\varphi \neq 0$ nor $\frac{\pi}{4}$

For arbitrary φ the polarization operators can be written as the following linear combinations

$$\mathbf{P} = \cos 2\varphi \mathbf{P}_{\text{chiral}} + \sin 2\varphi \mathbf{P}_{\text{polar}}. \quad (4.26)$$

Only the $\Theta C_2^{\perp 2}$ symmetry remains and it generates the magnetic point group $D_1(C_1) = 2'$ (see Table 4.3 and Fig. 4.6(b)). This group is chiral and polar, a static $P^{\perp 2}$ is allowed. Neither C_2^{\parallel} nor σ^{\parallel} is a symmetry element anymore, so \mathbf{P} may have finite matrix elements between any of the $(\pm i)$ states. The situation is different for the spin components: As the

spin states still respect the quantum number of C_2^{\parallel} (the Hamiltonian (4.15) does not know anything about the orientation of the tetrahedron), the associated selection rules given in Eq. (4.22) hold for S^{\parallel} , $S^{\perp 1}$, and $S^{\perp 2}$. And this is good news: Since the ME susceptibility is composed from a product of matrix elements of \mathbf{S} and \mathbf{P} , it inherits the selection rules of the matrix element of \mathbf{S} . All in all, the system shows NDD in the Faraday geometry for the $1 \rightarrow 2$, $2 \rightarrow 3$, $1 \rightarrow 4$, and $3 \rightarrow 4$ transitions with $\chi^{me} \propto \cos 2\varphi$ coming from the chiral part, and it shows NDD in the Voigt geometry according to the selection rules set by the polar case with $\chi^{me} \propto \sin 2\varphi$.

Now we finish the study of the single ion problem, and turn to the lattice problem. We will see that the analysis of such a simple toy model was not done in vain: Some of the above results –mutatis mutandis– survive to the lattice case.

4.8 The lattice problem

In this section we describe the selection rules when we place the alternating tetrahedra on the square lattice and reevaluate the results we had for the single-ion model. Furthermore, we give the analytical form of the transition energies by taking into account the exchange coupling between the spins in the lowest order in perturbation theory, and as a side effect we show why the simple minded single-ion model described the experiments so well (see the orange dots in Fig. 4.5(a)).

4.8.1 Magneto-chiral dichroism and selection rules in the lattice problem

In the real material the tetrahedra are alternatingly tilted (see Fig. 4.1), so the situation is neither pure chiral nor pure polar as defined in the previous section. But the situation is not that bad as it seems at first sight: We can use the space group of the material to say something about the selection rules. Let us assume –as in the actual measurement– that the external field points in the [100] direction. The unitary part of the magnetic space group (aside from lattice translations) consists of the screw axis $\{C_2^{\parallel} | [\frac{1}{2}00]\}$ (black half-arrow in Fig. 4.1, formerly denoted by 2_1). This operation interchanges the sublattices A and B . We will use this symmetry to label the eigenstates and operators (this operation is the symmetry of the Hamiltonian (4.1)). Another symmetry operation (this is present for any in-plane field direction) is a twofold rotation followed by time reversal $\{\Theta C_2^{\perp 2} | [000]\}$ (red ellipse in Fig. 4.1): This keeps the sublattices fixed. We have a third screw axes, followed by time reversal $\{\Theta C_2^{\perp 1} | [0\frac{1}{2}0]\}$ (black half-arrow in Fig. 4.1). The magnetic point group of this nonsymmorphic space group is isomorphic to the $D_2(C_2) = 22'2'$ magnetic point group of a single tetrahedron in the chiral case

$$\left\{ \mathbf{1}, \{C_2^{\parallel} | [\frac{1}{2}00]\}, \{\Theta C_2^{\perp 2} | [000]\}, \{\Theta C_2^{\perp 1} | [0\frac{1}{2}0]\} \right\} \cong \left\{ \mathbf{1}, C_2^{\parallel}, \Theta C_2^{\perp 2}, \Theta C_2^{\perp 1} \right\}. \quad (4.27)$$

Let us examine the selection rules based on the single-ion calculations. The total magnetization and total polarization operators are defined in Eq. (4.5). We express them in

field-fixed coordinates and decompose them into even (\mathbf{M}_0) and odd (\mathbf{M}_π) parts based on the unitary symmetry element $\{C_2^\parallel | [\frac{1}{2}00]\}$. To do this we need the transformation properties of the magnetization components under this symmetry

$$\{C_2^\parallel | [\frac{1}{2}00]\} : \begin{pmatrix} M_A^\parallel \\ M_A^{\perp 1} \\ M_A^{\perp 2} \end{pmatrix} \rightarrow \begin{pmatrix} M_B^\parallel \\ -M_B^{\perp 1} \\ -M_B^{\perp 2} \end{pmatrix} \text{ and } \begin{pmatrix} M_B^\parallel \\ M_B^{\perp 1} \\ M_B^{\perp 2} \end{pmatrix} \rightarrow \begin{pmatrix} M_A^\parallel \\ -M_A^{\perp 1} \\ -M_A^{\perp 2} \end{pmatrix}, \quad (4.28)$$

and we do the same to the polarization operators. The even and odd parts can then be expressed as

$$\mathbf{M}_0 = \frac{1}{2} \left(\mathbf{M} + \{C_2^\parallel | [\frac{1}{2}00]\} \mathbf{M} \right), \quad (4.29)$$

$$\mathbf{M}_\pi = \frac{1}{2} \left(\mathbf{M} - \{C_2^\parallel | [\frac{1}{2}00]\} \mathbf{M} \right). \quad (4.30)$$

This way the total magnetization becomes $\mathbf{M} = \mathbf{M}_0 + \mathbf{M}_\pi$, and we can do the same decomposition for the polarization operators.

The effect of the time-reversed operation $\{\Theta C_2^{\perp 2} | [000]\}$ on the spin and polarization components reads

$$\{\Theta C_2^{\perp 2} | [000]\} : \begin{pmatrix} M_A^\parallel \\ M_A^{\perp 1} \\ M_A^{\perp 2} \end{pmatrix} \rightarrow \begin{pmatrix} M_A^\parallel \\ M_A^{\perp 1} \\ -M_A^{\perp 2} \end{pmatrix} \text{ and } \begin{pmatrix} P_A^\parallel \\ P_A^{\perp 1} \\ P_A^{\perp 2} \end{pmatrix} \rightarrow \begin{pmatrix} -P_A^\parallel \\ -P_A^{\perp 1} \\ P_A^{\perp 2} \end{pmatrix}, \quad (4.31)$$

and similarly on sublattice B .

Selection rules for the even M_0 and P_0 components

Using the decomposition (4.29) the even part of \mathbf{M} becomes

$$M_0^\parallel = M_A^\parallel + M_B^\parallel, \quad (4.32a)$$

$$M_0^\perp = 0, \quad (4.32b)$$

where $\perp = \perp 1, \perp 2$. Repeating the above procedure for the polarization results

$$P_0^\parallel = \sin 2\kappa \sum_j (-1)^j P_{j,\text{polar}}^\parallel - \cos 2\kappa \sum_j P_{j,\text{chiral}}^\parallel, \quad (4.33a)$$

$$P_0^\perp = 0, \quad (4.33b)$$

where the index j runs over all the sites being an even integer on A and an odd integer on the B sublattice; $P_{j,\text{chiral}}^\parallel$ is defined by Eq. (4.24a) and $P_{j,\text{polar}}^\parallel$ by Eq. (4.25a), with the corresponding spin operators at site j . The light does not interact with the system in the Faraday geometry in the even channel because $P_0^\perp = M_0^\perp = 0$.

Selection rules for the odd M_π and P_π components

Using the odd representation (4.30) for M_π and similarly for P_π , and following the steps we used to obtain the even components above, the corresponding magnetization and polarization components are

$$M_\pi^\parallel = 0, \quad (4.34a)$$

$$M_\pi^\perp = M_A^\perp - M_B^\perp \quad (4.34b)$$

and

$$P_\pi^\parallel = 0, \quad (4.35a)$$

$$P_\pi^\perp = \sin 2\kappa \sum_j (-1)^j P_{j,\text{polar}}^\perp - \cos 2\kappa \sum_j P_{j,\text{chiral}}^\perp, \quad (4.35b)$$

where $\perp = \perp 1, \perp 2$. Due to the nonvanishing perpendicular components $\{M_\pi^{\perp 1}, P_\pi^{\perp 2}\}$ and $\{M_\pi^{\perp 2}, P_\pi^{\perp 1}\}$ a finite ME susceptibility and NDD appears in the Faraday geometry for the odd channel.

Now we analyze the effect of the time-reversed operation $\{\Theta C_2^{\perp 2} | [000]\}$ (4.31). Just like for the single-ion, the $M_\pi^{\perp 1}$ and $P_\pi^{\perp 2}$ belong to the same irrep, as well as the $M_\pi^{\perp 2}$ and $P_\pi^{\perp 1}$. The matrix elements are therefore real or pure imaginary, and the products of the magnetization and polarization matrix elements in the ME susceptibility are real.

Although the symmetry classification obtained above did not consider the DM interaction, it describes the selection rules obtained from the exact diagonalization. This is because the DM interaction is compatible with the $D_2 (C_2) = 22'2'$ magnetic point group considered above. In the next subsection we incorporate the effects of the interactions in first order of perturbation theory.

4.8.2 Perturbative effects of the exchange coupling

We have not considered the effect of exchange interactions in the Hamiltonian (4.1) yet. In what follows we start from the single-ion limit $J = J_z = D_z = 0$ in Eq. (4.1) considered so far, and include effects of the interactions in the first order of perturbation theory. This process will result in a tight-binding-like model. We decompose the Hamiltonian (4.1) as

$$\mathcal{H} = \mathcal{H}_0 + \mathcal{H}', \quad (4.36)$$

where \mathcal{H}_0 is just the sum of the already solved on-site terms (see Eq. (4.15) and below) and \mathcal{H}' is interaction part we treat perturbatively (one can remember that the anisotropy is seven times stronger than the strongest exchange, and this strongest exchange is already reached by a tiny field of 1.5 T).

Neglecting interactions the ground state of \mathcal{H}^0 is

$$|\text{GS}\rangle = \prod_j |\psi_1^{(-i)}(j)\rangle, \quad (4.37)$$

where j runs over both the A and B sublattice sites. We define the local single-ion excitation at site l as

$$|\Psi_2(l)\rangle = |\psi_2^{(+i)}(l)\rangle \prod_{j \neq l} |\psi_1^{(-i)}(j)\rangle. \quad (4.38)$$

For the local wavefunctions $|\psi_\alpha^{(\pm i)}(l)\rangle$ see Eq. (4.21). We can see that all the sites are in the lowest energy state with energy ε_1 , except site l that is in the first excited state 2 with excitation energy ε_2 . We have totally neglected higher energy states or multiple-site excitations. Denoting the number of (all) sites by N , the noninteracting ground state energy becomes $E_1^0 = N\varepsilon_1$ and the excited states $|\Psi_2(l)\rangle$ have energies $E_2^0 = (N-1)\varepsilon_1 + \varepsilon_2$ and are N -fold degenerate. To see how the above degeneracy is lifted we do a first order degenerate perturbation calculation in \mathcal{H}' . We diagonalize the perturbing matrix \mathcal{H}' on the subspace spanned by the single-site excitations $|\Psi_2(l)\rangle$

$$\mathcal{H}'_{l'l} = \langle \Psi_2(l') | \mathcal{H}' | \Psi_2(l) \rangle. \quad (4.39)$$

The matrix $\mathcal{H}'_{l'l}$ describes a local excitation hopping with equal amplitudes in different directions¹⁶. Since the problem is translationally invariant it can be solved by Fourier transform.

Here we have translation invariance for the original unit cell containing two Co ions, with primitive lattice translations $\mathbf{a}_1 = (1, 1)$ and $\mathbf{a}_2 = (1, -1)$ in the (x, y) coordinate system (see Fig. 4.1). The two ions in the unit cell lead to two branches of excitations in the BZ defined by reciprocal lattice vectors $\mathbf{b}_1 = \pi(1, 1)$ and $\mathbf{b}_2 = \pi(1, -1)$, corresponding to the above translations. The spin Hamiltonian does not know anything about the two orientations of the tetrahedra, so the on-site energies are the same for the A and B sites. The Hamiltonian reads in Fourier space

$$\mathcal{H}^{\text{tb}}(\mathbf{k}) = \varepsilon \begin{pmatrix} 1 & 0 \\ 0 & 1 \end{pmatrix} + t_{AB} \begin{pmatrix} 0 & f^*(\mathbf{k}) \\ f(\mathbf{k}) & 0 \end{pmatrix}, \quad (4.40)$$

with $\mathbf{k} \in \text{BZ}$.

The tight-binding parameters can be inferred from Eq. (4.39):

$$E^{\text{GS}} = N\varepsilon_1 + 2Nb_{1,1}, \quad (4.41a)$$

$$E^2 = (N-1)\varepsilon_1 + \varepsilon_2 + (2N-4)b_{1,1} + 4b_{1,2}, \quad (4.41b)$$

$$\varepsilon = E^2 - E^{\text{GS}} = \varepsilon_2 - \varepsilon_1 + 4(b_{1,2} - b_{1,1}), \quad (4.41c)$$

¹⁶Our cumbersome notation hides that this is nothing more than a simple tight-binding model. Let us forget for a moment that we have a two-ion unit cell, and consider a simple square lattice. The only information contained in Eq. (4.38) is that we have an excitation at site l , and we denote it as $|l\rangle$. This excitation cannot do much (since we have restricted ourselves to the subspace of single-site excitations): It can sit in its site having some energy ε or hop to the neighboring sites with an amplitude $t_{l'l}$, which we assume to be real. This results the Hamiltonian

$$\mathcal{H}^{\text{tb}} = \varepsilon \sum_l |l\rangle \langle l| + \sum_{l'l} t_{l'l} |l'\rangle \langle l|,$$

where the model parameters can be inferred from the original spin Hamiltonian \mathcal{H} . The on-site energy is just the energy of the local excitation $\varepsilon = \varepsilon_2 - \varepsilon_1$, and from Eq. (4.39) the energy gain associated with the hopping is $t_{l'l} = \mathcal{H}'_{l'l}$.

where N is the number of Co-sites in the crystal, $b_{1,1}$ stands for a bond when both endpoints are in state 1, and $b_{1,2}$ is the strength for a bond when one endpoint is in state 1 and the other in state 2. ε is the diagonal energy, the difference between the ground state energy E^{GS} and the excitation energy E^2 where the state of one site is flipped from 1 to 2, changing four bonds from $b_{1,1}$ to $b_{1,2}$. t_{AB} is the hopping amplitude of the state 2 from one site to its neighboring one. The diagonal matrix elements from the spin model Eq. (4.39) are

$$b_{1,1} = J (\langle \psi_1^A | S^x | \psi_1^A \rangle \langle \psi_1^B | S^x | \psi_1^B \rangle + \langle \psi_1^A | S^y | \psi_1^A \rangle \langle \psi_1^B | S^y | \psi_1^B \rangle) + J_z \langle \psi_1^A | S^z | \psi_1^A \rangle \langle \psi_1^B | S^z | \psi_1^B \rangle + \text{DM terms}, \quad (4.42a)$$

$$b_{1,2} = J (\langle \psi_1^A | S^x | \psi_1^A \rangle \langle \psi_2^B | S^x | \psi_2^B \rangle + \langle \psi_1^A | S^y | \psi_1^A \rangle \langle \psi_2^B | S^y | \psi_2^B \rangle) + J_z \langle \psi_1^A | S^z | \psi_1^A \rangle \langle \psi_2^B | S^z | \psi_2^B \rangle + \text{DM terms}, \quad (4.42b)$$

and the off-diagonal matrix elements are

$$t_{AB} = J (\langle \psi_2^A | S^x | \psi_1^A \rangle \langle \psi_1^B | S^x | \psi_2^B \rangle + \langle \psi_2^A | S^y | \psi_1^A \rangle \langle \psi_1^B | S^y | \psi_2^B \rangle) + J_z \langle \psi_2^A | S^z | \psi_1^A \rangle \langle \psi_1^B | S^z | \psi_2^B \rangle + \text{DM terms}, \quad (4.43)$$

and we will neglect the Dzyaloshinskii-Moriya part ‘‘DM terms’’. Here we use a notation for the *normalized* eigenfunctions (4.21a) and (4.21b) where the site indices A and B are introduced, but we suppressed the C_2^{\parallel} quantum numbers ($\pm i$). One has to be careful, in the above equations field-fixed operators have to be used, i.e. $S^x \rightarrow S^{\parallel}$, $S^y \rightarrow S^{\perp 1}$, and $S^z \rightarrow S^{\perp 2}$. The function $f(\mathbf{k})$ in Eq. (4.40) reads

$$f(\mathbf{k}) = 1 + e^{i\mathbf{k}\cdot\mathbf{a}_1} + e^{i\mathbf{k}\cdot\mathbf{a}_2} + e^{i\mathbf{k}\cdot(\mathbf{a}_1+\mathbf{a}_2)}. \quad (4.44)$$

The eigenenergies and eigenvectors of (4.40) read

$$\omega_{\pm}^{1\rightarrow 2}(\mathbf{k}) = \varepsilon \pm t_{AB} |f(\mathbf{k})|, \quad (4.45)$$

$$\mathbf{v}_{\pm}^{1\rightarrow 2}(\mathbf{k}) = (\pm \sqrt{f^*(\mathbf{k})}, \sqrt{f(\mathbf{k})}), \quad (4.46)$$

and in the midpoint $\mathbf{k} = \mathbf{0}$ of the crystallographic BZ the function $f(\mathbf{0}) = 4$ and $\omega_{\pm}^{1\rightarrow 2}(\mathbf{0}) = \varepsilon \pm 4t_{AB}$.

Computing the quantities in Eqs. (4.41) and (4.42) with the wavefunctions (4.21) is straightforward but tiresome. Here we give the excitation energies in the limiting cases of strong field and strong single-ion anisotropy. We substitute $\mathbf{k} = \mathbf{0}$ in Eq. (4.46), and we denote $\omega_{+}^{1\rightarrow 2}(\mathbf{0})$ by $\omega_{\pi}^{1\rightarrow 2}$ and $\omega_{-}^{1\rightarrow 2}(\mathbf{0})$ by $\omega_0^{1\rightarrow 2}$ referring to the odd and even channels.

We can Taylor expand in Λ/h in the strong field limit $h \gg \Lambda \gg J, J_z$ (we set $D_z = 0$ in what follows). From the expanded spin operator components given in Eqs. (H.5) one can infer the tight-binding parameters in Eqs. (4.41) and (4.42) as $\varepsilon = h + \Lambda - 6J$, $b_{1,1} = 9J/4$, $b_{1,2} = 3J/4$, and $t_{AB} = 3(J + J_z)/4$. The excitation energies are

$$\omega_0^{1\rightarrow 2} = h + \Lambda - 9J - 3J_z, \quad (4.47a)$$

$$\omega_{\pi}^{1\rightarrow 2} = h + \Lambda - 3J + 3J_z. \quad (4.47b)$$

Perturbation theory works well for the measurements in the high-field limit. In Subsection 4.8.1 we have seen that only the π modes absorb in Faraday geometry. In ED we also have

observed the strongest absorption for the $\omega_\pi^{1\rightarrow 2}$ excitation. This is not surprising: This is the single magnon mode in the weak anisotropy limit $\Lambda \ll J, J_z$. In the absence of anisotropy $\Lambda = 0$, it is just the paramagnetic mode $\omega_\pi^{1\rightarrow 2} = h$, as can be seen in Eq. (4.47b). It is worth to compare this to the single-ion result: From Eqs. (H.4) (a)-(b) the first excitation energy is $\omega^{1\rightarrow 2} = \varepsilon_2 - \varepsilon_1 = h + \Lambda + \mathcal{O}(\Lambda^2/h)$. The difference between the perturbative and single-ion results is a mere $3(J - J_z)$ (this vanishes for isotropic exchange $J = J_z$, and in the experiments is also small). This also explains why the single-ion model works so well for large fields, $h \gg \Lambda, J, J_z$ (see the experimental points in Fig. 4.5(a)).

We can also expand in h/Λ in the strong anisotropy limit $\Lambda \gg h, J, J_z$. From the expanded spin operator components given in H.2 one can infer the tight-binding parameters in Eqs. (4.41) and (4.42) as $\varepsilon = 2h - 8J$, $b_{1,1} = +J$, $b_{1,2} = -J$, and $t_{AB} = J + (1/4)J_z$. And the excitation energies are

$$\omega_0^{1\rightarrow 2} = 2h - 12J - J_z, \quad (4.48a)$$

$$\omega_\pi^{1\rightarrow 2} = 2h - 4J + J_z. \quad (4.48b)$$

The single-ion result Eqs. (H.1)(a)-(b) shows an excitation energy of $\omega^{1\rightarrow 2} = \varepsilon_2 - \varepsilon_1 = 2h + \mathcal{O}(h^2/\Lambda)$ to be compared to $\omega_\pi^{1\rightarrow 2}$. The difference between the perturbative and single-ion results is now larger $-4J + J_z$, but still moderate (compared to Λ or the fields h used in the experiment).

4.9 Summary

In this chapter we developed a theory of the non-reciprocal directional dichroism in the high temperature (paramagnetic) phase of the multiferroic $\text{Sr}_2\text{CoSi}_2\text{O}_7$. Magneto-chiral dichroism was observed by our experimental collaborators in this material for the excitations of the $S = 3/2$ spin of the Co^{2+} ion up to 100K –an order of magnitude larger than the Néel temperature $T_N = 7$ K. The temperature dependence of the resonance positions, their intensities, and the sign of the dichroism for the different spin modes are well described by exact diagonalization on a small 4-site cluster of $S = 3/2$ spins.

To elucidate the physics of the system we analyzed a simple model consisting of one $S = 3/2$ spin in a magnetic field and a strong easy-plane anisotropy via group theory. Oxygen ions coordinate the spin tetrahedrally and give rise to an electric polarization \mathbf{P} expressed by spin quadrupoles. Both the magnetization \mathbf{M} and polarization \mathbf{P} couple to the THz radiation. Finite magnetoelectric susceptibility arises if the components of \mathbf{M} and \mathbf{P} transform the same way under the combined symmetry of the tetrahedron and the spin model containing the external field.

Our most interesting finding turned out to be that the time-reversed (antiunitary) elements of the magnetic symmetry group can constrain the matrix elements of \mathbf{M} and \mathbf{P} to real or purely imaginary values, having a profound effect on the magnetoelectric susceptibility. Fig. 4.5 shows that in high fields and low temperatures, when the gap between the two lowest levels $\varepsilon_2 - \varepsilon_1 \leq k_B T$, the magnetic dipolar transition from the ground state $|1\rangle \rightarrow |2\rangle$ dominates the NDD spectrum.

The two inequivalent Co^{2+} ions in the centers of the alternately oriented tetrahedra in the unit cell interact with (slightly anisotropic) Heisenberg exchanges. Incorporating these interactions perturbatively, and considering the two-ion unit cell helped us refine the single-ion picture, giving a better agreement with the experiments and the exact diagonalization.

Chapter 5

Thesis statements

Here I enumerate my major results.

1. Using the Luttinger-Tisza method I constructed the ground state (zero temperature) phase diagram of the classical isotropic Heisenberg model up to third neighbor interactions of arbitrary sign on the face-centered cubic lattice. I gave a detailed analysis of the commensurate phases: I showed that multiple-Q orders lead to non-collinear or even non-coplanar orders, and in the case of the Type III antiferromagnet, a chiral ground state. I demonstrated that the introduction of the third neighbor interaction leads to a qualitatively new feature of the model: Incommensurate spin spirals with propagation vectors along special directions in the Brillouin zone appear [102].
2. I showed that at triple points and special phase boundaries of the phase diagram of the third neighbor classical isotropic Heisenberg model extended ground state manifolds appear in Fourier space: Three one dimensional manifolds and one two dimensional manifold. At these points I expressed the Hamiltonian as a sum of complete squares of spins over appropriate finite motifs tessellating the lattice. Thereby I explicitly constructed large classes of ground states and explained the degeneracy of the manifolds. These families of exact ground state configurations consist of, among others, frustratingly interacting ferromagnetic chains and randomly stacked ferro- or antiferromagnetic planes [102].
3. I gave a recipe for constructing classical isotropic Heisenberg models on Bravais lattices possessing codimension-one ground state manifolds (i.e. curves in two, and spin spiral surfaces in three dimensions). The models are either fine-tuned or have a few free parameters: In the latter case I showed that varying the parameters allows for topological (Lifshitz) transitions. For the face-centered and simple cubic lattices I calculated the low temperature free energy and demonstrated that the thermal or quantum fluctuations select commensurate phases on the spin spiral surfaces by the order by disorder mechanism [84].
4. I constructed a one-spin model that describes the non-reciprocal directional dichroism of the magnetoelectric multiferroic åkermanite crystal $\text{Sr}_2\text{CoSi}_2\text{O}_7$ in its paramagnetic phase under strong external fields. The model takes into account the external field, the strong in-plane anisotropy, and the electric polarization induced by the metal-ligand hybridization mechanism. Despite its simplicity the model gives

the field dependence of the excitation energy correctly. Based on a group theoretical analysis I derived the magnetoelectric selection rules. Promoting the single-ion model to a lattice and treating interactions perturbatively I also explained the success of the one-ion approach in the paramagnetic phase [145].

5. Ordinary selection rules guarantee that matrix elements of perturbing operators of a symmetric Hamiltonian vanish, provided these operators transform according to certain irreducible representations of the group of the Hamiltonian. I generalized this concept and showed that (in magnetic models of arbitrary spin length and arbitrary magnetic symmetry) the antiunitary symmetry elements of the group of the Hamiltonian connect the real and imaginary parts of matrix elements of operators. As a special case: If a two-fold rotation together with time reversal is a symmetry of the Hamiltonian, and the perturbing operators are even (odd) under this symmetry their matrix elements are real (pure imaginary). Applying this result to the magnetization and polarization operators in the case of $\text{Sr}_2\text{CoSi}_2\text{O}_7$ led to new selection rules as confirmed by the magneto-optical absorption measurements in the paramagnetic [145] and ordered [146] phases.

Publications related to the thesis statements

1. [102] Péter Balla, Yasir Iqbal, and Karlo Penc
Degenerate manifolds, helimagnets, and multi-Q chiral phases in the classical Heisenberg antiferromagnet on the face-centered-cubic lattice.
Physical Review Research **2**, 043278 (2020)
2. [84] Péter Balla, Yasir Iqbal, and Karlo Penc
Affine lattice construction of spiral surfaces in frustrated Heisenberg models
Physical Review B **100**, 140402(R) (2019)
3. [145] J. Virok, U. Nagel, T. Rődöm, D. G. Farkas, P. Balla, D. Szaller, V. Kocsis, Y. Tokunaga, Y. Taguchi, Y. Tokura, B. Bernáth, D. L. Kamenskyi, I. Kézsmárki, S. Bordács, and K. Penc
Directional dichroism in the paramagnetic state of multiferroics: A case study of infrared light absorption in $\text{Sr}_2\text{CoSi}_2\text{O}_7$ at high temperatures
Physical Review B **99**, 014410 (2019)
4. [146] J. Vít, J. Virok, L. Peedu, T. Rődöm, U. Nagel, V. Kocsis, Y. Tokunaga, Y. Taguchi, Y. Tokura, I. Kézsmárki, P. Balla, K. Penc, J. Romhányi, and S. Bordács
In Situ Electric-Field Control of THz Nonreciprocal Directional Dichroism in the Multiferroic $\text{Ba}_2\text{CoGe}_2\text{O}_7$
Physical Review Letters **127**, 157201 (2021)

Further publication

5. [147] A. Szilva, P. Balla, O. Eriksson, G. Zaránd, and L. Szunyogh

Universal distribution of magnetic anisotropy of impurities in ordered and disordered nanograins

Physical Review B **91**, 134421 (2015)

Appendix A

Fourier transform conventions and relations

In this Appendix we collect our Fourier transform conventions, derive the Fourier form of a spin Hamiltonian and some useful relations between real and Fourier space.

We adopt the following convention for the Fourier transform of the spins on a lattice:

$$\mathbf{S}_{\mathbf{q}} = \frac{1}{N} \sum_i \mathbf{S}_i e^{i\mathbf{q}\cdot\mathbf{R}_i}, \quad \mathbf{S}_i = \sum_{\mathbf{q}\in\text{BZ}} \mathbf{S}_{\mathbf{q}} e^{-i\mathbf{q}\cdot\mathbf{R}_i}, \quad (\text{A.1})$$

and in the following sums i, j run through the unit cells of the crystal, \mathbf{q}, \mathbf{q}' run over the Brillouin zone (BZ), and N is the number of unit cells, taken to be very large. If we chose $1/\sqrt{N}$ in both formulas we would have a unitary transform. We will extensively use the following form of the *lattice sum* [7]:

$$\sum_i e^{i(\mathbf{q}-\mathbf{q}')\cdot\mathbf{R}_i} = N\delta_{\mathbf{q},\mathbf{q}'}, \quad (\text{A.2})$$

where we have restricted ourselves to the first BZ. Of course a similar formula works the other way around: $\sum_{\mathbf{q}} e^{i\mathbf{q}\cdot(\mathbf{R}_i-\mathbf{R}_j)} = N\delta_{ij}$.

A basic property of the complex amplitudes is

$$\mathbf{S}_{\mathbf{q}} = \mathbf{S}_{-\mathbf{q}}^*, \quad (\text{A.3})$$

which is the consequence of the reality of the real space spins $\mathbf{S}_i = \mathbf{S}_i^*$, and the definition (A.1). The *global/average spin length constraint* in Fourier space reads:

$$\sum_i |\mathbf{S}_i|^2 = N \Leftrightarrow \sum_{\mathbf{q}\in\text{BZ}} |\mathbf{S}_{\mathbf{q}}|^2 = 1, \quad (\text{A.4})$$

which is just the manifestation of the isometric property of the Fourier transform (up to the factor N). To prove it we substitute the definition (A.1) in (A.4) and use the lattice sum (A.2) and the reality condition (A.3):

$$N = \sum_i |\mathbf{S}_i|^2 = \sum_i \sum_{\mathbf{q}, \mathbf{q}'} \mathbf{S}_{\mathbf{q}} \cdot \mathbf{S}_{\mathbf{q}'} e^{-i(\mathbf{q}+\mathbf{q}')\cdot\mathbf{R}_i} = N \sum_{\mathbf{q}, \mathbf{q}'} \mathbf{S}_{\mathbf{q}} \cdot \mathbf{S}_{\mathbf{q}'} \delta_{\mathbf{q}, -\mathbf{q}'} = N \sum_{\mathbf{q}} |\mathbf{S}_{\mathbf{q}}|^2, \quad (\text{A.5})$$

the other direction works similarly.

The *Heisenberg Hamiltonian* is given as

$$\mathcal{H} = \sum_{\langle i,j \rangle} J_{ij} \mathbf{S}_i \cdot \mathbf{S}_j = \frac{1}{2} \sum_{i,\delta} J_\delta \mathbf{S}_i \cdot \mathbf{S}_{i+\delta}, \quad (\text{A.6})$$

where with $\langle i,j \rangle$ we indicate that we sum each bond once, $\delta = \mathbf{R}_j - \mathbf{R}_i$ is a lattice separation vector. We have used translational invariance $J_{ij} \equiv J(\mathbf{R}_j - \mathbf{R}_i) \equiv J_\delta$, and the factor $1/2$ compensates for the double counting of the bonds. In order to write the Hamiltonian in Fourier space we define the Fourier transform of the exchange as

$$J(\mathbf{q}) = \frac{1}{2} \sum_{\delta} J_\delta e^{-i\mathbf{q}\cdot\delta}, \quad (\text{A.7})$$

and we will prove

$$\mathcal{H} = N \sum_{\mathbf{q}} J(\mathbf{q}) \mathbf{S}_{\mathbf{q}} \cdot \mathbf{S}_{-\mathbf{q}}. \quad (\text{A.8})$$

We substitute the definition (A.1) in (A.6), apply the definition of (A.7) and use the lattice sum (A.2):

$$\mathcal{H} = \frac{1}{2} \sum_{i,\delta} J_\delta \mathbf{S}_i \cdot \mathbf{S}_{i+\delta} = \frac{1}{2} \sum_{i,\delta} \sum_{\mathbf{q},\mathbf{q}'} J_\delta \mathbf{S}_{\mathbf{q}} \cdot \mathbf{S}_{\mathbf{q}'} e^{-i(\mathbf{q}+\mathbf{q}')\cdot\mathbf{R}_i} e^{-i\mathbf{q}'\cdot\delta} = \quad (\text{A.9})$$

$$= \sum_{\mathbf{q},\mathbf{q}'} \mathbf{S}_{\mathbf{q}} \cdot \mathbf{S}_{\mathbf{q}'} \sum_i e^{-i(\mathbf{q}+\mathbf{q}')\cdot\mathbf{R}_i} \frac{1}{2} \sum_{\delta} J_\delta e^{-i\mathbf{q}'\cdot\delta} = \quad (\text{A.10})$$

$$= N \sum_{\mathbf{q},\mathbf{q}'} J(\mathbf{q}') \mathbf{S}_{\mathbf{q}} \cdot \mathbf{S}_{\mathbf{q}'} \delta_{\mathbf{q},-\mathbf{q}'} = N \sum_{\mathbf{q}} J(\mathbf{q}) \mathbf{S}_{\mathbf{q}} \cdot \mathbf{S}_{-\mathbf{q}}, \quad (\text{A.11})$$

where in the last step we made a substitution in the dummy variables $\mathbf{q}' \rightarrow \mathbf{q}$.

Next we examine the consequences of the *local length constraints* in Fourier space:

$$|\mathbf{S}_i|^2 = 1, \forall i \Rightarrow \sum_{\mathbf{q}} \mathbf{S}_{\mathbf{q}} \cdot \mathbf{S}_{\mathbf{q}-\mathbf{q}} = \delta_{\mathbf{q}',\mathbf{0}}. \quad (\text{A.12})$$

In order to prove the implication above we substitute the Fourier decomposition Eq. (A.1) in the local length constraints $|\mathbf{S}_i|^2 = 1$:

$$\sum_{\mathbf{q},\mathbf{q}''} \mathbf{S}_{\mathbf{q}} \cdot \mathbf{S}_{\mathbf{q}''} e^{-i(\mathbf{q}+\mathbf{q}'')\cdot\mathbf{R}_i} = |\mathbf{S}_i|^2 = 1 \forall i, \quad (\text{A.13})$$

this is a set of N equations. We perform a Fourier transform by multiplying the i -th equation by $e^{i\mathbf{q}'\cdot\mathbf{R}_i}$ and sum over i :

$$\sum_i \sum_{\mathbf{q},\mathbf{q}''} \mathbf{S}_{\mathbf{q}} \cdot \mathbf{S}_{\mathbf{q}''} e^{-i(\mathbf{q}+\mathbf{q}''-\mathbf{q}')\cdot\mathbf{R}_i} = \sum_i e^{i\mathbf{q}'\cdot\mathbf{R}_i}. \quad (\text{A.14})$$

Performing the sums with the aid of (A.2) yields

$$\sum_{\mathbf{q}} \mathbf{S}_{\mathbf{q}} \cdot \mathbf{S}_{\mathbf{q}-\mathbf{q}} = \delta_{\mathbf{q}',\mathbf{0}}, \quad (\text{A.15})$$

which is true for every configuration, even for the ones on \mathcal{M}_{GS} , resulting Eqs. (2.13–2.14).

Appendix B

Phase boundaries of the J_1 - J_2 - J_3 model

We give the analytical form of the phase boundaries and the type of phase transitions of the $J_1 - J_2 - J_3$ Heisenberg model on the face-centered cubic lattice in Table B.1 below.

Table B.1: Equations of phase boundaries between the phases (shown in Fig. 2.2) with ordering vectors \mathbf{Q}_A and \mathbf{Q}_B (see Fig. 2.3) are presented in the third column, with the order of the corresponding transition in the fourth column. The incommensurate ordering vectors are optimized according to Eqs. (2.44–2.46).

\mathbf{Q}_A	\mathbf{Q}_B	$\varepsilon(\mathbf{Q}_A) = \varepsilon(\mathbf{Q}_B)$	Order
$\Gamma(0, 0, 0)$	$\Delta(q_\Delta, 0, 0)$	$J_1 + J_2 + 6J_3 = 0$	2nd
$\Gamma(0, 0, 0)$	$\Lambda(q_\Lambda, q_\Lambda, q_\Lambda)$	$J_1 + J_2 + 6J_3 = 0$	2nd
$X(1, 0, 0)$	$\Delta(q_\Delta, 0, 0)$	$J_1 - J_2 - 2J_3 = 0$	2nd
$L(\frac{1}{2}, \frac{1}{2}, \frac{1}{2})$	$\Lambda(q_\Lambda, q_\Lambda, q_\Lambda)$	$J_1 + J_2 - 2J_3 = 0$	2nd
$\Gamma(0, 0, 0)$	$X(1, 0, 0)$	$J_1 + 2J_3 = 0$	1st
$\Gamma(0, 0, 0)$	$W(1, \frac{1}{2}, 0)$	$4J_1 + J_2 + 4J_3 = 0$	1st
$\Gamma(0, 0, 0)$	$L(\frac{1}{2}, \frac{1}{2}, \frac{1}{2})$	$J_1 + J_2 + 2J_3 = 0$	1st
$X(1, 0, 0)$	$L(\frac{1}{2}, \frac{1}{2}, \frac{1}{2})$	$J_1 - 3J_2 + 2J_3 = 0$	1st
$\Delta(q_\Delta, 0, 0)$	$L(\frac{1}{2}, \frac{1}{2}, \frac{1}{2})$	$J_1^2 - J_1J_2 - 2J_2^2 - 6J_2J_3 + 12J_3^2 = 0$	1st
$\Delta(q_\Delta, 0, 0)$	$\Lambda(q_\Lambda, q_\Lambda, q_\Lambda)$	$3J_2 - 4J_3 = 0$	1st
$\Gamma(0, 0, 0)$	$\Sigma(q_\Sigma, q_\Sigma, 0)$	$19J_1 + 6J_2 + 46J_3 + 8\sqrt{6J_1^2 + 5J_1J_2 + 2J_2^2} = 0$	1st
$X(1, 0, 0)$	$\Sigma(q_\Sigma, q_\Sigma, 0)$	$-11J_1 + 10J_2 - 14J_3 + 8\sqrt{2J_1^2 - 3J_1J_2 + 2J_2^2} = 0$	1st
$L(\frac{1}{2}, \frac{1}{2}, \frac{1}{2})$	$\Sigma(q_\Sigma, q_\Sigma, 0)$	$\varepsilon(\mathbf{Q}_L) = \varepsilon(\mathbf{Q}_\Sigma)^1$	1st
$W(1, \frac{1}{2}, 0)$	$\Sigma(q_\Sigma, q_\Sigma, 0)$	$\varepsilon(\mathbf{Q}_W) = \varepsilon(\mathbf{Q}_\Sigma)^2$	1st

¹The equation for the phase boundary $\varepsilon(\mathbf{Q}_L) = \varepsilon(\mathbf{Q}_\Sigma)$ is:

$$J_1^4 + 3J_1^3J_2 - 2J_1^2J_2^2 - 12J_1J_2^3 - 8J_2^4 - 64J_1^3J_3 + 58J_1^2J_2J_3 + 104J_1J_2^2J_3 - 24J_2^3J_3 + 376J_1^2J_3^2 - 28J_1J_2J_3^2 - 728J_2^2J_3^2 - 768J_1J_3^3 - 264J_2J_3^3 + 528J_3^4 = 0.$$

²The equation for the phase boundary $\varepsilon(\mathbf{Q}_W) = \varepsilon(\mathbf{Q}_\Sigma)$ is:

$$(J_2 - 4J_3)(J_1^3 + 2J_1^2J_2 - 4J_1J_2^2 - 8J_2^3 - 50J_1^2J_3 + 120J_1J_2J_3 - 72J_2^2J_3 + 172J_1J_3^2 - 232J_2J_3^2 - 152J_3^3) = 0.$$

Appendix C

Some notions of chirality for non-coplanar states

We have seen in Section 2.5 that a commensurate ordering can be non-collinear or even non-coplanar if we choose multiple arms of the stars of the ordering vector on the fcc lattice. Such non-coplanar (or triple-Q) states can be constructed e.g. by choosing all the ξ , η and ζ finite in Eq. (2.21). We can also make the analogous choice in Eq. (2.28) or Eq. (2.41). Unfortunately non-coplanar states are rarely observed in isotropic systems, since *order by disorder* (either quantum or thermal) mechanisms favor collinear (or coplanar) orderings [17]. Nonetheless, examples of non-collinear or non-coplanar orders can be found in extended models including ring-exchanges on Bravais lattices, e.g. the tetrahedral phase on the triangular lattice [148, 149, 150]. The presence of longer range exchanges on non-Bravais lattices can also result non-coplanar orders, e.g. the cuboctahedral orders on the kagome lattice [151, 152]. *Disorder* mechanisms can select non-collinear orders [18], so the fate of these states depends on further details.

Such non-coplanar states can show *chirality*: The ordering can manifest itself in either a left handed or a right handed pattern. In the following we recall some notions of chirality scattered in the literature, and we analyze the commensurate and non-coplanar orders found in Section 2.5 according to them.

C.1 Scalar chirality

A non-coplanar magnetic order has a finite *scalar chirality* [99, 153, 154, 115], which we define on an oriented triangular plaquette with vertices ABC as

$$\chi_{ABC} = \mathbf{S}_A \cdot (\mathbf{S}_B \times \mathbf{S}_C), \quad (\text{C.1})$$

i.e. as the *signed* volume of the parallelepiped spanned by the three spins sitting on these vertices. By this definition the finite value of the scalar chirality on a triangular plaquette is equivalent to a non-coplanar spin configuration. The faces of elementary octahedra on the fcc lattice define the triangular plaquettes and the octahedra being edge-sharing no triangle is shared between two octahedra (see Fig. 2.1(d)), therefore we can use the right hand rule for the outward pointing normals on the faces of the octahedra to define the orientation ABC of the vertices. All the commensurate phases found in Section 2.5 can be chiral in the above sense if we use enough arms of the star of the ordering vector, see Eq. (2.21), Eq. (2.28), and Eq. (2.41).

C.1.1 The $X(1, 0, 0)$ phase, Type I

If we choose all the ξ , η , and ζ in Eq. (2.23) finite, then the resulting Type I order is non-coplanar and it is depicted in Fig. 2.4(a). The scalar chirality χ is then finite with $|\chi| = |4\xi\eta\zeta|$ on *all* faces of *every* tetrahedron, and the sign alternates on the two types of tetrahedra.

C.1.2 The $L(\frac{1}{2}, \frac{1}{2}, \frac{1}{2})$ phase, Type II

In this phase the spins on antipodal points of elementary octahedra point in opposite directions as depicted in Fig. 2.4(b). Consequently the scalar chirality is equal on all six faces of a chosen octahedron. Having four types of octahedra we have four different values of scalar chiralities in the lattice for a non-coplanar configuration.

C.1.3 The $W(1, \frac{1}{2}, 0)$ phase, Type III

We evaluated the scalar chirality χ directly in the triple-Q phase (when none of the ξ , η , ζ is zero in Eq. (2.41)) and show the result in Fig. C.1. The chirality equals on the faces of every elementary tetrahedron, but we have three different types of tetrahedra: On one fourth of the tetrahedra the chiralities alternate between the $\chi = 4\xi\eta\zeta$ and $\chi = -4\xi\eta\zeta$ and on the remaining tetrahedra the chirality is zero. The chirality changes sign when translated by the $(\pm 1, 0, 0)$, $(0, \pm 1, 0)$, and $(0, 0, \pm 1)$ vectors, and it is invariant when translated by $(1, 1, 0)$ or equivalent vectors.

C.2 Chiral enantiomers

Another notion of chirality closely related to handedness is the following [99]: For a given spin pattern apply a mirror plane to the configuration that is a symmetry of the underlying lattice. If the resulting spin configuration cannot be transformed back to the original spin pattern by any *proper* space group operation to the original one, we call the configuration *chiral*.¹ This notion of chirality is the direct generalization of the concept of chirality introduced for molecules: A molecule is chiral if it cannot be rotated to its mirror image. These pairs of reflection-related partners are called enantiomers, or enantiomorphic/chiral partners. In the following we elaborate the above concept and analyze the commensurate orders found on the fcc lattice according to it.

A space group operation (either proper or improper) is denoted by $g_\delta \equiv \{\mathbf{G}|\delta\}$ and acts on a lattice point \mathbf{R}_i as:

$$\mathbf{R}'_i = g_\delta \mathbf{R}_i \equiv \{\mathbf{G}|\delta\} \mathbf{R}_i = \mathbf{G} \cdot \mathbf{R}_i + \delta, \quad (\text{C.2})$$

¹About terminology: In three-dimensional space a rotation is dubbed proper (an element of $SO(3)$) if it does not change the orientation of a basis. Point group operations that do not preserve orientation are either called roto-reflections or improper rotations, this includes the inversion $I : \mathbf{R}_i \rightarrow -\mathbf{R}_i$, the orthogonal group is the direct product $O(3) = SO(3) \times \{E, I\}$, with E being the identity. In other words improper rotations are the elements of $O(3) \setminus SO(3)$. We also note that every Bravais lattice is inversion symmetric by construction.

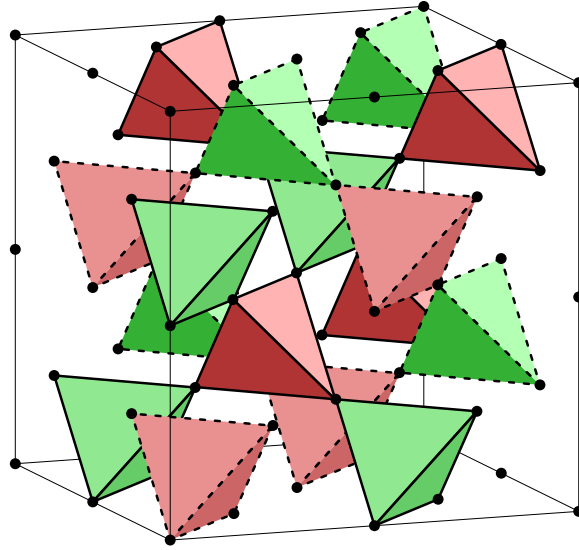


Figure C.1: Tetrahedra with triangular faces having nonvanishing scalar chirality χ in the triple- \mathbf{Q} $W(1, \frac{1}{2}, 0)$ state are shown within a 32 site cubic cell defined by the lattice vectors $(2, 0, 0)$, $(0, 2, 0)$, and $(0, 0, 2)$ on the fcc lattice. The red and green color depict triangles with equal size but opposite signs of χ . The lattice of the corner-sharing alternating red and green tetrahedra corresponds to two interpenetrating pyrochlore lattices, the two pyrochlore lattices are shown by solid and dashed lines.

where \mathbf{G} is the $O(3)$ matrix of a point group element followed by a lattice translation δ . On a spin –since it is an axial vector– the point group element acts as $\mathbf{S}' = \mathbf{G}^A \cdot \mathbf{S}$, where $\mathbf{G}^A = (\det \mathbf{G})\mathbf{G}$ is the axial-vector representative of the group element g (it agrees with \mathbf{G} for proper rotations and it is $-\mathbf{G}$ for improper rotations). The inverse of a space group operation is $g_\delta^{-1} = \{\mathbf{G}^{-1} | -\mathbf{G}^{-1} \cdot \delta\}$. The transformation rule for a spin configuration reads:

$$\mathbf{S}'_{\mathbf{R}_i} = \{\mathbf{G}|\delta\}\mathbf{S}_{\mathbf{R}_i} = \mathbf{G}^A \cdot \mathbf{S}_{g_\delta^{-1}\mathbf{R}_i}. \quad (\text{C.3})$$

This is the so-called *active* view of a transformation: We grab the spin pattern together with the lattice points and transform them as a rigid body.

Any improper rotation is the product of a proper rotation and inversion, e.g. a mirror plane with normal $\hat{\mathbf{n}}$ is a composition of a twofold rotation around the axis $\hat{\mathbf{n}}$ and inversion. And inversion acts in spin space as the identity, $I : \mathbf{S} \rightarrow \mathbf{S}$. Every Bravais-lattice is inversion-symmetric, hence instead of a mirror plane we can use inversion to define chirality. This definition has a practical advantage: The spins are invariant under inversion. Now we can formulate chirality for spin patterns defined on Bravais-lattices: Let us apply inversion to a spin pattern $\mathbf{S}_{\mathbf{R}_i}$:

$$\mathbf{S}'_{\mathbf{R}_i} = \{I|0\}\mathbf{S}_{\mathbf{R}_i} = \mathbf{S}_{-\mathbf{R}_i}. \quad (\text{C.4})$$

If there is no *proper* space group element $\{\mathbf{G}|\delta\}$, with $\mathbf{G} \in SO(3)$, that can transform back the spin pattern to the original one in Eq. (C.4),

$$\{\mathbf{G}|\delta\}\mathbf{S}'_{\mathbf{R}_i} \neq \mathbf{S}_{\mathbf{R}_i}, \quad (\text{C.5})$$

then we call the pattern *chiral*. Here we have considered the case when the mirror plane contains a lattice point, i.e. the inversion used instead of the mirror plane is centered at that point, but for other cases –when for example the mirror plane is the perpendicular bisector plane of a bond (and consequently the inversion center is the midpoint of the bond)– the above discussion is still valid with the proper modifications.

Now we discuss if the non-coplanar but commensurate spin configurations discussed in Section 2.5 are chiral in the above sense or not. The spin pattern of the $X(1, 0, 0)$ and $L(\frac{1}{2}, \frac{1}{2}, \frac{1}{2})$ phases remains intact when inverted about a lattice site (see Fig. 2.4(a) and (b)). Therefore *neither* of these states is chiral in the sense defined above.

But the case of the $W(1, \frac{1}{2}, 0)$ considered in Subsection 2.5.4 phase is *different*. In the original paper (see Section D and Appendix C of [102]) we have analyzed the effect of translations and inversion on the $W(1, \frac{1}{2}, 0)$ configurations and found that there are two disjoint sets of ground states related by inversion: i.e. we have chiral partners (or enantiomorphic pairs).

C.3 Time-reversal and chirality

In Refs. [151, 155] yet another definition of chirality is given: If time reversal (named “spin inversion” in Refs. [151, 155]) applied to a spin configuration cannot be changed back using a proper $SO(3)$ rotation acting on the spins, then the pattern is called chiral (we will use this notion of chirality below).

By this definition any non-coplanar and commensurate $X(1, 0, 0)$, $L(\frac{1}{2}, \frac{1}{2}, \frac{1}{2})$, and $W(1, \frac{1}{2}, 0)$ spin configurations are chiral. If we allow translations besides proper rotations, the $L(\frac{1}{2}, \frac{1}{2}, \frac{1}{2})$ and $W(1, \frac{1}{2}, 0)$ orderings are not chiral, since they are invariant under time reversal followed by a translation. The cuboc orders considered in Refs. [151, 152] are chiral by means of the time-reversal symmetry considered here [155], and are also chiral by the definition given in Subsection C.2, since time reversal and spatial inversion about the center of a hexagon is equivalent in this case: Both of them flip all the spins and this flipping cannot be changed back by any proper space group operation.

Appendix D

Tables for the affine construction in two and three dimensions

Here we give the allowed δ^* vectors needed for the affine construction described in Chapter 3 for all the Bravais lattices in two (Table D.1) and three dimensions (Table D.2). We used the tables of the Bilbao Crystallographic Server[133].

Table D.1: Allowed δ^* vectors for the affine construction described in Chapter 3 for all the two dimensional Bravais lattices. The first column gives the lattice system, the second one the centering of the Bravais lattice, the third one the symbol of the space group of the Bravais lattice, the fourth one gives its number, the fifth one the point group of the lattice (which is isomorphic to the point group of all the allowed δ^* 's), the sixth column gives the allowed δ^* 's (in primitive lattice vector units, for details of the coordinate system consult[133]), and the last column gives the multiplicity of the δ^* 's (if they are viewed as Wyckoff positions).

Lattice System	Bravais Lattice	Symbol	No.	\mathcal{G}	Allowed δ^* -s	Mult.
Oblique		p2	2	C_2	All four points valid.	1
Rectangular	Simple	p2mm	6	D_2	All four points valid.	1
	Centered	c2mm	9		$\mathbf{0}, (0, \frac{1}{2})$	2
Square		p4mm	11	D_4	$\mathbf{0}, (\frac{1}{2}, \frac{1}{2})$	1
Hexagonal		p6mm	17	D_6	$\mathbf{0}$	1

Table D.2: Allowed δ^* vectors for the affine construction described in Chapter 3 for all the three dimensional Bravais lattices. The first column gives the lattice system, the second one the centering of the Bravais lattice, the third one the symbol of the space group of the Bravais lattice, the fourth one gives its number, the fifth one the point group of the lattice (which is isomorphic to the point group of all the allowed δ^* 's), the sixth column gives the allowed δ^* 's (in primitive lattice vector units, for details of the coordinate system consult[133]), and the last column gives the multiplicity of the δ^* 's (if they are viewed as Wyckoff positions).

Lattice System	Bravais Lattice	Symbol	No.	\mathcal{G}	Allowed δ^* -s	Multiplicity
Triclinic		$P\bar{1}$	2	C_i	All eight points valid.	1
Monoclinic	Simple	$P2/m$	10	C_{2h}	All eight points valid.	1
	Base-centered	$C2/m$	12		$\mathbf{0}, (0, \frac{1}{2}, 0), (0, 0, \frac{1}{2}), (0, \frac{1}{2}, \frac{1}{2})$	2
Orthorhombic	Simple	$Pmmm$	47	D_{2h}	All eight points valid.	1
	Base-centered	$Cmmm$	65		$\mathbf{0}, (\frac{1}{2}, 0, 0), (\frac{1}{2}, 0, \frac{1}{2}), (0, 0, \frac{1}{2})$	2
	Face-centered	$Fmmm$	69		$\mathbf{0}, (0, 0, \frac{1}{2})$	4
	Body-centered	$Immm$	71		$\mathbf{0}, (0, \frac{1}{2}, \frac{1}{2}), (\frac{1}{2}, \frac{1}{2}, 0), (\frac{1}{2}, 0, \frac{1}{2})$	2
Tetragonal	Simple	$P4/mmm$	123	D_{4h}	$\mathbf{0}, (0, 0, \frac{1}{2}), (\frac{1}{2}, \frac{1}{2}, 0), (\frac{1}{2}, \frac{1}{2}, \frac{1}{2})$	1
	Body-centered	$I4/mmm$	139		$\mathbf{0}, (0, 0, \frac{1}{2})$	2
Rhombohedral		$R\bar{3}m$	166	D_{3d}	$\mathbf{0}, (0, 0, \frac{1}{2})$	3
Hexagonal		$P6/mmm$	191	D_{6h}	$\mathbf{0}, (0, 0, \frac{1}{2})$	1
Cubic	Simple	$Pm\bar{3}m$	221	O_h	$\mathbf{0}, (\frac{1}{2}, \frac{1}{2}, \frac{1}{2})$	1
	Face-centered	$Fm\bar{3}m$	225		$\mathbf{0}, (\frac{1}{2}, \frac{1}{2}, \frac{1}{2})$	4
	Body-centered	$Im\bar{3}m$	229		$\mathbf{0}$	2

Appendix E

Low temperature free energy of spin spirals

Here we wish to calculate the low temperature free energy of a fluctuating single spin spiral to find the states selected by thermal fluctuations. We follow [20] and especially its supplement here. Caveat: This appendix is very technical and formula heavy, and is basically an expanded and more down-to-earth version of the above mentioned supplement.

We start with the Hamiltonian

$$\mathcal{H} = \frac{1}{2} \sum_{i,j} J_{ij} \mathbf{S}_i \cdot \mathbf{S}_j, \quad (\text{E.1})$$

and assume that it has a degenerate ground state manifold (denoted by \mathcal{M}_{GS} , and having ground state energy $\mathcal{E}_0 = J(\mathbf{Q})$, this quantity is constant on the manifold) consisting of spin spirals of propagation vectors \mathbf{Q} parametrizing the manifold. The free energy by definition is

$$\mathcal{F}(\mathbf{Q}) = \mathcal{E}_0 - T\mathcal{S}(\mathbf{Q}), \quad (\text{E.2})$$

with temperature T (which we will assume to be small) and entropy $\mathcal{S}(\mathbf{Q})$, and the latter is explicitly \mathbf{Q} dependent, and the thermal order by disorder effect is driven by the difference of entropies of different states. The above free energy can be calculated by

$$\mathcal{F} = -\frac{1}{\beta} \ln \mathcal{Z}, \quad (\text{E.3})$$

where $\beta = 1/T$ is the inverse temperature and \mathcal{Z} is the partition sum defined by

$$\mathcal{Z} = \int \prod_i d\Omega_i e^{-\beta\mathcal{H}(\{\mathbf{S}_i\})}, \quad (\text{E.4})$$

and $d\Omega_i$ is the measure on the unit sphere of the i 'th spin. In what follows we assume a spiral ground state and calculate the fluctuations above that state.

The model being isotropic without loss of generality we assume the ground state spin spiral lying in the xy -plane. We denote the ground state configuration by $\bar{\mathbf{S}}_i$ for a spiral with ordering vector \mathbf{Q} :

$$\bar{\mathbf{S}}_i = (\bar{S}_i^x, \bar{S}_i^y, 0) = (\cos(\mathbf{Q} \cdot \mathbf{R}_i), \pm \sin(\mathbf{Q} \cdot \mathbf{R}_i), 0), \quad (\text{E.5})$$

and \pm corresponds to the two chiralities, we will use the $+$ sign in applications. We parametrize the spin deviations from the ground state as

$$\mathbf{S}_i = \bar{\mathbf{S}}_i + \delta\mathbf{S}_i = \boldsymbol{\rho}_i + \bar{\mathbf{S}}_i \sqrt{1 - \rho_i^2}, \quad \bar{\mathbf{S}}_i \perp \boldsymbol{\rho}_i, \quad (\text{E.6})$$

where $\boldsymbol{\rho}_i$ and $\bar{\mathbf{S}}_i \sqrt{1 - \rho_i^2}$ describe the transverse and longitudinal fluctuations, respectively. This parametrization automatically satisfies the spin-length constraint $|\mathbf{S}_i|^2=1$ (it is important to keep the exact length constraint at this point). Soon we will assume, that $\rho_i^2 \ll 1$ are small, but at this point they are arbitrary points in the 3D unit ball: $\rho_i^2 \leq 1$.

Momentarily we drop the site indices for simplicity. With real η and χ we can write $\boldsymbol{\rho}$ as:

$$\boldsymbol{\rho} = \hat{\mathbf{z}}\eta + (\hat{\mathbf{z}} \times \bar{\mathbf{S}})\chi = (-\bar{S}^y \chi, \bar{S}^x \chi, \eta), \quad (\text{E.7})$$

with $\hat{\mathbf{z}}$ being the unit vector in the z -direction. Since $\rho^2 = \eta^2 + \chi^2 \leq 1$ the domain of the parameters (η, χ) is the unit disk. With this parametrization we can describe the hemisphere with "north pole" at the tip of $\bar{\mathbf{S}}$. From this form it is seen that χ describes the in-plane fluctuations and η the out-of plane ones. Small χ modes are the usual spin waves over the given spiral but η -modes connect energetically equivalent but different ground state spirals. Substituting Eq. (E.7) in Eq. (E.6) yields for the fluctuating spin (remember: $\rho^2 = \eta^2 + \chi^2$):

$$\mathbf{S} = (\bar{S}^x \sqrt{1 - \rho^2} - \bar{S}^y \chi, \bar{S}^y \sqrt{1 - \rho^2} + \bar{S}^x \chi, \eta). \quad (\text{E.8})$$

Finally, we need some integration in the partition sum: The measure on the unit sphere with the new parameters is given by the following Jacobian

$$d\Omega = \left| \frac{\partial \mathbf{S}}{\partial \eta} \times \frac{\partial \mathbf{S}}{\partial \chi} \right| d\eta d\chi = (1 - \rho^2)^{-\frac{1}{2}} d\eta d\chi. \quad (\text{E.9})$$

Now we turn to the calculation of the partition sum, so we reinsert the site indices:

$$\mathcal{Z} = \int \prod_i d\eta_i d\chi_i \left\{ (1 - \rho_i^2)^{-\frac{1}{2}} e^{-\beta \mathcal{H}(\{\bar{\mathbf{S}}_i, \eta_i, \chi_i\})} \right\}, \quad (\text{E.10})$$

and we emphasize that the Hamiltonian is expressed in the new coordinates, and the integrations are to be performed on the unit disks of $\eta_i \chi_i$ -planes.¹ By putting the Jacobian to the exponent we can cast the partition sum in the form

$$\mathcal{Z} := \int \prod_i d\eta_i d\chi_i e^{-\mathcal{S}(\{\bar{\mathbf{S}}_i, \eta_i, \chi_i\})}, \quad (\text{E.11})$$

and in this context \mathcal{S} is called the *action*, not to be confused with the entropy \mathcal{S} or the spin length S .² The action reads:

$$\mathcal{S}(\{\bar{\mathbf{S}}_i, \eta_i, \chi_i\}) = \beta \mathcal{H}(\{\bar{\mathbf{S}}_i, \eta_i, \chi_i\}) + \frac{1}{2} \sum_i \ln(1 - \rho_i^2), \quad (\text{E.12})$$

¹And to be totally precise, we should also include another parametrization (e.g. by flipping $\bar{\mathbf{S}}_i \rightarrow -\bar{\mathbf{S}}_i$ in Eq. (E.6)) to describe the other hemisphere of the fluctuating spin, but we are interested in small fluctuations so we do not bother.

²I am fully aware that this notation is unfortunate, but since all these "S"-s are standard I have no brighter idea than using different fonts.

where of course we have to substitute the new parameters Eq. (E.8) in the Hamiltonian (E.1).

No we turn to the small fluctuation (low temperature) approximation, i.e. we assume $\rho_i^2 \ll 1$, and we extend the integration domains to the whole $\eta_i \chi_i$ -planes. For small ρ Taylor expansion leads to $\ln(1 - \rho^2) = -\rho^2 + \mathcal{O}(\rho^3)$ in Eq. (E.12) and $\sqrt{1 - \rho^2} = 1 - \rho^2/2 + \mathcal{O}(\rho^3)$ in Eq. (E.8). Even if we stop at second order (the approximated action is denoted by S_2) in the variables η_i and χ_i the calculations are tedious, the result is:

$$S \approx S_2 = \frac{\beta}{2} \sum_{i,j} \left(\tilde{J}_{ij} \eta_i \eta_j + W_{ij} \chi_i \chi_j \right) - \frac{1}{2} \sum_j (\eta_j^2 + \chi_j^2). \quad (\text{E.13})$$

Here $\tilde{J}_{ij} = J_{ij} - J(\mathbf{Q})\delta_{ij}$ is the exchange matrix, with its smallest eigenvalue removed: this makes it positive semidefinite (thereby stabilizing the Gaussian when exponentiated in Eq. (E.11)), at the Hamiltonian level this is nothing more than a constant energy shift with no physical consequences (and note, $J(\mathbf{Q})$ is constant on the whole \mathcal{M}_{GS} , so \tilde{J}_{ij} is \mathbf{Q} -independent). $W_{ij}(\mathbf{Q}) = \tilde{J}_{ij}(\bar{\mathbf{S}}_i \cdot \bar{\mathbf{S}}_j)$, and this is where the ground state properties and the \mathbf{Q} -dependence enter the picture, see Eq. (E.5), and the last term comes from the Jacobian of the change of measure. With the aid of Eq. (E.5) we can evaluate

$$W_\delta(\mathbf{Q}) = \tilde{J}_\delta(\bar{\mathbf{S}}_i \cdot \bar{\mathbf{S}}_{i+\delta}) = \tilde{J}_\delta \cos(\mathbf{Q} \cdot \boldsymbol{\delta}) = \frac{1}{2} \tilde{J}_\delta (e^{i\mathbf{Q} \cdot \boldsymbol{\delta}} + e^{-i\mathbf{Q} \cdot \boldsymbol{\delta}}), \quad (\text{E.14})$$

where as usual $\boldsymbol{\delta} = \mathbf{R}_j - \mathbf{R}_i$ is a lattice separation vector, and the simplicity of this formula is the consequence of the isotropy of the model, and the simplicity of a spiral ground state.

Now we substitute S_2 in Eq. (E.11) and use that we are at very low temperature $\beta \gg 1$ and make a saddle-point approximation which basically removes the last term in Eq. (E.13):³

$$\mathcal{Z} \approx \int \prod_i d\eta_i d\chi_i e^{-\frac{\beta}{2} \sum_{i,j} (\tilde{J}_{ij} \eta_i \eta_j + W_{ij} \chi_i \chi_j)}. \quad (\text{E.15})$$

Here we can use the formula for an N -dimensional Gaussian integral (the matrix \mathbf{A} with components A_{ij} is positive definite, symmetric):

$$\int_{\mathbb{R}^N} d^N \mathbf{x} e^{-\frac{1}{2} \sum_{i,j} A_{ij} x_i x_j} = [\det(\mathbf{A}/2\pi)]^{-\frac{1}{2}}. \quad (\text{E.16})$$

To calculate the free energy we substitute Eq. (E.15) as evaluated by Eq. (E.16) in Eq. (E.3) and use the fact that (that is true under reasonable circumstances)⁴

$$\ln \det \mathbf{A} = \text{Tr} \ln \mathbf{A}. \quad (\text{E.17})$$

³The saddle point approximation (or Laplace's method), applied to our very simple case consists of the following. We want to approximate the integral (here we show the method in one dimension for clarity): $I = \int_{\mathbb{R}} \exp\{-\beta J x^2/2\} g(x) dx$, with $J > 0$, $\beta \gg 1$ and g being a healthy function, here $g(x) = \exp\{+x^2/2\}$. Since β is large, the Gaussian $\exp\{-\beta J x^2/2\}$ is very sharply peaked at the origin, so it picks up the largest contribution from $g(x)$ around the origin, so we can Taylor expand $g(x)$ there. In our case we assume that the lowest order approximation is good enough, $g(x) \approx g(x=0) = g_0 = 1$, so $I \approx g_0 \int_{\mathbb{R}} \exp\{-\beta J x^2/2\} dx = \int_{\mathbb{R}} \exp\{-\beta J x^2/2\} dx = \sqrt{(2\pi)/(\beta J)}$, and in the last step we used the well known formula for Gaussian integrals.

⁴For diagonalizable \mathbf{A} this can easily be seen by noting that both the determinant and the trace is invariant under a change of basis, and that the determinant is just the product of the eigenvalues, and the trace is the sum of them.

The \mathbf{Q} -dependent part of the low temperature free energy becomes

$$\mathcal{F}(\mathbf{Q}) \approx T \left[\text{Tr} \ln \left(\tilde{\mathbf{J}}/2\pi T \right) + \text{Tr} \ln \left(\mathbf{W}(\mathbf{Q})/2\pi T \right) \right], \quad (\text{E.18})$$

where we have typeset the matrices of \tilde{J}_{ij} and $W_{ij}(\mathbf{Q})$ in boldface. The first term does not discriminate between states on the \mathcal{M}_{GS} , but the second one *does*. Our last task is to evaluate the traces above: We diagonalize $\tilde{\mathbf{J}}$ and $\mathbf{W}(\mathbf{Q})$ by Fourier transform and afterwards the above traces simply become Brillouin-zone sums. We define the Fourier transforms as usual (and of course it can be defined for any lattice translation invariant matrix A_δ the same way, making it diagonal)

$$\tilde{J}(\mathbf{q}) = \frac{1}{2} \sum_{\delta} \tilde{J}_\delta e^{-i\mathbf{q}\cdot\delta}, \text{ and } W_{\mathbf{Q}}(\mathbf{q}) = \frac{1}{2} \sum_{\delta} W_\delta(\mathbf{Q}) e^{-i\mathbf{q}\cdot\delta}, \quad (\text{E.19})$$

and traces in the free energy Eq. (E.18) can be evaluated as BZ-sums, e.g.

$$\text{Tr} \ln \tilde{\mathbf{J}} = \sum_{\mathbf{q} \in \text{BZ}} \ln \tilde{J}(\mathbf{q}). \quad (\text{E.20})$$

To summarize: The final result for the free energy is:

$$\mathcal{F}(\mathbf{Q}) \approx T \left[\sum_{\mathbf{q} \in \text{BZ}} \ln \left(\tilde{J}(\mathbf{q})/2\pi T \right) + \sum_{\mathbf{q} \in \text{BZ}} \ln \left(W_{\mathbf{Q}}(\mathbf{q})/2\pi T \right) \right]. \quad (\text{E.21})$$

This formula can further be manipulated to taste (see e.g. Eq. (3.20), where we cast it in a form emphasizing the analogy between quantum and thermal selection mechanisms), but to find the thermally chosen free energy it is enough to perform the BZ-sum (numerically) in the second term of Eq. (E.21) with \mathbf{Q} on the \mathcal{M}_{GS} , and find the \mathbf{Q} with the minimal free energy.

Appendix F

Magneto-optical response

We have magnetoelectric cross-correlation effects when in a material external magnetic field induces electric polarization and external electric field induces magnetization. Assuming linear response the effects can be described by the *magnetoelectric tensors* defined as:

$$P_\mu = \varepsilon_0 \sum_{\nu=x,y,z} \chi_{\mu\nu}^{ee} E_\nu + \sqrt{\frac{\varepsilon_0}{\mu_0}} \mu_0 \sum_{\nu=x,y,z} \chi_{\mu\nu}^{em} H_\nu, \quad (\text{F.1})$$

$$M_\mu = \sum_{\nu=x,y,z} \chi_{\mu\nu}^{mm} H_\nu + \sqrt{\frac{\varepsilon_0}{\mu_0}} \sum_{\nu=x,y,z} \chi_{\mu\nu}^{me} E_\nu, \quad (\text{F.2})$$

where ε_0 is the vacuum permittivity, μ_0 is the vacuum permeability (remember $c = 1/\sqrt{\varepsilon_0\mu_0}$ the speed of light) and $\mu, \nu = x, y, z$ are Cartesian tensor indices. \mathbf{P} and \mathbf{M} are the electric polarization and magnetization vectors, respectively, \mathbf{E} and \mathbf{H} are the electric and magnetic field vectors, respectively. $\chi_{\mu\nu}^{ee}$ and $\chi_{\mu\nu}^{mm}$ are the electric and magnetic susceptibilities, respectively. $\chi_{\mu\nu}^{em}$ and $\chi_{\mu\nu}^{me}$ are the magnetoelectric tensors that are not independent: The following relations hold among them (a consequence of the Kubo formula [140]):

$$\chi_{\mu\nu}^{me} = [\chi_{\mu\nu}^{me}]' + i [\chi_{\mu\nu}^{me}]'', \quad (\text{F.3})$$

$$\chi_{\mu\nu}^{em} = [\chi_{\nu\mu}^{me}]' - i [\chi_{\nu\mu}^{me}]'', \quad (\text{F.4})$$

where $[\chi_{\mu\nu}^{me}]'$ and $[\chi_{\mu\nu}^{me}]''$ are the real and imaginary parts of the respective matrix elements. This is good news: One has to measure or calculate only $\chi_{\mu\nu}^{me}$ and $\chi_{\mu\nu}^{em}$ follows. All the fields and susceptibility tensors are allowed to be frequency dependent, and they actually are: This dependence is what we are interested in.

Appendix G

Reality of matrix elements in a magnetic point group

It is well known that unitary symmetry elements of the symmetry group of a Hamiltonian lead to selection rules, i.e. force some matrix elements of linear operators to become zero. Here we will show that antiunitary symmetry elements of a magnetic group can relate the matrix elements of linear operators to each other. In an extreme case these antiunitary symmetry elements can force the matrices of linear operators to have only real or purely imaginary matrix elements, as was shown in Appendix A of our paper [145].

We will illustrate our findings on the group $D_2(C_2)$, relevant for the $\varphi = 0$ case of our singe-ion model (4.15), the case most closely related to the measurements on $\text{Sr}_2\text{CoSi}_2\text{O}_7$ (see Subsection 4.7.2). Here we use the notation of the field-fixed coordinate system (see Fig. 4.4), but for a more familiar notation just substitute the indices $\perp 1 \rightarrow x$, $\perp 2 \rightarrow y$, $\parallel \rightarrow z$. The argumentation also works for arbitrary spin length.

The chiral but apolar magnetic point group $D_2(C_2) \equiv 22'2'$ consists of the elements

$$D_2(C_2) = \{ \mathbf{1}, C_2^{\parallel}, \Theta C_2^{\perp 1}, \Theta C_2^{\perp 2} \}, \quad (\text{G.1})$$

where C_2 are twofold rotations about the axis indicated in the upper index, and Θ stands for time reversal (we mention that $\Theta C_2 \equiv 2'$, the first notation is due to Schoenflies, the second one is called the Hermann–Mauguin notation). For generators of the group we choose C_2^{\parallel} and $\Theta C_2^{\perp 2}$, and its character table together with the symmetry classification of the spin and polarization components is summarized in Table 4.3. Our conclusions are valid whenever $\Theta C_2^{\perp 2}$ is a group member, just in the case when $\varphi = \pi/4$ and we have the polar symmetry group

$$C_{2v}(C_{1h}) = \{ \mathbf{1}, \sigma^{\parallel}, \Theta C_2^{\perp 2}, \Theta \sigma^{\perp 1} \}, \quad (\text{G.2})$$

see Subsection 4.7.2.

The operator $\hat{C}_2^{\perp 2}$ is represented on the $S = 3/2$ spin space by the matrix:

$$\hat{C}_2^{\perp 2} = e^{i\pi \hat{S}^{\perp 2}} = \begin{pmatrix} 0 & 0 & 0 & 1 \\ 0 & 0 & -1 & 0 \\ 0 & 1 & 0 & 0 \\ -1 & 0 & 0 & 0 \end{pmatrix}. \quad (\text{G.3})$$

The antiunitarity operator of time-reversal is represented by¹

$$\hat{\Theta} = \hat{C}_2^{\perp 2} \mathcal{K} = e^{i\pi \hat{S}^{\perp 2}} \mathcal{K} = \begin{pmatrix} 0 & 0 & 0 & 1 \\ 0 & 0 & -1 & 0 \\ 0 & 1 & 0 & 0 \\ -1 & 0 & 0 & 0 \end{pmatrix} \mathcal{K}, \quad (\text{G.4})$$

where \mathcal{K} is complex conjugation, conjugating every matrix or vector component on the right, but leaving the basis functions intact [156]. Therefore the matrix of $\Theta C_2^{\perp 2}$ reads:

$$\hat{\Theta} \hat{C}_2^{\perp 2} = \hat{C}_2^{\perp 2} \mathcal{K} \hat{C}_2^{\perp 2} = e^{i2\pi \hat{S}^{\perp 2}} \mathcal{K} = -\hat{\mathbf{1}} \mathcal{K}, \quad (\text{G.5})$$

with $\hat{\mathbf{1}}$ being the 4×4 identity matrix.

Physical observables –e.g. the spin or polarization components represented by a linear operator \mathcal{O} , see Table 4.3 for the chiral and polar cases– are either even or odd under $\Theta C_2^{\perp 2}$:

$$\Theta C_2^{\perp 2} \{\mathcal{O}\} = \pm \mathcal{O}. \quad (\text{G.6})$$

The corresponding linear operator $\hat{\mathcal{O}}$ transforms as

$$\left(\hat{\Theta} \hat{C}_2^{\perp 2}\right) \hat{\mathcal{O}} \left(\hat{\Theta} \hat{C}_2^{\perp 2}\right)^{-1} = \pm \hat{\mathcal{O}}. \quad (\text{G.7})$$

Substituting the form (G.5) results:

$$\left(\hat{\Theta} \hat{C}_2^{\perp 2}\right) \hat{\mathcal{O}} \left(\hat{\Theta} \hat{C}_2^{\perp 2}\right)^{-1} = \mathcal{K} \hat{\mathcal{O}} \mathcal{K} = \hat{\mathcal{O}}^*, \quad (\text{G.8})$$

since acting on an arbitrary vector v :

$$\left(\mathcal{K} \hat{\mathcal{O}} \mathcal{K}\right) v = \mathcal{K} \hat{\mathcal{O}} (\mathcal{K} v) = \mathcal{K} \left(\hat{\mathcal{O}} v^*\right) = \hat{\mathcal{O}}^* v. \quad (\text{G.9})$$

Eqs. (G.7) and (G.8) together mean that:

$$\hat{\mathcal{O}} = \pm \hat{\mathcal{O}}^*, \quad (\text{G.10})$$

thus, matrix elements of the operators even (odd) under $\Theta C_2^{\perp 2}$ are real (pure imaginary).

This is a powerful result and has a profound effect on the magneto-optical properties as has been seen in Subsection 4.7.2. To obtain this result we heavily relied on the concrete form of the antiunitary symmetry operator (G.5). When we have another antiunitary –time reversed– operator in the magnetic point group it may give us less beautiful results, but it will still relate the imaginary and real parts of matrix elements of an observable. We basically repeat the argumentation presented above, but for general spin length S , and we will use a general antiunitary symmetry element A instead of $\Theta C_2^{\perp 2}$, for our original derivation, see the end of the Supplement of our paper [146].

¹Analogously for $S = 1/2$, time reversal can be represented by $\hat{\Theta} = i\hat{\sigma}^y \mathcal{K}$, where $\hat{\sigma}^y$ is the second Pauli matrix.

We use standard xyz coordinates and consider a spin of length S , with S^z eigenvalues $m, m' = -S, -S+1, \dots, S-1, S$ and all our matrices will be of size $(2S+1) \times (2S+1)$. The time reversal operation Θ can be represented as

$$\hat{\Theta} = \hat{C}_2^y \mathcal{K} = e^{i\pi \hat{S}^y} \mathcal{K} = (-1)^{(S-m)} \delta_{m', -m} \mathcal{K}, \quad (\text{G.11})$$

with $(\hat{C}_2^y)^{-1} = \pm \hat{C}_2^y$ and consequently $\hat{\Theta}^{-1} = \pm \hat{\Theta}$, where the $+$ ($-$) sign stands for the integer (half-integer) values of S . We assume that the Hamiltonian is invariant under the antiunitary symmetry $A = U\Theta$ (here we use the little more convenient convention where Θ acts first, this choice has no physical consequences), where U is some geometric symmetry represented by a unitary matrix \hat{U} , with the property $\hat{U}^{-1} = \hat{U}^\dagger$. We are interested in the constraints on the matrix elements of the observable \mathcal{O} . We assume that we know the transformation properties of \mathcal{O} under A :

$$A \{\mathcal{O}\} = \mathcal{O}', \quad (\text{G.12})$$

and the corresponding matrix $\hat{\mathcal{O}}$ transforms as

$$\hat{A} \hat{\mathcal{O}} \hat{A}^{-1} = \hat{\mathcal{O}}'. \quad (\text{G.13})$$

We substitute the matrix form $\hat{A} = \hat{U} \hat{\Theta} = \hat{U} \hat{C}_2^y \mathcal{K}$ in the equation above (G.13):

$$\hat{\mathcal{O}}' = \left(\hat{U} \hat{C}_2^y \mathcal{K} \right) \hat{\mathcal{O}} \left(\hat{U} \hat{C}_2^y \mathcal{K} \right)^{-1} = \left(\hat{U} \hat{C}_2^y \right) \left(\mathcal{K} \hat{\mathcal{O}} \mathcal{K} \right) \left(\hat{U} \hat{C}_2^y \right)^{-1}. \quad (\text{G.14})$$

We use Eq. (G.8) in the right hand side

$$\hat{\mathcal{O}}' = \left(\hat{U} \hat{C}_2^y \right) \hat{\mathcal{O}}^* \left(\hat{U} \hat{C}_2^y \right)^{-1}, \quad (\text{G.15})$$

and see that the matrices $\hat{\mathcal{O}}'$ and $\hat{\mathcal{O}}^*$ are *unitary equivalent* with equivalence given by the unitary matrix $\hat{U} \hat{C}_2^y$. If we wish we can simplify this formula further using $(\hat{C}_2^y)^{-1} = \pm \hat{C}_2^y$ and $\hat{U}^{-1} = \hat{U}^\dagger$:

$$\hat{\mathcal{O}}' = \pm \left(\hat{U} \hat{C}_2^y \right) \hat{\mathcal{O}}^* \left(\hat{C}_2^y \hat{U}^\dagger \right), \quad (\text{G.16})$$

where the $+$ ($-$) sign stands for the integer (half-integer) values of S . In applications it is worth to choose a coordinate system in which the geometrical symmetry U is somehow related to the y -axis, thereby simplifying the form of $\hat{U} \hat{C}_2^y$.

In conclusion, the unitary symmetries determine the selection rules (the non-vanishing matrix elements), whereas antiunitary elements give constraints on the reality of the remaining ones. These rules and the matrix elements calculated by the actual wavefunctions of the microscopic model (4.15) are given in Appendix H, and are in perfect agreement.

Appendix H

Matrix elements for the single Co-ion problem

H.1 Large anisotropy and small field: $\Lambda \gg h$

From the series expansion of the single spin energies (4.20) in h/Λ , we have

$$\varepsilon_1 = \frac{\Lambda}{4} - h - \frac{3h^2}{8\Lambda} + \dots, \quad (\text{H.1a})$$

$$\varepsilon_2 = \frac{\Lambda}{4} + h - \frac{3h^2}{8\Lambda} + \dots, \quad (\text{H.1b})$$

$$\varepsilon_3 = \frac{9\Lambda}{4} + \frac{3h^2}{8\Lambda} + \dots, \quad (\text{H.1c})$$

$$\varepsilon_4 = \frac{9\Lambda}{4} + \frac{3h^2}{8\Lambda} + \dots. \quad (\text{H.1d})$$

The spin operators up to leading order in each component are:

$$S^{\parallel} = \begin{pmatrix} 1 & 0 & -\frac{\sqrt{3}}{2} & 0 \\ 0 & -1 & 0 & -\frac{\sqrt{3}}{2} \\ -\frac{\sqrt{3}}{2} & 0 & -\frac{3h}{4\Lambda} & 0 \\ 0 & -\frac{\sqrt{3}}{2} & 0 & -\frac{3h}{4\Lambda} \end{pmatrix}, \quad (\text{H.2a})$$

$$S^{\perp 1} = \begin{pmatrix} 0 & 1 & 0 & -\frac{\sqrt{3}}{2} \\ 1 & 0 & \frac{\sqrt{3}}{2} & 0 \\ 0 & \frac{\sqrt{3}}{2} & 0 & \frac{9h^2}{16\Lambda^2} \\ -\frac{\sqrt{3}}{2} & 0 & \frac{9h^2}{16\Lambda^2} & 0 \end{pmatrix}, \quad (\text{H.2b})$$

$$S^{\perp 2} = i \begin{pmatrix} 0 & -\frac{1}{2} & 0 & \frac{\sqrt{3}h}{4\Lambda} \\ \frac{1}{2} & 0 & -\frac{\sqrt{3}h}{4\Lambda} & 0 \\ 0 & \frac{\sqrt{3}h}{4\Lambda} & 0 & -\frac{3}{2} \\ -\frac{\sqrt{3}h}{4\Lambda} & 0 & \frac{3}{2} & 0 \end{pmatrix}. \quad (\text{H.2c})$$

The polarization operators are:

$$P_{\text{chiral}}^{\parallel} = -P_{\text{polar}}^{\perp 1} = i \begin{pmatrix} 0 & 0 & -\sqrt{3} & 0 \\ 0 & 0 & 0 & -\sqrt{3} \\ \sqrt{3} & 0 & 0 & 0 \\ 0 & \sqrt{3} & 0 & 0 \end{pmatrix}, \quad (\text{H.3a})$$

$$P_{\text{polar}}^{\parallel} = P_{\text{chiral}}^{\perp 1} = i \begin{pmatrix} 0 & -\frac{3h}{2\Lambda} & 0 & \sqrt{3} \\ \frac{3h}{2\Lambda} & 0 & -\sqrt{3} & 0 \\ 0 & \sqrt{3} & 0 & \frac{3h}{2\Lambda} \\ -\sqrt{3} & 0 & -\frac{3h}{2\Lambda} & 0 \end{pmatrix}, \quad (\text{H.3b})$$

$$P_{\text{chiral}}^{\perp 2} = \begin{pmatrix} 0 & \frac{3h}{2\Lambda} & 0 & -\sqrt{3} \\ \frac{3h}{2\Lambda} & 0 & -\sqrt{3} & 0 \\ 0 & -\sqrt{3} & 0 & -\frac{3h}{2\Lambda} \\ -\sqrt{3} & 0 & -\frac{3h}{2\Lambda} & 0 \end{pmatrix}, \quad (\text{H.3c})$$

$$P_{\text{polar}}^{\perp 2} = \begin{pmatrix} \frac{3h}{2\Lambda} & 0 & -\sqrt{3} & 0 \\ 0 & -\frac{3h}{2\Lambda} & 0 & \sqrt{3} \\ -\sqrt{3} & 0 & -\frac{3h}{2\Lambda} & 0 \\ 0 & \sqrt{3} & 0 & \frac{3h}{2\Lambda} \end{pmatrix}. \quad (\text{H.3d})$$

H.2 Large field and small anisotropy: $h \gg \Lambda$

Expanding in Λ/h in (4.20) results for the energies

$$\varepsilon_1 = -\frac{3h}{2} + \frac{3\Lambda}{4} - \frac{3\Lambda^2}{8h} + \dots, \quad (\text{H.4a})$$

$$\varepsilon_2 = -\frac{h}{2} + \frac{7\Lambda}{4} - \frac{3\Lambda^2}{8h} + \dots, \quad (\text{H.4b})$$

$$\varepsilon_3 = \frac{h}{2} + \frac{7\Lambda}{4} + \frac{3\Lambda^2}{8h} + \dots, \quad (\text{H.4c})$$

$$\varepsilon_4 = \frac{3h}{2} + \frac{3\Lambda}{4} + \frac{3\Lambda^2}{8h} + \dots. \quad (\text{H.4d})$$

The spin operators are:

$$S^{\parallel} = \begin{pmatrix} \frac{3}{2} & 0 & -\frac{\sqrt{3}\Lambda}{2h} & 0 \\ 0 & \frac{1}{2} & 0 & -\frac{\sqrt{3}\Lambda}{2h} \\ -\frac{\sqrt{3}\Lambda}{2h} & 0 & -\frac{1}{2} & 0 \\ 0 & -\frac{\sqrt{3}\Lambda}{2h} & 0 & -\frac{3}{2} \end{pmatrix}, \quad (\text{H.5a})$$

$$S^{\perp 1} = \begin{pmatrix} 0 & \frac{\sqrt{3}}{2} & 0 & -\frac{9\Lambda^2}{16h^2} \\ \frac{\sqrt{3}}{2} & 0 & 1 & 0 \\ 0 & 1 & 0 & \frac{\sqrt{3}}{2} \\ -\frac{9\Lambda^2}{16h^2} & 0 & \frac{\sqrt{3}}{2} & 0 \end{pmatrix}, \quad (\text{H.5b})$$

$$S^{\perp 2} = i \begin{pmatrix} 0 & -\frac{\sqrt{3}}{2} & 0 & \frac{3\Lambda^2}{16h^2} \\ \frac{\sqrt{3}}{2} & 0 & -1 & 0 \\ 0 & 1 & 0 & -\frac{\sqrt{3}}{2} \\ -\frac{3\Lambda^2}{16h^2} & 0 & \frac{\sqrt{3}}{2} & 0 \end{pmatrix}. \quad (\text{H.5c})$$

The polarization operators are:

$$P_{\text{chiral}}^{\parallel} = -P_{\text{polar}}^{\perp 1} = i \begin{pmatrix} 0 & 0 & -\sqrt{3} & 0 \\ 0 & 0 & 0 & -\sqrt{3} \\ \sqrt{3} & 0 & 0 & 0 \\ 0 & \sqrt{3} & 0 & 0 \end{pmatrix}, \quad (\text{H.6a})$$

$$P_{\text{polar}}^{\parallel} = P_{\text{chiral}}^{\perp 1} = i \begin{pmatrix} 0 & -\sqrt{3} & 0 & \frac{3\Lambda}{2h} \\ \sqrt{3} & 0 & -\frac{3\Lambda}{2h} & 0 \\ 0 & \frac{3\Lambda}{2h} & 0 & \sqrt{3} \\ -\frac{3\Lambda}{2h} & 0 & -\sqrt{3} & 0 \end{pmatrix}, \quad (\text{H.6b})$$

$$P_{\text{chiral}}^{\perp 2} = \begin{pmatrix} 0 & \sqrt{3} & 0 & -\frac{3\Lambda}{2h} \\ \sqrt{3} & 0 & -\frac{3\Lambda}{2h} & 0 \\ 0 & -\frac{3\Lambda}{2h} & 0 & -\sqrt{3} \\ -\frac{3\Lambda}{2h} & 0 & -\sqrt{3} & 0 \end{pmatrix}, \quad (\text{H.6c})$$

$$P_{\text{polar}}^{\perp 2} = \begin{pmatrix} \frac{3}{2} & 0 & -\frac{\sqrt{3}}{2} & 0 \\ 0 & -\frac{3}{2} & 0 & -\frac{\sqrt{3}}{2} \\ -\frac{\sqrt{3}}{2} & 0 & -\frac{3}{2} & 0 \\ 0 & -\frac{\sqrt{3}}{2} & 0 & \frac{3}{2} \end{pmatrix}. \quad (\text{H.6d})$$

Bibliography

- [1] John Hubbard. Electron correlations in narrow energy bands. *Proceedings of the Royal Society of London. Series A. Mathematical and Physical Sciences*, 276(1365):238–257, 1963.
- [2] Martin C. Gutzwiller. Effect of correlation on the ferromagnetism of transition metals. *Phys. Rev. Lett.*, 10:159–162, Mar 1963.
- [3] Junjiro Kanamori. Electron Correlation and Ferromagnetism of Transition Metals. *Progress of Theoretical Physics*, 30(3):275–289, 09 1963.
- [4] W. Heisenberg. Zur theorie des ferromagnetismus. *Zeitschrift für Physik*, 49(9):619–636, September 1928.
- [5] Russell W. Millar. The specific heats at low temperatures of manganous oxide, manganous-manganic oxide and manganese dioxide. *J. Am. Chem. Soc.*, 50:1875–1883, 1928.
- [6] C. G. Shull, W. A. Strauser, and E. O. Wollan. Neutron diffraction by paramagnetic and antiferromagnetic substances. *Phys. Rev.*, 83:333–345, Jul 1951.
- [7] J. Sólyom. *Fundamentals of the Physics of Solids: Volume 1: Structure and Dynamics*. Fundamentals of the Physics of Solids. Springer Berlin Heidelberg, 2007.
- [8] A. S. Sukhanov, Y. A. Onykiienko, R. Bewley, C. Shekhar, C. Felser, and D. S. Inosov. Magnon spectrum of the Weyl semimetal half-Heusler compound GdPtBi. *Phys. Rev. B*, 101:014417, Jan 2020.
- [9] C. Lacroix, P. Mendels, and F. Mila. *Introduction to Frustrated Magnetism: Materials, Experiments, Theory*. Springer Series in Solid-State Sciences. Springer Berlin Heidelberg, 2011.
- [10] P. Fazekas. *Lecture Notes on Electron Correlation and Magnetism*. EBL-Schweitzer. World Scientific, 1999.
- [11] C. Kittel. *Introduction to Solid State Physics*. Wiley, 2004.
- [12] A P Ramirez. Strongly geometrically frustrated magnets. *Annual Review of Materials Science*, 24(1):453–480, 1994.
- [13] V. Fritsch, J. Hemberger, N. Büttgen, E.-W. Scheidt, H.-A. Krug von Nidda, A. Loidl, and V. Tsurkan. Spin and orbital frustration in mnsc_2s_4 and fesc_2s_4 . *Phys. Rev. Lett.*, 92:116401, Mar 2004.

- [14] G. H. Wannier. Antiferromagnetism. the triangular ising net. *Phys. Rev.*, 79:357–364, Jul 1950.
- [15] Kenzi Kanô and Shigeo Naya. Antiferromagnetism. The Kagomé Ising Net. *Progress of Theoretical Physics*, 10(2):158–172, 08 1953.
- [16] J. Villain, R. Bidaux, J.-P. Carton, and R. Conte. Order as an Effect of Disorder. *J. Phys. II (France)*, 41(11):1263, 1980.
- [17] C. L. Henley. Ordering by disorder: Ground-state selection in fcc vector antiferromagnets. *J. Appl. Phys.*, 61:3962–3964, April 1987.
- [18] Christopher L. Henley. Ordering due to disorder in a frustrated vector antiferromagnet. *Phys. Rev. Lett.*, 62:2056–2059, Apr 1989.
- [19] S Alexander and P Pincus. Phase transitions of some fully frustrated models. *J. Phys. A: Math. Gen.*, 13(1):263, 1980.
- [20] Doron Bergman, Jason Alicea, Emanuel Gull, Simon Trebst, and Leon Balents. Order-by-disorder and spiral spin-liquid in frustrated diamond-lattice antiferromagnets. *Nat. Phys.*, 3:487, 05 2007.
- [21] Shang Gao, Oksana Zaharko, Vladimir Tsurkan, Yixi Su, Jonathan S. White, Gregory S. Tucker, Bertrand Roessli, Frederic Bourdarot, Romain Sibille, Dmitry Chernyshov, Tom Fennell, Alois Loidl, and Christian Rüegg. Spiral spin-liquid and the emergence of a vortex-like state in MnSc_2S_4 . *Nat. Phys.*, 13:157, 10 2016.
- [22] Shang Gao, H. Diego Rosales, Flavia A. Gómez Albarracín, Vladimir Tsurkan, Guratinder Kaur, Tom Fennell, Paul Steffens, Martin Boehm, Petr Čermák, Astrid Schneidewind, Eric Ressouche, Daniel C. Cabra, Christian Rüegg, and Oksana Zaharko. Fractional antiferromagnetic skyrmion lattice induced by anisotropic couplings. *Nature*, 586(7827):37–41, October 2020.
- [23] E. F. Shender. *Antiferromagnetic Garnets with Fluctuationally Interacting Sublattices*. *Zh. Eksp. Teor. Fiz.*, 56(1):178, 1982.
- [24] Hikaru Kawamura. Spin-wave analysis of the antiferromagnetic plane rotator model on the triangular lattice—symmetry breaking in a magnetic field. *J. Phys. Soc. Jpn.*, 53(8):2452–2455, 1984.
- [25] R. Moessner and J. T. Chalker. Properties of a classical spin liquid: The Heisenberg pyrochlore antiferromagnet. *Phys. Rev. Lett.*, 80:2929–2932, Mar 1998.
- [26] R. Moessner and J. T. Chalker. Low-Temperature Properties of Classically Frustrated Antiferromagnets. *Phys. Rev. B*, 58:12049–12062, Nov 1998.
- [27] J. Knolle and R. Moessner. A field guide to spin liquids. *Annual Review of Condensed Matter Physics*, 10(1):451–472, 2019.

- [28] Lucile Savary and Leon Balents. Quantum spin liquids: a review. *Reports on Progress in Physics*, 80(1):016502, nov 2016.
- [29] John Stephenson. Ising-model spin correlations on the triangular lattice. *Journal of Mathematical Physics*, 5(8):1009–1024, 1964.
- [30] John Stephenson. Ising-model spin correlations on the triangular lattice. iii. isotropic antiferromagnetic lattice. *Journal of Mathematical Physics*, 11(2):413–419, 1970.
- [31] C. L. Henley. Power-law spin correlations in pyrochlore antiferromagnets. *Phys. Rev. B*, 71:014424, Jan 2005.
- [32] Christopher L. Henley. The “coulomb phase” in frustrated systems. *Annual Review of Condensed Matter Physics*, 1(1):179–210, 2010.
- [33] Linus Pauling. The Structure and Entropy of Ice and of Other Crystals with Some Randomness of Atomic Arrangement. *J. Am. Chem. Soc.*, 57(12):2680–2684, 1935.
- [34] S. R. Giblin, M. Twengström, L. Bovo, M. Ruminy, M. Bartkowiak, P. Manuel, J. C. Andresen, D. Prabhakaran, G. Balakrishnan, E. Pomjakushina, C. Paulsen, E. Lhotel, L. Keller, M. Frontzek, S. C. Capelli, O. Zaharko, P. A. McClarty, S. T. Bramwell, P. Henelius, and T. Fennell. Pauling entropy, metastability, and equilibrium in $\text{dy}_2\text{ti}_2\text{o}_7$ spin ice. *Phys. Rev. Lett.*, 121:067202, Aug 2018.
- [35] Masashige Matsumoto, Kosuke Chimata, and Mikito Koga. Symmetry analysis of spin-dependent electric dipole and its application to magnetoelectric effects. *Journal of the Physical Society of Japan*, 86(3):034704, 2017.
- [36] H. Murakawa, Y. Onose, S. Miyahara, N. Furukawa, and Y. Tokura. Ferroelectricity induced by spin-dependent metal-ligand hybridization in $\text{Ba}_2\text{CoGe}_2\text{O}_7$. *Phys. Rev. Lett.*, 105:137202, Sep 2010.
- [37] Shin Miyahara and Nobuo Furukawa. Theory of magnetoelectric resonance in two-dimensional $S = 3/2$ antiferromagnet $\text{Ba}_2\text{CoGe}_2\text{O}_7$ via spin-dependent metal-ligand hybridization mechanism. *J. Phys. Soc. Jpn.*, 80(7):073708, 2011.
- [38] Hosho Katsura, Naoto Nagaosa, and Alexander V. Balatsky. Spin current and magnetoelectric effect in noncollinear magnets. *Phys. Rev. Lett.*, 95:057205, Jul 2005.
- [39] Taka-hisa Arima. Ferroelectricity induced by proper-screw type magnetic order. *J. Phys. Soc. Jpn.*, 76(7):073702, 2007.
- [40] A. Pimenov, A. A. Mukhin, V. Yu. Ivanov, V. D. Travkin, A. M. Balbashov, and A. Loidl. Possible evidence for electromagnons in multiferroic manganites. *Nature Physics*, 2(2):97–100, February 2006.
- [41] Y. Takahashi, R. Shimano, Y. Kaneko, H. Murakawa, and Y. Tokura. Magneto-electric resonance with electromagnons in a perovskite helimagnet. *Nature Physics*, 8:121–125, 2012.

- [42] Y. Takahashi, Y. Yamasaki, and Y. Tokura. Terahertz magnetoelectric resonance enhanced by mutual coupling of electromagnons. *Phys. Rev. Lett.*, 111:037204, Jul 2013.
- [43] K. Penc, J. Romhányi, T. Rőöm, U. Nagel, Á. Antal, T. Fehér, A. Jánossy, H. Engelkamp, H. Murakawa, Y. Tokura, D. Szaller, S. Bordács, and I. Kézsmárki. Spin-stretching modes in anisotropic magnets: Spin-wave excitations in the multiferroic $\text{Ba}_2\text{CoGe}_2\text{O}_7$. *Phys. Rev. Lett.*, 108:257203, Jun 2012.
- [44] L.D. Barron. *Molecular Light Scattering and Optical Activity*. Cambridge University Press, 2009.
- [45] Dávid Szaller, Sándor Bordács, and István Kézsmárki. Symmetry conditions for nonreciprocal light propagation in magnetic crystals. *Phys. Rev. B*, 87:014421, Jan 2013.
- [46] I. Kézsmárki, D. Szaller, S. Bordács, V. Kocsis, Y. Tokunaga, Y. Taguchi, H. Murakawa, Y. Tokura, H. Engelkamp, T. Rőöm, and U. Nagel. One-way transparency of four-coloured spin-wave excitations in multiferroic materials. *Nature Comm.*, 5:3203, 2014.
- [47] G. L. J. A. Rikken and E. Raupach. Observation of magneto-chiral dichroism. *Nature*, 390:493–494, 1997.
- [48] G. L. J. A. Rikken, C. Strohm, and P. Wyder. Observation of magnetoelectric directional anisotropy. *Phys. Rev. Lett.*, 89(13):133005, Sep 2002.
- [49] I. Kézsmárki, N. Kida, H. Murakawa, S. Bordács, Y. Onose, and Y. Tokura. Enhanced directional dichroism of terahertz light in resonance with magnetic excitations of the multiferroic $\text{Ba}_2\text{CoGe}_2\text{O}_7$ oxide compound. *Phys. Rev. Lett.*, 106:057403, Feb 2011.
- [50] Sandor Bordács, Istvan Kézsmárki, David Szaller, Laszlo Demkó, Noriaki Kida, Hiroshi Murakawa, Yoshinori Onose, Ryo Shimano, Toomas Rőöm, Urmas Nagel, Shin Miyahara, N. Furukawa, and Yoshinori Tokura. Chirality of matter shows up via spin excitations. *Nature Physics*, 8:734–738, 2012.
- [51] A. M. Kuzmenko, V. Dziom, A. Shuvaev, Anna Pimenov, M. Schiebl, A. A. Mukhin, V. Yu. Ivanov, I. A. Gudim, L. N. Bezmaternykh, and A. Pimenov. Large directional optical anisotropy in multiferroic ferroborate. *Phys. Rev. B*, 92:184409, Nov 2015.
- [52] I. Kézsmárki, U. Nagel, S. Bordács, R. S. Fishman, J. H. Lee, Hee Taek Yi, S.-W. Cheong, and T. Rőöm. Optical diode effect at spin-wave excitations of the room-temperature multiferroic BiFeO_3 . *Phys. Rev. Lett.*, 115:127203, Sep 2015.
- [53] J. Ricardo de Sousa and J. A. Plascak. Phase transitions in the classical n -vector model on the fcc lattice. *Phys. Rev. B*, 77:024419, Jan 2008.

- [54] Mohindar S. Seehra and T. M. Giebultowicz. Magnetic structures of fcc systems with nearest-neighbor and next-nearest-neighbor exchange interactions. *Phys. Rev. B*, 38:11898–11900, Dec 1988.
- [55] R. Peierls. Statistical theory of superlattices with unequal concentrations of the components. *Proc. R. Soc. London, Ser. A*, 154(881):207–222, 1936.
- [56] C. E. Easthope. The Dependence on Composition of the Critical Ordering Temperature in Alloys. *Proc. Cambridge Philos. Soc.*, 33(4):502–517, 1937.
- [57] W. Shockley. Theory of Order for the Copper Gold Alloy System. *J. Chem. Phys.*, 6(3):130–144, 1938.
- [58] A. Danielian. Ground State of an Ising Face-Centered Cubic Lattice. *Phys. Rev. Lett.*, 6:670–671, Jun 1961.
- [59] A. Danielian. Low-Temperature Behavior of a Face-Centered Cubic Antiferromagnet. *Phys. Rev.*, 133:A1344–A1349, Mar 1964.
- [60] K. Binder. Ordering of the Face-Centered-Cubic Lattice with Nearest-Neighbor Interaction. *Phys. Rev. Lett.*, 45:811–814, Sep 1980.
- [61] Hagai Meirovitch. Computer simulation study of hysteresis and free energy in the fcc Ising antiferromagnet. *Phys. Rev. B*, 30:2866–2874, Sep 1984.
- [62] S. Kämmerer, B. Dünweg, K. Binder, and M. d’Onorio de Meo. Nearest-neighbor Ising antiferromagnet on the fcc lattice: Evidence for multicritical behavior. *Phys. Rev. B*, 53:2345–2351, Feb 1996.
- [63] J.-P. Ader. Magnetic order in the frustrated Heisenberg model for the fcc type-I configuration. *Phys. Rev. B*, 65:014411, Nov 2001.
- [64] A. D. Beath and D. H. Ryan. fcc antiferromagnetic Ising model in a uniform external field solved by mean-field theory. *Phys. Rev. B*, 72:014455, Jul 2005.
- [65] A. D. Beath and D. H. Ryan. Thermodynamic properties of the fcc Ising antiferromagnet obtained from precision density of states calculations. *Phys. Rev. B*, 73:174416, May 2006.
- [66] A. D. Beath and D. H. Ryan. Latent heat of the fcc Ising antiferromagnet. *J. Appl. Phys.*, 101(9):09G102, 2007.
- [67] H. T. Diep and H. Kawamura. First-order phase transition in the fcc Heisenberg antiferromagnet. *Phys. Rev. B*, 40:7019–7022, Oct 1989.
- [68] Julio F. Fernández, Horacio A. Farach, Charles P. Poole, and Marcello Puma. Monte Carlo study of a Heisenberg antiferromagnet on an fcc lattice with and without dilution. *Phys. Rev. B*, 27:4274–4280, Apr 1983.

- [69] Marko T. Heinilä and Aarne S. Oja. Long-range order produced by the interaction between spin waves in classical fcc heisenberg models. *Phys. Rev. B*, 48:16514–16523, Dec 1993.
- [70] M. V. Gvozdikova and M. E. Zhitomirsky. A Monte Carlo study of the first-order transition in a Heisenberg FCC antiferromagnet. *JETP Lett.*, 81(5):236–240, 2005.
- [71] D. T. Haar and M. E. Lines. A Molecular-Field Theory of Anisotropic Ferromagnetica. *Philos. Trans. R. Soc. A*, 254(1046):521–555, April 1962.
- [72] E. V. Kuz'min. Quantum spin liquid in the FCC lattice. *J. Exp. Theor. Phys*, 96(1):129–139, 2003.
- [73] P. W. Anderson. Antiferromagnetism. Theory of Superexchange Interaction. *Phys. Rev.*, 79:350–356, Jul 1950.
- [74] J. M. Luttinger and L. Tisza. Theory of dipole interaction in crystals. *Phys. Rev.*, 70:954–964, Dec 1946.
- [75] E. F. Bertaut. Configurations Magnétiques. Méthode de Fourier. *J. Phys. Chem. Solids*, 21(3):256 – 279, 1961.
- [76] I. E. Dzyaloshinskii. Theory of Helicoidal Structures in Antiferromagnets. I. Non-metals. *Zh. Eksp. Teor. Fiz.*, 46:1420, 1964.
- [77] I. E. Dzyaloshinskii. The Theory of Helicoidal Structures in Antiferromagnets. II. Metals. *Zh. Eksp. Teor. Fiz.*, 47:336, 1964.
- [78] Daniel I. Khomskii. *Basic Aspects of the Quantum Theory of Solids*. Cambridge University Press, 2010.
- [79] P. Chandra and B. Douçot. Possible spin-liquid state at large S for the frustrated square Heisenberg lattice. *Phys. Rev. B*, 38:9335–9338, Nov 1988.
- [80] L. B. Ioffe and A. I. Larkin. Effective action of a two-dimensional antiferromagnet. *Int. J. Mod. Phys. B*, 02(02):203–219, 1988.
- [81] E. Rastelli, A. Tassi, and L. Reatto. Non-simple magnetic order for simple hamiltonians. *Physica B+C*, 97(1):1 – 24, 1979.
- [82] J. B. Fouet, P. Sindzingre, and C. Lhuillier. An investigation of the quantum J1-J2-J3 model on the honeycomb lattice. *Eur. Phys. J. B*, 20(2):241–254, 2001.
- [83] A. Mulder, R. Ganesh, L. Capriotti, and A. Paramekanti. Spiral order by disorder and lattice nematic order in a frustrated heisenberg antiferromagnet on the honeycomb lattice. *Phys. Rev. B*, 81:214419, Jun 2010.
- [84] Péter Balla, Yasir Iqbal, and Karlo Penc. Affine lattice construction of spiral surfaces in frustrated heisenberg models. *Phys. Rev. B*, 100:140402, Oct 2019.

- [85] Jan Attig and Simon Trebst. Classical spin spirals in frustrated magnets from free-fermion band topology. *Phys. Rev. B*, 96:085145, Aug 2017.
- [86] Nils Niggemann, Max Hering, and Johannes Reuther. Classical spiral spin liquids as a possible route to quantum spin liquids. *Journal of Physics: Condensed Matter*, 32(2):024001, oct 2019.
- [87] J. T. Chalker, P. C. W. Holdsworth, and E. F. Shender. Hidden order in a frustrated system: Properties of the heisenberg kagomé antiferromagnet. *Phys. Rev. Lett.*, 68:855–858, Feb 1992.
- [88] M. E. Zhitomirsky. Octupolar ordering of classical kagome antiferromagnets in two and three dimensions. *Phys. Rev. B*, 78:094423, Sep 2008.
- [89] J. N. Reimers, A. J. Berlinsky, and A.-C. Shi. Mean-field approach to magnetic ordering in highly frustrated pyrochlores. *Phys. Rev. B*, 43:865–878, Jan 1991.
- [90] J. N. Reimers. Absence of Long-Range Order in a Three-Dimensional Geometrically Frustrated Antiferromagnet. *Phys. Rev. B*, 45:7287–7294, Apr 1992.
- [91] Yasir Iqbal, Tobias Müller, Pratyay Ghosh, Michel J. P. Gingras, Harald O. Jeschke, Stephan Rachel, Johannes Reuther, and Ronny Thomale. Quantum and Classical Phases of the Pyrochlore Heisenberg Model with Competing Interactions. *Phys. Rev. X*, 9:011005, Jan 2019.
- [92] Yasir Iqbal, Tobias Müller, Harald O. Jeschke, Ronny Thomale, and Johannes Reuther. Stability of the spiral spin liquid in MnSc_2S_4 . *Phys. Rev. B*, 98:064427, Aug 2018.
- [93] Yuji Yamamoto and Takeo Nagamiya. Spin arrangements in magnetic compounds of the rocksalt crystal structure. *J. Phys. Soc. Jpn.*, 32(5):1248–1261, 1972.
- [94] Karsten Grosse-Brauckmann. Triply periodic minimal and constant mean curvature surfaces. *Interface Focus*, 2(5):582–588, 2012.
- [95] J. Villain. La structure des substances magnetiques. *J. Phys. Chem. Solids*, 11(3):303 – 309, 1959.
- [96] Akio Yoshimori. A New Type of Antiferromagnetic Structure in the Rutile Type Crystal. *J. Phys. Soc. Jpn.*, 14(6):807–821, 1959.
- [97] Masaya Uchida, Yoshinori Onose, Yoshio Matsui, and Yoshinori Tokura. Real-Space Observation of Helical Spin Order. *Science*, 311(5759):359–361, 2006.
- [98] A. Revelli, C. C. Loo, D. Kiese, P. Becker, T. Fröhlich, T. Lorenz, M. Moretti Sala, G. Monaco, F. L. Buessen, J. Attig, M. Hermanns, S. V. Streltsov, D. I. Khomskii, J. van den Brink, M. Braden, P. H. M. van Loosdrecht, S. Trebst, A. Paramekanti, and M. Grüninger. Spin-orbit entangled $j = \frac{1}{2}$ moments in $\text{Ba}_2\text{CeIrO}_6$: A frustrated fcc quantum magnet. *Phys. Rev. B*, 100:085139, Aug 2019.

- [99] Villain, J. A magnetic analogue of stereoisomerism : application to helimagnetism in two dimensions. *J. Phys. France*, 38(4):385–391, 1977.
- [100] Zohar Nussinov. Commensurate and Incommensurate O(n) Spin Systems: Novel Even-Odd Effects, A Generalized Mermin-Wagner-Coleman Theorem, and Ground States. *arXiv e-prints*, pages cond-mat/0105253, May 2001.
- [101] A. N. Ignatenko and V. Yu. Irkhin. Frustrated Heisenberg Antiferromagnets on Cubic Lattices: Magnetic Structures, Exchange Gaps, and Non-Conventional Critical Behaviour. *J. Sib. Fed. Univ.: Math. Phys. (Ž. Sib. Fed. Univ., Ser. Mat. Fiz. (Online))*, 9:454, Jan 2016.
- [102] Péter Balla, Yasir Iqbal, and Karlo Penc. Degenerate manifolds, helimagnets, and multi- q chiral phases in the classical heisenberg antiferromagnet on the face-centered-cubic lattice. *Phys. Rev. Research*, 2:043278, Nov 2020.
- [103] Zhentao Wang, Yoshitomo Kamiya, Andriy H. Nevidomskyy, and Cristian D. Batista. Three-dimensional crystallization of vortex strings in frustrated quantum magnets. *Phys. Rev. Lett.*, 115:107201, Sep 2015.
- [104] T. A. Kaplan. Classical spin-configuration stability in the presence of competing exchange forces. *Phys. Rev.*, 116:888–889, Nov 1959.
- [105] Pratyay Ghosh, Tobias Müller, Francesco Parisen Toldin, Johannes Richter, Rajesh Narayanan, Ronny Thomale, Johannes Reuther, and Yasir Iqbal. Quantum paramagnetism and helimagnetic orders in the heisenberg model on the body centered cubic lattice. *Phys. Rev. B*, 100:014420, Jul 2019.
- [106] L. M. Corliss, N. Elliott, and J. M. Hastings. Antiferromagnetic Structure of CrN. *Phys. Rev.*, 117:929–935, Feb 1960.
- [107] Tommaso Coletta, M. E. Zhitomirsky, and Frédéric Mila. Quantum stabilization of classically unstable plateau structures. *Phys. Rev. B*, 87:060407, Feb 2013.
- [108] P. W. Anderson. Ordering and Antiferromagnetism in Ferrites. *Phys. Rev.*, 102:1008–1013, May 1956.
- [109] P. A. McClarty, O. Sikora, R. Moessner, K. Penc, F. Pollmann, and N. Shannon. Chain-based order and quantum spin liquids in dipolar spin ice. *Phys. Rev. B*, 92:094418, Sep 2015.
- [110] Ning-Ning Sun and Huai-Yu Wang. The J_1 - J_2 model on the face-centered-cubic lattices. *J. Magn. Magn. Mater.*, 454:176 – 184, 2018.
- [111] Jonas Sonnenschein, Aishwarya Chauhan, Yasir Iqbal, and Johannes Reuther. Projective symmetry group classifications of quantum spin liquids on the simple cubic, body centered cubic, and face centered cubic lattices, 2020.

- [112] Shravani Chillal, Yasir Iqbal, Harald O. Jeschke, Jose A. Rodriguez-Rivera, Robert Bewley, Pascal Manuel, Dmitry Khalyavin, Paul Steffens, Ronny Thomale, A. T. M. Nazmul Islam, Johannes Reuther, and Bella Lake. Evidence for a three-dimensional quantum spin liquid in $\text{PbCuTe}_2\text{O}_6$. *Nat. Commun.*, 11(1):2348, 2020.
- [113] Yoshinori Tokura and Naoya Kanazawa. Magnetic skyrmion materials. *Chemical Reviews*, 121(5):2857–2897, 2021.
- [114] Albert Fert, Nicolas Reyren, and Vincent Cros. Magnetic skyrmions: advances in physics and potential applications. *Nature Reviews Materials*, 2(7):17031, June 2017.
- [115] G. Baskaran. Novel local symmetries and chiral-symmetry-broken phases in $s=1/2$ triangular-lattice heisenberg model. *Phys. Rev. Lett.*, 63:2524–2527, Nov 1989.
- [116] Daniel Grohol, Kittiwit Matan, Jin-Hyung Cho, Seung-Hun Lee, Jeffrey W. Lynn, Daniel G. Nocera, and Young S. Lee. Spin chirality on a two-dimensional frustrated lattice. *Nature Materials*, 4(4):323–328, April 2005.
- [117] Yutaka Akagi and Yukitoshi Motome. Spin chirality ordering and anomalous hall effect in the ferromagnetic kondo lattice model on a triangular lattice. *Journal of the Physical Society of Japan*, 79(8):083711, 2010.
- [118] Manuel Laubach, Darshan G. Joshi, Johannes Reuther, Ronny Thomale, Matthias Vojta, and Stephan Rachel. Quantum disordered insulating phase in the frustrated cubic-lattice Hubbard model. *Phys. Rev. B*, 93:041106, Jan 2016.
- [119] Yasir Iqbal, Ronny Thomale, Francesco Parisen Toldin, Stephan Rachel, and Johannes Reuther. Functional renormalization group for three-dimensional quantum magnetism. *Phys. Rev. B*, 94:140408, Oct 2016.
- [120] J. Oitmaa. Frustrated $J_1 - J_2 - J_3$ Heisenberg antiferromagnet on the simple cubic lattice. *Phys. Rev. B*, 95:014427, Jan 2017.
- [121] A. F. Andreev and I. A. Grishchuk. Spin nematics. *JETP Lett.*, 60:267, May 1984.
- [122] Nic Shannon, Tsutomu Momoi, and Philippe Sindzingre. Nematic Order in Square Lattice Frustrated Ferromagnets. *Phys. Rev. Lett.*, 96:027213, Jan 2006.
- [123] P. Sindzingre, N. Shannon, and T. Momoi. Nematic order in square lattice frustrated ferromagnets. *J. Magn. Magn. Mater.*, 310(2, Part 2):1340 – 1342, 2007.
- [124] Philippe Sindzingre, Nic Shannon, and Tsutomu Momoi. Phase diagram of the spin-1/2 J_1 - J_2 - J_3 Heisenberg model on the square lattice. *J. Phys.: Conf. Ser.*, 200(2):022058, 2010.
- [125] Ryuichi Shindou and Tsutomu Momoi. $SU(2)$ slave-boson formulation of spin nematic states in $S = \frac{1}{2}$ frustrated ferromagnets. *Phys. Rev. B*, 80:064410, Aug 2009.

- [126] Ryuichi Shindou, Seiji Yunoki, and Tsutomu Momoi. Projective studies of spin nematics in a quantum frustrated ferromagnet. *Phys. Rev. B*, 84:134414, Oct 2011.
- [127] J. Richter, R. Darradi, J. Schulenburg, D. J. J. Farnell, and H. Rosner. Frustrated spin- $\frac{1}{2}$ $J_1 - J_2$ heisenberg ferromagnet on the square lattice studied via exact diagonalization and coupled-cluster method. *Phys. Rev. B*, 81:174429, May 2010.
- [128] N. Shannon, B. Schmidt, K. Penc, and P. Thalmeier. Finite temperature properties and frustrated ferromagnetism in a square lattice heisenberg model. *Eur. Phys. J. B*, 38(4):599–616, 2004.
- [129] Nic Shannon, Karlo Penc, and Yukitoshi Motome. Nematic, vector-multipole, and plateau-liquid states in the classical $O(3)$ pyrochlore antiferromagnet with bi-quadratic interactions in applied magnetic field. *Phys. Rev. B*, 81:184409, May 2010.
- [130] Luis Seabra, Philippe Sindzingre, Tsutomu Momoi, and Nic Shannon. Novel phases in a square-lattice frustrated ferromagnet : $\frac{1}{3}$ -magnetization plateau, helicoidal spin liquid, and vortex crystal. *Phys. Rev. B*, 93:085132, Feb 2016.
- [131] Yasir Iqbal, Pratyay Ghosh, Rajesh Narayanan, Brijesh Kumar, Johannes Reuther, and Ronny Thomale. Intertwined nematic orders in a frustrated ferromagnet. *Phys. Rev. B*, 94:224403, Dec 2016.
- [132] A. I. Smirnov, T. A. Soldatov, O. A. Petrenko, A. Takata, T. Kida, M. Hagiwara, A. Ya. Shapiro, and M. E. Zhitomirsky. Order by Quenched Disorder in the Model Triangular Antiferromagnet $\text{RbFe}(\text{MoO}_4)_2$. *Phys. Rev. Lett.*, 119:047204, Jul 2017.
- [133] Mois Ilia Aroyo, Juan Manuel Perez-Mato, Cesar Capillas, Eli Kroumova, Svetoslav Ivantchev, Gotzon Madariaga, Asen Kirov, and Hans Wondratschek. Bilbao Crystallographic Server: I. Databases and crystallographic computing programs. *Z. Kristallogr. Cryst. Mater*, 221:15–27, Jan 2006.
- [134] M. Tinkham. *Group Theory and Quantum Mechanics*. Dover Books on Chemistry. Dover Publications, 2012.
- [135] I. M. Lifshitz. Anomalies of electron characteristics of a metal in the high pressure region. *Zh. Eksp. Teor. Fiz.*, 11(5):1130, 1960.
- [136] B. R. Cooper and R. J. Elliott. Spin-wave theory of magnetic resonance in spiral spin structures: Effect of an applied field. *Phys. Rev.*, 131:1043–1056, Aug 1963.
- [137] M. Akaki, H. Iwamoto, T. Kihara, M. Tokunaga, and H. Kuwahara. Multiferroic properties of an åkermanite $\text{Sr}_2\text{CoSi}_2\text{O}_7$ single crystal in high magnetic fields. *Phys. Rev. B*, 86:060413, Aug 2012.
- [138] M. Akaki, T. Tadokoro, T. Kihara, M. Tokunaga, and H. Kuwahara. High magnetic field dependence of magnetodielectric properties in $\text{Sr}_2\text{CoSi}_2\text{O}_7$ crystal. *J. Low Temp. Phys.*, 170(5-6):291–295, 2013.

- [139] Dávid Szaller, Sándor Bordács, Vilmos Kocsis, Toomas Rõõm, Urmas Nagel, and István Kézsmárki. Effect of spin excitations with simultaneous magnetic- and electric-dipole character on the static magnetoelectric properties of multiferroic materials. *Phys. Rev. B*, 89:184419, May 2014.
- [140] Ryogo Kubo. Statistical-mechanical theory of irreversible processes. i. general theory and simple applications to magnetic and conduction problems. *Journal of the Physical Society of Japan*, 12(6):570–586, 1957.
- [141] S. Miyahara and N. Furukawa. Theory of antisymmetric spin-pair-dependent electric polarization in multiferroics. *Phys. Rev. B*, 93:014445, Jan 2016.
- [142] S.L. Altmann and P. Herzig. *Point-group Theory Tables*. Oxford science publications. Clarendon Press, 1994.
- [143] L.D. Barron and J. Vrbancich. Magneto-chiral birefringence and dichroism. *Molec. Phys.*, 51:715–730, 1984.
- [144] Mitsuru Akaki, Daichi Yoshizawa, Akira Okutani, Takanori Kida, Judit Romhányi, Karlo Penc, and Masayuki Hagiwara. Direct observation of spin-quadrupolar excitations in $\text{Sr}_2\text{CoGe}_2\text{O}_7$ by high-field electron spin resonance. *Phys. Rev. B*, 96:214406, Dec 2017.
- [145] J. Viirok, U. Nagel, T. Rõõm, D. G. Farkas, P. Balla, D. Szaller, V. Kocsis, Y. Tokunaga, Y. Taguchi, Y. Tokura, B. Bernáth, D. L. Kamenskyi, I. Kézsmárki, S. Bordács, and K. Penc. Directional dichroism in the paramagnetic state of multiferroics: A case study of infrared light absorption in $\text{Sr}_2\text{CoSi}_2\text{O}_7$ at high temperatures. *Phys. Rev. B*, 99:014410, Jan 2019.
- [146] J. Vít, J. Viirok, L. Peedu, T. Rõõm, U. Nagel, V. Kocsis, Y. Tokunaga, Y. Taguchi, Y. Tokura, I. Kézsmárki, P. Balla, K. Penc, J. Romhányi, and S. Bordács. In situ electric-field control of the nonreciprocal directional dichroism in the multiferroic $\text{Ba}_2\text{CoGe}_2\text{O}_7$. *Phys. Rev. Lett.*, 127:157201, Oct 2021.
- [147] A. Szilva, P. Balla, O. Eriksson, G. Zaránd, and L. Szunyogh. Universal distribution of magnetic anisotropy of impurities in ordered and disordered nanograins. *Phys. Rev. B*, 91:134421, Apr 2015.
- [148] S. E. Korshunov. Chiral phase of the heisenberg antiferromagnet with a triangular lattice. *Phys. Rev. B*, 47:6165–6168, Mar 1993.
- [149] Tsutomu Momoi, Kenn Kubo, and Koji Niki. Possible chiral phase transition in two-dimensional solid ^3He . *Phys. Rev. Lett.*, 79:2081–2084, Sep 1997.
- [150] Kenn Kubo and Tsutomu Momoi. Ground state of a spin system with two- and four-spin exchange interactions on the triangular lattice. *Zeitschrift für Physik B Condensed Matter*, 103(3):485–489, April 1997.

-
- [151] J.-C. Domenge, P. Sindzingre, C. Lhuillier, and L. Pierre. Twelve sublattice ordered phase in the $J_1 - J_2$ model on the kagomé lattice. *Phys. Rev. B*, 72:024433, Jul 2005.
- [152] O Janson, J Richter, and H Rosner. Intrinsic peculiarities of real material realizations of a spin-1/2 kagomé lattice. *Journal of Physics: Conference Series*, 145:012008, jan 2009.
- [153] X. G. Wen, Frank Wilczek, and A. Zee. Chiral spin states and superconductivity. *Phys. Rev. B*, 39:11413–11423, Jun 1989.
- [154] P.B. Wiegmann. Towards a gauge theory of strongly correlated electronic systems. *Physica C: Superconductivity*, 153-155:103–108, 1988.
- [155] L. Messio, C. Lhuillier, and G. Misguich. Lattice symmetries and regular magnetic orders in classical frustrated antiferromagnets. *Phys. Rev. B*, 83:184401, May 2011.
- [156] J.J. Sakurai and J. Napolitano. *Modern Quantum Mechanics*. Addison-Wesley, 2011.